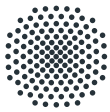

Universität Stuttgart

Collective Modes of the Superconducting Condensate

Von der Fakultät für Mathematik und Physik der Universität Stuttgart zur Erlangung der Würde eines Doktors der Naturwissenschaften (Dr. rer. nat.) genehmigte Abhandlung

Vorgelegt von

Rafael Haenel

aus Berlin

Hauptberichter:	Prof. Dr. Maria Daghofer
Mitberichter:	Prof. Dr. Dirk Manske
	Prof. Dr. Martin Dressel
	Prof. Dr. Ilya Eremin
	Prof. Dr. Marcel Franz
	Prof. Dr. Mona Berciu
	Prof. Dr. Andrew MacFarlane

Tag der mündlichen Prüfung: 8. Mai 2023

Universität Stuttgart und Max-Planck-Institut für Festkörperforschung

University of British Columbia

2023

Collective Modes of the Superconducting Condensate

by

Rafael Haenel

B. Sc., Technical University of Berlin, 2017

M. Sc., University of British Columbia, 2019

A THESIS SUBMITTED IN PARTIAL FULFILLMENT
OF THE REQUIREMENTS FOR THE DEGREE OF

Doctor of Philosophy

in

THE FACULTY OF GRADUATE AND POSTDOCTORAL STUDIES

(Physics)

The University of British Columbia

(Vancouver)

June 2023

The following individuals certify that they have read, and recommend to the Faculty of Graduate and Postdoctoral Studies for acceptance, the thesis entitled:

Collective Modes of the Superconducting Condensate

submitted by **Rafael Haenel** in partial fulfillment of the requirements for the degree of **Doctor of Philosophy** in **Physics**.

Examining Committee:

Marcel Franz, Professor, Department of Physics and Astronomy, University of British Columbia
Supervisor

Maria Daghofer, Professor, Department of Physics, University of Stuttgart
Co-Supervisor

Dirk Manske, Professor, Max-Planck-Institute for Solid State Research, Stuttgart
Supervisory Committee Member

Mona Berciu, Professor, Department of Physics and Astronomy, University of British Columbia
University Examiner

Andrew MacFarlane, Professor, Department of Chemistry, University of British Columbia
University Examiner

Martin Dressel, Professor, Department of Physics, University of Stuttgart
Additional Examiner

Ilya Eremin, Professor, Department of Physics, Ruhr Universität Bochum
External Examiner

Additional Supervisory Committee Members:

Douglas Bonn, Professor, Department of Physics and Astronomy, University of British Columbia
Supervisory Committee Member

Robert Raussendorf, Professor, Department of Physics and Astronomy, University of British Columbia
Supervisory Committee Member

Gordon Semenoff, Professor, Department of Physics and Astronomy, University of British Columbia
Supervisory Committee Member

Abstract

When a continuous symmetry is spontaneously broken, collective modes emerge. Usually, their spectrum is dominated by the low-energy physics of massless Goldstone modes. Superconductors, that break $U(1)$ symmetry, are different. Here, the Goldstone boson is gapped out due to the Anderson-Higgs mechanism.

The superconducting condensate can therefore host a zoo of massive collective excitations that are stable for lack of a gapless decay channel. The most prominent of them is the Higgs mode. Spectroscopy of collective modes can serve as a probe to reveal the nature of the superconducting state.

In this thesis, we study the signatures of collective modes in nonlinear optical experiments. We explore the theoretical description of a new spectroscopic excitation scheme. We show how impurity scattering significantly enhances the optical Higgs mode response. We apply group theoretical methods to multi-order-parameter theories and investigate microscopic signatures of coupled modes in third harmonic generation experiments. We study the phenomenology and collective mode spectrum of an exotic system of twisted cuprate bilayers that supports topological superconductivity. Finally, we propose a novel device implementation of the superconducting diode effect.

These results contribute to the emerging field of collective mode spectroscopy.

Zusammenfassung

Die spontane Symmetriebrechung ist das grundlegende Konzept einer breiten Klasse von Materialphasen. Diese Phasen können durch einen lokalen Ordnungsparameter charakterisiert werden, der auf die spontane Brechung einer Symmetrie hinweist. *Spontan* bedeutet in diesem Kontext, dass der quantenmechanische Grundzustand eine bestimmte Symmetrie verletzt, obwohl die zugrunde liegenden physikalischen Bewegungsgleichungen symmetrisch sind.

Zu den Beispielen spontaner Symmetriebrechung gehören Kristallisation, bei der die kontinuierliche Translationssymmetrie gebrochen wird, Ferromagnetismus mit gebrochener Spin-Rotations-Symmetrie SU(2) und Suprafluidität und Supraleitung, mit gebrochener U(1) Symmetrie. Nach dem Goldstone Theorem garantiert die Brechung jeder kontinuierlichen Symmetrie die Existenz einer masselosen bosonischen Anregung. Im Falle von Kristallen und Suprafluiden ist dies das Phonon, bei Magneten das sogenannte Magnon.

Zusätzlich zu den Goldstone-Bosonen können spontan Symmetrie-gebrochene Phasen massereiche bosonische Anregungen beherbergen. Ihr Phasenraum wird jedoch stark von Zerfallskanälen zu den Goldstone-Moden mit niedrigeren Energien dominiert. Daher sind massereiche kollektive Anregungen in der Regel instabil.

Die Supraleitung stellt einen besonderen Fall dar. Der komplexe Supraleitungs-Ordnungsparameter beschreibt ein geladenes Kondensat von Elektronen. Daher koppelt der Ordnungsparameter an das elektromagnetische Eichfeld. Die spontan gebrochene U(1)-Symmetrie ist Teil der größeren lokalen Eichsymmetrie. Als solche stellt sie keine eigentliche Symmetrie dar, sondern eine Eichredundanz. Folglich beherbergen Supraleiter keine masselosen Goldstone-Moden.

Die energetisch tiefst-liegende Anregung in einem Supraleiter ist daher eine massive kollektive Mode des supraleitenden Kondensats. In einigen Fällen können solche Anregungen aufgrund der Abwesenheit der Goldstone Zerfallskanäle stabil und langlebig sein.

Die bekannteste kollektive supraleitende Mode ist die Higgs Mode. Sie verkörpert Amplitudenfluktuationen des supraleitenden Ordnungsparameters und tritt in jeder theoretischen Beschreibung eines Supraleiters auf, unabhängig von der Anzahl der supraleitenden Ordnungsparameter. In komplexeren Theorien mit n Ordnungsparametern, treten $2n - 1$ kollektive Moden auf. Zu diesen gehören Leggett und Bardasis-Schrieffer Moden, welche Phasenfluktuation der komplexen Ordnungsparameter beschreiben.

Kollektive Anregungen des supraleitenden Kondensats liegen im THz-Bereich und können mit nichtlinearen THz-spektroskopischen Methoden experimentell untersucht werden.

Die vorliegende Dissertation wendet einen diagrammatischen Quasi-Gleichgewichts-Formalismus an, der zeitlich aufgelöste Observablen störungstheoretisch berechnet, um spektroskopische Experimente zu

modellieren.

Die Hauptansätze für THz-Anregungen bestehen aus zwei Methoden. Für erste werden supraleitende Materialien in einem Pump-Probe-Setup beleuchtet, wobei eine Anregung der Higgs-Mode durch einen kurzen Pump-Laserpuls erfolgt, und die optische Leitfähigkeit des Supraleiters nach einer variablen Zeitverzögerung mit einem Probe-Puls sondiert wird. In einem zweiten Experimenttyp werden kollektive Moden durch einen multizyklischen THz-Puls mit einer wohldefinierten Trägerfrequenz angeregt, was zu einer resonanten Erzeugung der dritten Harmonischen im transmittierten oder reflektierten Puls führt. Die Messung der Intensität der generierten dritten Harmonischen gibt Aufschluss über das Spektrum kollektiver Moden.

In dieser Dissertation wird eine neue experimentelle Plattform theoretisch analysiert, bei welcher eine Abfolge von einem optischen Pump-Puls und einem multizyklischen THz-Puls angewandt wird. Hierbei wir die Generierung der dritten Harmonischen in einem gepumpten Zustand untersucht. Es wird dargestellt, wie Signaturen von kollektiven Moden in 2D-spektroskopischen Diagrammen untersucht werden können.

Supraleitende Theorien mit mehreren Ordnungsparametern beherbergen eine Vielfalt kollektiver Moden. Die Struktur solcher Theorien ist stark von Symmetrien der zugrundeliegenden mikroskopischen Kristallstrukturen diktiert und kann mithilfe gruppentheoretischer Methoden analysiert werden. Insbesondere gehören Ordnungsparameter zu irreduziblen Darstellungen einer Punktgruppe. Die Analyse aller irreduziblen Darstellungen einer Symmetriegruppe ist daher aufschlussgebend für alle möglichen Ordnungsparameter in einem Supraleiter. Mikroskopisch können Multi-Ordnungsparameter entweder Supraleitung in mehreren Bändern beschreiben oder Kondensation von mehreren Symmetriekanälen innerhalb eines Bandes.

In dieser Dissertation werden verschiedene Konsequenzen von Multi-Ordnungsparameter-Strukturen beleuchtet. Es wird die Auswirkung der Präsenz mehrerer gekoppelter Ordnungsparameter auf die Generierung der dritten Harmonischen in nichtlinearen THz-Experimenten untersucht. Hierbei wir gezeigt, dass die Messung der elektromagnetischen Phasenverschiebung des reflektierten oder transmittierten THz-Pulses Informationen über das kollektive Modenspektrum enthalten kann. Eine interessante Anwendung besteht in dem Fall, dass neben der optisch aktiven Higgs-Mode eine weitere optisch inaktive kollektive Mode existiert. Solange diese beiden Moden miteinander gekoppelt sind, kann die Spektroskopie der Higgs Mode Aufschluss über die Resonanz-Struktur der nicht-sichtbaren Mode geben. In diesem Sinne kann die Higgs-Mode prinzipiell als spektroskopische Sonde fungieren.

Weiterhin wird der Einfluss von nicht-magnetischen Störstellen in einem Zweiband-Supraleiter auf das Spektrum der kollektiven Moden untersucht. Es wird gezeigt, dass Störstellen die elektromagnetische Antwort der Higgs-Mode in der nichtlinearen optischen Leitfähigkeit drastisch verstärken, während das optische Verhalten der Leggett-Mode unabhängig von der Störstellenkonzentration ist.

In den Vergangenen Jahren hat die Einführung von verdrehten Doppel-Lagen von 2D Materialien einen neuen Ansatzpunkt zur Untersuchung von Materialeigenschaften insbesondere im Hinblick auf Supraleitfähigkeit eröffnet. Üblicherweise beruhen diese Eigenschaften auf Bandstruktur-Effekten. Bei einer Verdrehung der beiden Atomlagen um einen sogenannten magischen Winkel von 1.1° entsteht im Falle von Graphen ein Flachband, in dem elektronische Korrelationen von dominierender Bedeutung sind. Im Zuge der Entwicklung des Feldes der *Twistronik* (aus *twist* und *Elektronik*) wurde kürzlich die Auswirkung

der Verdrehung von supraleitenden Doppellagen untersucht. Hierbei wurde gezeigt, dass zwei um 45° verdrehte Cuprat-Monolagen spontan die Zeitumkehr-Symmetrie brechen und einen topologischen supraleitenden Grundzustand realisieren. Dieser Effekt beruht nicht auf Korrelationseffektiven, sondern allein auf der Symmetrie der Ordnungsparameter der individuellen Monolagen. In dieser Dissertation wird die spontane Symmetriebrechung von verdrehten Cuprat-Bi-Lagen gruppentheoretisch erklärt. Zudem wird das Spektrum kollektiver Moden berechnet und ein realistisches mikroskopisches Model untersucht, das eine inkohärente Kopplungen der beiden Monolagen voraussetzt.

Im letzten Teil dieser Arbeit wird ein neuartiger supraleitender Josephson-Schaltkreis vorgeschlagen, der den supraleitenden Diodeneffekt realisiert. Der supraleitende Diodeneffekt tritt auf, wenn der maximale Tunnelstrom zwischen zwei Supraleitern eines Josephson-Kontakts von der Polarität abhängt. Der Diodeneffekt wurde in verdrehten Cuprat-Doppellagen und einer Vielzahl von Materialien gemessen.

Während aktuelle experimentelle und theoretische Umsetzungen des Diodeneffekts auf komplexen Materialplattformen beruhen, kann das hier beschriebene Gerät mithilfe industrieller supraleitender Materialien und skalierbarer Halbleiterfertigungstechnologien fabriziert werden.

Lay Summary

We investigate the signatures of collective modes of superconductors in nonlinear optical experiments. Superconductors are materials that expel magnetic fields and have zero electrical resistance. They are characterized by macroscopic coherence of the quantum mechanical phase and an excitation gap in their electronic spectrum. Collective modes lead to oscillations of the superconducting excitation gap and the quantum phase. The most ubiquitous collective excitation is the Higgs mode.

The study of superconducting collective modes reveals information about fundamental properties of superconductors. In this thesis, we theoretically introduce a new spectroscopic platform to measure the collective excitation spectrum. We demonstrate that experimental signatures of the Higgs mode are strongly enhanced by impurities in a material. Further, the collective excitations of a stack of two atomically thin superconducting films that are twisted relative to each other are examined. This stacked structure can be used to engineer a novel electronic device, called a superconducting diode, whose properties and implementation we study in detail.

The results in this thesis contribute to the emerging field of superconducting collective mode spectroscopy.

Preface

The work presented in this thesis is adapted from the following publications:

- Chapter 4 is based on key ideas presented in *Transient excitation of Higgs and high-harmonic generation in superconductors with quench-drive spectroscopy* by M. Puviani, **R.H.**, D. Manske, Phys. Rev. B 107, 094501 (2023). It is motivated by experimental work by M. Kim and S. Kaiser. The key idea that lead to successful interpretation of the experimental data was generated by myself. For this thesis, the content of the manuscript has been completely rewritten and I have created new figures from my independent numerical calculations.

  Results of above publication have also been published in the experimental work *Tracing the dynamics of the superconducting order via transient Third Harmonic Generation* by M. Kim, S. Kovalev, M. Udina, **R.H.**, G. Kim, M. Puviani, G. Cristiani, I. Ilyakov, T. V. de Oliveira, A. Ponomaryov, J.C. Deinert, G. Logvenov, B. Keimer, D. Manske, L. Benfatto, S. Kaiser, arXiv:2303.03288 (2023).

- Chapter 5 is published as *Time-resolved optical conductivity and Higgs oscillations in two-band dirty superconductors* by **R.H.**, P. Froese, D. Manske, L. Schwarz, Phys. Rev. B 104, 134504 (2021). The project was supervised by Lukas Schwarz and Dirk Manske. I performed all diagrammatic calculations, density-matrix equation of motions were numerically solved by Paul Froese. The manuscript was written by myself. P.F. contributed a technical appendix that is not used in this thesis.

- Chapter 6 is published as *Phase signatures in the third-harmonic response of Higgs and coexisting modes in superconductors* by L. Schwarz, **R.H.**, D. Manske, Phys. Rev. B 104, 174508 (2021). The manuscript was drafted by Lukas Schwarz with contributions and input from myself. Analytical calculations were performed by L. S. and myself. Numerical calculations were performed by L.S. with an impurity calculation contributed by myself.

  Additionally, parts of this chapter have been published as an appendix to the experimental work *Fano interference between collective modes in cuprate high-T_c superconductors* by H. Chu, S. Kovalev, Z. X. Wang, L. Schwarz, T. Dong, L. Feng, R. Haenel, M. Kim, P. Shabestari, L. P. Hoang, K. Honasoge, R. D. Dawson, D. Putzky, G. Kim, M. Puviani, M. Chen, N. Awari, A. N. Ponomaryov, I. Ilyakov, M. Bluschke, F. Boschini, M. Zonno, S. Zhdanovich, M. Na, G. Christiani, G. Logvenov, D. J. Jones, A. Damascelli, M. Minola, B. Keimer, D. Manske, N. Wang, J. C. Deinert, S. Kaiser, Nature Communications 14, 1343 (2023).

- Chapter 7 is published as *Incoherent tunneling and topological superconductivity in twisted cuprate bilayers* by **R.H.**, T. Tummuru, M. Franz, Phys. Rev. B 106, 104505 (2022). I have appended the chapter by a section on collective modes. The project was supervised by M.F.. I performed all numerical calculations in the continuum limit and generated the corresponding figures. Lattice calculations were done by Tarun Tummuru. The manuscript was written by myself, with contributions from T.T. and input from M.F.

- Chapter 8 has been published as a preprint *Superconducting diode from flux biased Josephson junction arrays* by **R.H.**, O. Can, arXiv:2212.02657. For this thesis, I have rewritten the introduction. The publication is based on an original idea of mine that was further developed together with Oguzhan Can. I performed numerical calculations and generated all figures. The manuscript was drafted by myself, with contributions from O.C..

Contents

List of Tables

List of Figures

List of Abbreviations

ARPES angle-resolved photoemission

BCS Bardeen, Cooper, Schrieffer

DFG Difference Frequency Generation

EOS electro-optic sampling

irrep irreducible representation

M-EELS momentum-resolved electron energy loss spectroscopy

SFG Sum Frequency Generation

THG Third Harmonic Generation

Acknowledgments

My time as a PhD student has been a very rewarding experience. During the past three years, I embarked on a journey of scientific growth. My innate desire to continuously learn has made this experience not only enjoyable, but also deeply fulfilling. None of this would have been possible without many people who I would like to acknowledge here.

I foremost would like to thank my co-supervisors, Marcel Franz, Dirk Manske, and Maria Daghofer. Their deep physical intuition, distinct advice, and continuous guidance have been the key support during my time as a graduate student in the international joint PhD program at UBC and Max-Planck-Institute Stuttgart.

My work has been the result of many collaborations and I would like to thank all my friends, colleagues, and collaborators for our countless physics discussions and derivations, supportive teamwork, and sometimes long working nights. They are Tarun Tummuru, Oguzhan Can, Sharmistha Sahoo, Pedro Lopes, Paul Froese, Robert Raussendorf in Vancouver and Lukas Schwarz, Matteo Puviani, Sida Tian, Paul Froese, Minjae Kim, Stefan Kaiser, Hao Chu in Stuttgart.

Particularly I am thankful to have been working among a fantastic research team: Sayak Dasgupta, Shannon Egan, Niclas Heinsdorf, Simon Klein, Etienne Lantagne-Hurtubise, Chengshu Li, Alberto Nocera, Vedangi Pathak, Stephan Plugge, Benjamin Zou. Not only did I learn a lot from all of you on an academic level, but I also drew a wonderful amount of motivation and inspiration from you.

Finally, my journey would not have been possible without the love, support, and encouragement I received from my family!

Chapter 1

Introduction

Spontaneous symmetry breaking lies at the heart of a wide range of physical phenomena. It is the underlying concept that defines many phases of matter. These phases can be characterized by a local order parameter that becomes finite at a phase transition, indicating the spontaneous breakdown of a symmetry.

Among the examples of spontaneous symmetry breaking are crystallization, where continuous translational symmetry is broken down to discrete translations; ferromagnetism, where spin-rotational symmetry $SU(2)$ is broken; superfluidity and superconductivity where the system spontaneously breaks $U(1)$. A spontaneously symmetry-broken phase hosts gapless collective excitations. This is guaranteed by the Goldstone theorem which states that there is one massless bosonic particle for each continuous broken symmetry. In the case of crystals and superfluids, this is the phonon. For magnets, one obtains magnons.

In addition to the Goldstone bosons, spontaneously broken phases might also host massive bosonic excitations. However, their phase space is strongly dominated by decay channels to the Goldstone modes at lower energies. Therefore, massive collective excitations are usually unstable.

Superconductivity is different. The superconducting order parameter describes a charged condensate of electrons. Therefore, the order parameter couples to the electromagnetic gauge field. The spontaneously broken $U(1)$ symmetry, it turns out, is actually part of the larger local gauge symmetry. As such, it does not constitute a real symmetry but merely reflects gauge redundancy. As a consequence, superconductors do not host a Goldstone mode. From a different viewpoint, the superconducting Goldstone mode is absorbed by the gauge field, which in turn becomes massive. This is the so-called Anderson Higgs mechanism, a central paradigm of superconductivity [8, 9, 64].

We see that superconductivity is a unique case. Superconductors allow for massive collective excitations that are stable due to the lack of a massless Goldstone decay channel. One such massive excitation is the Higgs mode. It corresponds to quantized amplitude excitations of the order parameter. Unfortunately, its energy coincides with the onset of the fermionic single-particle excitation continuum. In a twist of fate, not the Goldstone mode, but decay into fermionic quasiparticle excitations make the Higgs mode strongly overdamped. Nevertheless, the Higgs mode has attracted remarkable theoretical and experimental interest [145]. Considerable effort has been invested in studying its signatures in nonlinear optical response experiments [37, 54, 80, 81, 86, 103, 104, 163]. The Higgs mode is a central theme in this thesis.

In more complicated superconducting systems, where multiple complex order parameters are needed to

describe the phase transition, additional collective modes arise. They correspond to various combinations of amplitude and phase fluctuations of the order parameters. The Leggett mode [91] or Bardasis-Schrieffer mode [18], for example, correspond to relative phase fluctuations in two-order-parameter superconductors. Notably, these additional collective modes can indeed exist below the single-particle continuum, where they constitute long-lived and stable bosonic excitations.

The study of collective modes can reveal properties of the superconducting condensate, such as the pairing symmetry [139]. Recent progress in studying the collective mode spectrum, along with the contents of this thesis, can therefore be contextualized to contribute to the advancement of the emerging field of *Higgs and collective mode spectroscopy*.

This thesis is organized as follows. In the remainder of this chapter, we introduce the phenomenology of superconductors within the Landau-Ginzburg framework of phase transitions of a single-component order parameter. In chapter 2 we generalize this to the case of multi-component order parameters. Here, we will see how the lattice symmetries of a microscopic crystal manifest itself in the structure of the Landau-Ginzburg theory. In chapter 3, we turn to a fully microscopic derivation of superconductivity from a path integral. We show that the superconducting order parameters of the Landau-Ginzburg theory can be identified with bosonic Hubbard-Stratonovich fields of the path integral. We derive the structure of the nonlinear optical susceptibility, that fully specifies the nonlinear optical response. In chapter 4, we outline how the results of THz spectroscopic experiments can be understood within the microscopic framework. These spectroscopic techniques comprise THz pump-probe spectroscopy, third harmonic generation, and a novel scheme that we call quench-drive spectroscopy.

In chapter 5, we study the effects of impurities on a two-band superconductor, relevant for MgB_2. Here, we introduce the Leggett mode for the first time. Higgs, Bardasis-Schrieffer, and competing charge density fluctuations are studied in chapter 6 where we emphasize their optical phase response in third-harmonic generation (THG) experiments.

In chapter 7 we analyze the effect of incoherent interlayer tunneling in twisted-cuprate bilayer samples that have been proposed to constitute the first known example of a high-T_c topological superconductor. We additionally examine the collective mode spectrum and propose that in-gap collective excitations could provide a signature of the topological phase transition.

Finally, in chapter 8, we leave the realm of collective fluctuations. We show that even the classically treated superconducting groundstate can give rise to novel concepts: the superconducting diode effect.

We conclude in chapter 9.

1.1 Superconductivity

The phenomenology of superconductivity can certainly be counted as one of the marvelous gifts of physics. In 1911 Onnes discovered that the electrical resistance of mercury vanishes below a temperature of $4.2\,\mathrm{K}$ [79]. This discovery came to the surprise of the theoretical community. While it was speculated that the electrical resistance of metals might tend towards zero into the zero Kelvin limit, no one had anticipated that the electrical resistance would vanish at a finite critical temperature T_c. Soon, different materials were discovered to become superconducting at low temperatures, such as lead, niobium, or, more recently, magne-

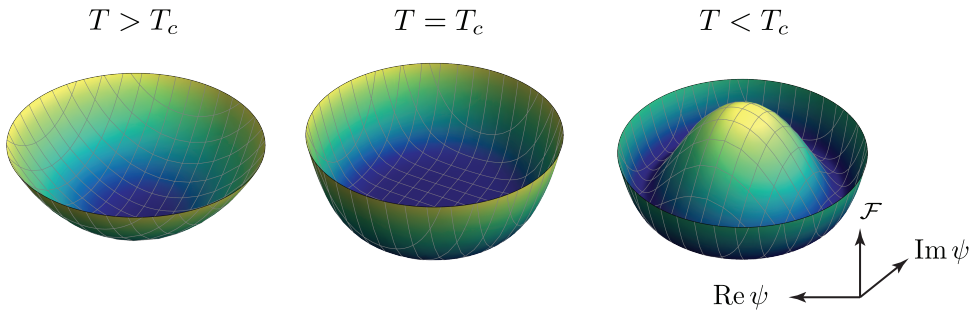

Figure 1.1: The free energy of a Landau-Ginzburg free energy of a complex order parameter above, at, and below the critical temperature T_c of the superconducting phase transition.

sium diboride (MgB_2) [117]. In 1933 it was discovered by Meissner that metals in the superconducting state expel magnetic fields [108]. The Meissner effect today serves as the main criterion of superconductivity.

The first successful theoretical description in terms of a phenomenological model in the general framework of phase transitions was put forward by Landau and Ginzburg [53]. Here, a striking difference between the superconducting state and the normal state is apparent: Whereas regular current flow in metals arises from quasiparticle excitations and necessarily invokes a resistance parameter due to impurity scattering, supercurrent flow is of different nature. It relies on the deformation of the phase of a macroscopic order parameter and is ballistic in the sense that it lacks a resistance parameter.

In 1957 a microscopic description of superconductivity was introduced by Bardeen, Cooper, Schrieffer (BCS) [19]. Their so-called BCS theory was later shown to reproduce the Landau-Ginzburg description as a limit case. In the microscopic description, the phase related to current flow can be seen to correspond to macroscopic coherence of paired electrons. In contrast to resistive current flow in regular conductors, it was shown by Anderson that the superconducting phenomenology is insensitive to impurity scattering [6].

In this chapter we will focus on the phenomenological description due to Landau and Ginzburg. In chapter 3 we will discuss the microscopic viewpoint.

1.2 Landau-Ginzburg formalism of spontaneous symmetry breaking

Within the Landau-Ginzburg framework, the free energy in the vicinity of the metal-superconductor phase transition is given in terms of a phenomenological complex order parameter $\psi(\boldsymbol{x})$ as

$$\mathcal{F}[\psi] = \alpha|\psi|^2 + \beta|\psi|^4 + \kappa|\nabla\psi|^2\,. \tag{1.1}$$

Here, α, β, κ can in principle be viewed as experimental fit parameters. For the free energy to have a global minimum, it is taken that $\beta > 0$ and $\kappa > 0$. These coefficients can be negative, in which case higher order terms must be considered to ensure stability of the theory. Without loss of generality, we will choose $\kappa = 1$.

Close to T_c we may expand $\alpha = \tilde{\alpha}(T - T_c)$. In the homogeneous state, $\psi(\boldsymbol{r}) = \psi$, the free energy is

then minimized at

$$\psi^{eq} = \begin{cases} 0 & T \geq T_c \\ \sqrt{-\tilde{\alpha}(T-T_c)/2\beta}\, e^{i\theta_0} & T < T_c \end{cases} . \tag{1.2}$$

We see that the amplitude of the order vanishes above T_c and then continuously develops a finite amplitude below T_c. This is characteristic of a second order phase transition.

A sketch of the free energy above, at, and below the critical temperature is shown in Fig. 1.1. At the critical temperature, the free energy is lacking a quadratic component. The potential 'bowl' becomes flat and admits fluctuations of the order parameter with vanishing cost in energy and a corresponding diverging correlation length. Below T_c, the free energy assumes the form a 'Mexican hat' with a range of minima along its rim. These minima are related by a $U(1)$ phase. When the order parameter selects one of these point as its groundstate, $U(1)$ symmetry will be broken. This is the well-known mechanism of spontaneous symmetry breaking within the Landau-Ginzburg framework.

1.2.1 Collective fluctuations and the Anderson-Higgs mechanism

Let us select the minimum $\theta_0 = 0$ for the order parameter and expand the free energy in small fluctuations of the amplitude $h(\boldsymbol{r})$ and the phase $\theta(\boldsymbol{r})$ according to

$$\psi = (\psi^{eq} + h(\boldsymbol{r}))e^{i\theta(\boldsymbol{r})} . \tag{1.3}$$

We also introduce the electromagnetic vector potential $\boldsymbol{A}$ by gauging the theory according to $\nabla \to \nabla - 2ie\boldsymbol{A}$, where 2e is the charge of the order parameter. The free energy becomes

$$\mathcal{F} = mh^2 + \kappa \left(\nabla + i\left(2e\boldsymbol{A} - \nabla\theta\right)\right)\left(\psi^{eq} + h\right)\left(\nabla - i(2e\boldsymbol{A} - \nabla\theta)\right)\left(\psi^{eq} + h\right) \tag{1.4}$$

Here, we have defined the mass of the amplitude fluctuations as $m = \left(\alpha + 6\beta\left(\psi^{eq}\right)^2\right) = 2|\alpha|$. The amplitude fluctuations around the condensation point ψ^{eq} of the superconducting order parameter are referred to as '*Higgs mode*' in the literature, in analogy to the elementary Higgs particle in high-energy physics.

In the particle-physics context, the Higgs field was postulated as a necessary ingredient to generate a mass for the otherwise massless Z^0, W^+, and W^- bosons. We will motivate that something similar happens in the condensed matter context. For a detailed overview of the similarities and differences of the Higgs mode in condensed matter and particle physics, see Appendix. A.

First, note that in Eq. (1.4) the phase θ appears only in the gauge invariant combination $2e\boldsymbol{A} - \nabla\theta$. This indicates that the phase θ is not a physical degree of freedom but merely a consequence of gauge redundancy. This is the striking difference between superfluidity and superconductivity. In the uncharged case of the superfluid, the phase θ represents the Goldstone particle. It is gapless since no mass term of the form $m_\theta\theta^2$ exists. For a charged superconductor, we can remove the phase by choosing a specific gauge. If

we do so, we find for the free energy

$$\mathcal{F} = mh^2 + (\nabla h)^2 + (2e\psi^{eq})^2 A^2 + 8e^2\psi^{eq}A^2 h \,. \tag{1.5}$$

Importantly, we note the presence of the term $(2e\psi^{eq})^2 A^2$. This is a mass term for the photon. Condensation of the order parameter has generated a photon mass. This is a manifestation of the Anderson-Higgs mechanism.

Another interesting consequence arises from Eq. 1.5. The lowest order coupling between the Higgs mode and the electromagnetic field is of the non-linear form hA^2, i.e., the Higgs mode only couples nonlinearly to light. This abstract result illustrates one of the main challenges in measuring experimental signatures of the Higgs mode. Since it does not couple linearly to electromagnetic fields, it can only be detected by non-linear spectroscopic techniques.

1.2.2 Meissner effect

The mass term of the photon has an important consequence: the Meissner effect. Intuitively, there will be a finite energy cost on the scale of the mass-gap for the photon to have finite probability of staying inside a superconducting material. Thus, it is energetically favored for photons to be expelled from the superconductor.

We can formalize this concept within the Landau-Ginzburg formalism. Together with the usual kinetic term for the field $\boldsymbol{A}$, the electromagnetic part of the free energy reads

$$\mathcal{F}_{EM} = -\frac{1}{2}\left(\partial_i A_j \partial_i A_j - \partial_i A_j \partial_j A_i\right) + 8e^2\psi^{eq}A^2 \,. \tag{1.6}$$

We assume that our gauge supports $\partial_i A_i = 0$ and derive the Euler Lagrange equations $\frac{\partial \mathcal{F}}{\partial A_i} - \partial_j \frac{\partial \mathcal{F}}{\partial(\partial_j A_i)}$ as

$$\nabla^2 \boldsymbol{A} = 2(2e\psi^{eq})^2 \boldsymbol{A} \,. \tag{1.7}$$

Taking the curl on both sides, this yields the familiar London model as an equation for the magnetic field,

$$\nabla^2 \boldsymbol{B} = \lambda^{-2} \boldsymbol{B} \,. \tag{1.8}$$

Solutions to this differential equation always decay exponentially within the penetration depth $\lambda = 1/2\sqrt{2}e\psi^{eq}$. As a physical consequence, magnetic fields only penetrate a thin layer of λ at the surface of a superconductor and are otherwise expelled. A superconductor is a perfect diamagnet.

1.2.3 Supercurrent flow

The current induced in a superconductor by an applied electromagnetic field can be obtained as a functional derivative of the gauge-invariant free energy (1.4) according to

$$\boldsymbol{j} = -\frac{\delta \mathcal{F}}{\delta \boldsymbol{A}} = \rho_s(\nabla\theta - 2e\boldsymbol{A}) \tag{1.9}$$

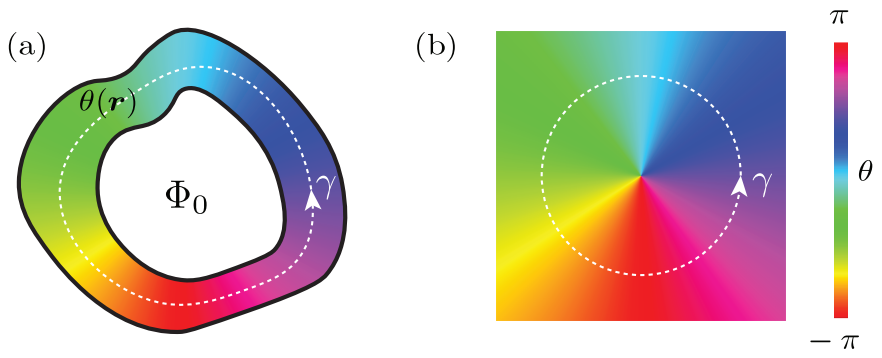

Figure 1.2: Phase winding of 2π of the superconducting order parameter for (a) a ring geometry and (b) a vortex defect. The phase $\theta(\boldsymbol{r})$ of the superconducting order parameter is shown as a false-color plot. If the contour γ is deep enough inside the superconductor, the flux through the area spanned by γ will be quantized to Φ_0.

where we have this time neglected Higgs fluctuations, $h = 0$, and $\rho_s = 2e\,(\psi^{eq})^2$ is the superfluid stiffness. Conceptually, this expression is very different from current flow in a regular conductor. Whereas a metallic current is linearly related to the electrical field via the conductivity tensor, here we have a direct relation to the electromagnetic vector potential. While conventional current originates from particle excitation, where scattering processes are important, supercurrent corresponds to a gauge invariant deformation of the superconducting phase of the macroscopic order parameter.

As a consequence of the Meissner effect, supercurrent is a surface phenomenon, i.e. superflow is only present within a layer λ of the surface.

1.2.4 Flux quantization

A remarkable consequence of supercurrent flow connected to spontaneous $U(1)$ symmetry breaking is the quantization of magnetic flux. As we learned, magnetic flux is expelled due to the Meissner effect. Magnetic fields may, however, penetrate a physical hole inside a superconducting ring, as given for example in the ring geometry sketched in Fig. 1.2(a).

The superconducting ring will only carry a current within the penetration depth λ of its surface. Deep in the bulk, we have $\boldsymbol{j} = 0$, and it follows from Eq. (1.9) that

$$\nabla\theta = 2e\boldsymbol{A}\,. \tag{1.10}$$

We now integrate this expression around a closed loop, indicated by a dashed white line in Fig. 1.2(a). The integration path is assumed to be deep in the bulk. Then, we get

$$2\pi n = 2e \oint_\gamma \boldsymbol{A}\cdot\boldsymbol{dl} = 2e \int (\nabla\times\boldsymbol{A})\cdot d\boldsymbol{\sigma} = \frac{2\pi}{\Phi_0}\Phi_\gamma\,. \tag{1.11}$$

where we have defined the superconducting flux quantum $2\pi/2e$, and Φ_γ is the magnetic flux threaded

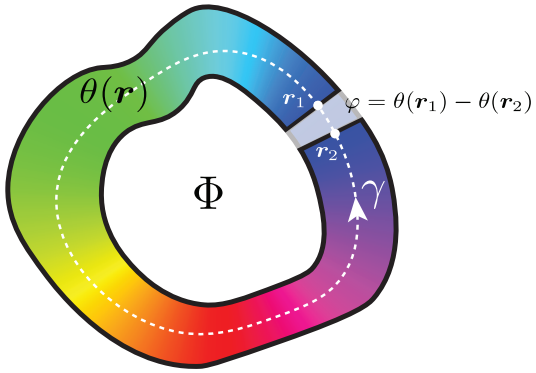

Figure 1.3: A superconducting ring that is interrupted by a weak link across which the phase jumps by φ.

through the contour γ. We see that phase continuity demands that the magnetic flux through the integration contour is quantized in units of Φ_0, i.e. $\Phi_\gamma = n\Phi_0$, where the phase winds n times along the integration path. Naturally, Eq. (1.11) only holds for loops γ along which the supercurrent vanishes. If we consider a loop that crosses within λ of the boundary of the ring, its flux will no longer be quantized.

Microscopically, flux quantization is achieved by circulating surface currents that adjust in just the right way to an externally applied flux, to always achieve quantization. It is intuitive that flux through a ring may not be quantized if the ring is too thin such that it cannot support enough supercurrent to generate the necessary induced flux contribution.

In certain superconductors, it is not even necessary to create a physical hole to pierce magnetic flux through it. Type-II superconductors can support vortex anomalies, exemplary sketched in Fig. 1.2(b). Vortices are points of vanishing order parameter around which the superconducting phase winds n times. Conceptually, a vanishing order parameter is equivalent to a physical hole in a superconductor. Flux quantization therefore applies to vortices, and they carry a flux of $n\Phi_0$.

1.2.5 Flux quantization in a Josephson junction

When the superconducting ring is interrupted by a small gap, a Josephson junction may be formed. This scenario is sketched in Fig. 1.3. Across the junction, the superconducting phase can discontinuously jump by a value φ. Integrating Eq. (1.10) again along a loop, we now have

$$\begin{aligned} 2\pi n &= -\varphi + \frac{2\pi}{\Phi_0}\int_{\boldsymbol{r}_1}^{\boldsymbol{r}_2} \mathbf{A}\cdot\mathbf{dl} = -\varphi + \left(\frac{2\pi}{\Phi_0}\int_{\boldsymbol{r}_2}^{\boldsymbol{r}_1} \mathbf{A}\cdot\mathbf{dl} - \frac{2\pi}{\Phi_0}\int_{\boldsymbol{r}_2}^{\boldsymbol{r}_1} \mathbf{A}\cdot\mathbf{dl}\right) + \frac{2\pi}{\Phi_0}\int_{\boldsymbol{r}_1}^{\boldsymbol{r}_2} \mathbf{A}\cdot\mathbf{dl} \\ &= -\varphi - \frac{2\pi}{\Phi_0}\int_{\boldsymbol{r}_2}^{\boldsymbol{r}_1} \mathbf{A}\cdot\mathbf{dl} + \frac{2\pi}{\Phi_0}\Phi = -\varphi^* + \frac{2\pi}{\Phi_0}\Phi\,. \end{aligned} \tag{1.12}$$

In the last step, we have defined the gauge invariant phase φ^*. We see that the flux is not necessarily quantized anymore. Instead, the phase jump across the junction is determined by the winding number n and

the magnetic flux,

$$\varphi^* = -2\pi n + \frac{2\pi}{\Phi_0}\Phi\,. \tag{1.13}$$

Chapter 2

Landau-Ginzburg phenomenology meets group theory

The simple picture of spontaneous symmetry breaking at a second order phase transition so far was restricted to a theory with a *single* complex order parameter ψ. In this chapter, we will generalize it to the case of a multi-component order parameter η_i. We will show that the point group symmetries of the underlying crystal play a vital role in determining the form of the free energy.

For now, we will not be concerned with the microscopic origin that necessitates such multicomponent structure. As we shall see in the following chapters, these different components can either correspond to different bands (Ch. 5) or different symmetry channels within a band (Ch. 6). A two-component order parameter will also be necessary to capture the physics of twisted cuprate bilayers that will be introduced in Ch. 7.

We will show that complex multicomponent Landau-Ginzburg theories give rise to a flurry of non-trivial phenomena, among them spontaneous time-reversal symmetry breaking, linear light-coupling to collective modes, and magnetic flux fractionalization.

2.1 Multi-component order parameters

A general expression of the free energy as a function of a multi-component order parameter η_i is given by

$$\mathcal{F}[\eta, \eta_i^*] = \alpha_{ij}\eta_i^*\eta_j + \beta_{ijkl}\eta_i^*\eta_j^*\eta_k\eta_l + R_{ijk}\eta_i^*\partial_j\eta_k + K_{ijkl}\partial_i\eta_j^*\partial_k\eta_l \,. \tag{2.1}$$

This equation can be significantly simplified by considering symmetry properties of the underlying material, formalized by the methods group theory. In the following discussion, we summarize main results of the group theoretical analysis applied in the literature [12, 76].

The free energy of the superconductor must be invariant under the symmetry group

$$G = G_p \times SU(2) \times U(1) \times \mathcal{T} \,, \tag{2.2}$$

where G_p is the point group of the crystal lattice unit cell, $SU(2)$ is the rotational group of the spin of the

order parameter, $U(1)$ is the group of global phase transformation of the complex order parameter, and $\mathcal{T}$ is the two-element group of time reversal.

In this chapter, we will only consider singlet pairing states, i.e. the order parameter only transforms under the trivial $1d$ singlet irrep of $SU(2)$ and the spin part can effectively be ignored. For the remaining structure of the group G, the order parameter then transforms under representations according to

$$\eta_i \to R_{ij}(g) e^{i\varphi} T^n \eta_j \,, \tag{2.3}$$

where R is a matrix representation of the group element $g \in G_p$, φ is the $U(1)$ phase, and time reversal acts as $T : \eta_i \to \eta_i^*$, and $n = 0, 1$. We note that the representation $R(g)$ is generally reducible.

The requirement of invariance of the free energy under these transformations constrains the allowed terms in Eq. (2.1). $U(1)$ symmetry demands that all terms include equal numbers of η_i and η_i^*. Time reversal imposes, e.g., that $\alpha_{ij} = \alpha_{ji}^*$. In the following we will focus on the restrictions imposed by the point group G_p, which for the quadratic terms are

$$R_{ia}^\dagger(g) \alpha_{ab} R_{bj}(g) = \alpha_{ij} \tag{2.4}$$

for every $g \in G_p$. Hence, the matrix α_{ij} commutes with representations of all group elements. According to Schur's lemma, α_{ij} can therefore be diagonalized into blocks of constants α_i times the unit matrix $\mathbb{1}_{n_i}$ of size n_i:

$$\alpha_{ij} = \begin{pmatrix} \alpha_1 \mathbb{1}_{n_1} & & \\ & \alpha_2 \mathbb{1}_{n_2} & \\ & & \ddots \end{pmatrix} = \bigoplus_i \alpha_i \mathbb{1}_{n_i} \tag{2.5}$$

Each block corresponds to an irreducible representation (irrep) of the point group. The dimensionality of the irrep sets the size n_i of the block.

We assume that we have performed transformation to a new basis $\psi_i = U_{ij}\eta_j$ that diagonalizes the matrix α_{ij} into the form (2.5). The sign of the coefficients α_i determine the shape of the Free energy for an individual order parameter. For negative α_i, one obtains a Mexican hat potential, while the potential is parabolic for $\alpha_i > 0$. Above T_c, all α_i are positive numbers. Upon lowering the temperature to T_c, a first of the α_i will become negative and its corresponding order parameters will condense. Close to T_c, the physics of the superconducting phase transition is therefore encoded by block i alone and we may discard all other order parameters. Note that the dimensionality of an irrep is at most $n = 5$ for any crystallographic point group. For the point group D_{4h}, relevant for the cuprates, irreps are at most two-dimensional. The block i is therefore at most of size 5×5 (or 2×2 for the cuprates). By considering the point group of a system, we see that a complicated Landau-Ginzburg theory with potentially hundreds of order parameters can always be distilled into an effective theory with at most a handful degrees of freedom.

Upon lowering the temperature, other α_i-blocks may become negative and additional order parameters will condense. However, few such successive superconducting phase transitions have been observed. A specific example of two successive phase transitions will be discussed in Ch. 7 for the cased of twisted

D_{4h}	Basis functions	E	$2C_4$	C_2	$2C_2'$	$2C_2''$	i	$2S_4$	σ_h	$2\sigma_v$	$2\sigma_d$
A_{1g}	1	1	1	1	1	1	1	1	1	1	1
A_{2g}	$xy(x^2-y^2)$	1	1	1	-1	-1	1	1	1	-1	-1
B_{1g}	x^2-y^2	1	-1	1	1	-1	1	-1	1	1	-1
B_{2g}	xy	1	-1	1	-1	1	1	-1	1	-1	1
E_g	(xz, yz)	2	0	-2	0	0	2	0	-2	0	0
A_{1u}	$xyz(x^2-y^2)$	1	1	1	1	1	-1	-1	-1	-1	-1
A_{2u}	z	1	1	1	-1	-1	-1	-1	-1	1	1
B_{1u}	$z(x^2-y^2)$	1	-1	1	1	-1	-1	1	-1	-1	1
B_{2u}	xyz	1	-1	1	-1	1	-1	1	-1	1	-1
E_u	(x, y)	2	0	-2	0	0	-2	0	2	0	0

Table 2.1: Character table of the point group D_{4h}

cuprate bilayers.

In the following, we will focus on the point group D_{4h} whose character table is listed in Tab. 2.1. The only *gerade* irrep that is two-dimensional is E_g. Under this representation, the free energy is given by

$$\mathcal{F}[\psi, \psi_i^*] = \alpha\psi_i^*\psi_i + \tilde{\beta}_{ijkl}\psi_i^*\psi_j^*\psi_k\psi_l + \tilde{R}_{ijk}\psi_i^*\partial_j\psi_k + \tilde{K}_{ijkl}\partial_i\psi_j^*\partial_k\psi_l\,, \tag{2.6}$$

where the indices run from $i = 1, 2$. The $\tilde{\beta}_{ijkl}$ transform as

$$\tilde{\beta}_{ijkl} \to \left(R_{ia}^{E_g}\right)^* \left(R_{jb}^{E_g}\right)^* R_{kc}^{E_g} R_{ld}^{E_g}\, \tilde{\beta}_{abcd}\,. \tag{2.7}$$

In more compact notation the $\tilde{\beta}$ transform under the direct product representation

$$(\mathrm{E}_g \otimes \mathrm{E}_g)^* \otimes \mathrm{E}_g \otimes \mathrm{E}_g\,. \tag{2.8}$$

Direct products are generally reducible, i.e. $\mathrm{E}_g \otimes \mathrm{E}_g = \mathrm{A}_{1g} \oplus \mathrm{A}_{2g} \oplus \mathrm{B}_{1g} \oplus \mathrm{B}_{2g}$. Since E_g is a real irrep, we have $\mathrm{E}_g^* = \mathrm{E}_g$ and find

$$(\mathrm{E}_g \otimes \mathrm{E}_g)^* \otimes \mathrm{E}_g \otimes \mathrm{E}_g = 4\mathrm{A}_{1g} \oplus 4\mathrm{A}_{2g} \oplus 4\mathrm{B}_{1g} \oplus 4\mathrm{B}_{2g} \tag{2.9}$$

For the $\tilde{\beta}$-term to be invariant under the point group symmetry, it must transform under the trivial representation A_{1g}. According to Eq. (2.9) four A_{1g} irreps are contained in the direct product. Thus, the $\tilde{\beta}$ tensor with $2^4 = 16$ components can be reduced to $N = 4$ invariant components.

The invariant subspaces of the tensor $\tilde{\beta}$ are found from

$$\tilde{\beta}_{ijkl}^* = \Pi_{ijkl,abcd}^{(A_{1g})} \tilde{\beta}_{abcd}\,. \tag{2.10}$$

where

$$\Pi^{(A_{1g})}_{ijkl,abcd} = \sum_{h\in G_p} R_{ijkl,abcd}(h) \tag{2.11}$$

is the projection operator of the A_{1g} subspace and we have denoted R as the reducible product representation

$$R_{ijkl,abcd}(h) = [E_g(h)]_{ia}\,[E_g(h)]_{jb}\,[E_g(h)]_{kc}\,[E_g(h)]_{ld}\ . \tag{2.12}$$

Let us interpret the product representation as matrices $R_{\alpha\beta}(h)$ by introducing the combined indices $\alpha = (ijkl)$ and $\beta = (abcd)$. It is clear that $\Pi_{\alpha\beta}$ is indeed a projection operator, because

$$R(h_0)\Pi = R(h_0)\sum_{h\in G_p} R(h) = \sum_{h\in G_p} R(h_0 h) = \sum_{h\in G_p} R(h) = \Pi\,, \tag{2.13}$$

since for a group $hG_p = G_p$. The rank of $\Pi_{\alpha\beta}$ must be $\mathrm{rank}(\Pi) = N = 4$, equal to the dimension of the invariant subspace. We separate the four invariants by finding the four independent row-vectors $v^{(n)}$ of Π using Gaussian elimination, where $n = 1,\ldots,N$. Then, the individual invariants are given by

$$\tilde{\beta}^{*(n)}_{\alpha} = \Pi^{(A_{1g})}_{\alpha\gamma} v^{(n)}_{\gamma} \tilde{\beta}_{\gamma}\,. \tag{2.14}$$

Explicitly, the four invariants for the D_{4h} case are

$$\begin{aligned}
&\psi_1^*\psi_1^*\psi_1\psi_1 + \psi_2^*\psi_2^*\psi_2\psi_2\\
&\psi_1^*\psi_2^*\psi_2\psi_1 + \psi_2^*\psi_1^*\psi_1\psi_2\\
&\psi_1^*\psi_2^*\psi_1\psi_2 + \psi_2^*\psi_1^*\psi_2\psi_1\\
&\psi_1^*\psi_1^*\psi_2\psi_2 + \psi_2^*\psi_2^*\psi_1\psi_1\,.
\end{aligned} \tag{2.15}$$

The second and third turn out to be identical, because the ψ_i commute. Consequently, we obtain a stationary free energy with only three parameters at fourth order,

$$\mathcal{F} = \alpha\left(|\psi_1|^2 + |\psi_2|^2\right) + \beta_1\left(|\psi_1|^4 + |\psi_2|^4\right) + \beta_2|\psi_1|^2|\psi_2|^2 + \beta_3\left((\psi_1^*)^2\psi_2^2 + (\psi_2^*)^2\psi_1^2\right)\ . \tag{2.16}$$

2.1.1 Spontaneous $\mathcal{T}$-breaking

Let us find the minima of (2.16). By symmetry, one must have

$$\begin{aligned}
\psi_1 &= |\psi^{eq}|e^{i\theta_1}\\
\psi_2 &= |\psi^{eq}|e^{i\theta_2}\,,
\end{aligned} \tag{2.17}$$

where both order parameters have the same amplitude and can only differ by a phase. The overall phase does not change the free energy, and the problem reduces to finding the phase difference $\varphi = \theta_1 - \theta_2$. Only

the last term in Eq. (2.16) depends on φ and we get

$$\mathcal{F}[\varphi] = 2\beta_3 |\psi^{eq}|^4 \cos 2\varphi + \textit{const.} \tag{2.18}$$

For $\beta_3 > 0$, the free energy is minimized at either of $\varphi = \pi/2$ or $\varphi = -\pi/2$. These two minima are related to each other by time reversal, since

$$T : \varphi \to -\varphi \,. \tag{2.19}$$

The groundstate will spontaneously select one of the two minima in the thermodynamic limit and spontaneously break $\mathcal{T}$. We see that the two order parameters develop a phase difference of $e^{i\pi/2}$. In the E_g irrep of D_{4h} this is referred to as $d_{xz} + id_{yz}$ superconductivity.

In the case $\beta < 0$, Eq. (2.18) is minimized at $\varphi = 0$ or π. None of these choices breaks $\mathcal{T}$, since each map to themselves under the time-reversal operation (2.19).

2.1.2 Collective modes

Collective modes correspond to fluctuations of the order parameter around the equilibrium configuration $\psi_i^{eq} = \psi^{eq}$ and $\theta_1^{eq} - \theta_2^{eq} = 0, \pm\pi/2$ where we parametrize the order parameter as

$$\psi_i = (\psi_i^{eq} + h_i) \exp\left(i(\theta_i^{eq} + \theta_i)\right) \,. \tag{2.20}$$

We find the eigenmodes by expanding the free energy in the small fluctuations $x_i = \{h_1, h_2, \theta_1, \theta_2\}$ up to quadratic order,

$$\mathcal{F} = \mathcal{F}_0 + \frac{1}{2} x_i M_{ij} x_j \,, \qquad \text{where} \qquad M = \frac{\partial^2}{\partial x_i \partial x_j} \mathcal{F}\big|_{\boldsymbol{x}=0} \,. \tag{2.21}$$

The linear terms in x_i are absent since we are expanding around a minimum of the free energy. The matrix M is explicitly

$$M = \begin{pmatrix} 8(\psi^{eq})^4\beta_1 & 4(\psi^{eq})^4(\beta_2 - 2|\beta_3|) & 0 & 0 \\ 4(\psi^{eq})^4(\beta_2 - 2|\beta_3|) & 8(\psi^{eq})^4\beta_1 & 0 & 0 \\ 0 & 0 & 0 & 0 \\ 0 & 0 & 0 & 8|\beta_3|(\psi^{eq})^4 \end{pmatrix} . \tag{2.22}$$

The eigenvectors of M are $(0,0,1,1), (1,1,0,0), (1,-1,0,0), (0,0,1,-1)$. These give the eigenmodes

$$\begin{aligned} \theta &= \theta_1 + \theta_2 \\ h_+ &= (h_1 + h_2)/\sqrt{2} \\ h_- &= (h_1 - h_2)/\sqrt{2} \\ \varphi &= \theta_1 - \theta_2 \end{aligned} \tag{2.23}$$

The Goldstone mode θ has zero eigenvalue as expected, and the other eigenvalues are

$$\begin{aligned} m_+ &= 4(\psi^{eq})^4\,(2\beta_1+\beta_2-2|\beta_3|) \\ m_- &= 4(\psi^{eq})^4\,(2\beta_1-\beta_2+2|\beta_3|) \\ m_\varphi &= 8(\psi^{eq})^4|\beta_3|\,, \end{aligned} \tag{2.24}$$

yielding the free energy

$$\mathcal{F} = \mathcal{F}_0 + \frac{1}{2}m_+h_+^2 + \frac{1}{2}m_-h_-^2 + \frac{1}{2}m_\varphi\varphi^2\,. \tag{2.25}$$

Note that for $|\beta_3| < \beta_2/2$ one has $m_- < m_+$. Microscopically, one finds that m_+ can usually be identified with the quasiparticle excitation gap. Then, for $|\beta_3| < \beta_2/2$ the anti-symmetric Higgs mode h_- will be a subgap excitation.

2.1.3 Linear coupling of light to collective modes

We next study the lowest order gradient term in the free energy Eq. (2.6) which is $\tilde{R}_{ijk}\psi_i^*\partial_j\psi_k$. Presence of this term has been shown to lead to a linear coupling of light to collective modes of relative phase oscillations of the order parameters in two-dimensional irreps [78]. This can be understood by considering a term of the form

$$r_i\psi_1^*(\partial_i - 2ieA_i)\psi_2 + c.c. \tag{2.26}$$

where we have gauged the theory using $\partial_i \to \partial_i - 2ieA_i$. We express the fields ψ_i as amplitude and phase fluctuations

$$\begin{aligned} \psi_1 &= (\psi_1^{eq} + h_1)e^{i(\theta+\varphi/2)} \\ \psi_2 &= (\psi_2^{eq} + h_2)e^{i(\theta-\varphi/2)} \end{aligned} \tag{2.27}$$

around the equilibrium point $(\psi_1^{eq}, \psi_2^{eq})$. Inserting this into (2.26), and expanding the fluctuations h_i, φ to first order, we obtain the terms

$$-2ei\,r_iA_i\,(\psi_1^{eq}h_2 + \psi_2^{eq}h_1 - i\psi_1^{eq}\psi_2^{eq}\varphi) + c.c.\,. \tag{2.28}$$

The equation above would imply that light can couple linearly to both amplitude fluctuations h_i and the relative phase mode φ. However, close to the Fermi energy, particle-hole symmetry is usually a good symmetry in superconductors since the density of states is nearly constant on the energy scale of the superconducting

gap. Particle hole symmetry acts as

$$P: \begin{array}{l} 2e \to -2e \\ h_i \to h_i \\ \varphi \to -\varphi \end{array} \tag{2.29}$$

and only leaves the term $4e\,\mathrm{Re}[r_i]A_i\psi_1^{eq}\psi_2^{eq}\varphi$ invariant. Thus, any linear coupling to the Higgs mode is strongly suppressed by particle hole symmetry while coupling to the phase mode is permitted.

We conclude that signatures of collective phase fluctuations can already be observable in the linear response regime for certain materials that are described by two-component Landau-Ginzburg theories. Specifically, this could be manifest as a subgap peak in the linear optical conductivity for fully gapped superconductors [78]. No such observation, however, has been made to date.

Let us deploy the methods of group theory to illustrate how point group symmetries may affect the linear phase mode coupling. We consider the case of the E_g irrep of D_{4h}. The spatial derivative transforms under $E_u \oplus A_{2u}$. Then, $\tilde{R}$ transforms under the direct product

$$E_u \otimes (E_u \oplus A_{2u}) \otimes E_u = A_{1u} \oplus A_{2u} \oplus B_{1u} \oplus B_{2u} \oplus 4E_u \tag{2.30}$$

which does not contain the trivial A_{1g} irrep. Thus, it holds $\tilde{R}_{ijk} = 0$, i.e., $\tilde{R}$ is symmetry forbidden and no linear coupling of light to collective modes exists.

More intuitively, the term $\tilde{R}$ will always transform under a product of odd numbers of ungerade irreps, and thus the product representation can only contain *ungerade* irreps and never the trivial irrep A_{1g}. It is therefore necessary to turn to systems without inversion symmetry. One example of a point group without inversion symmetry will be studied in the next section. Another possible avenue is the point group D_{3h} that is relevant for single or odd-layer $NbSe_2$ which has attracted recent interest as part of the transition metal dichalcogenide family [60, 172].

2.2 The point group D_{4d}

D_{4d}	Basis functions	E	$2S_8$	$2C_4$	$2(S_8)^3$	C_2	$4C_2'$	$4\sigma_d$
A_1	1	1	1	1	1	1	1	1
A_2	$z\left((x^2-y^2)^2-4x^2y^2\right)$	1	1	1	1	1	-1	-1
B_1	$(x^2-y^2)^2-4x^2y^2$	1	-1	1	-1	1	1	-1
B_2	z	1	-1	1	-1	1	-1	1
E_1	(x,y)	2	$\sqrt{2}$	0	$-\sqrt{2}$	-2	0	0
E_2	(x^2-y^2,xy)	2	0	-2	0	2	0	0
E_3	(xz,yz)	2	$-\sqrt{2}$	0	$\sqrt{2}$	-2	0	0

Table 2.2: Character table of the point group D_{4d}

Now that we have introduced the group theoretical procedures to derivate all symmetry-allowed terms of the Landau-Ginzburg potential for a specific point group, let us consider another example: the point group

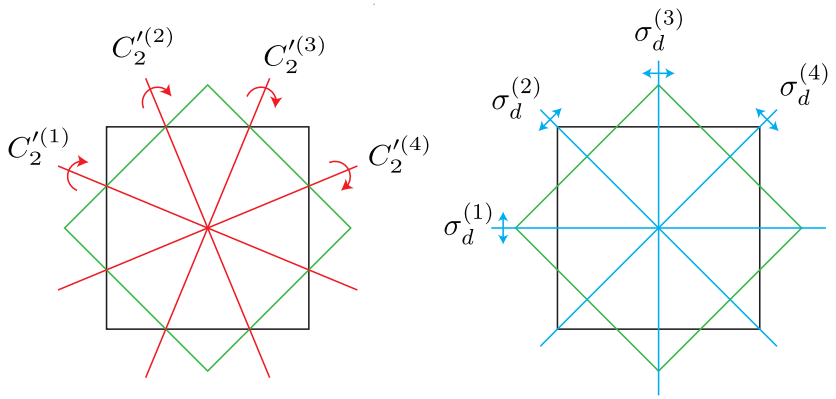

Figure 2.1: Illustration of C_2' rotations and σ_d mirror planes of the point group D_{4d} of symmetry operations of twisted cuprates. Top and bottom cuprate layers and depicted as green and black squares. Red lines indicate C_2'-rotation axes in between cuprate layers. Blue lines indicate cross-sections of mirror planes σ_d.

D_{4d}. This point group will be relevant in Ch. 7, where we will see that it reflects the symmetry group of twisted cuprate bilayers.

The character table of D_{4d} is listed in Tab. 2.2. The group is of order 16. It has an abelian subgroup S_8, where the element $S_8 = C_8\sigma_h$ is composed of a $2\pi/8$-rotation around the z-axis and a horizontal xy mirror plane reflection. The 8-fold rotational symmetry implies that D_{4d} is not a crystallographic point group. It can, however, still be relevant for quasicrystals and molecules. Indeed, twisted cuprate bilayers are known to realize a quasicrystal at the critical twist angle of $\pi/4$ [28].

Additionally, D_{4d} contains four in-plane C_2' rotations and four vertical mirror planes σ_d which are illustrated in Fig. 2.1.

From the basis functions in character table 2.2 it is apparent that E_2 is the only irrep of D_{4d} that possesses d-wave character in the xy-plane. This motivates us to adopt E_2 as the single viable choice to describe twisted cuprates, since cuprates in bulk form or as individual layers are known to be d-wave superconductors. We note that cuprates are usually described by a single-component Landau-Ginzburg theory with the order parameter transforming as B_{1g} or B_{2g} in the group D_{4h}. This is in stark contrast to twisted cuprates, which necessarily need to be described by two order parameters transforming as E_2 in D_{4d}.

It is straightforward to construct the product representations of the tensors $\tilde{\beta}, \tilde{R}, \tilde{K}$ of the general expression (2.6). The results are listed in Tab. 2.3 next to the decomposition of the product representations into A_1 invariants. Using the projection operator method, we explicitly find the free energy as

$$\begin{aligned}\mathcal{F} = \alpha\left(|\psi_1|^2 + |\psi_2|^2\right) + \beta_1\left(|\psi_1|^4 + |\psi_2|^4\right) + \beta_2|\psi_1|^2|\psi_2|^2 + \beta_3\left((\psi_1^*)^2\psi_2^2 + (\psi_2^*)^2\psi_1^2\right) \\ + \left(r(\psi_1^*\partial_z\psi_1 - \psi_2^*\partial_z\psi_2) + c.c.\right) + \kappa_1\left(|\partial_z\psi_1|^2 + |\partial_z\psi_2|^2\right) \\ + \kappa_2\left(|\partial_x\psi_1|^2 + |\partial_x\psi_2|^2 + |\partial_y\psi_1|^2 + |\partial_y\psi_2|^2\right) . \end{aligned} \tag{2.31}$$

The term $\psi_1^*\partial_z\psi_1 - \psi_2^*\partial_z\psi_2$ could in principle give rise to linear coupling of electromagnetic fields to the Higgs mode. However, it is not invariant under particle hole symmetry, $P : \psi_i \to \psi_i^*, \partial_i \to \partial_i$, and

D_{4d}	Product representation	# of A_1 irreps	# of invariants
$\tilde{\beta}_{ijkl}$	$E_2 \otimes E_2 \otimes E_2 \otimes E_2$	4	3
$\tilde{R}_{ijk}$	$E_2 \otimes (B_2 \oplus E_1) \otimes E_2$	1	1
$\tilde{K}_{ijkl}$	$(B_2 \oplus E_1) \otimes E_2 \otimes (B_2 \oplus E_1) \otimes E_2$	3	2

Table 2.3: Invariant components of quartic and gradient tensors of the free energy where order parameter transforms as E_2 of D_{4d}. The number of invariants can be less than the A_1 content, if invariants vanish due to commutation structure of order parameters and derivatives.

should be strongly suppressed.

2.2.1 Transition splitting

D_4	Basis functions	E	$2C_4$	C_2	$2C_2'$	$2C_2''$
A_1	1	1	1	1	1	1
A_2	z	1	1	1	-1	-1
B_1	$x^2 - y^2$	1	-1	1	1	-1
B_2	xy	1	-1	1	-1	1
E_1	(x, y)	2	0	-2	0	0

Table 2.4: Character table of the point group D_4.

Under a deformation that lowers the symmetry from D_{4d} to D_4, the $2d$ irrep E_2 would split into two one-dimensional irreps

$$E_2 \to B_1 \oplus B_2 \,. \tag{2.32}$$

The characters of D_4 are listed in Tab. 2.4. In the D_{4d} symmetric case, there can only be a single superconducting phase transition. Upon lowering the symmetry do D_4, two T_c transition temperatures should be measurable, corresponding to the irreps B_1 and B_2.

2.2.2 Fractional flux quantization

In Sec. 1.2.4, we derived that magnetic flux, piercing through a hole in a superconductor, is necessarily quantized as a consequence of phase continuity. Here, we will apply the same concept to the two-dimensional E_2 order parameter of D_{4d}. For simplicity, let us consider an electromagnetic vector potential in the xy-plane, $\boldsymbol{A} = (A_x, A_y)$. From the derivative of the free energy (2.31), the supercurrent in the xy-plane is given by

$$\boldsymbol{j} = \rho_s(\nabla\theta_1 - 2e\boldsymbol{A}) + \rho_s(\nabla\theta_2 - 2e\boldsymbol{A}) \tag{2.33}$$

where $\rho_s = 8e^2\kappa_2 \left(\psi^{eq}\right)^2$. As in the $1d$ case, we consider the superconducting ring geometry of Fig. 1.2. In the bulk of a superconductor, $\boldsymbol{j} = 0$, and it holds that

$$\nabla\theta_1 + \nabla\theta_2 = 4e\boldsymbol{A} \,. \tag{2.34}$$

Integrating this expression around a loop, we obtain, in analogy to Eq. (1.11),

$$2\pi(n_1 + n_2) = 4e \oint \boldsymbol{A} \cdot \boldsymbol{dl} = 4e \int (\nabla \times \boldsymbol{A}) \cdot d\boldsymbol{\sigma} = \frac{4\pi}{\Phi_0}\Phi \,. \tag{2.35}$$

Thus, for n_1 and n_2 windings of the superconducting phases θ_1 and θ_2, we find that the flux must be quantized to

$$\Phi = \frac{n_1 + n_2}{2}\Phi_0 \,. \tag{2.36}$$

Remarkably, when $n_1 + n_2$ is odd, the flux is *half* quantized. Half-quantization is only possible when the two order parameters have different winding numbers. These configurations correspond to local minima in the free energy which, for a single vortex, have an extensive energy cost due to the Josephson coupling term $\beta_3 \left((\psi_1^*)^2\psi_2^2 + (\psi_2^*)^2\psi_1^2\right)$. As such, a single fractional flux quantization is exponentially suppressed in system size and half-quantized vortex pairs attract each other to favor a fully-quantized boundstate at low temperatures.

Chapter 3

Path integral formulation of superconductivity

The Landau-Ginzburg formalism provides an excellent phenomenological description of superconductivity. It does, however, lack a microscopic justification. We will provide this justification in the present chapter where we will derive the Landau-Ginzburg theory starting from the general interacting single band Hamiltonian

$$\mathcal{H} = \sum_{\boldsymbol{k},\sigma=\downarrow\uparrow} \xi_{\boldsymbol{k}} c^\dagger_{\boldsymbol{k}\sigma} c_{\boldsymbol{k}\sigma} + \sum_{\boldsymbol{k}_1\boldsymbol{k}_2\boldsymbol{k}_3} V_{\boldsymbol{k}_1\boldsymbol{k}_2\boldsymbol{k}_3} c^\dagger_{\boldsymbol{k}_1\uparrow} c^\dagger_{\boldsymbol{k}_2\downarrow} c_{\boldsymbol{k}_3\downarrow} c_{\boldsymbol{k}_1+\boldsymbol{k}_2-\boldsymbol{k}_3\uparrow} \,. \tag{3.1}$$

Here, $\xi_{\boldsymbol{k}} = \epsilon_{\boldsymbol{k}} - \mu$ is the microscopic bandstructure. The interacting potential $V_{\boldsymbol{k}_1\boldsymbol{k}_2\boldsymbol{k}_3}$ is often phonon mediated but can have diverse physical origins. Both $\xi_{\boldsymbol{k}}$ and $V_{\boldsymbol{k}_1\boldsymbol{k}_2\boldsymbol{k}_3}$ reflect the point group symmetries of the microscopic crystal lattice.

3.1 Hubbard-Stratonovich channels

A first approximation consists of restricting the sum over the $\boldsymbol{k}_i$ to a smaller subspace of the parameter space. We do that by introducing the momentum variable $\boldsymbol{q}$ which is understood to be summed only over the small region $|\boldsymbol{q}| \ll 1/a$, where a is the lattice constant. Next, we arrange the four operators of the interacting term into pairs of two, whereby each pair creates a net-momentum of $\pm\boldsymbol{q}$. Three such pairings exist:

$$\begin{aligned}\sum_{\boldsymbol{k}_1\boldsymbol{k}_2\boldsymbol{k}_3} V_{\boldsymbol{k}_1\boldsymbol{k}_2\boldsymbol{k}_3} c^\dagger_{\boldsymbol{k}_1\uparrow} c^\dagger_{\boldsymbol{k}_2\downarrow} c_{\boldsymbol{k}_3\downarrow} c_{\boldsymbol{k}_1+\boldsymbol{k}_2-\boldsymbol{k}_3\uparrow} &= \sum_{\boldsymbol{k}\boldsymbol{k}'\boldsymbol{q}} V_{\boldsymbol{k}+\boldsymbol{q},-\boldsymbol{k},-\boldsymbol{k}'}\, c^\dagger_{\boldsymbol{k}+\boldsymbol{q}\uparrow} c^\dagger_{-\boldsymbol{k}\downarrow} c_{-\boldsymbol{k}'\downarrow} c_{\boldsymbol{k}'+\boldsymbol{q}\uparrow} \\ &+ \sum_{\boldsymbol{k}\boldsymbol{k}'\boldsymbol{q}} V_{\boldsymbol{k}+\boldsymbol{q},\boldsymbol{k}'-\boldsymbol{q},\boldsymbol{k}'}\, c^\dagger_{\boldsymbol{k}+\boldsymbol{q}\uparrow} c_{\boldsymbol{k}\uparrow} c^\dagger_{\boldsymbol{k}'-\boldsymbol{q}\downarrow} c_{\boldsymbol{k}'\downarrow} - \sum_{\boldsymbol{k}\boldsymbol{k}'\boldsymbol{q}} V_{\boldsymbol{k}+\boldsymbol{q},\boldsymbol{k}'-\boldsymbol{q},\boldsymbol{k}}\, c^\dagger_{\boldsymbol{k}+\boldsymbol{q}\uparrow} c_{\boldsymbol{k}\downarrow} c^\dagger_{\boldsymbol{k}'-\boldsymbol{q}\downarrow} c_{\boldsymbol{k}'\uparrow}\end{aligned} \tag{3.2}$$

These three terms are referred to as *Cooper channel*, *density channel*, and *exchange channel*, respectively. We have diagrammatically summarized them in Fig. 3.1. Under our assumption of small $\boldsymbol{q}$, all three channels evaluate the potential $V_{\boldsymbol{k}_1\boldsymbol{k}_2\boldsymbol{k}_3}$ in mostly different regions of $(\boldsymbol{k}_1, \boldsymbol{k}_2, \boldsymbol{k}_3)$-parameter space and one may safely

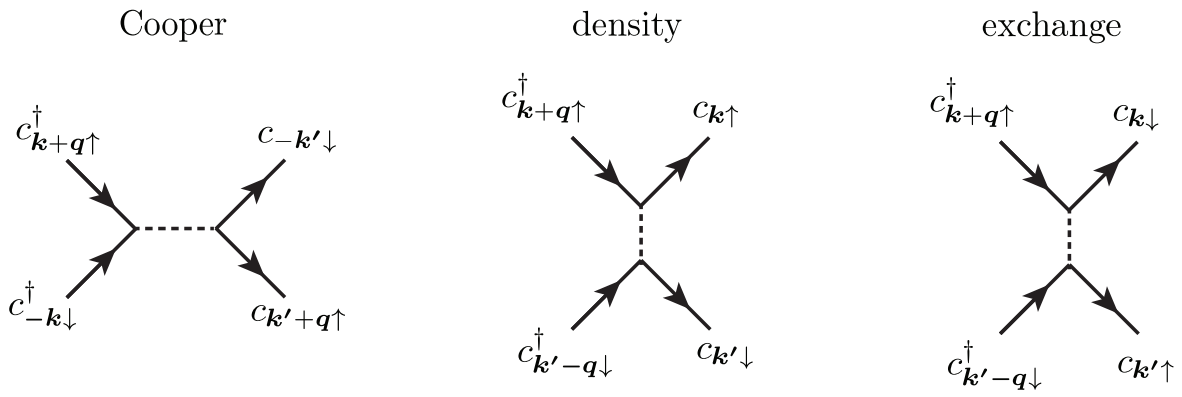

Figure 3.1: Diagrammatic representation of the Cooper, density, and exchange channel in Eq. (3.2).

neglect the small overlap.

The three channels have principally different effects on the physics of the model. The density channel can lead to a Mott-gap and renormalizes the chemical potential, while the exchange channel is related to magnetic phenomena. The Cooper channel leads to BCS-superconductivity. Which and how many of these channels are relevant depends on the underlying material and is encoded into the form of the interacting potential $V_{\boldsymbol{k}_1\boldsymbol{k}_2\boldsymbol{k}_3}$. Here, we will be concerned with generic superconducting systems where the Cooper channel is the only relevant interacting term.

To make progress in studying the Cooper channel, we neglect the $\boldsymbol{q}$ dependence of the pairing function and factorize it into the form

$$V_{\boldsymbol{k}+\boldsymbol{q},-\boldsymbol{k},-\boldsymbol{k}'} \approx -\sum_i V^{(i)} f^{(i)}_{\boldsymbol{k}} f^{(i)}_{\boldsymbol{k}'} \tag{3.3}$$

Here, the index i runs over irreducible representations of the underlying point group of the crystal lattice and the $f^{(i)}_{\boldsymbol{k}}$ are the corresponding basis functions. For the case of the cuprates the basis functions were listed in character table 2.1 of Ch. 2. Since cuprates are known to be d-wave superconductors, the relevant basis functions are $f^{(B_{1g})}_{\boldsymbol{k}} = \cos k_x - \cos k_y$ and $f^{(B_{1g})}_{\boldsymbol{k}} = \sin k_x \sin k_y$.

We next choose the imaginary time coherent state partition function [3] as a method of perturbation theory that we will outline in the following. In this formalism, the partition function $\mathcal{Z}$ is given by the path integral

$$\mathcal{Z} = \int \mathcal{D}(c^\dagger c) e^{-S} \quad \text{with} \quad S = \int_0^\beta d\tau \left(\sum_{\boldsymbol{k}\sigma} c^\dagger_{\boldsymbol{k}\sigma} \partial_\tau c_{\boldsymbol{k}\sigma} + \mathcal{H} \right), \tag{3.4}$$

Here, τ is the imaginary time variable that is integrated from 0 to $\beta = 1/T$, where T is the temperature. Note that we are working in units where natural constants are set to $k_b = \hbar = 1$. The fermionic fields $c, c^\dagger$ are now treated as anticommuting Grassmann functions.

The interacting term in the Hamiltonian $\mathcal{H}$ can be decoupled by means of the Hubbard Stratonovich

transformation

$$\exp\left(\int d\tau \sum V^{(i)} \left(\sum_{\boldsymbol{k}} f_{\boldsymbol{k}}^{(i)} c_{\boldsymbol{k}+\boldsymbol{q}\uparrow}^{\dagger} c_{-\boldsymbol{k}\downarrow}^{\dagger}\right)\left(\sum_{\boldsymbol{k}'} f_{\boldsymbol{k}'}^{(i)} c_{-\boldsymbol{k}'\downarrow} c_{\boldsymbol{k}'+\boldsymbol{q}\uparrow}\right)\right)$$
$$= \int \mathcal{D}(\bar{\psi}_i\psi_i) \exp\left(-\int d\tau \sum_{\boldsymbol{q}i}\left[|\psi_i(\boldsymbol{q})|^2/V^{(i)} - \sum_{\boldsymbol{k}}\left(\psi_i(\boldsymbol{q}) f_{\boldsymbol{k}}^{(i)} c_{\boldsymbol{k}+\boldsymbol{q}\uparrow}^{\dagger} c_{-\boldsymbol{k}\downarrow}^{\dagger} + \bar{\psi}_i(\boldsymbol{q}) f_{\boldsymbol{k}}^{(i)} c_{-\boldsymbol{k}\downarrow} c_{\boldsymbol{k}+\boldsymbol{q}\uparrow}\right)\right]\right) \tag{3.5}$$

3.2 Microscopic derivation of Landau-Ginzburg theory

Introducing the Nambu-basis $\Psi_{\boldsymbol{k}} = \left(c_{\boldsymbol{k}\uparrow},\, c_{-\boldsymbol{k}\downarrow}^{\dagger}\right)$, we rewrite the decoupled action as

$$S[c^{\dagger}c, \bar{\psi}\psi] = \sum_{i\boldsymbol{q}\Omega_n} |\psi_i(\boldsymbol{q},\Omega_n)|^2/V^{(i)} - \sum_{\boldsymbol{k}\boldsymbol{k}'}\int d\tau \Psi_{\boldsymbol{k}}^{\dagger}(\omega_n) G^{-1}(\boldsymbol{k}\boldsymbol{q},\omega_n,\Omega_m)\Psi_{\boldsymbol{k}+\boldsymbol{q}}(\omega_n+\Omega_m)\,, \tag{3.6}$$

where the Green's function is defined as

$$\begin{aligned} G^{-1}(\boldsymbol{k}\boldsymbol{q},\omega_n,\Omega_m) &= G_0^{-1}(\boldsymbol{k},\omega_n)\delta_{\boldsymbol{q},0}\delta_{\Omega_m,0} - \Sigma(\boldsymbol{k}\boldsymbol{q},\Omega_m) \\ G_0^{-1}(\boldsymbol{k},\omega_n) &= i\omega_n - \xi_{\boldsymbol{k}}\sigma_3 \\ \Sigma(\boldsymbol{k}\boldsymbol{q},\Omega_m) &= -\sum_i f_{\boldsymbol{k}}^{(i)}\left(\psi_i(\boldsymbol{q},\Omega_n)\sigma_+ + \bar{\psi}_i(\boldsymbol{q},\Omega_n)\sigma_-\right)\,. \end{aligned} \tag{3.7}$$

Here, we have introduced $\sigma_{\pm} = (\sigma_x \pm i\sigma_y)/2$ with Pauli matrices σ_i. The $\omega_n = (2n+1)\pi/\beta$ are fermionic Matsubara frequencies, and the $\Omega_n = 2\pi n/\beta$ are bosonic. G_0 is the unperturbed Green's function in the normal, non-superconducting state and Σ is usually referred to as the self-energy.

One notes that Eq. (3.6) is quadratic in the Grassmann fields. Thus, the fermionic path integral can be performed by means of Gaussian integration. The new action is

$$S[\bar{\psi}\psi] = \sum_{i\boldsymbol{q}\Omega_n} |\psi_i(\boldsymbol{q},\Omega_n)|^2/V^{(i)} - \mathrm{Tr}\ln\left[-G^{-1}\right]\,. \tag{3.8}$$

We next expand the logarithm according to

$$\mathrm{Tr}\ln\left(-G^{-1}\right) = \mathrm{Tr}\ln\left(-G_0^{-1}(1-G_0\Sigma)\right) = \mathrm{Tr}\ln\left(-G_0^{-1}\right) - \mathrm{Tr}\sum_{n=1}^{\infty}\frac{1}{n}(G_0\Sigma)^n\,. \tag{3.9}$$

Considering terms up to fourth order in the self-energy, we obtain

$$S[\bar{\psi}\psi] = \sum_{i\boldsymbol{q}\Omega_n} |\psi_i(\boldsymbol{q},\Omega_n)|^2/V^{(i)} - \mathrm{Tr}\ln\left[-G_0^{-1}\right] + \frac{1}{2}\mathrm{Tr}\left[G_0\Sigma G_0\Sigma\right] + \frac{1}{4}\mathrm{Tr}\left[G_0\Sigma G_0\Sigma G_0\Sigma G_0\Sigma\right]\,. \tag{3.10}$$

We note that terms of odd order in Σ vanish, which is reminiscent of the $U(1)$-symmetry of the model.

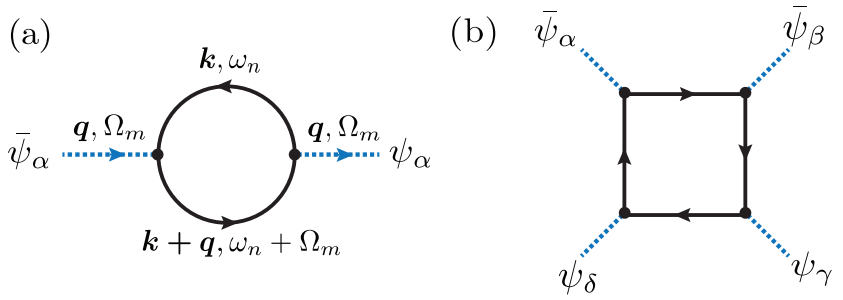

Figure 3.2: Diagrammatic representation of the terms $\mathrm{Tr}(G_0\Sigma)^n$ for (a) $n = 2$ and (b) $n = 4$.

The multiplication inside the trace should be understood as matrix multiplication, where momenta $\boldsymbol{k}, \boldsymbol{q}$ and Matsubara sums ω_n, Ω_m are interpreted as matrix degrees of freedom. For example, for the second order term, $n = 2$, on finds explicitly

$$\mathrm{Tr}\left[G_0\Sigma G_0\Sigma\right] \equiv \mathrm{Tr}\left[G_0(\boldsymbol{k},\omega_n)\Sigma(\boldsymbol{q},\Omega_n)G_0(\boldsymbol{k}+\boldsymbol{q},\omega_n+\Omega_m)\Sigma(-\boldsymbol{q},-\Omega_n)\right] . \tag{3.11}$$

and sums over $\boldsymbol{k}, \boldsymbol{q}, \omega_n, \Omega_m$ are implied. These expressions are more elegantly represented diagrammatically in Fig. 3.2. Here, the Green's functions $G_0(\boldsymbol{k}, \omega_n)$ are drawn as straight black lines. The overall cyclic structure of the trace is apparent in the circular topology of diagrams. The fields $\psi(\boldsymbol{q}, \Omega_m)$ are represented as blue-dashed lines that inject momentum $\boldsymbol{q}$ and energy Ω_m.

To connect the present derivation to the Landau-Ginzburg formalism of the previous chapter, we restrict ourselves to the stationary state $\boldsymbol{q} = \Omega_m = 0$. Here, we have

$$S[\bar{\psi}\psi] = -\mathrm{Tr}\ln\left[-G_0^{-1}\right] + \sum_{ij}\alpha_{ij}\bar{\psi}_i\psi_j + \sum_{ijkl}\tilde{\beta}_{ijkl}\bar{\psi}_i\bar{\psi}_j\psi_k\psi_l\,. \tag{3.12}$$

with

$$\begin{aligned}\alpha_{ij} &= \delta_{ij}/V^{(i)} + \mathrm{Tr}\left[G_0(\boldsymbol{k},\omega_n)f^{(i)}_{\boldsymbol{k}}\sigma_- G_0(\boldsymbol{k},\omega_n)f^{(j)}_{\boldsymbol{k}}\sigma_+\right]\\ \tilde{\beta}_{ijkl} &= \mathrm{Tr}\left[G_0 f^{(i)}_{\boldsymbol{k}}\sigma_- G_0 f^{(j)}_{\boldsymbol{k}}\sigma_- G_0 f^{(k)}_{\boldsymbol{k}}\sigma_+ G_0 f^{(l)}_{\boldsymbol{k}}\sigma_+\right]\\ &\quad + \mathrm{Tr}\left[G_0 f^{(i)}_{\boldsymbol{k}}\sigma_- G_0 f^{(k)}_{\boldsymbol{k}}\sigma_+ G_0 f^{(j)}_{\boldsymbol{k}}\sigma_- G_0 f^{(l)}_{\boldsymbol{k}}\sigma_+\right] .\end{aligned} \tag{3.13}$$

Equation (3.12) exactly matches Eq. (2.6) of the previous chapter. We have therefore provided a microscopic derivation of the coefficients $\alpha, \tilde{\beta}$ for the case of a single-band model.

3.2.1 Symmetry considerations

Let us expand on the connection of the microscopic model to the group theoretical considerations of the previous chapter. Consider first the case of a single order parameter. In that case $f^{(i)}_{\boldsymbol{k}} = f_{\boldsymbol{k}}$ and the tensors $\alpha_{ij} = \alpha$ and $\beta_{ijkl} = \beta$ become simple numbers. In this case the order parameter can only transform

under a one-dimensional irrep. In the microscopic model, the invariance of the action can always be verified explicitly by transforming the individual components G_0 and $f_{\boldsymbol{k}}$ in the definition (3.13). In the $1d$-irrep case this is obvious, since the $f_{\boldsymbol{k}}$ at most undergo a sign change under a symmetry transformation and all coefficients contain even orders of $f_{\boldsymbol{k}}$. It is straightforward to see that G_0 is invariant under all symmetry transformations in the single-band case, as well.

For a higher-dimensional irreps, all $V^{(i)}$ corresponding to that irrep must be equal to ensure $\alpha_{ii} = \alpha$. The off-diagonal components $a_{ij}, i \neq j$ vanish as expected, since $\sum_{\boldsymbol{k}} f^{(i)}_{\boldsymbol{k}} f^{(j)}_{\boldsymbol{k}} = 0, i \neq j$. The $\tilde{\beta}_{ijkl}$ can now be explicitly seen to transform like the object $f^{(i)}_{\boldsymbol{k}} f^{(j)}_{\boldsymbol{k}} f^{(k)}_{\boldsymbol{k}} f^{(l)}_{\boldsymbol{k}}$ which transforms under a direct product representation, as defined in Eq. (2.7).

3.3 BCS equation

In Sec. 3.2 we presented a microscopic derivation of the free energy potential. Now we shall be interested not in the full shape of the potential itself, but in the energetically optimal order parameter configuration.

To this end, we perform a variation of the action Eq. (3.8) with respect to the order parameter in the stationary limit, $\boldsymbol{q} = \Omega_m = 0$. We find

$$0 = \frac{\delta}{\partial \bar{\psi}_i} S[\bar{\psi}\psi]\bigg|_{\psi_i \to \psi_i^{eq}} = \frac{1}{V^{(i)}} \psi_i^{eq} - \frac{\delta}{\partial \bar{\psi}_i} \mathrm{Tr}\left[-G \frac{\delta}{\partial \bar{\psi}_i} G^{-1}\right] \bigg|_{\psi_i \to \psi_i^{eq}} . \tag{3.14}$$

Evaluating the derivative and the trace, we get

$$\psi_i^{eq} = V^{(i)} \sum_{\boldsymbol{k}, \omega_n} \frac{\psi_i^{eq} f^{(i)}_{\boldsymbol{k}} f^{(i)}_{\boldsymbol{k}}}{E^2_{\boldsymbol{k}} + \omega_n^2} \tag{3.15}$$

with $E_{\boldsymbol{k}} = \sqrt{\xi^2 + \left| f^{(i)}_{\boldsymbol{k}} \psi_i^{eq} \right|^2}$. Explicitly performing the Matsubara sum, we obtain the BCS equation

$$\psi_i^{eq} = V^{(i)} \sum_{\boldsymbol{k}} \frac{\psi_i^{eq} f^{(i)}_{\boldsymbol{k}} f^{(i)}_{\boldsymbol{k}}}{2E_{\boldsymbol{k}}} \tanh \beta E_{\boldsymbol{k}}/2 \tag{3.16}$$

as the stationary saddle point of the action. The BCS equation is usually solved self-consistently for ψ_i^{eq}.

3.4 Saddle point fluctuations

For the following discussion, we will restrict ourselves to a single order parameter that transforms under a $1d$ irrep. We would like to expand the action around the mean field saddle point. To this end, we introduce the small amplitude deviation $\Delta(\tau, \boldsymbol{r})$ from the equilibrium configuration ψ^{eq} and the phase $\theta(\tau, \boldsymbol{r})$,

$$\begin{aligned} \psi(\tau, \boldsymbol{r}) &= (\psi^{eq} + \Delta(\tau, \boldsymbol{r})) e^{i\theta(\tau, \boldsymbol{r})} \\ \bar{\psi}(\tau, \boldsymbol{r}) &= (\psi^{eq} + \Delta(\tau, \boldsymbol{r})) e^{-i\theta(\tau, \boldsymbol{r})} . \end{aligned} \tag{3.17}$$

Separation of the order parameter into amplitude and phase fluctuations requires treatment of the path integral in real space. For an intuitive understanding, let us revisit the Hubbard Stratonovich decoupling introduced in the beginning of this chapter, but this time we adopt a real space perspective. In real space, one usually deals with some type of Coulomb interaction, e.g., $\sum_{\boldsymbol{r}\boldsymbol{r}'} V(\boldsymbol{r}-\boldsymbol{r}')c^\dagger_{\boldsymbol{r}\uparrow}c^\dagger_{\boldsymbol{r}'\downarrow}c_{\boldsymbol{r}'\downarrow}c_{\boldsymbol{r}\uparrow}$. We proceed by factorizing the potential in a gradient expansion,

$$\sum_{\boldsymbol{r}\boldsymbol{r}'} V(\boldsymbol{r}-\boldsymbol{r}')c^\dagger_{\boldsymbol{r}\uparrow}c^\dagger_{\boldsymbol{r}'\downarrow}c_{\boldsymbol{r}'\downarrow}c_{\boldsymbol{r}\uparrow} = -\sum_{\boldsymbol{r}\alpha} V^{(i,\alpha)} \underbrace{\left(c^\dagger_{\boldsymbol{r}\uparrow}\frac{\partial^\alpha}{\partial \boldsymbol{r}_i^\alpha}c^\dagger_{\boldsymbol{r}\downarrow}\right)}_{\text{HS: }\psi^\dagger(\boldsymbol{r})} c_{\boldsymbol{r}\downarrow}\frac{\partial^\alpha}{\partial \boldsymbol{r}_i^\alpha}c_{\boldsymbol{r}\uparrow}\,. \tag{3.18}$$

This step is reminiscent of Eq. (3.3) where we factorized the interaction potential in $\boldsymbol{k}$-space. Next, the quartic term is decoupled using a Hubbard-Stratonovich transformation, analogous to Eq. (3.5). We get

$$\sum_{\boldsymbol{r}} \psi^\dagger(\boldsymbol{r})c_{\boldsymbol{r}\downarrow}\underbrace{\sum_\alpha V^{(i,\alpha)}\frac{\partial^\alpha}{\partial \boldsymbol{r}_i^\alpha}}_{f_{-i\nabla}} c_{\boldsymbol{r}\uparrow} = \sum_{\boldsymbol{r}} \psi^\dagger(\boldsymbol{r})c_{\boldsymbol{r}\downarrow}f_{-i\nabla}c_{\boldsymbol{r}\uparrow}\,, \tag{3.19}$$

where we recover the symmetry function $f_{\boldsymbol{k}}$ with $\boldsymbol{k}\to -i\nabla$. With this insight, we can now intuitively understand the symmetry of pairing in real space. For s-wave pairing, we have $f_{\boldsymbol{k}}=1\to f_{-i\nabla}=1$. Inserting this into Eq. (3.18), we obtain an onsite interaction. For d-wave symmetry we have $f_{\boldsymbol{k}}=k_x^2-k_y^2\to f_{-i\nabla}=-\partial_x^2+\partial_y^2$. If we discretize the derivative, this appears as an attractive nearest-neighbor pairing along y and a repulsive nearest-neighbor interaction along x.

We can now express the Green's function in real space. If we also introduce the electromagnetic gauge fields ϕ, $\boldsymbol{A}$, this yields

$$G^{-1} = \begin{pmatrix} -\partial_\tau - e\phi(\tau,\boldsymbol{r}) - \xi_{-i\nabla - e\boldsymbol{A}(\tau,\boldsymbol{r})} & (\psi^{eq}+\Delta(\tau,\boldsymbol{r}))e^{i\theta(\tau,\boldsymbol{r})}f_{-i\nabla} \\ (\psi^{eq}+\Delta(\tau,\boldsymbol{r}))e^{-i\theta(\tau,\boldsymbol{r})}f_{i\nabla} & -\partial_\tau + e\phi(\tau,\boldsymbol{r}) + \xi_{i\nabla - e\boldsymbol{A}(\tau,\boldsymbol{r})} \end{pmatrix}. \tag{3.20}$$

Next, it will be convenient to make the transformation

$$V = \exp(i\theta(\tau,\boldsymbol{r})\sigma_3/2) \tag{3.21}$$

to separate the amplitude and phase degrees of freedom of the Hubbard Stratonovich field. We are allowed to perform such a transformation, since we are integrating over the Nambu basis vectors Ψ in the effective action which results in the cyclic trace (cf. Eq. 3.8),

$$\mathrm{Tr}\ln\left[-G_i^{-1}\right] = \mathrm{Tr}\ln\left[-G^{-1}VV^\dagger\right] = \mathrm{Tr}\ln\left[-V^\dagger G^{-1}V\right] = \mathrm{Tr}\ln\left[-\tilde{G}^{-1}\right]. \tag{3.22}$$

The transformed Green's function is

$$\tilde{G}^{-1} = \begin{pmatrix} -\partial_\tau - i\partial_\tau\theta - e\phi(\tau,\boldsymbol{r}) - \xi_{-i\nabla+\nabla\theta-e\boldsymbol{A}(\tau,\boldsymbol{r})} & (\psi^{eq}+\Delta(\tau,\boldsymbol{r}))f_{-i\nabla} \\ (\psi^{eq}+\Delta(\tau,\boldsymbol{r}))f_{i\nabla} & -\partial_\tau + i\partial_\tau\theta + e\phi(\tau,\boldsymbol{r}) + \xi_{i\nabla+\nabla\theta-e\boldsymbol{A}(\tau,\boldsymbol{r})} \end{pmatrix} . \tag{3.23}$$

We note that for non-s-wave symmetries, $f_{-i\nabla} \neq 1$, there should be additional $\nabla\theta$ terms, stemming from $f_{-i\nabla}$ acting on the transformation V. These terms, however, can be shown to be safely neglected [22].

The Green's function in Eq. (3.23) is manifestly gauge invariant, since the electromagnetic potentials only occur in the gauge invariant combinations $i\partial_\tau\theta + e\phi$, $\nabla\theta - e\boldsymbol{A}$.

Next, we perform a series of approximations. First, we assume an electrical field that only varies in time, such that $\phi = 0$ and $\boldsymbol{A}(\tau,\boldsymbol{r}) = \boldsymbol{A}(\tau)$. Time-varying, spatially uniform fields are strictly speaking not allowed by Maxwell's equations. We should thus think of this as an approximation which holds when field is mostly uniform on the relevant scale of the lattice spacing [50]. Put differently, we are neglecting the photon momentum. Second, we expand the band dispersion in order of $\boldsymbol{A}$,

$$\xi_{\boldsymbol{k}-e\boldsymbol{A}} = \xi_{\boldsymbol{k}} - e\frac{\partial\xi_{\boldsymbol{k}}}{\partial k_i}A_i + \frac{e^2}{2}\frac{\partial^2\xi_{\boldsymbol{k}}}{\partial k_i k_j}A_{ij}^2\sigma_3 \,. \tag{3.24}$$

We transform our Green's function back to momentum space, and again separate $\tilde{G}^{-1}$ into the stationary part G_0^{-1} and the fluctuating part Σ:

$$\begin{aligned} \tilde{G}^{-1}(\boldsymbol{k}\boldsymbol{q},\omega_n\Omega_m) &= G_0^{-1}(\boldsymbol{k},\omega_n)\delta_{\boldsymbol{q},0}\delta_{\Omega_m,0} - \Sigma\left(\boldsymbol{k}\boldsymbol{q},\Omega_m\right) \\ G_0^{-1}(\boldsymbol{k},\omega_n) &= i\omega_n - \xi_{\boldsymbol{k}}\sigma_3 + \psi^{eq}f_{\boldsymbol{k}}\sigma_1 \\ \Sigma(\boldsymbol{k}\boldsymbol{q},\Omega_m) &= -f_{\boldsymbol{k}}\Delta(\boldsymbol{q},\Omega_m)\sigma_1 + \frac{\Omega_m}{2}\theta(\boldsymbol{q},\Omega_m)\sigma_3 - e\frac{\partial\xi_{\boldsymbol{k}}}{\partial k_i}A_i(\Omega_m) + e^2\frac{1}{2}\frac{\partial^2\xi_{\boldsymbol{k}}}{\partial k_i k_j}A_{ij}^2(\Omega_m)\sigma_3 \,. \end{aligned} \tag{3.25}$$

Integrating over the fermionic Grassmann fields, we obtain the bosonic action

$$S[\Delta,\theta,\boldsymbol{A}] = \sum_{i\boldsymbol{q}\Omega_n} \left|\psi^{eq}+\Delta(\boldsymbol{q},\Omega_n)\right|^2/V - \mathrm{Tr}\ln\left(-G_0^{-1}\right) + \mathrm{Tr}\sum_{n=1}^{\infty}\frac{1}{n}\left(G_0\Sigma\right)^n \,. \tag{3.26}$$

Our strategy in the perturbation expansion of the action $S[\Delta,\theta,\boldsymbol{A}]$ will be the following: We will expand the action up to fourth order in the electromagnetic field $\boldsymbol{A}$ and up to quadratic order in the collective fields Δ,θ. Then it is possible to perform the path integration over the quadratic modes by Gaussian integration. The resulting effective action $S[\boldsymbol{A}]$ will only depend on the electromagnetic fields. We readily obtain the expectation value of the current operator as

$$\boldsymbol{j}(t) = -\frac{\delta}{\partial\boldsymbol{A}}S[\boldsymbol{A}] \,. \tag{3.27}$$

Terms in the expanded action $S[\Delta,\theta,\boldsymbol{A}]$ up to quadratic order in the collective fields are represented by

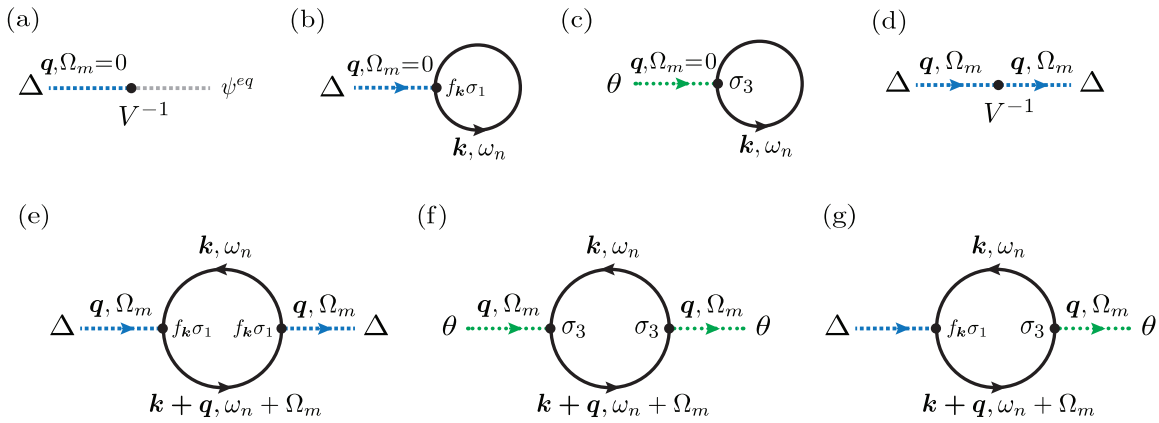

Figure 3.3: Diagrams of first and second order in the collective modes Δ, θ. Diagrams (a+b) cancel out, since no linear fluctuations are possible around a saddle point. Diagram (c) vanishes. Diagrams (d-f) define the propagators of the collective mode.

diagrams in Figs. 3.3. Fig. 3.7 shows mixing terms between collective fields and $\boldsymbol{A}$ and Fig. 3.5 shows the remaining $\boldsymbol{A}$-dependent terms.

3.4.1 The Higgs propagator

Let us now study the individual diagrams. Figure 3.3(a,d) correspond to the expansion of the term

$$|\psi^{eq} + \Delta(\boldsymbol{q}, \Omega_n)|^2 / V \,.$$

The linear term $\psi^{eq}\Delta/V$ in Fig. 3.3(a) is canceled out by 3.3(b), since

$$\text{(a)+(b)} = 2\psi^{eq}\Delta(\boldsymbol{q}=0,\Omega_n=0)/V + \sum_{\boldsymbol{k}\omega_n} \mathrm{Tr}\left[G_0(\boldsymbol{k},\omega_n)\sigma_1\right] f_{\boldsymbol{k}}\Delta(\boldsymbol{q}=0,\Omega_m=0) \tag{3.28}$$

$$= 2\sum_{\boldsymbol{k}} \frac{\psi^{eq} f_{\boldsymbol{k}} f_{\boldsymbol{k}}}{2E_{\boldsymbol{k}}} \tanh(\beta E_{\boldsymbol{k}}/2)\Delta(0) + \sum_{\boldsymbol{k}\omega_n} \frac{2\psi^{eq} f_{\boldsymbol{k}} f_{\boldsymbol{k}}}{(i\omega_n)^2 - E_{\boldsymbol{k}}^2} \tanh(\beta E_{\boldsymbol{k}}/2)\Delta(0) = 0\,, \tag{3.29}$$

after evaluation of the Matsubara sum. Here, we have made use of the gap equation (3.16) to replace the term $2\psi^{eq}\Delta/V$. Cancellation of the linear terms is, of course, expected since we are expanding the action around the saddle point. Correspondingly, the linear θ-term, diagram 3.3(c), vanishes as well.

In the following it will be convenient to introduce the susceptibilities X_{ij} and their momentum average χ_{ij},

$$X_{ij}(\boldsymbol{k},\boldsymbol{q},\Omega_m) = \sum_{\omega_n} \mathrm{Tr}\left[G_0(\boldsymbol{k},\omega_n)\sigma_i G_0(\boldsymbol{k}+\boldsymbol{q},\omega_n+\Omega_m)\sigma_j\right] \tag{3.30}$$

$$\chi_{ij}(\Omega_m) = \sum_{\boldsymbol{k}} X_{ij}(\boldsymbol{k},\boldsymbol{q}=0,\Omega_m)\,. \tag{3.31}$$

They correspond to fermionic bubbles that only differ in their vertices σ_i, σ_j. Explicitly evaluating the Matsubara sum, one has

$$X_{11}(\boldsymbol{k}, \boldsymbol{q}=0, \Omega_m) = -\frac{4}{E_{\boldsymbol{k}}} \frac{\xi_{\boldsymbol{k}}^2}{4E_{\boldsymbol{k}}^2 - (i\Omega_m)^2} \tag{3.32}$$

$$X_{33}(\boldsymbol{k}, \boldsymbol{q}=0, \Omega_m) = -\frac{4}{E_{\boldsymbol{k}}} \frac{f_{\boldsymbol{k}}^2 \left(\psi^{eq}\right)^2}{4E_{\boldsymbol{k}}^2 - (i\Omega_m)^2} \tag{3.33}$$

$$X_{13}(\boldsymbol{k}, \boldsymbol{q}=0, \Omega_m) = \frac{4}{E_{\boldsymbol{k}}} \frac{\xi_{\boldsymbol{k}} f_{\boldsymbol{k}} \psi^{eq}}{4E_{\boldsymbol{k}}^2 - (i\Omega_m)^2} \,. \tag{3.34}$$

Using these definitions, Fig. 3.3(d-e) yield

$$\begin{aligned} \text{Fig. 3.3 (d)+(e)} &= \Delta(\boldsymbol{q}, \Omega_m) \left[V^{-1}\delta_{\boldsymbol{q},0} + \chi_{11}(\boldsymbol{q}, \Omega_m)\right] \Delta(-\boldsymbol{q}, -\Omega_m) \\ &\equiv \frac{1}{2}\Delta(\boldsymbol{q}, \Omega_m) H^{-1}(\boldsymbol{q}, \Omega_m) \Delta(-\boldsymbol{q}, -\Omega_m) \,. \end{aligned} \tag{3.35}$$

Here, H is the retarded Higgs propagator. The propagator can also be thought to originate from an RPA summation, which becomes apparent when we expand it as the geometric series

$$H = \left[V^{-1} + \chi_{11}\right]^{-1} = V \sum_{n=0}^{\infty} \left(-\chi_{11} V\right)^n \,. \tag{3.36}$$

Explicitly, one finds for the Higgs propagator at finite momentum $\boldsymbol{q}$,

$$H^{-1}(\boldsymbol{q}, \Omega_m) = \sum_{\boldsymbol{k}} \frac{E_{\boldsymbol{k}} + E_{\boldsymbol{k}+\boldsymbol{q}}}{2E_{\boldsymbol{k}} E_{\boldsymbol{k}+\boldsymbol{q}}} \frac{f_{\boldsymbol{k}} f_{\boldsymbol{k}+\boldsymbol{q}} \left(\psi^{eq}\right)^2 + E_{\boldsymbol{k}}^2 + E_{\boldsymbol{k}+\boldsymbol{q}}^2 + E_{\boldsymbol{k}} E_{\boldsymbol{k}+\boldsymbol{q}} - \xi_{\boldsymbol{k}}\xi_{\boldsymbol{k}+\boldsymbol{q}} + \Omega_m^2}{\left(E_{\boldsymbol{k}} + E_{\boldsymbol{k}+\boldsymbol{q}}\right)^2 + \Omega_m^2} \tag{3.37}$$

where we have used the approximate gap equation

$$V^{-1} = \frac{1}{2} \sum_{\Omega_m} \left(\frac{1}{E_{\boldsymbol{k}}^2 + \Omega_m^2} + \frac{1}{E_{\boldsymbol{k}+\boldsymbol{q}}^2 + \Omega_m^2} \right) = \frac{E_{\boldsymbol{k}} + E_{\boldsymbol{k}+\boldsymbol{q}}}{4E_{\boldsymbol{k}} E_{\boldsymbol{k}+\boldsymbol{q}}} \,. \tag{3.38}$$

To order $O(\boldsymbol{q}^2)$ and for a circular Fermi-surface and an s-wave gap, $f_{\boldsymbol{k}} = 1$, one can approximate this as

$$H = \frac{1}{N_0} \frac{\sqrt{\left(2\psi^{eq}\right)^2 - \omega^2}}{\left(2\psi^{eq}\right)^2 - \omega^2 + v_F^2 \boldsymbol{q}^2} \frac{1}{\sin^{-1}\left(|\omega/2\psi^{eq}|\right)} \,, \tag{3.39}$$

where we have performed the analytical continuation $i\Omega_m \to \omega + i\eta$ [151]. The infinitesimal constant η is omitted for clarity. A plot of the absolute, real, and imaginary part of Higgs propagator is shown in Fig. 3.4. The energy spectrum of the Higgs mode is apparent as a peak in $|H|$.

We notice that H is different from a usual propagating mode where one would expect a δ-peak in the spectral function, which is given by the imaginary part of the retarded propagator, $-\mathrm{Im}H$. Instead, both the imaginary and real part undergo a sign change at the mode resonance. In fact, a closer look at Eq. (3.4) reveals that H does not possess a simple pole as would be the case for a regular bosonic particle. Instead, it

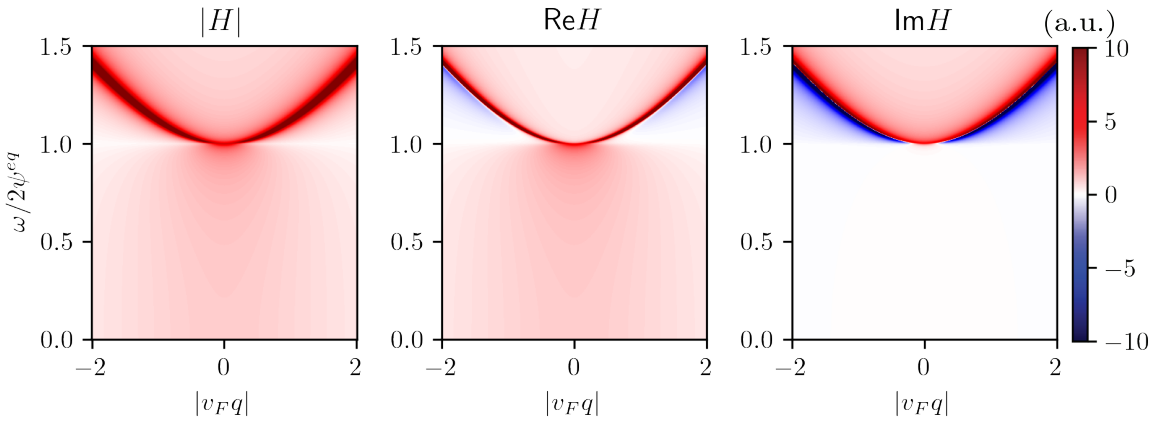

Figure 3.4: Absolute, real, and imaginary part of the Higgs propagator.

has a square-root divergence at $\omega = 2\psi^{eq}$ for $\boldsymbol{q} = 0$ [33].

This peculiar analytic structure physically arises due to quasi-particle damping. The mode resonance is located at $2\psi^{eq}$, where it coincides with the onset of the quasiparticle continuum. As such, it can decay into quasiparticles and is strongly overdamped. While the Higgs mode does not constitute a stable bosonic excitation, its presence may still lead to signatures in the optical response, as we shall see.

3.4.2 Phase mode and phase-Higgs coupling

The phase field θ always occurs in conjunction with the factor $\Omega_m/2$. For readability, we will absorb this factor into the new variable $\tilde{\theta}(\Omega_m) = \theta(\Omega_m)\Omega_m/2$. This redefinition corresponds to a change of the path integral measure. In this convention, the phase mode propagator in Fig. 3.3(f) is simply given by χ_{33}^{-1}.

The phase mode may also couple to the Higgs mode, via the coupling term $\chi_{13}\Delta\theta$ in Fig. 3.3(g). Note that, according to Eq. (3.34), χ_{13} is odd in $\xi_{\boldsymbol{k}}$. Presence of the Higgs-phase coupling therefore relies on an asymmetric distribution of states below and above the Fermi-surface, i.e. breaking of particle-hole symmetry $\sum_{\boldsymbol{k}} \xi_{\boldsymbol{k}} \neq 0$. In general, this coupling term is strongly suppressed.

As we noted in Ch. 1, the phase mode does not constitute a physical mode. We will see later that its contribution is intimately connected to the electromagnetic contribution in diagram 3.5(c) and should not be viewed independently.

3.4.3 Bare electromagnetic response

Figure 3.5 shows the diagrammatic expansion in the electromagnetic vector potential $\boldsymbol{A}$. They are composed of two different vertices: The *paramagnetic* vertex $\partial_i \xi_{\boldsymbol{k}} A_i \, \sigma_0$ and the *diamagnetic* vertex $\partial_i \partial_j \xi_{\boldsymbol{k}} A_i A_j \, \sigma_3$. For zero external photon momentum, we find that all diagrams with paramagnetic vertices vanish identically, i.e. diagrams 3.5(a,d,e) are zero.

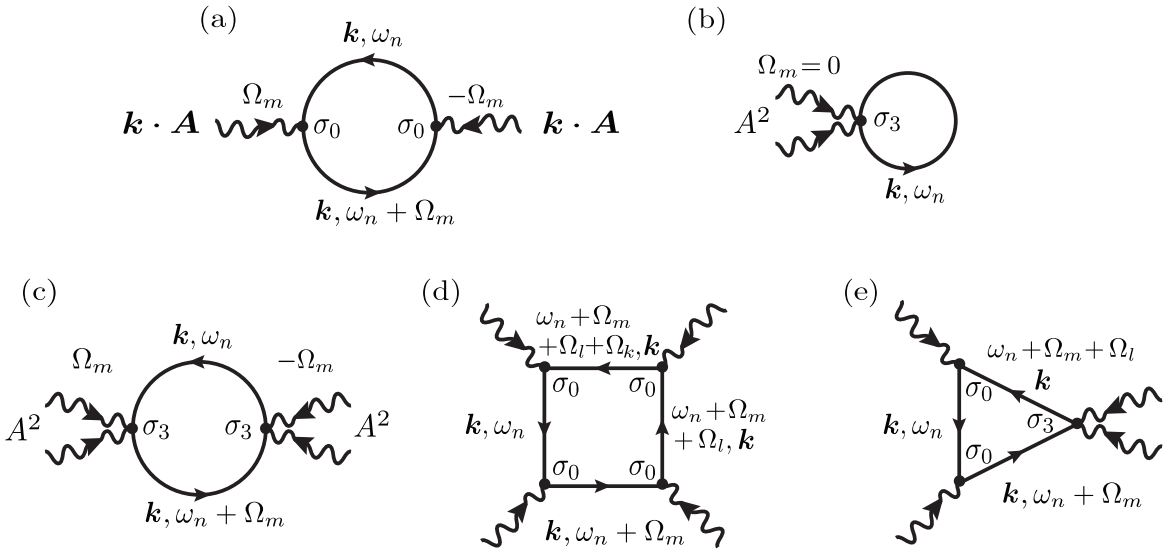

Figure 3.5: Terms in the action that are quadratic (a-b) and cubic (c-e) in the electric fields. Odd-order terms vanish due to inversion symmetry, $\boldsymbol{k} \to -\boldsymbol{k}$.

The only quartic diagram that we need to consider is 3.5(c). It is given by the expression

$$K^0_{ij,kl}(\Omega_m) = \sum_{\boldsymbol{k}} \frac{\partial \xi_{\boldsymbol{k}}}{\partial \boldsymbol{k}_i \partial \boldsymbol{k}_j} \frac{\partial \xi_{\boldsymbol{k}}}{\partial \boldsymbol{k}_k \partial \boldsymbol{k}_l} X_{33}(\boldsymbol{k}, \boldsymbol{q} = 0, \Omega_m)\,. \tag{3.40}$$

Coupling terms between light and collective modes are shown in Fig. 3.6. Again, only diamagnetic diagrams (c, d) are non-zero. They are given, respectively, by

$$\kappa_{ij,H}(\Omega_m) = \sum_{\boldsymbol{k}} \frac{\partial \xi_{\boldsymbol{k}}}{\partial \boldsymbol{k}_i \partial \boldsymbol{k}_j} f_{\boldsymbol{k}} X_{31}(\boldsymbol{k}, \boldsymbol{q} = 0, \Omega_m) \tag{3.41}$$

$$\kappa_{ij,3}(\Omega_m) = \sum_{\boldsymbol{k}} \frac{\partial \xi_{\boldsymbol{k}}}{\partial \boldsymbol{k}_i \partial \boldsymbol{k}_j} X_{33}(\boldsymbol{k}, \boldsymbol{q} = 0, \Omega_m)\,. \tag{3.42}$$

Putting everything together, we obtain the action for collective modes, coupling terms, and the electric fields,

$$\begin{aligned} S[\Delta, \tilde{\theta}, \boldsymbol{A}] = &\sum_{\Omega_m} \begin{pmatrix} \Delta(\Omega_m) \\ \tilde{\theta}(\Omega_m) \end{pmatrix} \begin{pmatrix} H^{-1} & \chi_{13} \\ \chi_{13} & \chi_{33} \end{pmatrix} \begin{pmatrix} \Delta(-\Omega_m) \\ \tilde{\theta}(-\Omega_m) \end{pmatrix} \\ &+ \sum_{\Omega_m, ij} A^2_{ij} \begin{pmatrix} \kappa_{ij,H}(\Omega_m) & \kappa_{ij,3}(\Omega_m) \end{pmatrix} \begin{pmatrix} \Delta(-\Omega_m) \\ \tilde{\theta}(-\Omega_m) \end{pmatrix} \\ &+ \sum_{\Omega_m} A^2_{ij}(\Omega_m) K^0_{ij,kl}(\Omega_m) A^2_{kl}(-\Omega_m)\,. \end{aligned} \tag{3.43}$$

Here, sums over the $ijkl$ are implied and $A^2_{ij}(\Omega_m) = \sum_{\Omega_l} A_i(\Omega_m - \Omega_l) A_j(\Omega_l)$ is a convolution of A_i and A_j in Matsubara space, stemming from the fact that is is a product term in imaginary time. Finally, we

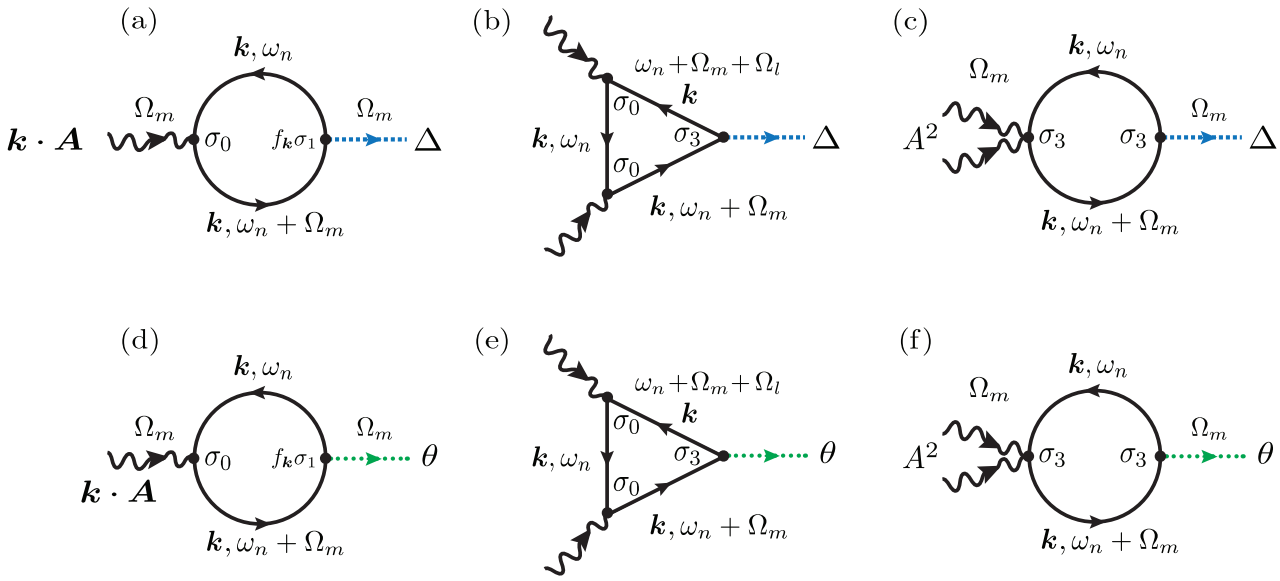

Figure 3.6: Diagrammatic representation of light-Higgs coupling (a-c) and light-phase mode coupling (d-f).

perform the Gaussian path integral over Δ, θ and obtain the effective action after analytical continuation.

$$\begin{aligned} S[\boldsymbol{A}] &= \int d\omega \begin{pmatrix} \kappa_{ij,H} & \kappa_{ij,3} \end{pmatrix} \begin{pmatrix} H^{-1} & \chi_{13} \\ \chi_{13} & \chi_{33} \end{pmatrix}^{-1} \begin{pmatrix} \kappa_{ij,H} \\ \kappa_{ij,3} \end{pmatrix} A^2_{ij}(\omega) A^2_{kl}(-\omega) + \int d\omega K^0_{ij,kl} A^2_{ij} A^2_{kl} \\ &= \int d\omega K_{ij,kl}(\omega) A^2_{ij}(\omega) A^2_{kl}(-\omega)\,. \end{aligned} \tag{3.44}$$

In the last equality, we have defined the electromagnetic kernel $K_{ij,kl}$ that encodes all information of the nonlinear response,

$$\begin{aligned} K_{ij,kl} &= \left(K^H_{ij,kl} + K^D_{ij,kl}\right) \\ K^D_{ij,kl} &= K^0_{ij,kl} - \frac{\kappa_{ij,3}\kappa_{jk,3}}{\chi_{33}} \\ K^H_{ij,kl} &= -\frac{(\kappa_{ij,H} - \kappa_{ij,3}\chi_{13}/\chi_{33})(\kappa_{kl,H} - \kappa_{kl,3}\chi_{13}/\chi_{33})}{H - \chi^2_{13}/\chi_{33}}\,. \end{aligned} \tag{3.45}$$

We have separated the kernel into the density response K^D and the Higgs response K^H. From here, we can obtain the expectation value of the current operator as a functional derivative

$$j_i(t) = \frac{\delta}{\delta A_i(t)} \ln Z[A] = -\frac{\delta}{\delta A_i(t)} S[A]\,. \tag{3.46}$$

The expression in Fourier space can be derived from the chain rule of functional derivation,

$$\begin{aligned}\frac{\delta S[A]}{\delta \tilde{A}_i(\omega)} &= \frac{\delta}{\delta \tilde{A}_i(\omega)} S[\mathcal{FT}[\tilde{A}]] = \int dt \frac{\delta S[A]}{\delta A_i(t)} \frac{\delta \mathcal{FT}^{-1}[\tilde{A}_i](t)}{\delta \tilde{A}(\omega)} \\ &= -\int dt j_i(t) e^{-i\omega t} = -j_i(-\omega)\,, \end{aligned} \tag{3.47}$$

where we have denoted the Fourier transform $\tilde{A}(\omega) = \mathcal{FT}[A](\omega) = \int \frac{d\omega}{2\pi} A(t) e^{i\omega t}$ by a tilde and $A = A(t)$. Explicitly performing the functional derivative of the quartic part of the action gives the final result

$$j_i(\omega) = \int d\omega' A_j(\omega - \omega') K_{ij,kl}(\omega') A^2_{kl}(\omega')\,. \tag{3.48}$$

3.4.4 The nonlinear optical kernel

The nonlinear optical kernel can also be derived as a functional derivative of the partition function

$$K_{ij,kl}(\omega) = \frac{\delta^2}{\partial A^2_{ij}(\omega) A^2_{kl}(-\omega)} \ln \mathcal{Z}\big|_{\boldsymbol{A}=0}\,. \tag{3.49}$$

In canonical formulation, it is therefore given by the retarded two-point correlation function

$$K_{ij,kl}(t - t') = -i\theta(t - t') \langle \big[\rho_{ij}(t), \rho_{kl}(t')\big] \rangle \tag{3.50}$$

where

$$\rho_{ij} = \sum_{\boldsymbol{k}\sigma} \frac{\partial^2}{\partial k_i \partial k_j} \xi_{\boldsymbol{k}}\, c^\dagger_{\boldsymbol{k}\sigma} c_{\boldsymbol{k}\sigma} \tag{3.51}$$

is an effective density operator.

Gauge invariance and the continuum limit

Let us examine the explicit form of the kernel in Eq. (3.45) a bit closer. First, we consider the continuum limit. For a parabolic band dispersion, the diamagnetic vertex function becomes

$$\frac{\partial^2}{\partial k_i \partial k_j} \xi_{\boldsymbol{k}} = \frac{1}{2m} \delta_{ij}\,. \tag{3.52}$$

Thus, the light coupling susceptibilities simplify to

$$\begin{aligned} K^0_{ij,kl} &= \delta_{ij}\delta_{kl}\chi_{33} \\ K^0_{ij,H} &= \delta_{ij}\chi_{13} \\ K^0_{ij,3} &= \delta_{ij}\chi_{33}\,. \end{aligned} \tag{3.53}$$

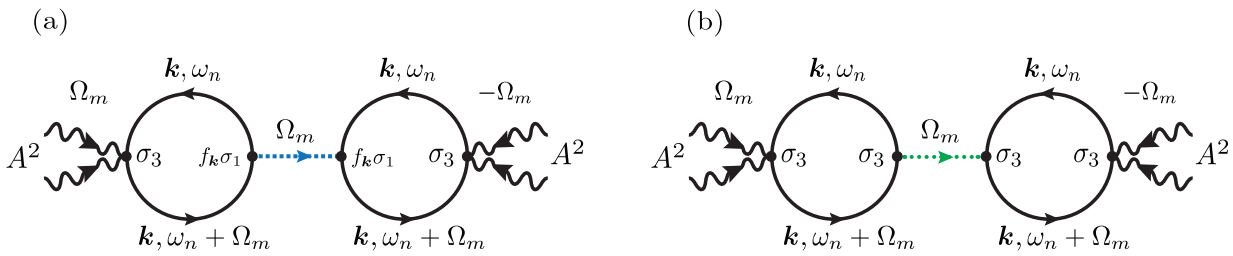

Figure 3.7: Diagrammatic representation of the nonlinear optical kernel in the particle-hole symmetric limit.

Inserting this into the expression for the full kernel (3.45), we find that nonlinear response vanishes completely, $K_{ij,kl} = 0$. This result is expected from gauge invariance. In the continuum limit, the two point correlator in Eq. (3.51) reduces to the two-point correlation function of particle number fluctuations since $\rho_{ij} = \delta_{ij} \frac{1}{2m} \hat{N}$ with $\hat{N} = \sum_{\boldsymbol{k}\sigma} c^\dagger_{\boldsymbol{k}\sigma} c_{\boldsymbol{k}\sigma}$. For a single band model, such fluctuations are forbidden due to particle number conservation and the optical response vanishes.

We emphasize that this result relies on renormalization of the kernel by the collective phase field θ. Had we not incorporated the effect of the phase mode, we would have obtained finite density-density fluctuations, which is a wrong result. The phase mode and electromagnetic vector potential must always be considered together since they are related by a gauge transformation.

The vanishing of the complete nonlinear response in the continuum limit reveals a common thread in the study of the Higgs mode. The non-linear response, and especially the Higgs response, is quite delicate in the sense that it vanishes in certain limits.

In Ch. 5 we will see that this situation can change in the case of multiband superconductors. Here, particle number fluctuations in one band can be compensated by another band, such that the nonlinear kernel need not vanish. This can yield a finite collective mode response even in the continuum limit. Additionally, we will see in Ch. 5 that effects of impurities change the above picture entirely. In this case, paramagnetic vertices no longer vanish and the Higgs mode contribution to the nonlinear response can become substantial.

Particle-hole symmetry

As we already noted, the susceptibility χ_{13} vanishes in the presence of particle-hole symmetry. In this case, the density and Higgs contributions simplify to

$$\begin{aligned} K^D_{ij,kl} &= K^0_{ij,kl} - \frac{\kappa_{ij,3}\kappa_{jk,3}}{\chi_{33}} \\ K^H_{ij,kl} &= -\frac{\kappa_{ij,H}\kappa_{kl,H}}{H} \,. \end{aligned} \tag{3.54}$$

These terms correspond to a bare quasiparticle response Fig. 3.5(c) and renormalizations by the phase and Higgs propagator, shown in Fig. 3.7.

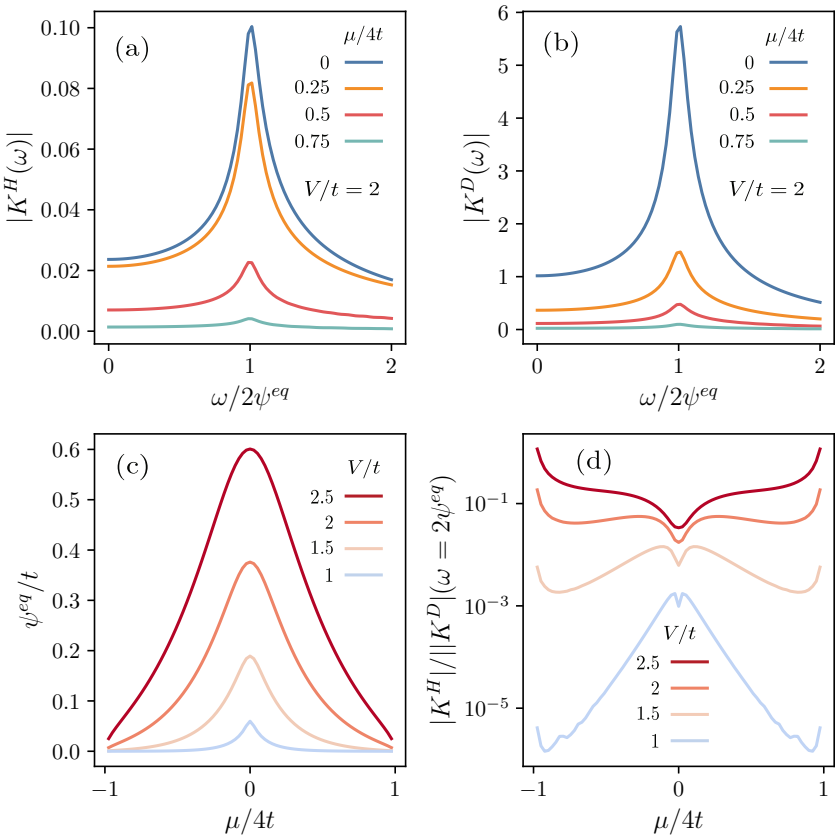

Figure 3.8: Frequency dependence (a) of Higgs kernel (b) density kernel. Both show a peak at $2\psi^{eq}$. We have used $\eta = 0.1\psi^{eq}$. (c) Plot of the meanfield gap ψ^{eq} as a function of band filling. (d) Ratio of absolute value of Higgs and density Kernel evaluated at the peak position $\omega = 2\psi^{eq}$.

Collective Higgs versus non-collective density contribution

The nonlinear kernel in Eq. (3.45) is composed of two contributions: density fluctuations from quasiparticle excitations K^D and fluctuations of the Higgs mode K^H. A plot of these two contributions is shown in Fig. 3.8(a-b) for a bandstructure on the square lattice of the form $\xi_{\boldsymbol{k}} = -2t(\cos k_x + \cos k_y) - \mu$ and an s-wave gap $f_{\boldsymbol{k}} = 1$. Both contributions yield a very similar spectrum, with a broad peak centered around $2\psi^{eq}$. Since both contributions have the same resonance structure, it is impossible to disentangle them.

It is, however, worthwhile to examine the relative magnitude of the respective contributions. The relative contribution of Higgs and quasiparticle density fluctuations has first been investigated in Ref. [34]. Here, we reproduce their results by plotting the quantity

$$\frac{|K^H(\omega = 2\psi^{eq})|}{|K^D(\omega = 2\psi^{eq})|}, \tag{3.55}$$

evaluated at the resonance peak position. The results are shown in Fig. 3.8(d) as a function of chemical potential μ for selected pairing strengths V. We find that the Higgs contribution is almost always subdominant. It becomes relevant only for strong pairing $V = 2.5t$ and chemical potential close to the band edge. Note

that the superconducting gap ψ^{eq} is strongly reduced close to the band edge as shown in panel (c).

3.5 Pseudospin formalism

An alternative to the diagrammatic treatment of the BCS Hamiltonian is given by the Anderson pseudospin model. This constitutes a very compact formulation of the problem that is amenable to numerical simulation. This new approach relies on the introduction of Anderson's pseudospins [7].

$$s_{i\boldsymbol{k}} = \frac{1}{2}\Psi^{\dagger}_{\boldsymbol{k}}\sigma_i\Psi_{\boldsymbol{k}}\,, \tag{3.56}$$

where $\Psi_{\boldsymbol{k}}$ are the Nambu spinors. The operator $\boldsymbol{s}_{\boldsymbol{k}}$ is not an actual spin operator. Instead, it may be thought of as a Bloch vector in a two level system of particle and hole excitations in momentum space. The operator satisfies the spin-$1/2$ $SU(2)$ algebra

$$[s_{i\boldsymbol{k}}, s_{j\boldsymbol{k}'}] = i\varepsilon_{ijl}s_{l\boldsymbol{k}}\delta_{\boldsymbol{k},\boldsymbol{k}'}\,. \tag{3.57}$$

With this, the BCS meanfield Hamiltonian represents an effective spin in a pseudo-magnetic field $\boldsymbol{b}_{\boldsymbol{k}}$,

$$H = \sum_{\boldsymbol{k}} \boldsymbol{b}_{\boldsymbol{k}}\cdot\boldsymbol{s}_{\boldsymbol{k}}\,, \tag{3.58}$$

where

$$\boldsymbol{b}_{\boldsymbol{k}} = \left(-2\psi' f_{\boldsymbol{k}},\, 2\psi'' f_{\boldsymbol{k}}, 2\xi_{\boldsymbol{k}}\right)\,. \tag{3.59}$$

The equation of motion,

$$\partial_t\langle s_{i\boldsymbol{k}}\rangle = -i\langle[s_{i\boldsymbol{k}}, H]\rangle = -i\langle[s_{i\boldsymbol{k}}, s_{j\boldsymbol{k}'}b_{j\boldsymbol{k}'}]\rangle = \epsilon_{ijl}b_{j\boldsymbol{k}}\langle s_{l\boldsymbol{k}}\rangle = \boldsymbol{b}_{\boldsymbol{k}}\times\langle s_{\boldsymbol{k}}\rangle\,, \tag{3.60}$$

describes precession of the pseudospins in the field $\boldsymbol{b}_{\boldsymbol{k}}$ at each point $\boldsymbol{k}$. Thus far, all pseudospins at momentum points $\boldsymbol{k}$ are independent. Coupling is induced via the BCS gap equation

$$\psi = V\sum_{\boldsymbol{k}} f_{\boldsymbol{k}}\langle c_{-\boldsymbol{k}\downarrow}c_{\boldsymbol{k}\uparrow}\rangle = V\sum_{\boldsymbol{k}} f_{\boldsymbol{k}}\langle s_{1\boldsymbol{k}} - is_{2\boldsymbol{k}}\rangle\,, \tag{3.61}$$

which results in collective motion of the pseudospins. The set of equations (3.60-3.61) must be solved self-consistently. Motion of the pseudospins affects the superconducting order parameter, which in turn modifies the pseudo-magnetic field.

In equilibrium, the groundstate is given by

$$\begin{aligned} s_{1\boldsymbol{k}} &= \frac{\psi^{eq} f_{\boldsymbol{k}}}{2E_{\boldsymbol{k}}} \tanh\left(\beta E_{\boldsymbol{k}/2}\right) \\ s_{2\boldsymbol{k}} &= 0 \\ s_{3\boldsymbol{k}} &= -\frac{\xi_{\boldsymbol{k}}}{2E_{\boldsymbol{k}}} \tanh\left(\beta E_{\boldsymbol{k}/2}\right) . \end{aligned} \tag{3.62}$$

At zero temperature the spins simply anti-align with the pseudo-magnetic field $\boldsymbol{b_k}$, and each spin is normalized to $|\boldsymbol{s_k}| = 1/2$. At finite temperature the length of the vector is reduced by the thermal $\tanh$ factor, resulting in a state that is no longer pure.

Let us assume that the pseudospins have been displaced from their equilibrium position. In the absence of collective motion, i.e. when the self-consistent condition (3.61) is ignored, they will precess around the $\boldsymbol{b_k}$-vectors with frequency $\omega_{\boldsymbol{k}} = |\boldsymbol{b_k}| = 2E_{\boldsymbol{k}}$. Around $|\boldsymbol{k}| \sim k_F$, one has $E_{\boldsymbol{k}} \gtrsim 2\psi^{eq}$ which will be the dominantly visible frequency upon averaging over momentum space. This explains the quasiparticle contributions to observables in the nonlinear response with the characteristic frequency $2\psi^{eq}$ in the s-wave case.

3.5.1 Two-point correlation functions in the pseudospin model

The pseudo-spin model can be used to numerically compute retarded two-point correlation functions in the time-domain. To do so, we add the perturbation

$$\boldsymbol{b_k} \to \boldsymbol{b_k} + \eta\gamma_{\boldsymbol{k}} a(t - t_0)\boldsymbol{b}'_k \,, \tag{3.63}$$

where $a(t) = \frac{1}{\sqrt{2\pi\tau^2}} \exp\left(-t^2/(2\tau^2)\right)$ and $\eta \to 0$ is a small constant.

The numerical solution $\langle \boldsymbol{s_k} \rangle(t)$ to the differential equation (3.60) will then be of the form

$$\langle \boldsymbol{s_k} \rangle(t) = \langle \boldsymbol{s} \rangle_0 - i\eta \int dt' \theta(t - t') \left\langle \left[\boldsymbol{s_k}(t),\, a(t' - t_0) \sum_{\boldsymbol{k}'} \gamma_{\boldsymbol{k}'} \boldsymbol{s_{k'}}(t') \cdot \boldsymbol{b}'_{\boldsymbol{k}'} \right] \right\rangle_0 + \mathcal{O}(\eta^2) \,, \tag{3.64}$$

where we have expressed the expectation value with respect to the unperturbed Hamiltonian $\boldsymbol{b_k}$ as $\langle \dots \rangle_0$. In the limit $\tau \to 0$, one has $a(t) = \delta(t)$ and we can obtain the expression

$$\lim_{\eta,\tau\to 0} \frac{1}{\eta} \left(\langle \boldsymbol{s_k} \rangle(t) - \langle \boldsymbol{s_k} \rangle_0 \right) = -i\theta(t - t_0) \sum_{i\boldsymbol{k}'} \gamma_{\boldsymbol{k}'} b'_{i\boldsymbol{k}'} \langle [\boldsymbol{s_k}(t),\, s_{i\boldsymbol{k}'}(t_0)] \rangle_0 \,. \tag{3.65}$$

Since $\langle \boldsymbol{s_k} \rangle_0$ simply corresponds to the equilibrium value of the pseudospin, the retarded two-point correlation function of the form $-i\theta(t - t_0)\langle [s_{i\boldsymbol{k}}(t), s_{j\boldsymbol{k}'}(t_0)] \rangle$ can readily be extracted.

Explicitly, setting $\gamma_{\boldsymbol{k}} = \partial_k \partial_l \xi_{\boldsymbol{k}}$ and $\boldsymbol{b_k} = (0, 0, 1)$, we reproduce the optical kernel as in the diagram-

matic case:

$$\lim_{\eta,\tau\to 0}\frac{1}{\eta}\sum_{\boldsymbol{k}}\partial_i\partial_j\xi_{\boldsymbol{k}}\left(\langle s_{3\boldsymbol{k}}\rangle(t)-\langle s_{3\boldsymbol{k}}\rangle_0\right)=-i\theta(t-t_0)\langle[\rho_{ij}(t),\rho_{kl}(t_0)]\rangle=K_{ij,kl}(t-t_0)\,. \tag{3.66}$$

This derivation underlines the well-known fact that the pseudospin model is identical to the diagrammatic description in the limit of weak perturbations, i.e. $\eta \to 0$. Indeed, the pseudospin model also permits an analytical solution which reproduces our results of the previous section [156].

Chapter 4

Higgs and collective mode spectroscopy

Collective excitations of the superconducting condensate are in the millielectronvolt range, on the scale of the superconducting gap $2\psi^{eq}$. Thus, they can be probed using THz spectroscopic techniques. Recent developments in ultrafast Terahertz spectroscopy have led to a surge in interest to study collective excitations in non-equilibrium superconductors both in theory [87–89, 123, 139, 156] and experiment [37, 54, 80, 81, 86, 103, 104, 163], where first experimental signatures of the Higgs mode have been reported for various materials [37, 103, 104].

While the development of high intensity THz light sources is challenging in itself [66], the field of THz spectroscopy bears a significant advantage over visible or infrared light sources. THz frequencies are low enough that they allow for measurement of *both* the amplitude and phase of the light via electro-optic sampling (EOS) [92, 171].

The main THz excitation schemes consist of two approaches. First, samples are illuminated in a pump-probe setup where an excitation of the Higgs mode by a single-cycle THz pump appears as an oscillation of the probe response as a function of pump-probe delay [103]. In a second type of experiment, referred to as Third Harmonic Generation (THG), the Higgs mode is resonantly driven by an intense multi-cycle pulse that yields an electrical field component of three times the incident frequency in the reflected or transmitted beam [37, 86, 104].

In this chapter, we will sketch the fundamental theoretical framework to model pump-probe and third harmonic generation experiments conducted in the context of collective mode spectroscopy. We will show how phase sensitivity of EOS protocols is the key driver of pump-probe studies. Concepts of pump-probe and THG spectroscopy introduced in Secs. 4.1-4.3 are widely applied and generally well understood [160]. Sec. 4.4 is adapted from Ref. [129] of the author of this thesis and motivated by an experimental platform first introduced by the Kaiser group at Max-Planck-Institute Stuttgart, where both a single-cycle pump pulse and a multi-cycle drive pulse are used to study cuprate thin films in a $2d$ time-resolved study [82].

4.1 Nonlinear THz spectroscopy

In the previous chapter we derived the expression

$$j_i(\omega) = \int d\omega' A_j(\omega - \omega') K_{ij,kl}(\omega') A^2_{kl}(\omega') \,. \tag{4.1}$$

for the supercurrent on the surface of a superconductor as a nonlinear response to an electromagnetic field. The induced current, in turn, is linearly related to the transmitted electromagnetic radiation in thin films or the reflected signal in bulk samples [46].

The nonlinear kernel $K_{ij,kl}$ encodes all information about elementary excitation in the system that affect the optical response. Specifically, we saw in Ch. 3 that quasiparticle density and Higgs fluctuations can lead to a peak at their characteristic frequency $\omega = 2\psi^{eq}$. Other superconducting modes, such as Leggett or Bardasis-Schrieffer excitations or, combinations of amplitude and phase modes will yield additional peaked structures at their excitation energies [54, 113, 151].

The tensorial structure of the nonlinear kernel $K_{ij,kl}$ can give further insight into the collective modes that can be probed by polarization dependent measurements [35]. In this chapter, we will assume an identical polarization for all light sources, such that we can find a basis in which the tensor $K_{ij,kl} = K$ reduces to a single invariant and the current is described by

$$j(\omega) = \int d\omega' A(\omega - \omega') K(\omega') A^2(\omega') \,. \tag{4.2}$$

An immediate consequence of Eq. (4.2) is that the frequency ω' of the kernel $K(\omega')$ is correlated with the frequency of the squared vector potential $A^2(\omega')$. This is a direct manifestation of the quadratic nature of the coupling of light to collective modes. We emphasize that $A^2(\omega')$ is defined as the Fourier transform of the *squared* electromagnetic vector potential $A(t)^2$ (note the order of the parentheses and square). As such, $A^2(\omega') = \int d\omega'' A(\omega' - \omega'') A(\omega'')$ is given by a self-convolution. A plot of $|A(\omega')|$ and $|A^2(\omega')|$ is shown in Fig. 4.1 for a Gaussian pulse of the form

$$A_0 \cos(\Omega t + \phi)\, e^{-t^2/2\tau^2} \tag{4.3}$$

with carrier frequency Ω and pulse duration τ. Left and right panels show the cases of a short quench pulse $\tau \leq 1/\nu$ and multi-cycle drive $\tau \gg 1/\nu$, respectively. Here, ν is the resonance frequency of the collective mode of interest. The spectrum of A is peaked around the carrier frequency $\pm\Omega$ (red curve), whereas the spectrum of A^2 is peaked around $0, \pm 2\Omega$. The two peaks are the consequence of Difference Frequency Generation (DFG) and Sum Frequency Generation (SFG) in a nonlinear two-photon process. The DFG and SFG peak width are given by the scale $1/\tau$.

To excite a collective mode, the power spectrum of A^2 must overlap with the resonance peaks of the collective modes in the nonlinear kernel K. In the quench scenario, this condition as always satisfied, since the DFG peak is of width ν and therefore guaranteed to have finite overlap with the mode resonance at ν, irrespective of the position 2Ω of the SFG peak. In contrast, a careful tuning of the carrier frequency Ω to the resonance condition $2\Omega = \nu$ is necessary in the drive scenario.

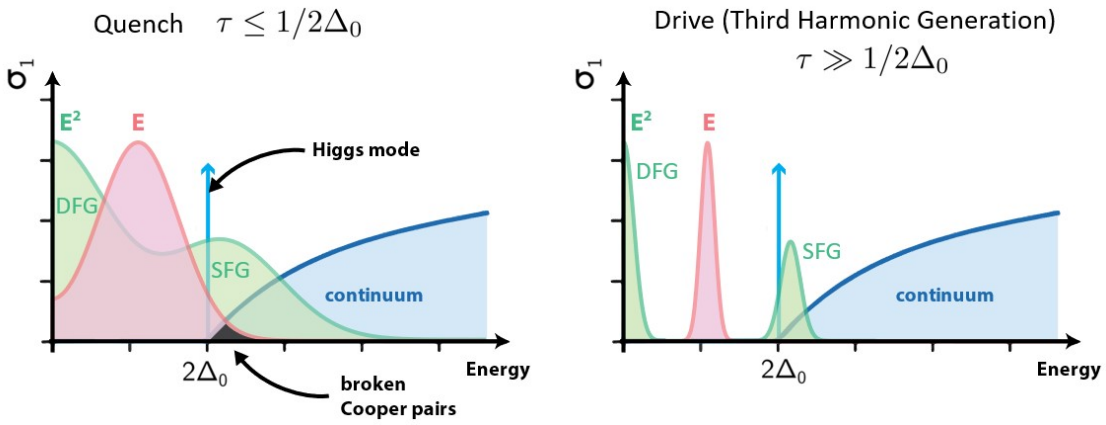

Figure 4.1: Power spectrum of the electrical field (red) and the squared electric field (green) for a broadband pulse (left) and a narrowband pulse (right). The pulse duration τ needs to be compared to the time scale of the collective mode $1/\nu$, where ν is the collective mode energy. In the case of the Higgs mode, indicated by a blue arrow, $\nu = 2\psi^{eq}$. The Higgs mode energy coincides with the onset of the quasiparticle continuum, shown in blue.

4.2 Third Harmonic Generation from collective modes

Let us focus on the case of a narrowband pulse, $\tau \gg 1/\nu$. In the limit of $\tau \to \infty$, one has $A(\omega) \sim \delta(\omega - \Omega) + \delta(\omega + \Omega)$ and $A^2(\omega) \sim 2\delta(\omega) + \delta(\omega - 2\Omega) + \delta(\omega + 2\Omega)$. Inserting this into expression (4.2), we find that the induced current only includes components at $\pm\Omega, \pm 3\Omega$ where the kernel is evaluated at

$$\begin{aligned} j(\pm 3\Omega) \sim & K(\pm 2\Omega) \\ j(\pm\Omega) \sim & K(0) + K(\pm 2\Omega)\,. \end{aligned} \tag{4.4}$$

The generation of current with three times the frequency of the incident field is referred to as Third Harmonic Generation (THG). Most notably, the THG signal is proportional to the nonlinear kernel evaluated at twice the incident frequency Ω, i.e., $j(3\Omega) \sim K(2\Omega)$. To map out the functional dependence of the nonlinear kernel, one therefore must vary the driving frequency Ω. This, however, is not easily achievable experimentally. Instead, most current experiments fix the driving frequency Ω and instead attempt to shift the resonance energies contained in K [37, 38, 86, 105]. For a superconducting mode, this is achieved by varying the temperature in the window $[0, T_C]$. The clear disadvantages of this method are that (a) knowledge of the temperature dependence of the resonances is required, (b) only modes above 2Ω are visible, and (c) thermal broadening effects are substantial.

THG experiments do not rely on measurement of the phase of the transmitted or reflected THz radiation. However, it has been suggested that the phase response in THz multi-cycle experiments can still contain useful information [37]. We will further investigate this proposal in Ch. 6.

4.3 Pump-probe spectroscopy

Within a THz pump-probe setup, two pulses are applied: an intense single-cycle pump pulse, and, after a time delay Δt, a weaker single-cycle probe pulse. We describe this pulse configuration by the total field

$$A(t) = A_{\text{pump}}(t + \Delta t) + A_{\text{probe}}(t)\,, \tag{4.5}$$

where the pump and probe pulse envelopes are assumed to be centered at $t = 0$. In frequency space, the time delay Δt of the pump results in a phase according to

$$A(\omega) = A_{\text{pump}}(\omega)e^{i\omega\Delta t} + A_{\text{probe}}(\omega)\,. \tag{4.6}$$

Inserting this into Eq. (4.2) and transforming to the time domain, we obtain

$$\begin{aligned} j(t;\Delta t) = A_{\text{probe}}(t) &\int d\omega' e^{i\omega' t} K(\omega') A^2_{\text{pump}}(\omega') e^{i\omega'\Delta t} \\ &+ A_{\text{pump}}(t+\Delta t) \int d\omega' e^{i\omega' t} K(\omega') A^2_{\text{pump}}(\omega') e^{i\omega'\Delta t} \\ &+ 2A_{\text{pump}}(t+\Delta t) \int d\omega' e^{i\omega' t} K(\omega') \int d\omega'' A_{\text{probe}}(\omega'-\omega'') A_{\text{pump}}(\omega'') e^{i\omega''\Delta t}\,, \end{aligned} \tag{4.7}$$

where we have only kept terms that are at most linear in the weak probe pulse. In pump-probe experiments, the current is measured at a specific time t_m after the pump, where only the probe pulse is present. Thus, only the first term Eq. (4.7) contributes. Finally, we make the simplifying assumption that the pump pulse is sufficiently short, i.e., it is a broadband pulse with $A_{\text{pump}}(\omega) \sim \textit{const}$ on the THz scale of interest. Then, Eq. (4.7) yields

$$j(t_m;\Delta t) \sim A_{\text{probe}}(t_m) K(t_m + \Delta t)\,. \tag{4.8}$$

Thus, by sweeping the delay time, the functional time-dependence of the nonlinear kernel can be mapped out. Presence of a collective mode at resonance energy ν will produce a kernel in the time domain that is oscillatory with frequency ν and the pump-probe signal will show ν-oscillations as Δt is swept. For the case of the Higgs mode, $\nu = 2\psi^{eq}$. These $2\psi^{eq}$ oscillations in the pump-probe delay have been first measured in Ref. [103].

When the measurement is repeated for sufficiently many delay times Δt, one can numerically Fourier transform the experimental data over the parametric variable Δt,

$$j(t_m;\omega_{\Delta t}) \sim A_{\text{probe}}(t_m) K(\omega_{\Delta t}) e^{-i\omega_{\Delta t} t_m}\,. \tag{4.9}$$

In this form, the pump-probe data is directly related to the nonlinear Kernel in frequency space.

We emphasize that measurement of the complex optical kernel $K(\omega_{\Delta t})$ relies on the ability to directly measure time-resolved electric field values using EOS, as opposed to measuring the amplitude information only.

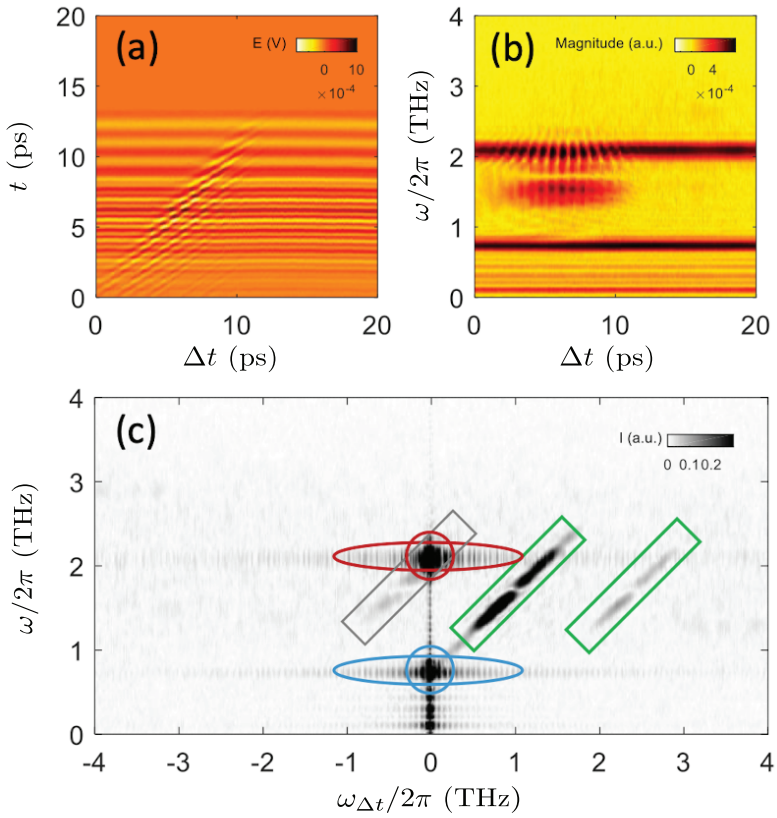

Figure 4.2: Experimental THz transmission spectra for thin film LSCO, adapted from [82]. Panel (a) shows two dimensional plots as a function of time t and quench-drive delay Δt. Panel (b) shows absolute values of the Fourier transform over the time domain. In panel (c) the absolute value of the $2d$ Fourier transform over both t and Δt is shown. Blue and red circles mark the first and third harmonic, respectively. Additionally, spectral weight is distributed along side bands marked by green boxes.

4.4 Quench-drive spectroscopy

Recently, a new experimental protocol has been introduced that resembles aspects of both THG measurements and pump-probe experiments. In this scheme, a sample is first perturbed by a visible $100\,\mathrm{fs}$ pulse and subsequently driven by a multi-cycle THG pulse of $10\,\mathrm{ps}$ duration [82]. The transmitted waveform is sampled as a function of time and pump-probe delay Δt. The coordinate system is chosen such that the multi-cycle driving pulse envelope is always centered at a fixed time $t = t_0$.

A typical two-dimensional dataset from Ref. [82] is presented in Fig. 4.2. Panel (a) shows the data in the time domain as a function of quench-drive delay Δt. Horizontal oscillations at first and third harmonic frequency of the drive are clearly visible. Here, the fundamental frequency of the drive is $\Omega/2\pi = 0.7\,\mathrm{THz}$. The first harmonic is strongly suppressed by a 3Ω bandpass filter to prevent saturation of the detector. The onset of the visible quench pulse is apparent as a diagonal line after which the THG signal is disturbed.

Panel (b) shows the same dataset after Fourier transform along the t-axis. Only the absolute value of the Fourier transform is shown. First and third harmonic signals are apparent as horizontal lines. The third

harmonic is modulated as a function of Δt. In addition, a side band below the third harmonic appears that displays modulations along the x axis.

The clearest representation of the data is obtained in $2d$ frequency space of $(\omega, \omega_{\Delta t})$, shown in panel (c). Here $\omega_{\Delta t}$ is the conjugate variable to the pump-probe delay parameter Δt. Again, only the magnitude of the $2d$ Fourier-transform is shown. The usual first and third harmonic signals are independent of the optical pump. Hence, they appear for $\omega_{\Delta t} = 0$ and $\omega = \Omega, 3\Omega$. The modulations result in two continuous side bands at $= \omega_{\Delta t} \pm \Omega$.

Let us apply the nonlinear response formalism to interpret the experimental data. To this end, we rewrite Eq. (4.2) once more into a different form,

$$j(\omega) = \int \prod_{i=1}^{3} d\omega_i \, \delta\big(\omega - \sum_i \omega_i\big) A(\omega_1) K(\omega_2 + \omega_3) A(\omega_2) A(\omega_3) \,. \tag{4.10}$$

In this representation, energy conservation is warranted by a δ-function constraint: Three photons of frequencies $\omega_1, \omega_2, \omega_3$ induce a current of frequency ω, which is constrained to $\omega = \omega_1 + \omega_2 + \omega_3$. We model the total electric field again as a sum of multi-cycle drive A_d and visible quench A_q, separated in time by Δt, i.e. $A(t) = A_q(t + \Delta t) + A_d(t)$. In frequency space, this yields $A(\omega) = e^{i\omega\Delta t} A_q(\omega) + A_d(\omega)$. We insert this into Eq. (4.10):

$$\begin{aligned} j(\omega; \Delta t) = \int \prod_{i=1}^{3} d\omega_i \, \delta\big(\omega - \sum_i \omega_i\big) \Big[& A_d(\omega_1) K(\omega_2 + \omega_3) A_d(\omega_2) A_d(\omega_3) \\ & + 2 A_q(\omega_1) K(\omega_2 + \omega_3) A_q(\omega_2) A_d(\omega_3) e^{i(\omega_1 + \omega_2)\Delta t} \\ & + A_d(\omega_1) K(\omega_2 + \omega_3) A_q(\omega_2) A_q(\omega_3) e^{i(\omega_2 + \omega_3)\Delta t} \Big] \,. \end{aligned} \tag{4.11}$$

Here, we have used that the quench-pulse is a visible pulse in the eV-regime: Since we are exclusively interested in current signals in the THz-regime, only terms with even powers of A_q need to be kept. Two pulses in the eV-regime can generate a THz contribution by means of a DFG process. Explicitly, since the quench has a pulse duration of $\tau = 100\,\mathrm{fs}$, the DFG signal will have a spread of roughly $1/\tau = 10\,\mathrm{THz}$ and thus constitutes a broadband THz excitation. An odd number of visible pulses, however, will always generate output photons of visible frequencies in a non-linear process.

Next, we perform a Fourier transform over the parametric variable Δt. We find,

$$\begin{aligned} j(\omega; \omega_{\Delta t}) &= \int d(\Delta t) e^{-i\omega_{\Delta t}\Delta t} j(\omega; \Delta t) \\ &= \int \prod_{i=1}^{3} d\omega_i \, \delta\big(\omega - \sum_i \omega_i\big) \Big[\delta\big(\omega_{\Delta t}\big) A_d(\omega_1) K(\omega_2 + \omega_3) A_d(\omega_2) A_d(\omega_3) \\ &\qquad + 2\delta\big(\omega_{\Delta t} - \omega_1 - \omega_2\big) A_q(\omega_1) K(\omega_{\Delta t} - \omega_1 + \omega_3) A_q(\omega_2) A_d(\omega_3) \\ &\qquad + 2\delta\big(\omega_{\Delta t} - \omega_2 - \omega_3\big) A_d(\omega_1) K(\omega_{\Delta t}) A_q(\omega_2) A_q(\omega_3) \Big] \end{aligned} \tag{4.12}$$

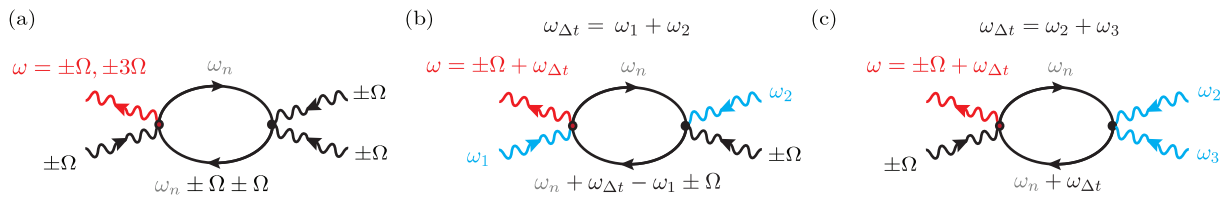

Figure 4.3: Diagrammatic representation of the three terms in Eq. 4.12. Current j is represented by a red wiggly line, quench and drive photons are drawn as blue and black wiggly lines, respectively. The kernel K is represented by a fermionic bubble. Energy conservation demands that the incoming three photons frequencies sum to equal the 'outgoing' current frequency.

The three terms can be diagrammatically represented as in Fig. 4.3. Here, the current is represented by a red wiggly line, quench and drive photons are drawn as blue and black wiggly lines, respectively. The kernel is represented by a fermionic bubble, its lowest order contribution, with internal fermionic Matsubara frequency ω_n.

Let us finally use the fact that A_d is a narrow band multi-cycle pulse. Inserting

$$A_d \sim A_{d,0}\left[\delta(\omega - \Omega) + \delta(\omega + \Omega)\right] ,$$

we get the expression

$$\begin{aligned} j(\omega;\omega_{\Delta t}) = {} & \delta\big(\omega \mp \Omega \mp \Omega\big)\delta\big(\omega_{\Delta t}\big)A_{d,0}^3 K(\pm\Omega \pm \Omega) \\ & + 2\delta\big(\omega - \omega_{\Delta t} \mp \Omega\big)\int d\omega_1\, A_q(\omega_1)K(\omega_{\Delta t} - \omega_1 \pm \Omega)A_q(\omega_{\Delta t} - \omega_1)A_{d,0} \\ & + \delta\big(\omega \mp \Omega - \omega_{\Delta t}\big)A_{d,0}K(\omega_{\Delta t})A_q^2(\omega_{\Delta t})\,. \end{aligned} \tag{4.13}$$

The first term simply corresponds to a usual THG process described in Sec. 4.3 and yields the $\Omega, 3\Omega$ peaks on the $\omega_{\Delta t}$ axis in Fig. 4.2. The remaining two terms are responsible for the side bands along the diagonals $\omega = \omega_{\Delta t} \pm \Omega$. They differ, however, in the distribution of spectral weight along the diagonals which is set by the nonlinear kernel K. In the presence of a collective mode with resonance energy ν, most of the contribution of the kernel stems from its peaks at $\pm\nu$. The last term in Eq. (4.13) yields to a peak along the diagonal at $\omega_{\Delta t} = \nu$. The middle term has no such characteristic feature, as the resonance structure encoded in the kernel K is evaluated at $\omega_{\Delta t} - \omega_1 \pm \Omega = \nu$, which is scrambled by integration over the variable ω_1.

To validate the discussion above, we numerically study a two-band superconducting Hamiltonian

$$\mathcal{H}_0 = \sum_{i\boldsymbol{k}\sigma} \xi_{i\boldsymbol{k}} c^\dagger_{i\boldsymbol{k}\sigma} c_{i\boldsymbol{k}\sigma} + \sum_{i\boldsymbol{k}} \psi_i c^\dagger_{i-\boldsymbol{k}\uparrow} c^\dagger_{i\boldsymbol{k}\downarrow} + h.c.\,, \tag{4.14}$$

where $\xi_{i\boldsymbol{k}} = s_i\left(\boldsymbol{k}^2/2m_i - \epsilon_{F_i}\right)$ is the parabolic dispersion of the i-th band with Fermi-energy ϵ_{F_i} and electron mass m_i. The factor $s_i = \pm 1$ sets the electron or hole character of the band.

We couple this model to an electrical field and rewrite it within the pseudospin formalism as $H =$

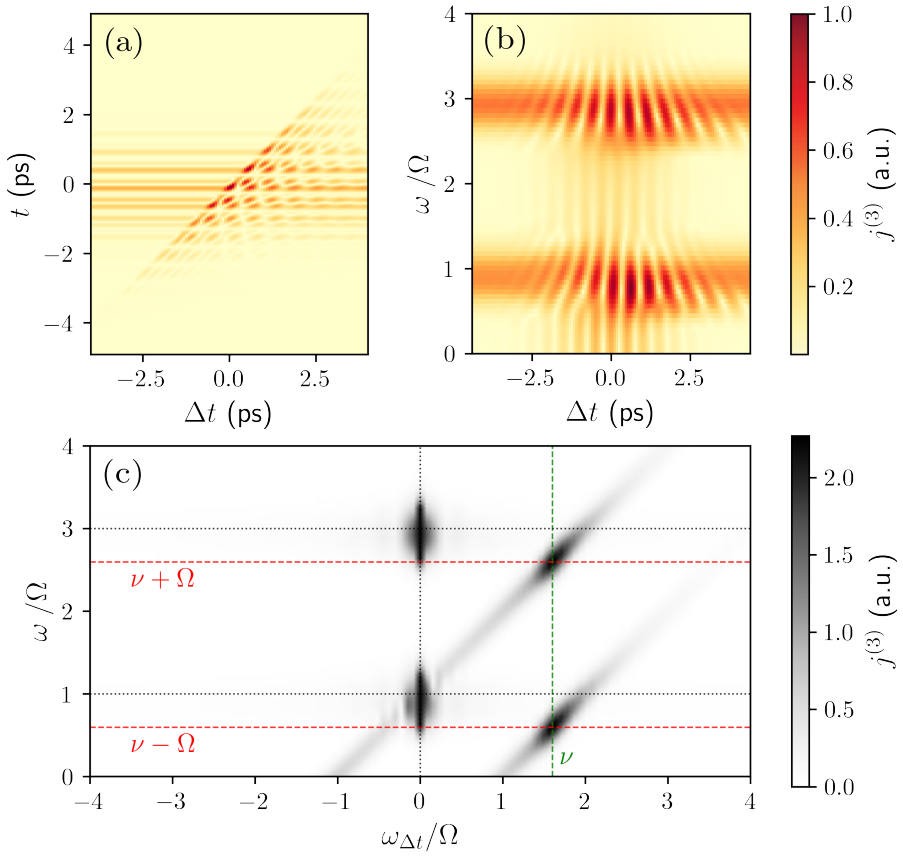

Figure 4.4: Third-order current $j^{(3)}$ for a two-band superconductor computed within a pseudospin model. Two-dimensional plots (a) in the time domain $t, \Delta t$, (b) in the frequency-delay-time domain $\omega, \Delta t$, and (c) $2d$ frequency domain $\omega, \omega_{\Delta t}$. We have chosen model parameters $\Delta_1 = 3\,\mathrm{meV}$, $\Delta_2 = 7\,\mathrm{meV}$, $\epsilon_{F,1} = 2.9\,\mathrm{eV}$, $\epsilon_{F,2} = 0.7\,\mathrm{eV}$, $m_1 = 0.85 m_e$, $m_2 = 1.38 m_e$, $\omega_D = 50\,\mathrm{meV}$, $s_1 = 1$, $s_2 = -1$, loosely reflective of MgB_2 [85]. The dimensionless coupling parameter of the two order parameters is $\alpha = 0.2$.

$\sum_{i\boldsymbol{k}} \boldsymbol{b}^i_{\boldsymbol{k}} \cdot \boldsymbol{s}^i_{\boldsymbol{k}}$, with pseudo-magnetic field $\boldsymbol{b}^i_{\boldsymbol{k}} = \left(-2\psi'_i,\, 2\psi''_i, 2\xi_{i\boldsymbol{k}} + e^2 A^2(t)/2m\right)$ and the gap equation

$$\psi_i = \sum_{j\boldsymbol{k}} V_{ij} \langle s^j_{1\boldsymbol{k}} - i s^j_{2\boldsymbol{k}} \rangle \,, \tag{4.15}$$

where the two gaps are coupled by the matrix

$$U_{ij} = \begin{pmatrix} U_{11} & \alpha U_{11} \\ \alpha U_{11} & U_{22} \end{pmatrix} . \tag{4.16}$$

As discussed in Ch. 3, a parabolic bandstructure results in vanishing of both Higgs response and density fluctuations. For finite dimensionless coupling parameter α in the gap equation, the two-band model does, however, possess a collective Leggett excitation that contributes to the nonlinear optical response even in the continuum limit [32, 58, 115, 116].

The numerically evaluated $2d$ spectrum is shown in Fig. 4.4 for coupling parameter $\alpha = 0.2$. It indeed shows the features derived in the nonlinear response formalism. Next to the first and third harmonic signals, at $\omega = \Omega, 3\Omega$ and $\omega_{\Delta t} = 0$, the simulation produces two side bands along $\omega = \omega_{\Delta t} \pm \Omega$. Most of their spectral weight is concentrated around the position $\omega_{\Delta t} = \nu$ which we numerically confirmed as the Leggett mode energy.

Having understood the composition of $2d$ spectra in a quench-drive scenario, it is worthwhile to revisit the experimental results from Fig. 4.2. Specifically, we observe that the experimentally measured sidebands do not show a clearly peaked signature of a collective mode. Instead, they show a dip at around $\omega/2\pi = 1.7\,\mathrm{THz}$. This dip, however, is likely an artifact of the transmission function of a bandpass filter employed in the experiment to reduce the first-harmonic contribution, and cannot be attributed to the form of the optical kernel K. Indeed, features of the optical kernel should modulate both sidebands as a function of $\omega_{\Delta t}$. Clearly, in Fig. 4.2, the dip of the sidabands is a modulation of the spectrum as function of ω.

4.5 Summary

In this chapter we have derived the main phenomenology of nonlinear THz spectroscopy experiments from the quasi-equilibrium response formalism of Ch. 3. We have shown how collective modes, encoded as resonance peaks in the nonlinear optical Kernel, are manifested at experimentally recorded THz transmission or reflection spectra. In the case of Third Harmonic Generation experiments, the THG amplitude is directly proportional to the nonlinear optical kernel evaluated at $K(2\Omega)$, where Ω is the carrier frequency of the incident multi-cycle THz waveform. In pump-probe techniques, and in the new technique of quench-drive spectroscopy, the analytical structure of the kernel K can be directly accessed by sweeping the pump-probe delay Δt.

The new method of quench-drive spectroscopy may be seen as a precursor to a more general toolset of $2d$ spectroscopic techniques on superconducting collective modes. Two-dimensional spectroscopy has proven to be an important method with wide applications ranging from rovibronic excitations in bio-molecular systems [61, 74, 111], excitons in semiconductors [40], to magnons in antiferromagnets [96]. However, to the best of our knowledge, $2d$ spectroscopy has never been applied to superconducting collective modes. In fact, only a single experimental $2d$ spectroscopic study on superconducting materials exists to date [98]. Extension of $2d$ techniques to the superconducting realm may therefore provide an important new avenue to investigate the physics of superconductors and may open a new field of $2d$ Higgs spectroscopy.

Another spectroscopic technique that bears great promise in future studies is the application of time resolved angle-resolved photoemission (ARPES) to superconducting collective modes. Momentum- and time resolved measurement of the superconducting gap out of equilibrium provides detailed information about the nature of unconventional superconductivity that goes beyond measurement of momentum-averaged quantities in current pump-probe techniques [26, 138, 168].

Finally, it is promising to leverage the inelastic Raman effect to study superconducting systems out of equilibrium [134]. Raman spectroscopy is an important technique to study electronic excitations of superconductors in the THz regime [45]. The Higgs mode and other collective condensate excitations are known to be Raman active [31, 32]. In yet another approach, there have been efforts to extend Raman

techniques to the realm of $2d$ spectroscopy [112, 153].

Chapter 5

Time-resolved optical conductivity and Higgs oscillations in two-band dirty superconductors

Recent studies have emphasized the importance of impurity scattering for the optical Higgs response of superconductors. In the dirty limit, an additional paramagnetic coupling of light to the superconducting condensate arises which drastically enhances excitation. So far, most work concentrated on the periodic driving with light, where the third-harmonic generation (THG) response of the Higgs mode was shown to be enhanced. In this chapter, we extend this analysis by calculating full temperature and frequency dependence of THG to better compare the theory with current experimental setups. We additionally calculate the time-resolved optical conductivity of single- and two-band superconductors in a two-pulse quench-probe setup, where we find good agreement with existing experimental results. We use the Mattis-Bardeen approach to incorporate impurity scattering and calculate explicitly the time-evolution of the system. In contrast to previous work we calculate the response not only within a time-dependent density matrix formalism but also in a diagrammatic picture derived from an effective action formalism which gives a deeper insight into the microscopic processes.

5.1 Introduction

When a continuous symmetry is spontaneously broken, collective excitations emerge. In the case of a superconductor, where the complex order parameter $\Delta e^{i\theta}$ acquires a finite value below a critical temperature T_c, two bosonic modes appear: the massive Higgs mode and a massless Goldstone mode [124, 162]. They may be seen as amplitude $\delta\Delta$ and phase $\delta\theta$ fluctuations of the complex order parameter in the Mexican hat-shaped free energy potential. When coupled to a gauge field, the Goldstone mode is shifted to the plasma frequency by means of the Anderson-Higgs mechanism while the Higgs mode remains a stable gapped excitation in the Terahertz regime [7].

In a two-band superconductor, two gapped Higgs modes and two phase modes exist. While the global phase fluctuation occurs again only at energies close to the plasma frequency for a charged condensate, the

relative phase fluctuation, quantized as the Leggett mode, persists as a gapped excitation at low energies [91].

Experimental observation of Higgs and Leggett collective modes is difficult. Since these fields are scalar quantities, no linear coupling to the electromagnetic field exists at zero momentum [124]. Thus, there are no direct experimental signatures in linear response. Therefore, experiments need to be performed in the non-linear regime. Here, the challenge is twofold: intense light sources are required but experiments also must be performed on energy scales mostly within the superconducting gap such that optical excitation of quasiparticles does not deplete the condensate.

The fact that characteristics of the Higgs mode in superconductors are observable in experiments is not self-evident. Early theoretical calculations in the clean limit predicted extremely weak experimental signatures that relied on breaking of the particle-hole symmetry. Therefore, the first observations [104] of the third-harmonic response generated by the Higgs mode was doubted [34] as it should be overlaid by much stronger charge fluctuations. Only recently, the role of impurities has been appreciated as it drastically enhances the coupling of light to the Higgs mode due to an additional paramagnetic coupling absent in the clean limit [115, 141, 147, 157]. This coupling becomes the dominant contribution even for small disorder. It was further shown that impurity scattering yields qualitatively different behavior in the polarization dependence of the driving pulses [141].

Previous studies on third-harmonic generation with impurities concentrated mostly on the frequency dependence for fixed temperature [115, 141, 147, 157] or temperature dependence for fixed frequency [147]. Here, we extend the analysis and calculate the full 2d temperature- and frequency-dependent THG signal which allows to better understand and compare the theory with current experimental setups where only the temperature can be swept for fixed driving frequency. We also calculate the individual contributions of density fluctuations, Leggett mode and Higgs mode to the third-harmonic generation response. Our results support the findings of a recent work, where the third-harmonic response in the two-band superconductor MgB_2 shows a resonance only for the lower gap [86]. This can be understood from the fact that the upper band is either in the clean limit or that the Fermi surface is very small.

In addition to the investigations of previous work, on the effect of impurities in the periodic driving scheme, in this chapter, we also explore the excitation with a two-pulse quench-probe scheme. We consider both one- and two-band superconductors where the bands can be in different impurity regimes. To calculate the time-resolved optical conductivity, we extend the density-matrix approach of [115] to a two-pulse excitation scheme. Here, the short first pulse acts as a quench, while the second probe pulse with variable time-delay probes the dynamics of the system.

We incorporate the effect of impurities in our model using the Mattis-Bardeen approximation [106]. This approach constitutes an excellent description for many conventional superconductors at least in the linear regime [140]. It has also been used in [115] in conjunction with a numerical density matrix approach.

The Mattis-Bardeen approximation should be contrasted with alternative methods of treating impurity scattering, such as the self-consistent Born-approximation [157] or quasiclassical Green's function formalism [147]. While the Mattis-Bardeen description affords the most efficient numerical calculations among the three approaches, it relies on a spherical Fermi surface approximation. As such it cannot resolve the polar-

ization dependence in optical experiments, for which latter two microscopic methods should be employed. However, we will show that all three methods yield similar qualitative results in terms of impurity-assisted activation of the Higgs mode [115, 147, 157].

Compared to the density-matrix approach in [115], we additionally consider a diagrammatic approach derived from an effective action formalism, where the Mattis-Bardeen ansatz is incorporated by an effective finite momentum interaction vertex. We show that this diagrammatic approach is equivalent to the density matrix formalism. There are several advantages of this approach. First, it is analytically tractable and thus provides a clearer picture of the underlying physics. Second, as the Matsubara sums in the expression can be analytically evaluated, this approach is computationally more efficient and allows calculations with more accuracy and greater variation of parameters such as a full 2d temperature and frequency sweep. And finally, in the diagrammatic approach it is natural to include Coulomb interactions to perform a fully gauge-invariant calculation.

5.2 Model

5.2.1 Hamiltonian

We consider the BCS multiband Hamiltonian

$$\mathcal{H}_0 = \sum_{i\mathbf{k}\sigma} \epsilon_{i\mathbf{k}} c^\dagger_{i\mathbf{k}\sigma} c_{i\mathbf{k}\sigma} - \sum_{ij\mathbf{k}\mathbf{k}'} U_{ij} c^\dagger_{i\mathbf{k}\uparrow} c^\dagger_{i-\mathbf{k}\downarrow} c_{j-\mathbf{k}'\downarrow} c_{j\mathbf{k}'\uparrow} \tag{5.1}$$

where $\epsilon_{i\mathbf{k}} = s_i \left(\mathbf{k}^2/2m_i - \epsilon_{F_i}\right)$ is the parabolic dispersion of the i-th band with Fermi-energy ϵ_{F_i} and electron mass m_i. The factor $s_i = \pm$ determines electron- or hole-like character of the respective band.

At the mean-field level the interacting term is decoupled in the pairing channel,

$$\sum_{i\mathbf{k}} \Delta_i c^\dagger_{i-\mathbf{k}\uparrow} c^\dagger_{i\mathbf{k}\downarrow} + h.c.\,, \tag{5.2}$$

where order parameters Δ_i are self-consistently determined by the BCS gap equation

(5.3)

The order parameters of different bands are mixed by off-diagonal terms in the coupling matrix U_{ij}. In the present work, we parametrize gap-mixing by a parameter v and define

$$U_{ij} = \begin{pmatrix} U_{11} & vU_{11} \\ vU_{11} & U_{22} \end{pmatrix}. \tag{5.4}$$

For given Δ_i and v we can find U_{11} and U_{22} such that the gap equation is satisfied.

To model an experimental probe with a laser pulse, we introduce a time-dependent vector potential

$\mathbf{A}(t) = A(t)\,\mathbf{e}$ with polarization vector $\mathbf{e}$ by means of minimal coupling,

$$\mathcal{H}_1 = -\sum_{i\mathbf{k}\mathbf{k}'\sigma} \mathbf{J}_{i\mathbf{k}\mathbf{k}'} \cdot \mathbf{A}\, c^\dagger_{i\mathbf{k}\sigma} c_{i\mathbf{k}'\sigma} + \sum_{i\mathbf{k}\sigma} \frac{s_i e^2}{2m_i} \mathbf{A}^2\, c^\dagger_{i\mathbf{k}\sigma} c_{i\mathbf{k}\sigma}\,, \tag{5.5}$$

where $J_{i\mathbf{k}\mathbf{k}'} = \langle i\mathbf{k}| \frac{e\mathbf{p}_i}{m_i} |i\mathbf{k}'\rangle$ are intraband transition matrix elements of the current operator. Here, we have neglected interband excitation, which for materials like MgB_2 is strongly suppressed by the separation of Fermi surfaces in the Brillouin zone. The two terms in $\mathcal{H}_1$ corresponds to the paramagnetic and diamagnetc coupling of the laser field, respectively. The full Hamiltonian is given by $\mathcal{H} = \mathcal{H}_0 + \mathcal{H}_1$.

5.2.2 Impurity scattering

In a clean system momentum conservation yields $\mathbf{J}_{i\mathbf{k}\mathbf{k}'} \sim \delta_{\mathbf{k}\mathbf{k}'}$, or $\mathbf{J}_{i\mathbf{k}\mathbf{k}'} \sim \delta_{\mathbf{k},\mathbf{k}'\pm\mathbf{q}}$ if a photon wavevector $\mathbf{q}$ is considered. In disordered systems, translational invariance is broken, so that transitions between states of different momenta are allowed. Here, we adopt the approach of Murotani and Shimano [115] and model the effects of impurities within the Mattis-Bardeen (MB) approximation [106]. Explicitly, impurities enter through the approximation

$$\langle |\mathbf{e}\cdot\mathbf{J}_{i\mathbf{k}\mathbf{k}'}|^2\rangle_{\mathrm{Av}} = \int \frac{d\Omega_{\mathbf{k}}}{4\pi}\frac{d\Omega_{\mathbf{k}'}}{4\pi} |\mathbf{e}\cdot\mathbf{J}_{i\mathbf{k}\mathbf{k}'}|^2 \approx \frac{(ev_{F_i})^2}{3N_i(0)} W(\epsilon_{i\mathbf{k}}, \epsilon_{i\mathbf{k}'})\,, \tag{5.6}$$

$$W(\epsilon_{i\mathbf{k}}, \epsilon_{i\mathbf{k}'}) = \frac{1}{\pi}\frac{\gamma_i}{\left(\epsilon_{i|\mathbf{k}|} - \epsilon_{i|\mathbf{k}'|}\right)^2 + \gamma_i^2} \tag{5.7}$$

with Fermi velocity v_{F_i}, density of states at the Fermi level $N_i(0)$ and impurity scattering rate γ_i. Intuitively, the energy level scale γ_i, determines the maximum separation of the energy levels, below which impurity scattering is allowed. These energy scales are related to their characteristic momentum scale by the Fermi velocity v_{F_i}. A derivation of this matrix element is given in Ref. [115].

The Mattis Bardeen approximation is applicable in the regime $\gamma_i \ll \epsilon_{F_i}$ for isotropic impurity scattering, and uniform charge density [106]. These conditions are met for the superconductors considered in the present chapter, where the dirty limit is already achieved when the impurity scale γ is of the order of the superconducting gap Δ. For example, for the two-band superconductor MgB_2, Ref. [57] experimentally determined the γ_i to be $12.4\,\mathrm{meV}$ and $85.6\,\mathrm{meV}$, for the two bands, respectively.

We see that impurity scattering broadens the $\delta_{\mathbf{k}\mathbf{k}'}$-distribution into a Lorentzian of width γ_i centered at zero momentum transfer. The bandstructure defined by $\mathcal{H}_0$ remains unaffected in this approximation. Instead of broadening the momentum resolution of the bandstructure, one may view impurities as effectively broadening the momentum of the photon.

While the simplicity of the Mattis-Bardeen approach is appealing, more realistic models of impurities rely on exact numerical treatment [141] or diagrammatic summation of impurity ladder corrections [147, 157].

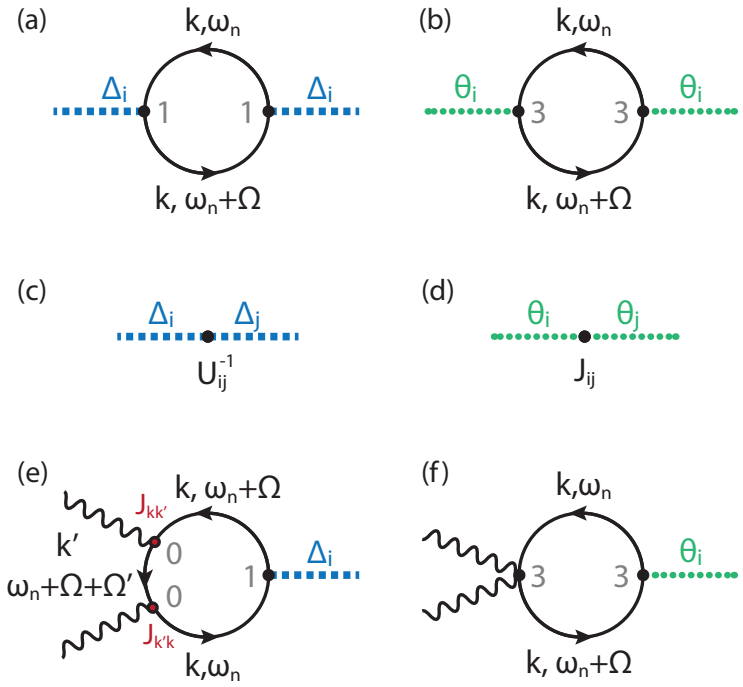

Figure 5.1: Diagrammatic representation of terms in the quadratic effective action $S[\Delta_i, \theta_i, \boldsymbol{A}]$ in Eq. (C.14) involving Higgs fields (left column) and phase fields (right column). Bubbles correspond to susceptibilities listed in Eqs. (C.24)-(C.28). The blue (green) dotted lines represent Higgs (Leggett) propagators, the wavy black line represents the electromagnetic field and the solid black line the Nambu Greens function. Numbers 0,1,3 at the vertices represent Pauli matrices $\sigma_0, \sigma_1, \sigma_3$ acting in Nambu space. (a,b) Higgs and phase susceptibilities $\chi_i^{\sigma_1\sigma_1}$, $\chi_i^{\sigma_3\sigma_3}$. (c) Coupling of Higgs modes where vertex is the inverse of Eq. (5.4). (d) Josephson coupling of phase modes responsible for Leggett mode. The coupling matrix J is defined in Eq. (C.18). (e) Paramagnetic coupling of Higgs modes with susceptibility $\chi^{\sigma_0\sigma_0\sigma_1}$. (f) Diamagnetic coupling of phase modes with $\chi^{\sigma_3\sigma_3}$. Other couplings at Gaussian level vanish in the presence of particle-hole symmetry.

5.2.3 Effective Action

We first present a perturbative solution of above Hamiltonian by a path-integral formalism in imaginary time τ [22, 35, 143, 161]. The full problem is formally captured by the partition function $\mathcal{Z} = \int \mathcal{D}(c^\dagger c) e^{-S}$ with the Euclidean action

$$S = \int_0^\beta d\tau \left(\sum_{i\mathbf{k}\sigma} c^\dagger_{i\mathbf{k}\sigma} \partial_\tau c_{i\mathbf{k}\sigma} + \mathcal{H} \right) . \tag{5.8}$$

As detailed in Appendix C.1, we decouple the interacting part of $\mathcal{H}$ in the pairing channel, introducing collective fields $\Delta_i(\omega_n) \exp(i\theta_i(\omega_n))$. Δ_i and θ_i describe amplitude and phase fluctuations, respectively, of the superconducting condensate. These collective fluctuations are dependent on time only, i.e. the Hamiltonian supports only $\mathbf{k} = 0$ excitations of Higgs and phase fields.

Performing the fermionic path integral results in an effective action $S[\Delta_i, \theta_i, \mathbf{A}]$ in bosonic and classical

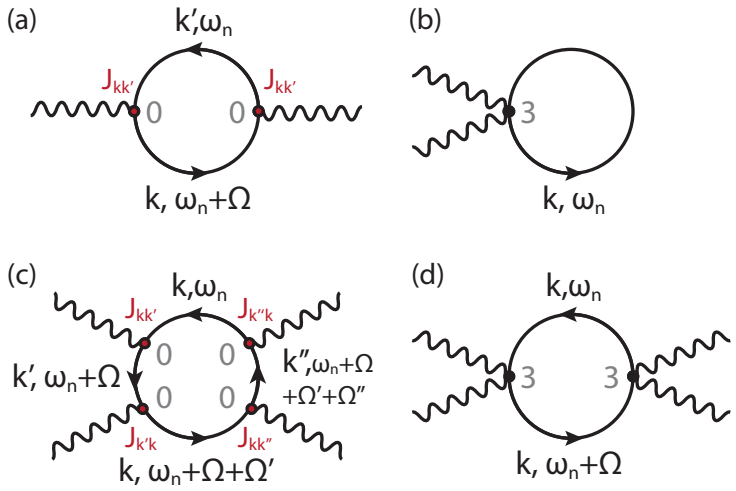

Figure 5.2: Diagrammatic representation of density fluctuation contributions in the effective action $S[\Delta_i, \theta_i, \mathbf{A}]$ Eq. (C.14). Paramagnetic (a) and diamagnetic (b) terms defining the linear response current $\mathbf{j}\big|_1$. The paramagnetic contribution (a) vanishes in the clean limit. Paramagnetic (c) and diamagnetic (d) terms contributing to nonlinear current $\mathbf{j}\big|_3$.

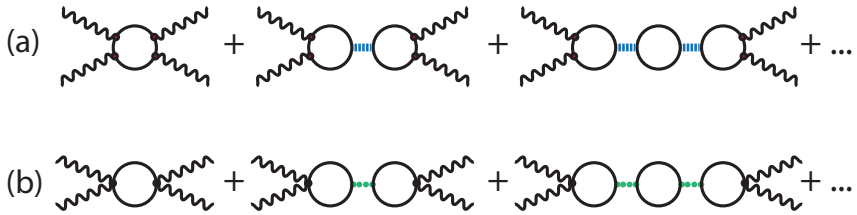

Figure 5.3: RPA summation of collective fields in the effective action. (a) Higgs modes renormalize paramagnetic non-linear current. Here, blue dashed lines correspond to the coupling matrix $U/2$. (b) Phase modes renormalize diamagnetic current. Green dotted lines denote coupling matrix J^{-1}.

EM fields (see Eq. (C.14)), where now

$$\mathcal{Z} = \int \prod_i \mathcal{D}\Delta_i \mathcal{D}_i \theta_i e^{-S[\Delta_i, \theta_i, \mathbf{A}]} .$$

We only keep terms quadratic in collective fields Δ_i, θ_i and to fourth order in $\mathbf{A}$. The resulting terms are diagrammatically presented in Fig. 5.1 and Fig. 5.2 and their integral expressions are derived in Appendix C.1.

The diagrammatic representation contains Higgs fields $\Delta_i(\omega)$ (blue-dashed lines), phase fields (green-dotted lines), and EM fields (wavy lines). Paramagnetic coupling to the photon field corresponds to vertices with a single photon field line, implying the factor $A(\omega)$. Diamagnetic vertices with two photon field lines contribute the term $A^2(\omega) = \int d\omega' A(\omega - \omega')A(\omega')$. Numeric labels $(0, 1, 3)$ indicate Pauli matrices $\sigma_0, \sigma_1, \sigma_3$ in Nambu space where σ_0 is the identity. Only paramagnetic vertices introduce external momen-

tum. Solid black lines correspond to mean-field Nambu Green's functions

$$G_{0,i} = [i\omega_n - \epsilon_{i\mathbf{k}}\sigma_3 + \Delta_i\sigma_1]^{-1} \tag{5.9}$$

and loops imply a trace over Nambu indices, frequencies, and momenta.

Figs. 5.1 and 5.2 are a complete representation of all terms in the quadratic action in the presence of particle-hole symmetry and impurities in the MB approximation.

In the clean limit paramagnetic photon lines no longer carry momentum and, as a consequence, diagrams 5.1(e) and 5.2(a) vanish. The inclusion of paramagnetic diagrams with vertices $J_{i\mathbf{k}\mathbf{k}'}$ determined by the MB model is the main difference of the diagrammatic formalism from other literature [32, 34].

Absence of diagram 5.1(e) in the clean limit implies that the Higgs mode does not couple to light without impurities. However, when a non-parabolicity of the bandstructure is taken into account, a diamagnetic coupling to the Higgs mode arises, yielding an additional, non-vanishing diagram [34, 115, 156].

We note that paramagnetic and diamagnetic terms do not mix in the present model. Consequently, the partition function factors into two contributions $\mathcal{Z} = \mathcal{Z}_{\text{para}}\mathcal{Z}_{\text{dia}}$. Since only the paramagnetic part is affected by impurities, and since $\mathcal{Z}_{\text{para}}$ does not contain phase contributions, we conclude that only the Higgs mode and density fluctuations are sensitive to impurity scattering in the MB approximation.

The path integrals over Δ_i, θ_i can be performed exactly at the Gaussian level. This is equivalent to an RPA renormalization of the density fluctuation terms diagrammatically represented in Fig. 5.3 where the dashed and dotted lines correspond to coupling matrices $U_{ij}/2$ and Josephson coupling matrices J_{ij}^{-1}, respectively. After Gaussian integration, one is left with $S[A(\omega)]$, explicitly given in Eq. (C.29). A functional derivative with respect to $A(\omega)$ gives the current

$$j(\omega) = -\frac{\delta S[A(\omega)]}{\delta A(-\omega)}\,. \tag{5.10}$$

In the single-band case, the diamagnetic RPA series Fig. 5.3(b) is exactly zero. This results from the cancellation of the diamagnetic density fluctuation contribution 5.2(d) with the phase mode contribution, shown in Eq. (C.32) of Appendix C.1. The cancellation is exact in the continuum limit and does not rely on particle-hole symmetry. For a lattice model, the cancellation is imperfect away from low or large filling. At half filling, where particle-hole symmetry is exact, the phase mode contribution vanishes and the diamagnetic current remains finite [34], hence no cancellation occurs.

In the two-band case, the phase supports both a Goldstone mode and the Leggett mode. Here, the Goldstone contribution cancels the diamagnetic third order current, while the Leggett mode is the remaining source of the total diamagnetic current.

The present results are insensitive to long-range Coulomb interaction. We show in Appendix C.2 how, in the presence of particle-hole symmetry, the same expression as in the uncharged case are derived for the continuum model.

5.2.4 Density matrix equations of motion

We solve for the time dynamics of above Hamiltonian using a density matrix approach. To this end, we define the density matrix $\rho = |\psi_0\rangle \langle\psi_0|$, or, in the basis of Bogoliubov–de Gennes,

$$\begin{pmatrix} \psi^1_{i\mathbf{k}} \\ \psi^2_{i\mathbf{k}} \end{pmatrix} = \begin{pmatrix} u_{i\mathbf{k}} & -v_{i\mathbf{k}} \\ v^*_{i\mathbf{k}} & u_{i\mathbf{k}} \end{pmatrix} \begin{pmatrix} c_{i\mathbf{k}\uparrow} \\ c^\dagger_{i(-\mathbf{k})\downarrow} \end{pmatrix} , \tag{5.11}$$

we have

$$\rho = \begin{pmatrix} \rho^{11}_{i\mathbf{k}\mathbf{k}'} & \rho^{12}_{i\mathbf{k}\mathbf{k}'} \\ \rho^{21}_{i\mathbf{k}\mathbf{k}'} & \rho^{22}_{i\mathbf{k}\mathbf{k}'} \end{pmatrix} = \begin{pmatrix} \langle \psi^{1\dagger}_{i\mathbf{k}} \psi^1_{i\mathbf{k}'} \rangle & \langle \psi^{1\dagger}_{i\mathbf{k}} \psi^2_{i\mathbf{k}'} \rangle \\ \langle \psi^{2\dagger}_{i\mathbf{k}} \psi^1_{i\mathbf{k}'} \rangle & \langle \psi^{2\dagger}_{i\mathbf{k}} \psi^2_{i\mathbf{k}'} \rangle \end{pmatrix} . \tag{5.12}$$

The time dependence of ρ is given by Heisenberg's equation of motion,

$$i\partial_t \rho = [\rho, H] , \tag{5.13}$$

where H is the operator $\mathcal{H}$ in the BdG basis.

We are interested in computing the dynamics of the current $\mathbf{j} = -\langle \frac{\delta \mathcal{H}}{\delta \mathbf{A}} \rangle = \mathbf{j}_P + \mathbf{j}_D$, consisting of a paramagnetic and diamagnetic contribution,

$$\mathbf{j}_P = \sum_{i\mathbf{k}\mathbf{k}'} \mathbf{J}_{i\mathbf{k}\mathbf{k}'\sigma} \langle c^\dagger_{i\mathbf{k}\sigma} c_{i\mathbf{k}'\sigma} \rangle , \tag{5.14}$$

$$\mathbf{j}_D = -\sum_{i\mathbf{k}\sigma} \frac{s_i e^2}{m_i} \mathbf{A} \langle c^\dagger_{i\mathbf{k}\sigma} c_{i\mathbf{k}\sigma} \rangle , \tag{5.15}$$

as well as the dynamics of the superconducting order parameter

$$\Delta_i = \sum_{j\mathbf{k}} U_{ij} \langle c_{j(-\mathbf{k})\downarrow} c_{j\mathbf{k}\uparrow} \rangle . \tag{5.16}$$

To apply the MB substitution, we further expand the above equations of motion in orders of $A(t)$. To account for effects of a THG response, we consider terms up to third order. For materials with a center of inversion the current only has odd order components $\mathbf{j} = \mathbf{j}\big|_0 + \mathbf{j}\big|_3 + \dots$ and the gap contains even contributions of A, $\Delta = \Delta\big|_0 + \delta\Delta\big|_2 + \dots$.

Finally, we exploit the rotational invariance of our model and perform the integral over angular degrees of freedom explicitly. Thus, by replacing all momentum summations by an integral $\sum_{\mathbf{k}} \to N_i(0) \int d\epsilon_{i\mathbf{k}} \int \frac{d\Omega_{\mathbf{k}}}{4\pi}$, we effectively reduce the model to a one-dimensional system. Note that rotational invariance of our continuum model neglects polarization dependence of observable quantities.

We are left to compute the equations of motion of the first order expectation values, $\rho_{i\mathbf{k}\mathbf{k}'}\big|_1$, and the

angle-averaged quantities

$$R_i^{ab}(\epsilon_{i|\mathbf{k}|},\epsilon_{i|\mathbf{k}'|}) = \frac{1}{\int \frac{d\Omega_\mathbf{k}}{4\pi}\frac{d\Omega_{\mathbf{k}'}}{4\pi}\,|\mathbf{J}_{i\mathbf{k}\mathbf{k}'}\cdot\mathbf{e}|^2}\int \frac{d\Omega_\mathbf{k}}{4\pi}\frac{d\Omega_{\mathbf{k}'}}{4\pi}\mathbf{e}\cdot\mathbf{J}_{i\mathbf{k}\mathbf{k}'}\rho^{ab}_{i\mathbf{k}\mathbf{k}'}\big|_3\,, \tag{5.17}$$

$$r_i^{ab}(\epsilon_{i|\mathbf{k}|}) = \int \frac{d\Omega_\mathbf{k}}{4\pi}\rho^{ab}_{i\mathbf{k}\mathbf{k}}\big|_2\,. \tag{5.18}$$

We solve them numerically using a Runge-Kutta solver on a discretized energy grid $\epsilon_{|\mathbf{k}_i|}$ of up to 10^3 points in the interval $[-\omega_D,\omega_D]$.

5.3 Single-band superconductivity

Motivated by the experiment of Matsunaga *et al.* [103] we choose parameters $\Delta = 1.3\,\mathrm{meV}$, $\epsilon_F = 1\,\mathrm{eV}$, $m = 0.78m_e$, $s = 1$, $\omega_D = 20\,\mathrm{meV}$ that reflect measurements and ab-initio calculations on NbN [14].

5.3.1 Optical conductivity

We begin by computing the optical conductivity in linear response,

$$\sigma(\omega) = \frac{j(\omega)\big|_1}{i\omega A(\omega)}\,. \tag{5.19}$$

This can be done in either of two ways. First, by implementing a time-dependent density matrix simulation with pulse $A(t)$. The numerically evaluated current $j(t)\big|_1$ and the pulse are then Fast-Fourier transformed and Eq. (5.19) is evaluated. Here, one needs to choose a pulse of sufficient ω-bandwidth such that the region of interest is covered.

The second way involves the functional derivative of the diagrams in Fig. 5.2(a,b) according to Eq. (5.10). At $T = 0$ one obtains the expression for the real part

$$\begin{aligned}\sigma'(\omega) &= \frac{1}{i\omega}\frac{v_F^2}{3N}\int d\epsilon d\epsilon' W(\epsilon,\epsilon')\chi''^{\sigma_0\sigma_0}(\epsilon,\epsilon',\omega) \\ &= \frac{1}{i\omega}\frac{v_F^2 N}{3}\int d\epsilon d\epsilon' W(\epsilon,\epsilon')\left(1-\frac{\epsilon\epsilon'+\Delta^2}{EE'}\right)\frac{E+E'}{(w+i\eta)^2-(E+E')^2}\end{aligned} \tag{5.20}$$

where $E' = \sqrt{\Delta^2+\epsilon'^2}$, $W(\epsilon,\epsilon')$ is the Lorentzian of Eq. (5.7), N the density of states at the Fermi surface, and η is an infinitesimal positive constant.

We can understand the analytical structure of $\sigma'(\omega)$ by inspecting the susceptibility $\chi''^{\sigma_0\sigma_0}(\epsilon,\epsilon',\omega)$. For $\omega < 2\Delta$ it vanishes exactly. For $\omega > 2\Delta$ its structure is shown in Fig. 5.4 for a representative value of $\omega = 4$. We observe two straight spectral lines at $\epsilon' = \pm\omega+\epsilon$. These features can be understood in the picture of a particle-hole or hole-particle excitation process, illustrated in Fig. 5.4(a). $\chi''^{\sigma_0\sigma_0}(\epsilon,\epsilon',\omega)$ has non-zero spectral weight at given ϵ,ϵ' if an occupied state at ϵ can be excited into a state at ϵ' by a photon of frequency ω. Multiplication of the integrand in Eq. (5.21) with $W(\epsilon-\epsilon')$ enforces momentum conservation.

In this picture it is easy to see that the total spectral weight $\chi''^{\sigma_0\sigma_0}(\omega) = \int d\epsilon d\epsilon'\chi''^{\sigma_0\sigma_0}(\epsilon,\epsilon',\omega)$ should be approximately proportional to $\Theta(\omega-2\Delta)(\omega-2\Delta)$, where Θ is the Heaviside function. Since $W(\epsilon-\epsilon')$

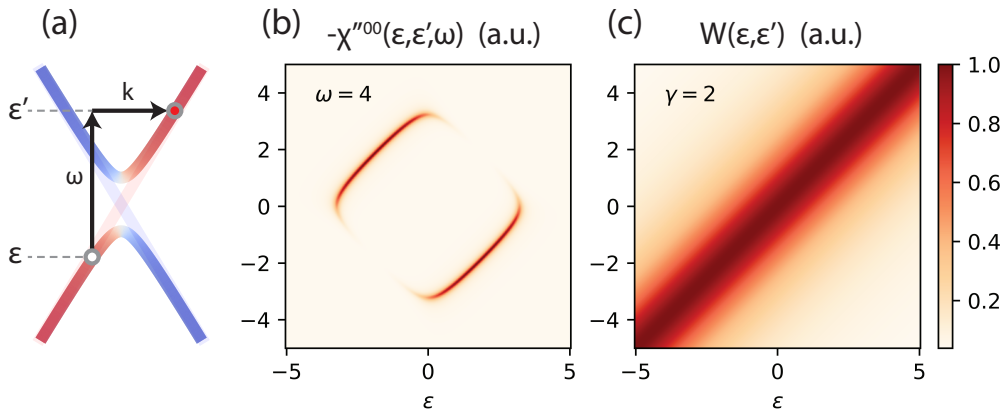

Figure 5.4: (a) Schematic of a particle-hole excitation process where the pulse contributes energy ω and momentum k. Red (blue) colors indicate electron (hole) character. (b) The susceptibility $-\chi''^{\sigma_0\sigma_0}$ has finite weight only for ϵ, ϵ' corresponding to valid state in an excitation process with $\omega = 4$. Rounded features are a result of the gap 2Δ. For $\omega < 2\Delta$, $\chi''^{\sigma_0\sigma_0}$ is identically zero since no optical excitation is not possible. (c) Momentum conservation is enforced by the factor $W(\epsilon - \epsilon')$ in Eq. (5.21).

is constant along contours $\epsilon' = \pm\omega + \epsilon$, we find the simple analytical approximation

$$\sigma'(\omega) \propto \Theta(\omega - 2\Delta)(\omega - 2\Delta)\frac{\gamma}{\omega^2 + \gamma^2} \tag{5.21}$$

that holds for $\omega \gg 2\Delta$ in the dirty limit $\gamma \gg \Delta$.

In Fig. 5.5 we plot numerically evaluated real and imaginary parts $\sigma'(\omega), \sigma''(\omega)$ of the optical conductivity for various impurity concentrations and temperatures. σ' shows a clear conductivity gap below 2Δ. In the clean limit, a pronounced peak is observed above 2Δ. Exactly at 2Δ, where single-particle wavefunctions are a perfect mix of electron and hole states, the conductivity always zero. For low amount of impurity scattering, $\gamma/2\Delta \ll 1$, the conductivity shows a steep increase and peak above 2Δ. The conductivity peak grows and shifts to higher ω as γ is increased. It then broadens into the characteristic dome shape frequently observed in experiment [103, 106, 182].

At finite temperatures we additionally observe spectral weight around $\omega = 0$ stemming from thermal quasiparticle excitations. The condensate δ-peak at $\wedge = 0$ is not numerically resolved. The imaginary part σ'' follows a $1/\omega$ power law as expected for a superconducting state.

The linear response optical conductivity contains information of the bandstructure only and is unaffected by collective modes. This can be inferred from the diagrammatic description where all terms in the RPA renormalization of diagram Fig. 5.2(a) containing $\mathbf{k} = 0$ collective fluctuations vanish exactly. To reveal the presence of collective modes, we turn to the dynamics of the superconducting order parameter and the non-linear current $j\big|_3$ and additionally model realistic THz pulses in a pump-probe setting.

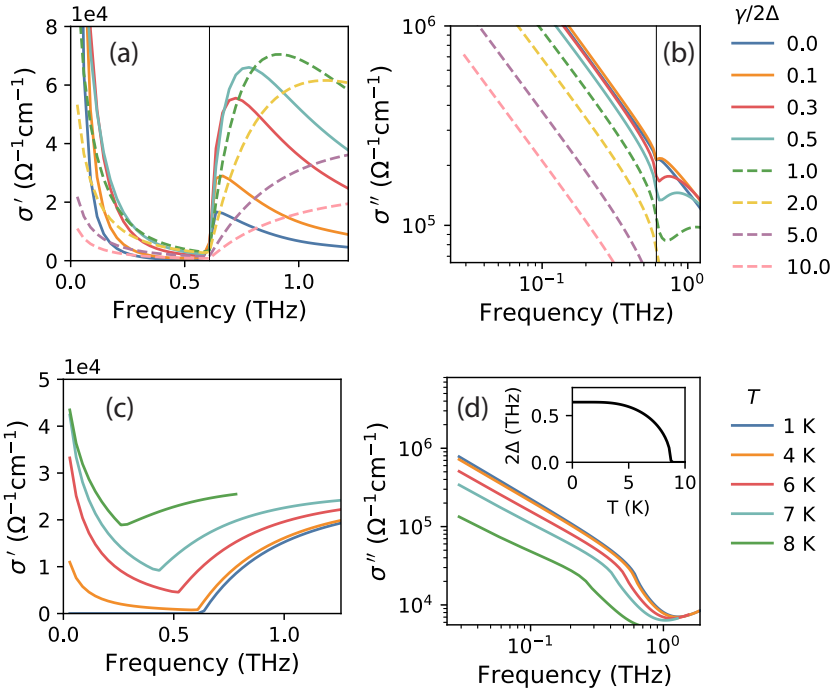

Figure 5.5: Real part σ' and imaginary part σ'' of the optical conductivity to first order in the vector potential A. (a),(b) Impurity scattering rates dependence for fixed temperature $T = 4\,\mathrm{K}$. (c),(d) Temperature dependence for fixed scattering rate $\gamma/2\Delta = 10$. σ' shows a characteristic conductivity gap below T_C and both σ', σ'' diverge in the static limit. The inset in (d) shows the temperature dependence of the gap.

5.3.2 Excitation of Higgs mode

We choose the electromagnetic pulse form $A(t) = A_0 \exp\left(-(t-t')^2/2\tau^2\right) \cos\Omega t$ with coefficients to match the reported data of Ref. [103]. The resulting waveform is shown in Fig. 5.6(a).

A characteristic property of a pump pulse is its pulse length τ compared to the natural timescale of the superconductor $1/\Delta$. For $\tau \ll 1/\Delta$ the superconductor is *quenched*, while it is *adiabatically driven* in the opposite limit of $\tau \gg 1/\Delta$.

The different behavior in the two limits can be intuitively understood within the diagrammatic picture. Here, the pulse induced change of the order parameter $\delta\Delta(\omega)$ is given by the diagram in Fig. 5.7(a) which has the integral expression

$$\delta\Delta(\omega) = \frac{1}{2}\int d\omega' \sum_{\mathbf{k}\mathbf{k}'} |J_{\mathbf{k}\mathbf{k}'}|^2 \frac{\chi^{\sigma_0\sigma_0\sigma_1}(\omega,\omega',\mathbf{k},\mathbf{k}')}{\chi^{\sigma_1\sigma_1}(\omega)+2/U} A(\omega')A(-\omega-\omega')\,. \tag{5.22}$$

Presence of a collective Higgs mode translates into a peak of the kernel $K(\omega) = (\chi^{\sigma_1\sigma_1}(\omega)+2/U)^{-1}$ at the characteristic mode energy $\omega_H = 2\Delta$. Excitation of the collective mode, however, is only possible if energy conservation is satisfied, i.e. if $A(\omega')A(-\omega_H-\omega')$ is finite for some ω'. Higgs oscillations are therefore expected when the Fourier transform of the squared vector potential $A^2(\omega) = \int d\omega' A(\omega-\omega')A(\omega')$ overlaps

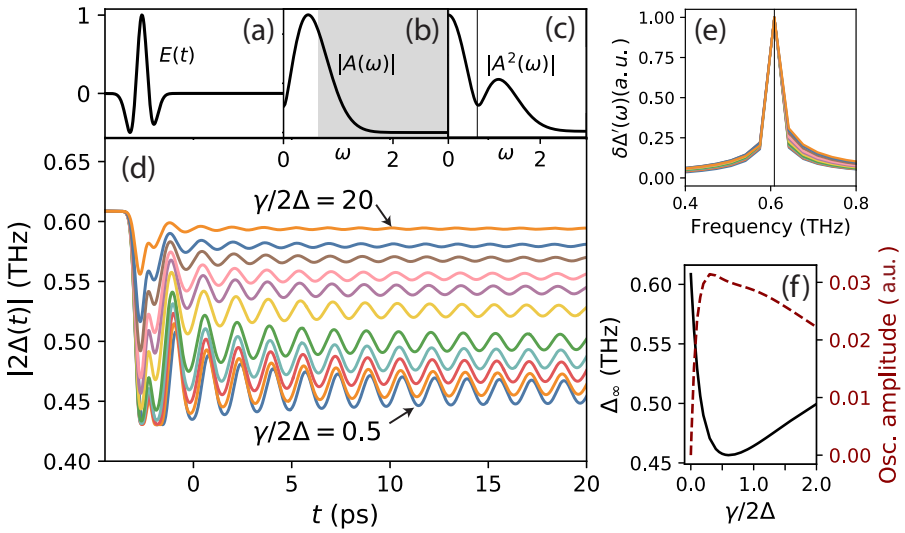

Figure 5.6: (a) Pulse field $E(t)$ realizing a quench. (b) Spectral composition $|A(\omega)|$. The gray shaded area illustrates the quasi-particle continuum. (c) Spectral composition $|A^2(\omega)| = |\int d\omega' A(\omega - \omega')A(\omega')|$ of the second order component $A^2(t)$ responsible for excitation of collective modes. The peak around zero frequency corresponds to a DFG process while the peak at finite $1.2\,\mathrm{THz}$ is a SFG process. (d) Evolution of the magnitude of the order parameter $|2\Delta(t)|$ for impurity strength varying from $\gamma/2\Delta = 0.5$ to 20 and Fourier spectrum of the gap oscillations (e). (f) Relaxation value Δ_∞ and amplitude of oscillation show a very similar dependence as a function of disorder strength which has maximum effect at around $\gamma \approx \Delta$.

with the mode-energy ω_H. The double-peaked structure of $A(\omega)$ is shown in Fig. 5.6(c). The first peak, centered at $\omega = 0$, corresponds to a difference frequency generation process (DFG), while the second peak at $\omega = 2\Omega$ corresponds to a sum frequency generation process (SFG). The resonance frequency of the Higgs mode, ω_H, is illustrated by a vertical line. Remaining terms in Eq. (5.22) describe the coupling to light in presence of impurities and ensure momentum conservation in a virtual two step excitation process.

Let us now consider two limiting cases of the optical pulse width. For $\Delta\tau \ll 1$, the frequency spectrum of $A^2(\omega)$ is very broad. The response of $\delta\Delta(\omega)$ is then dominated by the sharp resonance peak of $K(\omega)$ giving rise to pronounced 2Δ-oscillations of the superconducting gap in the time domain. Since the DFG peak is guaranteed to overlap with the Higgs resonance, these oscillations will always be present, independent of the frequency of the optical pulse. The SFG process only contributes if the pulse frequency lies in the vicinity of $\Omega \approx \Delta$.

In the transient limit, $\Delta\tau \gg 1$, the spectrum of $\delta\Delta(\omega)$ is finite only for a narrow region around 2Ω. In the time-domain, the gap shows forced 2Ω-oscillations which are resonantly enhanced for $2\Omega \approx 2\Delta$.

Following Matsunaga [103], we choose a pulse with $\Delta\tau = 0.68$, closest to the quench scenario, and perform simulations within the density-matrix formulation. The order parameter responds to the THz pulse by a marked drop followed by damped oscillations around a new asymptotic value $\Delta_\infty = \Delta(t \to \infty)$ of frequency $2\Delta = 0.6\,\mathrm{THz}$ as displayed in Figs. 5.6(d-e). The drop of the equilibrium gap is captured by the $\omega = 0$ component of $\delta\Delta$. Evaluating Eq. (5.22) for $\omega = 0$, one finds that $\chi^{\sigma_0\sigma_0\sigma_1}(\omega = 0, \omega', \mathbf{k}, \mathbf{k}')$ is finite

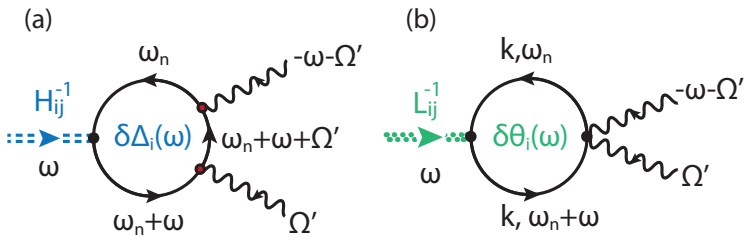

Figure 5.7: Diagrammatic representation of (a) $\delta\Delta_i(\omega)$ and (b) $\delta\theta_i(\omega)$. Double lines correspond to the RPA summation of Fig. 5.3.

only for $\omega' > 2\Delta$, similar to the discussion in Sec. 5.3.1. Consequently, $\delta\Delta(0)$ is non-zero only if $|A(\omega)|^2$ overlaps with the quasiparticle continuum, which is illustrated in Fig. 5.6(b). In physical terms, depletion of the superconducting order parameter is a consequence of quasiparticle excitation by $A(\omega)$.

Both the oscillation amplitude and Δ_∞ show a strong dependence on the impurity scattering rate and are peaked at $\gamma \approx \Delta$ as shown in Fig. 5.6(f). This is a consequence of momentum conservation. For $\gamma \to 0$, Higgs oscillations vanish exactly.

We note that order parameter dynamics are expected to show oscillations of frequency $2\Delta_\infty$ and not, as in our case, $2\Delta(t = 0)$ [87, 176]. $2\Delta_\infty$ oscillations have also been observed in experiment [103]. The discrepancy can be attributed to the expansion in powers of the pump field $A(t)$ performed in the time-dependent density matrix formalism. If contributions to $\delta\Delta$ beyond the second order are considered, the oscillation frequency of the order parameter should correctly reflect the non-equilibrium value $2\Delta_\infty$.

From the diagrammatic point of view this discrepancy arises since calculations are performed within a quasi-equilibrium framework. Here, we are capturing the nonlinear response of the $U(1)$ symmetry broken equilibrium ground state. An intense pump pulse is known to weaken this ground state, i.e. it decreases the gap Δ. Strictly speaking the experimental nonlinear response is then measured with respect to the weakened ground state. Our theoretical description does not capture this induced change. It fully loses its validity when the pump induces a phase transition from the superconducting to the normal state [160]. It is nevertheless interesting that present day pump probe experiments are performed in a regime where the induced change of the groundstate only quantitatively affects the nonlinear response. Hence, the quasi-equilibrium effective action approach has been established as a description not only of THG but also of pump probe experiments in the literature [160].

5.3.3 Pump-probe spectroscopy

Higher orders of the optical conductivity include contributions of collective modes that smooth out the absorption edge and add spectral weight inside the conductivity gap. Here, we calculate the non-linear contribution,

$$\sigma(\omega, \delta t_{pp}) = \frac{j(\omega)\big|_1 + j(\omega)\big|_3}{i\omega A(\omega)}\,, \tag{5.23}$$

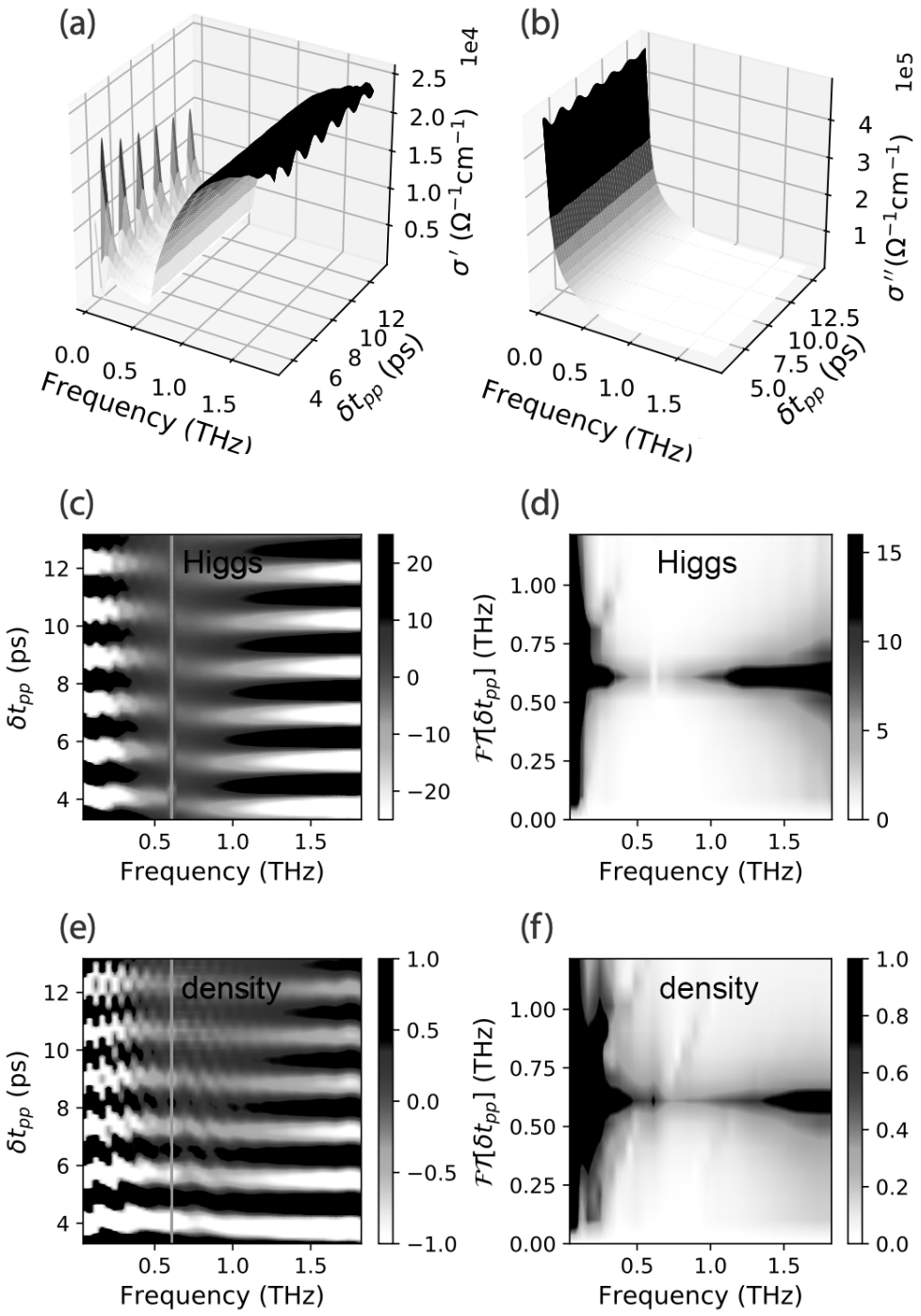

Figure 5.8: (a,b) Real and imaginary part of conductivity spectra for swept pump-probe delay δt_{pp} including the nonlinear contribution in A. (c) Real part of isolated nonlinear Higgs contribution and (d) Fourier transform showing that frequency of conductivity oscillation is peaked at 2Δ. (e) Real part of the nonlinear contribution from density fluctuations and (f) Fourier transform. This Higgs contribution exceeds the charge density contribution by one order of magnitude.

in a pump-probe setting of the time-dependent density-matrix formalism.

To this end, we pump the system with an intense pulse of $A_0 = 0.5 \times 10^{-8} \mathrm{J\,s\,C^{-1}\,m^{-1}}$ and, after a delay δt_{pp}, apply a weak probe pulse. Following experimental schemes [102], we perform two simulations. First, we simulate both a pump and a probe pulse to compute j_{pp}. In a second simulation we apply the pump only, obtaining j_p. We then compute the optical conductivity from the difference in currents $j = j_{pp} - j_p$. This ensures that residual contributions of the pump do not affect the optical conductivity.

Figs. 5.8(a-b) show the real and imaginary part of the optical conductivity $\sigma(\omega, \delta t_{pp})$ as a function of frequency and pump-probe delay. The third-order contribution $j\big|_3$ adds spectral weight to the conductivity below absorption gap. The conductivity shows clear oscillations in δt_{pp}, as emphasized in Fig. 5.8(c,e) where only the nonlinear contribution is plotted for the contributions from Higgs and density fluctuations, respectively. A Fourier transform of these oscillations, shown in Fig. 5.8(d,e), reveals that the oscillation frequency matches the resonance frequency of the Higgs mode 2Δ. Additionally, the Higgs signal exceeds the density fluctuations by one order of magnitude.

Our results show that signatures of the Higgs mode are measurable in the pump-probe response of the optical conductivity. Yet, to excite the Higgs mode, impurities are crucial. We find that the calculated time-resolved optical response of a single-band superconductor in the dirty-limit is in good agreement with the experimentally measured response [103].

5.4 Multi-band superconductivity

We now turn to the case of a two-band superconductor. For concreteness, we focus on the superconducting state of MgB_2. We model the π- and σ-bands believed to be responsible for superconductivity by choosing material parameters $\Delta_\pi = 3\,\mathrm{meV}$, $\Delta_\sigma = 7\,\mathrm{meV}$, $\epsilon_{F,\pi} = 2.9\,\mathrm{eV}$, $\epsilon_{F,\sigma} = 0.7\,\mathrm{eV}$, $m_\pi = 0.85 m_e$, $m_\sigma = 1.38 m_e$, $\omega_D = 50\,\mathrm{meV}$, $s_\pi = 1$, $s_\sigma = -1$ [85].

Convincing evidence for the two-band character of MgB_2 has been found in tunneling measurements [55, 71] and ARPES [155]. However, optical linear response probes have only revealed signatures of a superconducting gap in the π-band [77, 86]. A recent work [86] on third harmonic generation presents strong evidence of a collective Higgs resonance in the π-band, but no collective response in the σ-band was observed.

5.4.1 Optical conductivity

The linear response optical conductivity of multi-band superconductors is additively composed of contributions from the two bands, $\sigma(\omega) = \sigma_\pi + \sigma_\sigma$, where the band-specific conductivities are determined by a straightforward generalization of Eq. (5.21). Figures 5.9(a-b) show optical conductivities for various different combinations of band impurity concentrations.

Experimental measurements of the optical conductivity of MgB_2 below T_C show a clear absorption gap below $2\Delta_\pi$ and a dome shaped onset above $2\Delta_\pi$. A second onset at the larger gap $\omega = 2\Delta_\sigma$ has so far not been observed. An exemplary experimental measurement of the real and imaginary optical conductivity from Ref. [44] is shown in Fig. 5.10.

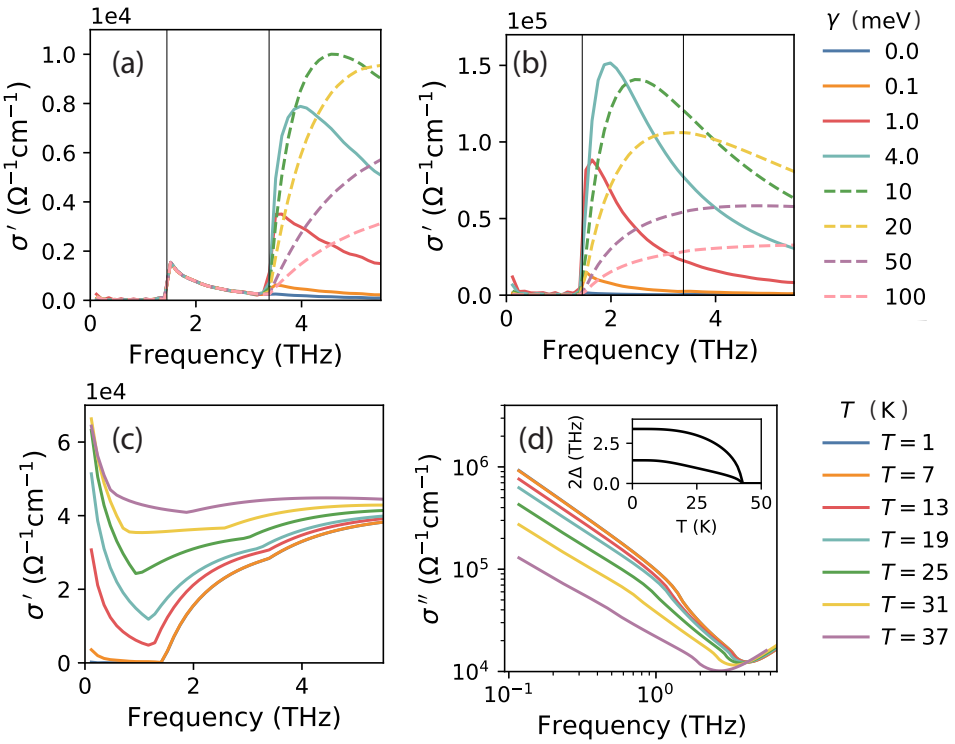

Figure 5.9: (a),(b) Real part σ' of linear response optical conductivity of a two-band superconductor for various impurity scattering rates at $T = 4\,\mathrm{K}$. In panel (a) the impurity of concentration of the first band is $\gamma_\pi = 0.01\,\mathrm{meV}$ and the second-band impurity scattering rates are given by the legend. In panel (b) the legend specifies γ_π and $\gamma_\sigma = 0.1\,\mathrm{meV}$. Vertical gray lines indicate the gap energies $2\Delta_\pi, 2\Delta_\sigma$. (c),(d) Plot of σ' and σ'' for various temperatures at $\gamma_1 = 100\,\mathrm{meV}$ and $\gamma_2 = 50\,\mathrm{meV}$. The imaginary part follows a $1/\omega$ power-law at small frequencies. (inset) BCS temperature dependence of the two gaps.

Our simulations reproduce the absence of the σ-gap in two different parameter regimes: in the dirty-clean limit ($\gamma_\pi \gg 2\Delta_\pi$, $\gamma_\sigma \ll 2\Delta_\sigma$), where only the first gap contributes to $\sigma(\omega)$, and in the dirty-dirty limit ($\gamma_\pi, \gamma_\sigma \gg 2\Delta_\pi$) shown in Fig. 5.9(c-d). Latter case only shows a weak onset of the σ-gap which may be unnoticeable with experimental noise. The reason of the subdominant contribution of the second gap lies in the small Fermi surface of the σ-band. Explicitly, this can be seen from the prefactor $v_{F_i} N_i$ in Eq. (5.21). For our choice of parameters, which include a high estimate of ϵ_{F_σ}, this yields a suppression of the σ-gap conductivity by a factor $v_{F_\pi} N_\pi / v_{F_\sigma} N_\sigma = 6.6$. For a more conservative estimate of ϵ_{F_σ}, the suppression should be even more pronounced.

5.4.2 Collective modes

Pulse induced changes of the two order parameters Δ_i with $i = \pi, \sigma$ in the two-band case are given by

$$\delta\Delta_i(\omega) = \frac{1}{2} \sum_{j\mathbf{k}\mathbf{k}'} H_{ij}^{-1}(\omega) |J_{j\mathbf{k}\mathbf{k}'}|^2 \int d\omega' \chi_j^{\sigma_0\sigma_0\sigma_1}(\omega, \omega', \mathbf{k}, \mathbf{k}') A(\omega') A(-\omega - \omega') \,, \tag{5.24}$$

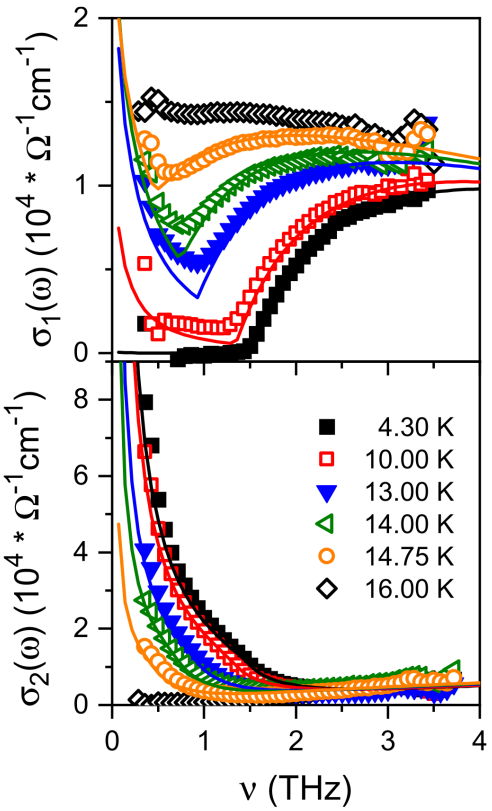

Figure 5.10: Experimental measurement of real (top) and imaginary (bottom) linear optical conductivity. Figure is taken from Ref. [44].

where

$$H = \begin{pmatrix} \chi_1^{\sigma_1\sigma_1} + 2U_{22}/\det U & -2U_{12}/\det U \\ -2U_{21}/\det U & \chi_2^{\sigma_1\sigma_1} + 2U_{11}/\det U \end{pmatrix} \tag{5.25}$$

and where susceptibilities $\chi_i^{\sigma_0\sigma_0\sigma_1}, \chi_i^{\sigma_1\sigma_1}$ are listed in Appendix C.1. The gaps exhibit two resonances which are determined by the Higgs propagator. In Fig. 5.11 we show a logarithmic false-color plot of the quantity $|\det H|^{-1}$, responsible for any divergence, as a function of frequency ω and interband coupling strength v. As expected, the two resonance energies are at $2\Delta_\pi$ and $2\Delta_\sigma$, illustrated by solid green horizontal lines. Resonances are sharp at small v but decrease and broaden in the strong interband coupling regime.

Energy conservation in Eq. (5.24) is established by the factor $A(\omega')A(-\omega-\omega')$. Oscillation of the gaps is therefore only possible for a finite overlap of $A^2(\omega)$ with the resonance frequencies. The matrix structure of H_{ij} further implies that both gaps will oscillate with all excited modes at finite v.

Dynamics of the phase modes θ_i in the frequency domain are determined by

$$\delta\theta_i(\omega) = \frac{1}{2}\sum_j \frac{s_j e^2}{2m_j\omega^2} L_{ij}^{-1}(\omega)\chi_j^{\sigma_3\sigma_3}(\omega)A^2(\omega)\,. \tag{5.26}$$

Due to the Anderson-Higgs mechanism only the dynamics of the phase difference $\delta\varphi = \delta\theta_\pi - \delta\theta_\sigma$ is

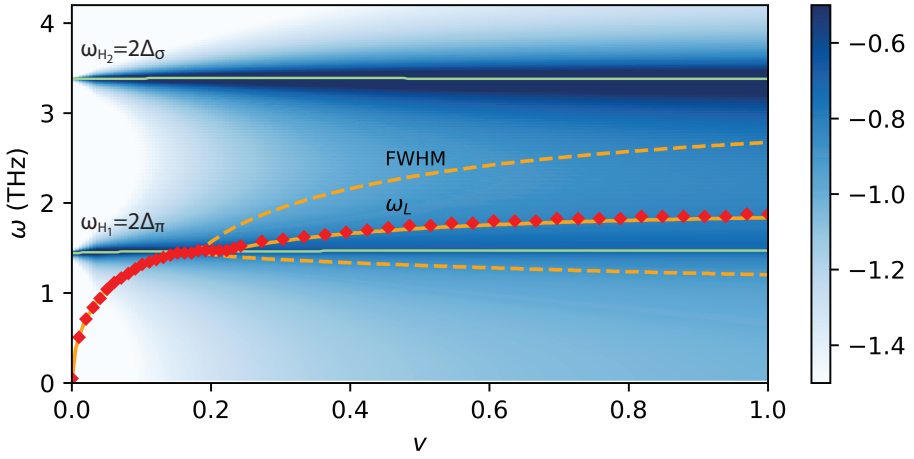

Figure 5.11: Plot of resonance spectrum of Higgs and Leggett modes with logarithmic color scale as a function of interband coupling parameter v. False-color plot was computed within the effective action formalism. Solid green line shows the frequency of the Higgs resonances. The solid and dashed orange lines mark the maximum and width of the Leggett mode. Red diamonds mark the Leggett oscillation frequencies extracted from a pumped time-dependent density-matrix simulation. The two approaches show excellent agreement.

physical. Inserting Eq. (5.26) yields the expression

$$\delta\varphi(\omega) = \frac{1}{4}A^2(\omega)\left(\frac{s_\pi}{m_\pi} - \frac{s_\sigma}{m_\sigma}\right)\left[\omega^2 + \frac{8\Delta_\pi\Delta_\sigma v}{U_{\sigma\sigma} - v^2U_{\pi\pi}}\frac{\chi_\pi^{\sigma_3\sigma_3} + \chi_\sigma^{\sigma_3\sigma_3}}{\chi_\pi^{\sigma_3\sigma_3}\chi_\sigma^{\sigma_3\sigma_3}}\right]^{-1}. \tag{5.27}$$

Solid and dashed orange lines in Fig. 5.11 trace the maximum and full width at half max (FWHM) of $\delta\varphi(\omega)/A^2(\omega)$. Red diamonds are the dominant oscillation frequency of the phase

$$\delta\varphi(t) \approx \frac{\delta\Delta_\pi''}{\Delta_\pi} - \frac{\delta\Delta_\sigma''}{\Delta_\sigma} \tag{5.28}$$

evaluated by computing $\delta\Delta_i''$ in a time-dependent density matrix formulation for a broadband optical pulse. The two methods show excellent agreement. At small coupling the phase exhibits completely undamped oscillations due to the absence of decay channels. The Leggett frequency ω_L increases for stronger coupling. Once its energy reaches the quasiparticle threshold it is increasingly damped, and the resonance broadens.

The present results reproduce the findings of Refs. [32, 116] which were obtained in the clean limit. This should come as no surprise since impurities do not change the frequency of the collective resonance within the MB approach and additionally the Leggett mode only couples diamagnetically to electromagnetic fields.

5.4.3 Pump-probe simulations

We proceed to model the pump-probe response of a two-band superconductor. Analogous to the single-band case we consider non-linear contributions to the optical conductivity and pump the system with an intense

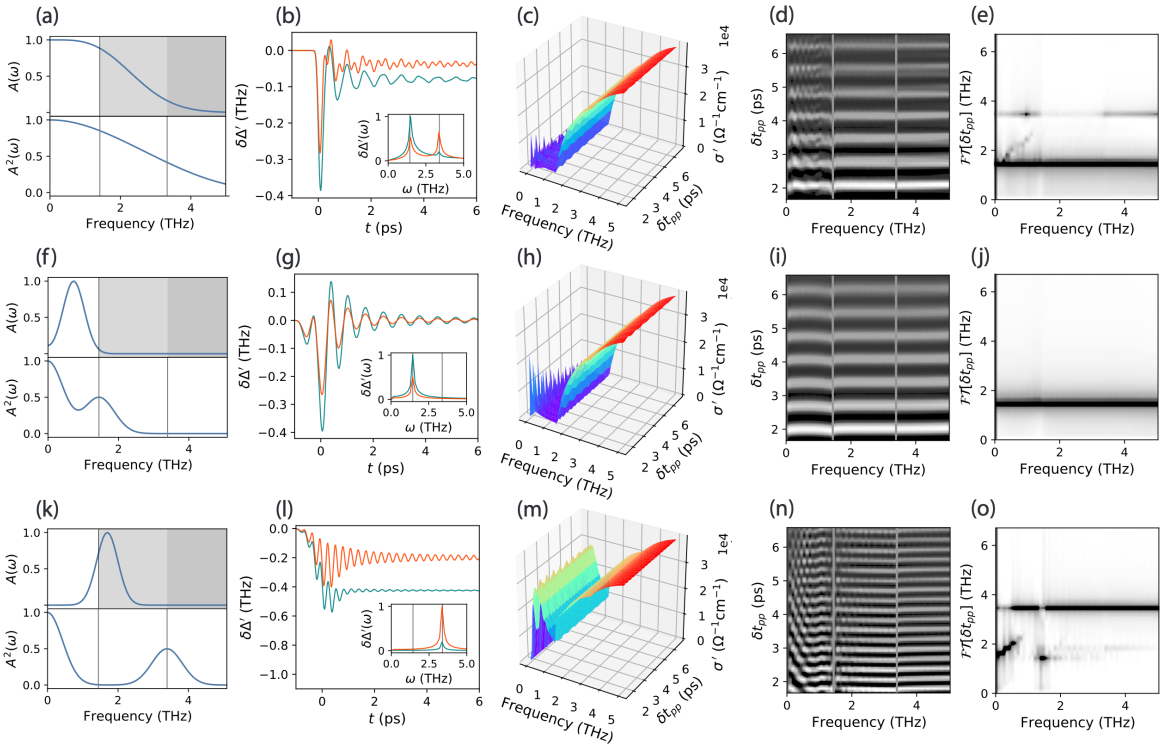

Figure 5.12: Time-resolved optical conductivity (c),(h),(m) for three optical pulses that resonantly excite (a) both Higgs modes, (f) the lower π-band Higgs resonance, and (k) the σ-Higgs mode for an interband coupling strength $v = 0.2$ in the dirty-dirty limit with $\gamma_\pi = 100\,\mathrm{meV}$ and $\gamma_\sigma = 50\,\mathrm{meV}$. (b),(g),(l) show the gap oscillations $\delta\Delta'(t)$ as a response to the pump pulse only. (d),(i),(n) show the background subtracted nonlinear optical conductivity. Their Fourier transforms are shown in panels (e),(j),(o).

pulse. After some time-delay δt_{pp}, the optical conductivity is probed in the linear response regime by a weak probe pulse.

In Fig. 5.12 we adopt the dirty-dirty limit with $\gamma_\pi = 100\,\mathrm{meV}$ and $\gamma_\sigma = 50\,\mathrm{meV}$ as a potential description of MgB_2 with $v = 0.2$ and select various pump pulses shown in the leftmost panels. Gray and dark gray areas illustrate the onset of the quasiparticle continuum of the two bands. Lower panels show $A^2(\omega)$ where Higgs resonance frequencies are marked by gray vertical lines. The second column shows the gap dynamics $\delta\Delta_i(t)$ following the pump pulse. The third column shows the real part of the time-resolved non-linear optical conductivity $\sigma'(\omega, \delta t_{pp})$. Panels (d,k,r) show the isolated nonlinear contribution of the real optical conductivity.

The first pump has a broad frequency spectrum such that it overlaps with both Higgs resonances. Following the excitation, both gaps oscillate with both frequencies. The overlap of $A(\omega)$ with the quasiparticle continuum induces a small drop of $\delta\Delta'$. The optical conductivity shows oscillations in the pump-probe delay δt_{pp} with mostly $2\Delta_\pi$ and a small $2\Delta_\sigma$ component. We attribute the subdominance of the $\delta\Delta_\sigma$-contribution to the small σ-band Fermi surface.

For a narrowband pulse centered at $\omega = \Delta_\pi$ (second row), we observe $2\Delta_\pi$ oscillations only. Here,

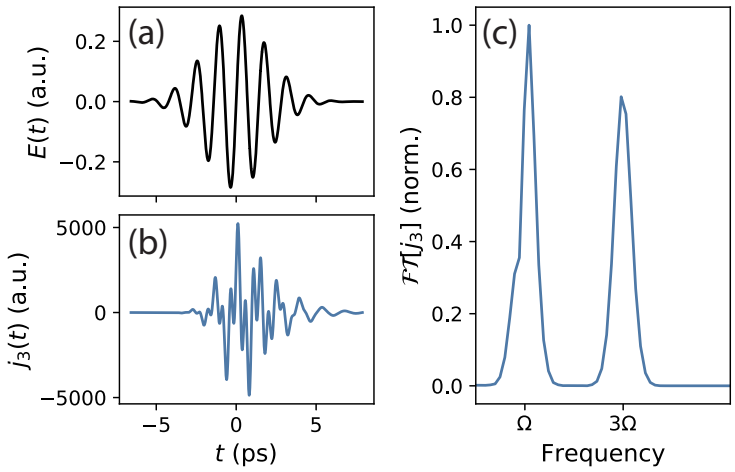

Figure 5.13: (a) Realistic multicycle pulse of main frequency Ω fed into time-dependent density matrix simulation. (b) Simulated third order current $j_3(t)$. (c) Next to the original Ω component, the Fourier transform $|j_3(\omega)|$ reveals an additional 3Ω component.

the pulse $A(\omega)$ does not overlap with the quasiparticle continuum. As a result, the gap oscillates around its equilibrium value $\Delta_\infty = \Delta$.

When the narrowband pulse is centered around the second Higgs resonance at $\omega = 2\Delta_\sigma$ (third row), the gap performs $2\Delta_\sigma$ oscillations only. However, the nonlinear current response is weak and numerically hard to resolve.

The last three columns of Fig. 5.12 show the Fourier transforms of panels (d),(k),(r) which are further separated into Higgs, charge density, and Leggett contributions. In all cases the current is dominated by the Higgs signal which exceeds the density fluctuations by roughly one order of magnitude. The Leggett frequency for $v = 0.2$ matches the energy of the lower Higgs modes $2\Delta_\pi$. It is, however, always small compared to the Higgs and density fluctuations. In panel Fig. 5.12(u) the Leggett contribution nearly vanishes since there is little overlap of the squared pulse $A^2(\omega)$ with its resonance frequency.

5.4.4 Third harmonic generation

Finally, we simulate the non-linear response of a multiband superconductor in a THG setup within the time-dependent density matrix framework. We model a realistic multi-cycle pulse of frequency Ω, exemplary shown in Fig. 5.13, and compute the third order current $j(t)\big|_3$. The Fourier transform of $j(t)\big|_3$ reveals a 3Ω third harmonic (TH) component next to the original first harmonic (FH) peak.

We adopt the dirty-dirty band description of MgB_2 with $\gamma_\pi = 100\,\mathrm{meV}, \gamma_\sigma = 50\,\mathrm{meV}$ and choose two different interband coupling strengths, $v = 0.05$ and $v = 0.4$. Then, we sweep temperature to investigate the resonant behaviour of the TH component. We consider three pulses of frequencies $\Omega = 0.5, 0.6, 0.7\,\mathrm{THz}$ and expect the TH component to be resonantly enhanced when $2\Omega = 2\Delta_i$.

Figs. 5.14(a-b) show the temperature dependence of the BCS gap. Horizontal lines mark pulse frequencies Ω used in independent simulations. Resonance conditions are satisfied at intersections with a gap. In the second row, Figs. 5.14(c-d), the amplitude of the TH peak is found as a function of temperature. In the

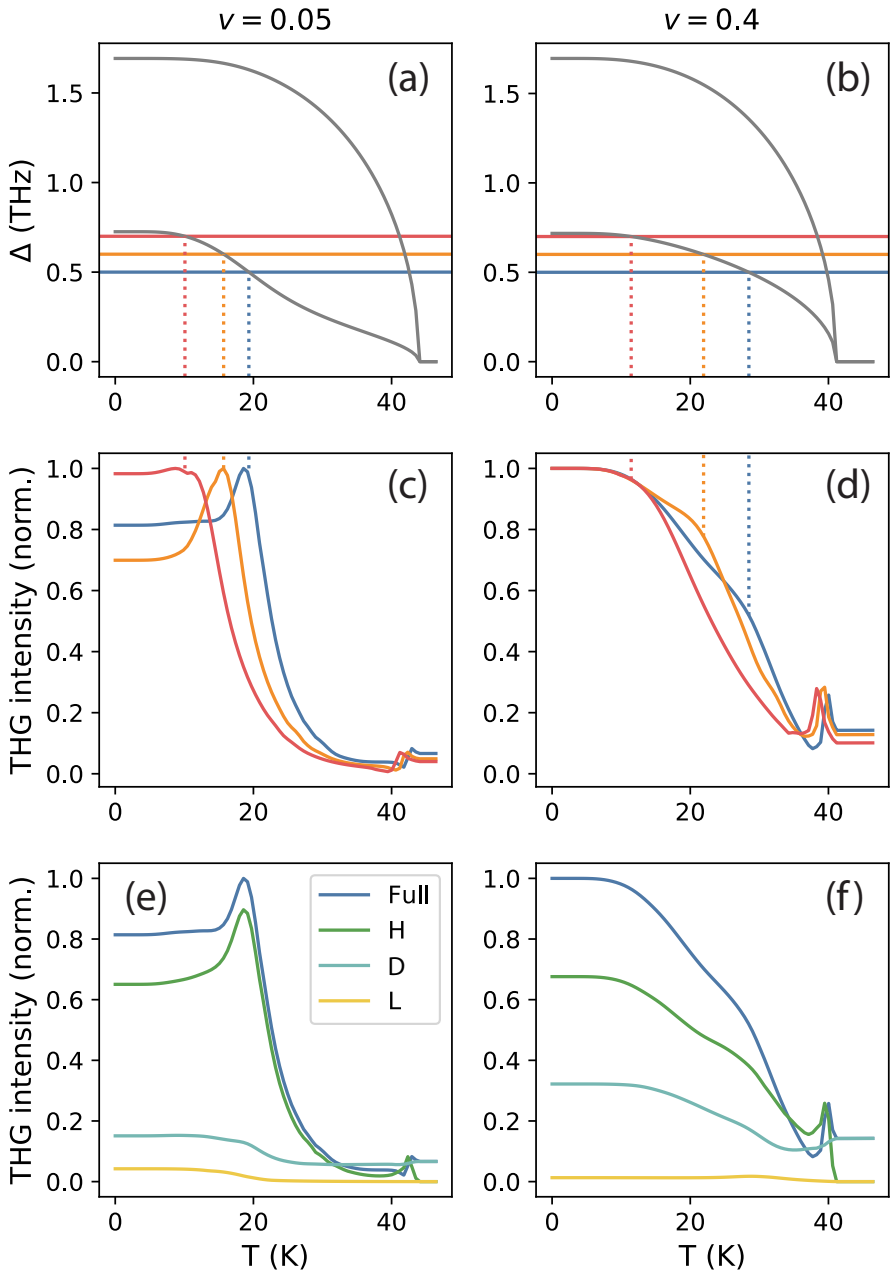

Figure 5.14: (a),(b) Temperature dependence of the BCS gaps at $v = 0.05$ and $v = 0.4$. Note that the T-dependence in the case $v = 0.05$ for the two-band BCS model does not match the familiar shape expected for a single band superconductor. Horizontal lines mark the three pulse frequencies $\Omega = 0.5, 0.6, 0.7\,\mathrm{THz}$. (c),(d) THG current as a function of temperature for three pulse frequencies Ω_j. We take the THG current as $j_3(\omega = 3\Omega)$, i.e. the amplitude of the second peak in Fig. 5.13(c) and sweep temperature. (e),(f) Decomposition of the THG signal for pulse of $\Omega = 0.5\,\mathrm{THz}$ in Higgs (H), density fluctuation (D) and Leggett (L) contributions. The main contribution stems from the collective Higgs mode in both the weak coupling (left) and strong coupling case (right).

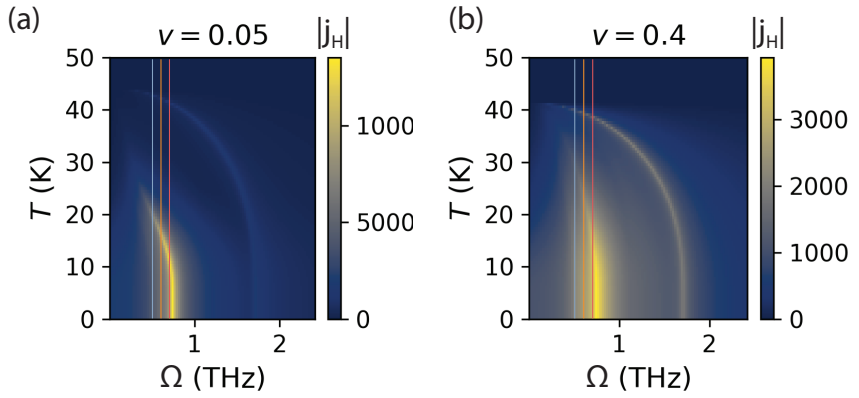

Figure 5.15: Nonlinear Higgs current as a function of temperature T and frequency Ω of a sinusoidal pulse computed within the effective action formalism (a) for $v = 0.05$ and (b) for $v = 0.4$. Vertical lines represent cuts according to the simulations in Fig. 5.14.

weak coupling case, $v = 0.05$, the THG signal for the lower two frequencies exhibits a pronounced peak at the resonance condition for the lower gap. The THG signal peak of the largest frequency is less pronounced, as this frequency is almost equal to the lower gap for a range of temperatures. We also observe much smaller peaks at temperatures where pulses are in resonance with the larger σ-gap.

In the strong coupling case, $v = 0.4$, we no longer observe a peak-like resonance for the lower π-band gap. This can be understood as a result of broadening of the Higgs resonance at large v, shown in Fig. 5.15. Here, we plot the nonlinear Higgs current as a function of temperature T and frequency Ω computed within the effective action formalism for a sinusoidal excitation. Vertical cuts correspond to the three simulations of Fig. 5.14. The resonance of the Higgs modes significantly broadens in the strong coupling case $v = 0.4$. Thus, the THG signal is already large when driven slightly below the $2\Delta_\pi$ resonance at $T = 0$ and no sharp peak occurs when the temperature is increased. This result is further discussed in Appendix C.4.

The σ-gap still induces a sharp resonance peak, albeit small in comparison to the low-temperature signal.

Panels (e),(f) of Fig. 5.14 decompose the THG signal for the $\Omega = 0.5$ THz pulse into contributions from the Higgs mode, density fluctuations, and Leggett mode. The Leggett mode contribution is found numerically by considering only the diamagnetic component of the current $j_D\big|_3$. The density fluctuation contribution is found by forcing $\delta\Delta_i = 0$ when solving the equations of motion, removing the self-consistency condition that induces collective modes. In both the weak coupling and large-v case the THG response is dominated by the Higgs mode. The relative contribution of density fluctuations increases in the strong interband coupling regime. The Leggett contribution is vanishingly small.

The present results are interesting when compared to the experimental findings of Ref. [86]. Our results affirm the claim that the THG response is mainly attributed to the Higgs resonance of the π-band. The small contribution of the σ-band Higgs mode and the Leggett mode in our simulation is consistent with the experiment where no signatures of the Leggett or second Higgs mode were observed. We have further computed the THG response in the dirty-clean limit where we found nearly identical results, apart from the absence of the small σ resonance peak at temperatures close to T_C.

The failure of our theory to produce resonance peaks of the π-Higgs mode at large v suggests that the

MB approximation might not correctly describe the THG response in the strong coupling limit as assumed for MgB_2 [24, 32]. A recent study has found that incorporating impurities beyond Mattis-Bardeen as random onsite-energies in a lattice model shows a stronger contribution of density fluctuations [141]. This, however, is beyond the scope of this chapter.

Chapter 6

Phase signatures in third-harmonic response of Higgs and coexisting modes in superconductors

6.1 Introduction

Experiments to excite the Higgs mode are usually performed in either of two ways. One option is to quench the system with an ultrafast, single-cycle THz pump pulse to abruptly change the system's parameter and bring it out of equilibrium. The order parameter starts to automatically oscillate around its new equilibrium state with the Higgs mode frequency. This general quench dynamics was theoretically studied for the first time in [4, 16, 17, 164, 177, 178] and later modeled with realistic light pulses in [87, 123]. Experimentally, it was measured in a pump-probe geometry, where the probe pulse scans the dynamics of the system with a variable time-delay after the pump pulse [103].

The second option is to drive the system periodically with a multi-cycle THz pulse at frequency Ω. This enforces the order parameter to oscillate with twice the driving frequency 2Ω due to the quadratic excitation process [34, 139, 156]. Furthermore, this leads to a third-harmonic generation (THG) process, which can be measured in the transmitted electric field. Tuning the driving frequency into resonance with the Higgs mode energy, i.e. $2\Omega = 2\Delta$, a resonance peak is visible in the signal. This can be achieved either by varying the driving frequency or, as it is currently done experimentally, by changing the value of the order parameter $\Delta(T)$ by sweeping the temperature T. The resonance can be used as a signature for the collective Higgs mode as it was demonstrated for the s-wave superconductor NbN [103, 105].

In many materials, more complicated effects may arise resulting from coexisting modes additionally contributing to the THG signal. Examples include quasiparticle excitations [34], Leggett modes in multiband systems [58, 115, 116], Josephson-Plasma modes in layered systems [51], Bardasis-Schrieffer modes in systems with subleading pairing channels [114], coexisting CDW fluctuations [31] or generally phonon and magnon excitations. Theoretical investigations of such systems with multiple collective modes have become even more important since THG experiments on several cuprates have recently been performed [37]. There,

an interesting phase signature indicating an interplay between two modes has been detected but was not fully understood theoretically. It is therefore important to understand the signatures of Higgs modes in spectroscopic experiments which can reveal the existence and interplay with other modes.

In this chapter, we therefore take into account the existence of another mode and we investigate the THG signal for such systems. Hereby, we concentrate on the phase of the 3Ω oscillations, which was not discussed theoretically so far. In comparison with a classical driven oscillator, we show that a driven BCS model contains additional microscopic details in the phase of the signal. Furthermore, we develop a general concept of antiresonance in a microscopic theory, which is an intrinsic signature for coexisting or coupled modes. We demonstrate this concept on two example systems, namely a coupling of the Higgs mode to a charge density wave and secondly a Higgs mode with a coexisting Bardasis-Schrieffer mode. Here, we propose that analyzing the phase of the THG signal in addition to the amplitude yields additional information valuable for understanding the interplay of superconductivity and other modes. Hereby, the nature and the symmetry of the coexisting modes is not important for the interplay mechanism such that our theory generally applies and can easily be extended to other system like d-wave superconductors.

6.2 Phase signature of a single mode

Before studying the full microscopic quantum mechanical model for superconductors and their collective modes, let us first consider a simple, well-known classical system. This will allow us to define and observe the crucial features which are important for the later discussion, and we can compare the similarities and differences between these systems. Hereby, we investigate classical driven oscillators which represent the collective modes of the system.

6.2.1 Harmonic oscillator

It is well known that a driven harmonic oscillator has a characteristic amplitude and phase response which depends on the driving frequency. With the eigenfrequency ω_0, damping factor γ, driving amplitude F_0 and driving frequency Ω, the equation of motion for the displacement $x(t)$ reads

$$\ddot{x}(t) + \omega_0^2 x(t) + \gamma \dot{x}(t) = F_0 \cos(\Omega t)\,. \tag{6.1}$$

The steady-state solution can be written as $x(t) = A\cos(\Omega t - \phi)$, where the frequency-dependent amplitude A and phase ϕ are given by

$$A(\Omega) = \frac{F_0}{\sqrt{(\omega_0^2 - \Omega^2)^2 + \gamma^2\Omega^2}}\,, \tag{6.2a}$$

$$\phi(\Omega) = \tan^{-1}\left(\frac{\gamma\Omega}{\omega_0^2 - \Omega^2}\right)\,. \tag{6.2b}$$

One observes that the amplitude has a resonance peak at $\Omega = \omega_0$ which is accompanied by an abrupt phase change from 0 to π. Thus, the oscillation is in-phase with the driving frequency below the resonance and lags behind with opposite phase above the resonance.

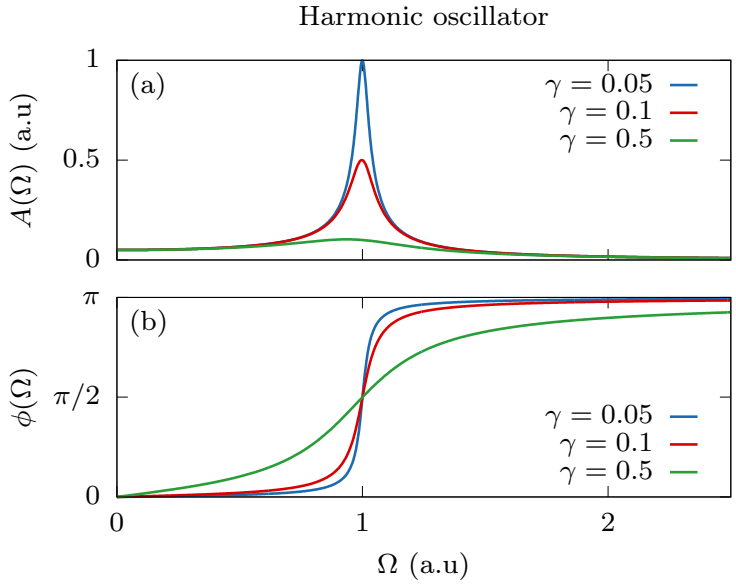

Figure 6.1: (a) Amplitude and (b) phase of a driven harmonic oscillator for different damping γ according to Eq. (6.2) with $F_0 = 1$ and $\omega_0 = 1$.

The amplitude and phase are plotted in Fig. 6.1 for different damping values γ. While for small damping a pronounced resonance peak is visible in the amplitude, for large damping, the resonance peak is heavily suppressed and broadened. In contrast, the phase still shows a phase change from 0 to π, even though it is broadened as well. This means that both amplitude and phase have a signature of the resonance, yet the phase change signature is more robust against the influence of damping. Hence, in a strongly damped system with suppressed resonance peak, the eigenmode would still be identifiable via the phase signature.

6.2.2 Ginzburg-Landau model

Let us investigate now whether we can observe such a behavior for THz-driven collective modes in superconductors as well. The oscillator corresponds to a collective mode which is driven by a THz light field. In the experiment, the driven collective mode is not measured directly. Instead, the induced current proportional to the transmitted electric field is recorded.

As a first step, we recapitulate the phenomenological Ginzburg-Landau model, where we will consider amplitude and phase fluctuations [124, 156]. The time-dependent Lagrangian of a superconductor coupled to a gauge field is given by

$$\mathcal{L} = (D_\mu \psi)^* (D^\mu \psi) - V(\psi) - \frac{1}{4} F_{\mu\nu} F^{\mu\nu} \,, \tag{6.3}$$

where ψ is the superconducting order parameter, $D_\mu = \partial_\mu + \mathrm{i}eA_\mu$ the covariant derivative with the four-vectors $\partial^\mu = (\partial_t, -\nabla)$ and $A_\mu = (\Phi, -\boldsymbol{A})$ and electromagnetic field tensor $F_{\mu\nu} = \partial_\mu A_\nu - \partial_\nu A_\mu$ in units where $c = 1$, with the electric potential Φ and the electromagnetic vector potential $\boldsymbol{A}$. In principle, the Lagrangian could also contain additional linear derivative terms. Yet, we assume perfect particle-hole

symmetry, such that the time dynamics of a superconductor is described only by a second-order derivative term [124, 162]. The potential $V(\psi) = \alpha|\psi|^2 + \frac{\beta}{2}|\psi|^4$ is the free energy of a superconductor with $\beta > 0$ and $\alpha = \alpha_0(T - T_c)$ such that for $T < T_c$ the potential takes the form of a Mexican hat with the ground state $\psi_0 = \sqrt{-\alpha/\beta}$. We introduce amplitude (Higgs) fluctuations $H(\boldsymbol{r}, t)$ and phase (Goldstone) fluctuations $\theta(\boldsymbol{r}, t)$ via

$$\psi(\boldsymbol{r}, t) = (\psi_0 + H(\boldsymbol{r}, t))\mathrm{e}^{\mathrm{i}\theta(\boldsymbol{r},t)}\,, \tag{6.4}$$

and choose a gauge $A_\mu \to A_\mu + \frac{1}{e}\partial_\mu\theta$ and $\psi \to \psi\mathrm{e}^{-\mathrm{i}\theta}$. Then, the Lagrangian up to second order in the fluctuations reads

$$\mathcal{L} = (\partial_\mu H)(\partial^\mu H) + 2\alpha H^2 - \frac{1}{4}F_{\mu\nu}F^{\mu\nu} + e^2\psi_0^2 A_\mu A^\mu + 2e^2\psi_0 A_\mu A^\mu H\,. \tag{6.5}$$

Hereby, the phase fluctuations are removed from the Lagrangian by the chosen gauge and are implicitly included in the longitudinal component of the transformed gauge field A_μ which obtains an additional mass term $\propto A_\mu A^\mu$. This effect is known as the Anderson-Higgs mechanism [8]. In a region close to the transition temperature, where the influence of normal carriers can be relevant, a low energy density fluctuation can remain, which is known as the Carlson-Goldman mode [13, 30, 137]. Such a scenario requires a two-fluid model description and might be interesting to study in future. Calculating the equations of motion for the Higgs mode H, neglecting spatial fluctuations for $\boldsymbol{q} \to 0$ and choosing a gauge with $\Phi = 0$, yields

$$\partial_t^2 H(t) - 2\alpha H(t) = -e^2\psi_0 A(t)^2\,. \tag{6.6}$$

The dynamics of the Higgs oscillations is governed by a harmonic oscillator with frequency $\omega_0 = \sqrt{-2\alpha}$. The driving term is quadratic in the vector potential $A(t)$. With a periodic light field $A(t) = A_0\cos(\Omega t)$, the system is effectively driven by 2Ω such that the resonance in the system occurs at $2\Omega = \omega_0$. Thus, on a phenomenological level, the collective Higgs oscillations of a superconductor and its amplitude and phase signature is described by the classical model discussed in Sec. 6.2.1. The measured transmitted field is described by the induced current given by [156]

$$j(t) = \frac{\partial\mathcal{L}}{\partial A} = -2e^2\psi_0^2 A(t) - 4e^2\psi_0 A(t)H(t)\,. \tag{6.7}$$

A nonlinear third-harmonic component in the current is induced as $A(t)\cdot H(t) \propto \cos(3\Omega t - \phi) + \ldots$ The resonance behavior of the amplitude and phase in the current $j(t)$ is directly given by the Higgs response $H(t)$.

6.2.3 Microscopic BCS model

While in the phenomenological model the coupling of light to the system contains no further details, in a microscopic model additional effects with frequency-dependent susceptibilities occur. Furthermore, there are quasiparticles in the microscopic model which render the Higgs mode less stable due to the additional

decay channel.

To address these effects, we proceed to the full microscopic theory using the usual effective action approach described for example in [3, 34]. We will derive known expressions but reanalyze these concentrating on the phase structure. The BCS Hamiltonian reads

$$H_{\mathrm{BCS}}(t) = \sum_{\boldsymbol{k},\sigma} \epsilon_{\boldsymbol{k}} c^\dagger_{\boldsymbol{k},\sigma} c_{\boldsymbol{k},\sigma} - \sum_{\boldsymbol{k},\boldsymbol{k}'} V_{\boldsymbol{k},\boldsymbol{k}'} c^\dagger_{\boldsymbol{k},\uparrow} c^\dagger_{-\boldsymbol{k},\downarrow} c_{-\boldsymbol{k}',\downarrow} c_{\boldsymbol{k}',\uparrow} + \frac{1}{2} \sum_{\boldsymbol{k},\sigma} \sum_{i,j} \partial^2_{ij} \epsilon_{\boldsymbol{k}} A_i(t) A_j(t) c^\dagger_{\boldsymbol{k},\sigma} c_{\boldsymbol{k},\sigma} \,. \tag{6.8}$$

Hereby, $\epsilon_{\boldsymbol{k}} = \xi_{\boldsymbol{k}} - \epsilon_{\mathrm{F}}$ is the electron dispersion $\xi_{\boldsymbol{k}}$ measured relative to the Fermi level ϵ_{F} and $c^\dagger_{\boldsymbol{k},\sigma}$ or $c_{\boldsymbol{k},\sigma}$ the electron creation or annihilation operators. The separable BCS pairing interaction is given by $V_{\boldsymbol{k},\boldsymbol{k}'} = V f_{\boldsymbol{k}} f_{\boldsymbol{k}'}$ with pairing strength V and symmetry $f_{\boldsymbol{k}}$. A coupling to light represented by the vector potential $\boldsymbol{A}(t)$ is realized by minimal coupling $\epsilon_{\boldsymbol{k}} \to \epsilon_{\boldsymbol{k}-\boldsymbol{A}(t)}$. An expansion in powers of $\boldsymbol{A}(t)$ yields the lowest non-vanishing diamagnetic coupling term shown above, while the linear paramagnetic coupling $\propto \partial_i A_i(t)$ vanishes due to parity symmetry. In the expression, we have introduced the short-hand notation $\partial^2_{ij} = \partial^2_{k_i k_j}$. Here, we initially neglect long-ranged Coulomb interaction and the coupling to phase fluctuations which is important in real materials. We will show later in Sec. 6.2.4 that including Coulomb interaction does not affect the phase signature. The action of the system in imaginary time τ is given by

$$S = \int_0^\beta \mathrm{d}\tau \left(\sum_{\boldsymbol{k},\sigma} c^\dagger_{\boldsymbol{k},\sigma}(\tau) \partial_\tau c_{\boldsymbol{k},\sigma}(\tau) + H(\tau) \right) . \tag{6.9}$$

We perform a Hubbard-Stratonovich transformation introducing the bosonic field Δ, with amplitude fluctuations $\Delta(t) = \Delta + \delta\Delta(t)$. After integration of fermions, we split the action in a mean-field and fluctuating part, which we expand up to fourth order in A. For more details about the calculation see Appendix D.1. The effective action with Matsubara frequencies $\mathrm{i}\omega_m$ in fourth order of the vector potential reads

$$S^{(4)} = \frac{1}{2}\frac{1}{\beta} \sum_{\mathrm{i}\omega_m} \delta\Delta(-\mathrm{i}\omega_m) H^{-1}(\mathrm{i}\omega_m) \delta\Delta(\mathrm{i}\omega_m) - 2\delta\Delta(-\mathrm{i}\omega_m) \sum_{i,j} \chi^{ij}_{\Delta A^2} A^2_{ij}(\mathrm{i}\omega_m) + \sum_{ijkl} A^2_{ij}(-\mathrm{i}\omega_m) \chi^{ijkl}_{A^2A^2}(\mathrm{i}\omega_m) A^2_{kl}(\mathrm{i}\omega_m) \,. \tag{6.10}$$

Hereby, $H^{-1}(\mathrm{i}\omega_m)$ is the inverse Higgs propagator defined as the renormalized pairing interaction V

$$H^{-1}(\mathrm{i}\omega_m) = \frac{2}{V} + \chi_{\Delta\Delta}(\mathrm{i}\omega_m) \,. \tag{6.11}$$

The susceptibilities are given by

$$\chi_{\Delta\Delta}(\mathrm{i}\omega_m) = \sum_{\boldsymbol{k}} f_{\boldsymbol{k}}^2 X_{11}(\boldsymbol{k}, \mathrm{i}\omega_m)\,, \tag{6.12a}$$

$$\chi_{\Delta A^2}^{ij}(\mathrm{i}\omega_m) = \sum_{\boldsymbol{k}} f_{\boldsymbol{k}}\, \frac{1}{2}\partial_{ij}^2 \epsilon_{\boldsymbol{k}}\, X_{13}(\boldsymbol{k}, \mathrm{i}\omega_m)\,, \tag{6.12b}$$

$$\chi_{A^2A^2}^{ijkl}(\mathrm{i}\omega_m) = \sum_{\boldsymbol{k}} \frac{1}{4}\partial_{ij}^2 \epsilon_{\boldsymbol{k}}\, \partial_{kl}^2 \epsilon_{\boldsymbol{k}}\, X_{33}(\boldsymbol{k}, \mathrm{i}\omega_m) \tag{6.12c}$$

with

$$X_{\alpha\beta}(\boldsymbol{k}, \mathrm{i}\omega_m) = \frac{1}{\beta}\sum_{\mathrm{i}\omega_n} \mathrm{tr}[G_0(\boldsymbol{k}, \mathrm{i}\omega_n)\tau_\alpha G_0(\boldsymbol{k}, \mathrm{i}\omega_m + \mathrm{i}\omega_n)\tau_\beta] \tag{6.13}$$

and the BCS Green's function $G_0^{-1} = \mathrm{i}\omega_m\tau_0 - \epsilon_{\boldsymbol{k}}\tau_3 + \Delta_{\boldsymbol{k}}\tau_1$ where τ_i are Pauli matrices. The indices Δ and A^2 in the susceptibilities represent the vertices, i.e., the coupling to the Higgs propagator via $f_{\boldsymbol{k}}\tau_1$ or the coupling to light via $\partial_{ij}^2\epsilon_{\boldsymbol{k}}\tau_3$, respectively. Integrating out the amplitude fluctuations and after analytic continuation $\mathrm{i}\omega_m \to \omega + \mathrm{i}0^+$ one obtains

$$S^{(4)} = \frac{1}{2}\int \mathrm{d}\omega \sum_{ijkl} \Big(\chi_{\Delta A^2}^{ij}(-\omega)\chi_{\Delta A^2}^{kl}(\omega)H(\omega) + \chi_{A^2A^2}^{ijkl}(\omega)\Big) A_{ij}^2(-\omega)A_{kl}^2(\omega)\,. \tag{6.14}$$

There are two contributions in the action, one containing the Higgs oscillations and one the quasiparticle response [34]. These contributions are shown diagrammatically in Fig. 6.2(a) and (b).

For simplicity, we will only consider linear-polarized light in x-direction, such that we can neglect the polarization indices in the following. With this, the third-harmonic response is given by

$$j^{(3)}(3\Omega) = -\left.\frac{\delta S^{(4)}}{\delta A(-\omega)}\right|_{3\Omega} \propto \chi_H(2\Omega) + \chi_Q(2\Omega) \tag{6.15}$$

with the Higgs (H) and quasiparticle (Q) contribution

$$\chi_H(\omega) = \chi_{\Delta A^2}(-\omega)\chi_{\Delta A^2}(\omega)H(\omega)\,, \tag{6.16a}$$

$$\chi_Q(\omega) = \chi_{A^2A^2}(\omega)\,. \tag{6.16b}$$

Comparing the response $j^{(3)}$ with the phenomenological Ginzburg-Landau model in Eq. (6.7), we can observe several differences which modify the response. First, the Higgs propagator $H(\omega)$ is a more complex object compared to the steady-state solution in Eq. (6.2) and does not have a simple resonance pole as we will see. Second, light does not directly couple to the Higgs mode but through the susceptibility $\chi_{\Delta A^2}(\omega)$. Third, there is an additional quasiparticle response given by $\chi_{A^2A^2}(\omega)$.

In the following, let us disentangle these effects. Evaluating the Matsubara sum and rewriting the momentum sum as an integral assuming s-wave symmetry, the Higgs propagator can be analytically evaluated

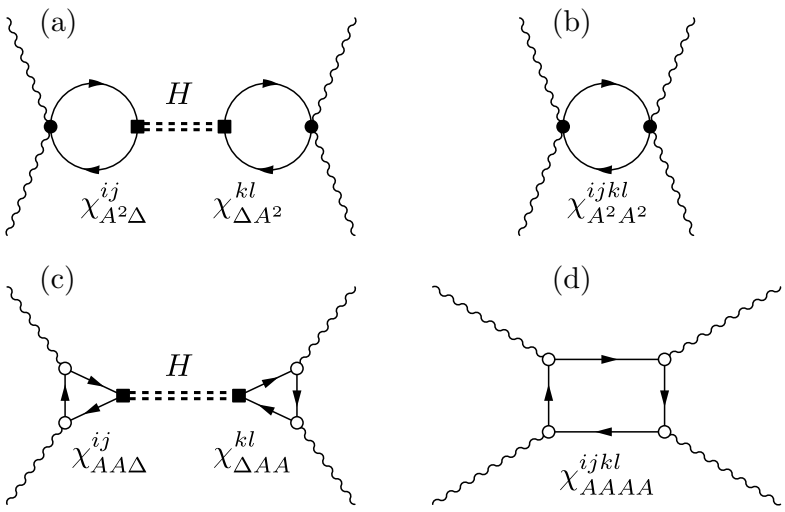

Figure 6.2: Diagrammatic representation of the effective action in the (a),(b) clean limit according to Eq. (6.16) and in the (c),(d) dirty limit according to Eq. (6.24). (a) Diamagnetic Higgs excitation. (b) Diamagnetic quasiparticle excitation. (c) Paramagnetic Higgs excitation. (d) Paramagnetic quasiparticle excitation. The wiggly lines represent the vector potential A, the solid lines the BCS Green's function G_0 and the double dashed line the Higgs propagator H. The filled square vertex corresponds to $f_{\boldsymbol{k}}\tau_1$, the filled circle vertex to $\partial^2_{ij}\epsilon_{\boldsymbol{k}}\tau_3$ and the empty circle vertex to $\partial_i\epsilon_{\boldsymbol{k}}\tau_0$.

at $T = 0$. Concentrating on the pole structure one obtains the well-known result [16, 31, 164, 177, 178]

$$H(\omega) \propto \frac{1}{\sqrt{4\Delta^2 - \omega^2}}\,. \tag{6.17}$$

It does not have a simple pole but a square root term in the denominator. This is in contrast to the solution of the classical oscillator Eq. (6.2), where a simple pole $1/(\omega_0^2 - \Omega^2)$ occurs for $\gamma = 0$. It is interesting to note that this behavior results from the different decay property of the intrinsic Higgs mode compared to the eigenmode of a classical oscillator. While the eigenmode of a classical oscillator is undamped without additional damping γ, the Higgs mode has a characteristic $1/\sqrt{t}$ decay in the time-domain even without damping [16, 164, 177, 178]. It can be understood as a decay into quasiparticles as the Higgs mode energy overlaps with the quasiparticle continuum at 2Δ. In addition to the obvious consequence of stronger damping, it also affects the phase response. The square root reduces the π phase change at the resonance frequency to $\pi/2$. Thus, the driven amplitude oscillation only lags behind a quarter cycle at high frequencies instead of being completely anti-phase as found in the phenomenological model.

The phase response of the Higgs mode is additionally affected by the susceptibilities $\chi^2_{\Delta A^2}$ in Eq. (6.16). However, this is an additive phase contribution that is continuous and slowly varying around the resonance at 2Δ. The observation of a phase jump is therefore directly related to the analytical structure of the Higgs propagator, Eq. (6.17).

Finally, let us examine the quasiparticle response which is actually known to be much larger than the Higgs response [34]. Evaluating the Matsubara sum of the respective susceptibility and solving the momen-

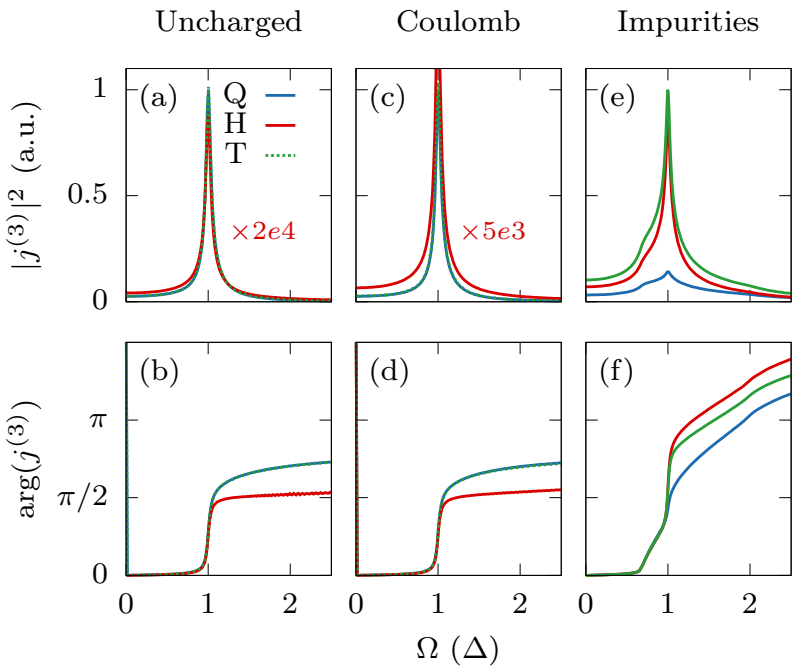

Figure 6.3: Intensity (top row) and (normalized to zero) phase (bottom row) of THG response for Higgs (H), quasiparticles (Q) and total (T). (a),(b) Uncharged BCS model without Coulomb interaction in Eq. (6.16). The Higgs contribution is scaled by $2 \cdot 10^4$ to be visible. (c),(d) BCS model including Coulomb interaction in Eq. (6.22). The Higgs contribution is scaled by $5 \cdot 10^3$ to be visible. (e),(f) BCS model with impurities using Mattis-Bardeen approach in Eq. (6.24)

tum sum (see Appendix D.1) one obtains for the pole structure

$$\chi_{A^2A^2}(\omega) \propto \frac{1}{\sqrt{4\Delta^2 - w^2}} + \dots \tag{6.18}$$

The quasiparticle response has the same square root pole structure as the Higgs mode, leading to the same $\pi/2$ phase change at the resonance frequency.

In Fig. 6.3(a) and (b) the amplitude and phase of the diamagnetic Higgs and quasiparticle response is shown using $\epsilon_{\boldsymbol{k}} = -2t(\cos k_x + \cos k_y) - \mu$, $t = 10\,\text{meV}$, $\mu = -10\,\text{meV}$, $\Delta = 1\,\text{meV}$ and a residual broadening $\omega \to \omega + \text{i}0.05\,\text{meV}$. Hereby, the momentum sums are evaluated numerically on a 2d grid with 2000×2000 points without approximation assuming linearly polarized light in x-direction. Confirming the analytic study, we can see that phase shows a $\pi/2$ phase change at the resonance frequency $2\Omega = 2\Delta$. Above the resonance, a drift is observable to higher values for the quasiparticles and lower values for the Higgs mode. As it has been emphasized in literature [34], the Higgs mode is much smaller in the clean-limit BCS theory.

6.2.4 Influence of Coulomb interaction

As a next step, we discuss the influence of Coulomb interaction given by an additional term in the Hamiltonian

$$H_c = \frac{1}{2} \sum_{\boldsymbol{k},\boldsymbol{k}',\boldsymbol{q}} \sum_{\sigma,\sigma'} V(\boldsymbol{q}) c^\dagger_{\boldsymbol{k}+\boldsymbol{q},\sigma} c_{\boldsymbol{k},\sigma} c^\dagger_{\boldsymbol{k}'-\boldsymbol{q},\sigma'} c_{\boldsymbol{k}',\sigma'} \tag{6.19}$$

where $V(\boldsymbol{q})$ is the Coulomb potential. We follow [34] and decouple the Coulomb interaction by means of an additional Hubbard-Stratonovich transformation introducing the density field $\rho(\boldsymbol{q},\tau) = \rho_0 + \delta\rho(\boldsymbol{q},\tau)$ and allow amplitude and phase fluctuations in the superconducting order parameter $\Delta(\tau) = (\Delta + H(\tau))\mathrm{e}^{\mathrm{i}\theta(\tau)}$. With this, one obtains for the fourth order action

$$\begin{aligned} S^{(4)}(\delta\Delta,\theta,\delta\rho) = \frac{1}{2}\frac{1}{\beta}\sum_{\mathrm{i}\omega_m} \Big[&\phi^\top(-\mathrm{i}\omega_m) M(\mathrm{i}\omega_m)\phi(\mathrm{i}\omega_m) + \phi^\top(-\mathrm{i}\omega_m) b(\mathrm{i}\omega_m) + b^\top(-\mathrm{i}\omega_m)\phi(\mathrm{i}\omega_m) \\ &+ \sum_{ijkl} A^2_{ij}(-\mathrm{i}\omega_m) A^2_{ij}(\mathrm{i}\omega_m) \chi^{ijkl}_{A^2A^2}(\mathrm{i}\omega_m) \Big] \end{aligned} \tag{6.20}$$

with

$$\phi^\top(\mathrm{i}\omega_m) = \begin{pmatrix} \delta\Delta(\mathrm{i}\omega_m) & \theta(\mathrm{i}\omega_m) & \delta\rho(\mathrm{i}\omega_m) \end{pmatrix}, \tag{6.21a}$$

$$M = \begin{pmatrix} H^{-1} & \frac{\mathrm{i}\omega_m}{2}\chi_{\Delta\rho} & \chi_{\Delta\rho} \\ -\frac{\mathrm{i}\omega_m}{2}\chi_{\rho\Delta} & \frac{\omega_m^2}{4}\chi_{\rho\rho} & -\frac{\mathrm{i}\omega_m}{2}\chi_{\rho\rho} \\ \chi_{\rho\Delta} & \frac{\mathrm{i}\omega_m}{2}\chi_{\rho\rho} & -\frac{1}{V(\boldsymbol{q})} + \chi_{\rho\rho} \end{pmatrix}, \tag{6.21b}$$

$$b(\mathrm{i}\omega_m) = \begin{pmatrix} \sum_{ij} A^2_{ij}(\mathrm{i}\omega_m)\chi^{ij}_{\Delta A^2}(\mathrm{i}\omega_m) \\ -\mathrm{i}\omega_m \sum_{ij} A^2_{ij}(\mathrm{i}\omega_m)\chi^{ij}_{\rho A^2}(\mathrm{i}\omega_m) \\ \sum_{ij} A^2_{ij}(\mathrm{i}\omega_m)\chi^{ij}_{\rho A^2}(\mathrm{i}\omega_m) \end{pmatrix}. \tag{6.21c}$$

The susceptibilities are given in Appendix D.2. Integrating the fluctuations and using $1/V(\boldsymbol{q}) \to 0$ for $\boldsymbol{q} \to 0$ one obtains for the third-order current $j^{(3)} = \chi_H + \chi_Q$

$$\chi_Q = \chi_{A^2A^2} - \frac{\chi^2_{A^2\rho}}{\chi_{\rho\rho}}, \tag{6.22a}$$

$$\chi_H = \frac{(\chi_{A^2\Delta} - \chi_{A^2\rho}\chi_{\Delta\rho}/\chi_{\rho\rho})^2}{H^{-1} - \chi^2_{\Delta_\rho}/\chi_{\rho\rho}}. \tag{6.22b}$$

The Coulomb interaction renormalizes the Higgs and quasiparticle response. Yet, due to obtained structure, the phase signature is not changed. The expressions in the numerator containing the terms $\chi_{A^2\rho}$ and $\chi_{\Delta\rho}$ do not contain poles and only add continuous phase contributions around 2Δ. This can be seen in Fig. 6.3(c),(d), where the respective expressions are numerically evaluated with the same parameters of the previous section. Except global scaling factors and small deviations resulting from the $1/\chi_{\rho\rho}$ contribution

the result is basically unchanged with a phase change of $\pi/2$ at the resonance.

6.2.5 Influence of impurities

Recently it was pointed out in several papers [58, 75, 115, 142, 147, 157] that nonmagnetic impurities allow an additional paramagnetic coupling of light to the condensate. This is shown diagrammatically in Fig. 6.2(c) and (d) where the light-coupling vertices are in the τ_0-channel. While these diagrams vanish in the clean limit, they have been shown to dominate the optical nonlinear response even for small disorder. To model impurities, different approaches have been used, e.g. quasiclassical Eilenberger equations equivalent to impurity ladder summations [147], the self-consistent Born approximation [157], or averaging disorder configurations in real-space [142]. Here, we adopt the Mattis-Bardeen approximation first applied to the nonlinear response in [115] and subsequently formulated in the effective action framework in [58]. This approach allows to model impurities with an effective vertex approximation and shows qualitatively similar results to [142, 147, 157].

Following [58], we implement a 3D continuum model, where we can express the THG current within the Mattis-Bardeen approximation as

$$j^{(3)}(3\Omega) = \chi_H(2\Omega) + \chi_Q(2\Omega) \tag{6.23}$$

with the Higgs (H) and quasiparticle (Q) susceptibilities

$$\chi_H(2\Omega) = 2\chi_{AA\Delta}(2\Omega,-\Omega)\chi_{AA\Delta}(-2\Omega,-\Omega)H(2\Omega)\,, \tag{6.24a}$$

$$\chi_Q(2\Omega) = \chi_{AAAA}(\Omega,2\Omega,-\Omega)\,. \tag{6.24b}$$

The triangle and square bubbles are defined as

$$\chi_{AA\Delta}(\omega_m,\omega_l) = \frac{1}{\beta}\sum_{\omega_n}\sum_{\boldsymbol{k}\boldsymbol{k}'}|J_{\boldsymbol{k}\boldsymbol{k}'}|^2\,\mathrm{tr}\left[G_0(\omega_n+\omega_m,\boldsymbol{k})G_0(\omega_n+\omega_m+\omega_l,\boldsymbol{k}')G_0(\omega_n,\boldsymbol{k})\tau_1\right], \tag{6.25a}$$

$$\begin{aligned}\chi_{AAAA}(\omega_m,\omega_l,\omega_p) = \frac{1}{\beta}\sum_{\omega_n}\sum_{\boldsymbol{k}\boldsymbol{k}'\boldsymbol{k}''}&|J_{\boldsymbol{k}\boldsymbol{k}'}|^2|J_{\boldsymbol{k}\boldsymbol{k}''}|^2\\ &\times\mathrm{tr}\left[G_0(\omega_n,\boldsymbol{k})G_0(\omega_n+\omega_m,\boldsymbol{k}')G_0(\omega_n+\omega_m+\omega_l,\boldsymbol{k})G_0(\omega_n+\omega_m+\omega_l+\omega_p,\boldsymbol{k}'')\right]\end{aligned} \tag{6.25b}$$

and are shown in Fig. 6.2(c) and (d). The transition matrix element $J_{\boldsymbol{k}\boldsymbol{k}'} = \langle\boldsymbol{k}|\frac{e\boldsymbol{p}}{m}|\boldsymbol{k}'\rangle$ is approximated by a Lorentzian distribution

$$|J_{\boldsymbol{k}\boldsymbol{k}'}|^2 \approx \frac{(ev_F)^2}{3N(0)}\frac{1}{\pi}\frac{\gamma}{(\epsilon_{\boldsymbol{k}}-\epsilon_{\boldsymbol{k}'})^2+\gamma^2} \tag{6.26}$$

with impurity scattering rate γ, Fermi velocity v_F, and density of states at Fermi surface $N(0)$. We choose the parameters $\Delta = 2\,\mathrm{meV}$, mass $m = 0.78m_e$ of the parabolic band dispersion, $\epsilon_F = 1\,\mathrm{eV}$, and impurity scattering rate $\gamma/\Delta = 10$. As $\gamma \gg 2\Delta$, the considered case corresponds to a superconductor in the dirty limit [115]. We evaluate Matsubara sums analytically and numerically compute the momentum integrals.

For further details about the calculation see [58]. While the Mattis-Bardeen approximation may not yield qualitatively accurate results in the nonlinear response, it serves well to discuss qualitative differences of the phase response compared to the clean limit.

The resulting amplitude and phase of the dirty superconductor are shown in Fig. 6.3(e) and (f). We find a pronounced resonance peak at $2\Omega = 2\Delta$. Here, the Higgs contribution is no longer subdominant but instead gives the main contribution to the THG signal. The resonance peak is accompanied by a positive phase jump of roughly π across the resonance. The detailed structure of this phase response as well as the value of the phase jump show some weak dependence on material parameters.

The more complex phase structure in the dirty limit can be understand as follows: While the clean phase response is dominated by the $\pi/2$ phase jump of the Higgs propagator, the phase contribution of the susceptibilities in the dirty case adds a steep positive drift above 2Δ, such that the overall phase change is increase to roughly π. The susceptibility is represented by the fermionic triangles $\chi_{AA\Delta}(2\Omega, -\Omega)\chi_{AA\Delta}(-2\Omega, -\Omega)$ and shown in Fig. 6.2(c). Thus, the phase response in the dirty limit is not only given by the Higgs propagator but has an additional contribution from the electron-mediated microscopic coupling of light to the Higgs mode.

6.3 Phase response of two modes

Now, we will consider systems which contain two modes and study the interaction between these. Again, we start by an analysis of the classic analogue of two coupled oscillators to understand the fundamental properties before proceeding to a microscopic model.

6.3.1 Coupled oscillators

If there are two modes in a system, interference effects occur in the driven system which can lead to the so-called antiresonance phenomenon. The usual way to understand this effect is based on the assumption that there are two modes in the system which are coupled and only *one* of these modes is externally driven. For a particular driving frequency, the external force on the driven mode cancels exactly with the force induced by the other coupled mode such that the amplitude of the oscillation of this mode vanishes – thus the name antiresonance. Furthermore, the antiresonance is accompanied by a negative phase jump of π, therefore it goes in the opposite direction compared to a resonance.

The same phase signature can also be obtained when *both* oscillators are driven, and the observed signal is comprised of the sum of both oscillation amplitudes. Here, this effect is a trivial consequence of a destructive interference and does not necessarily rely on a coupling between the modes. An additional coupling between the modes allows for a tuning of the antiresonance frequency. We refer to this scenario as *antiresonance behavior* as well.

To make this effect more clear, let us first investigate again the classic model where we consider now

two coupled and driven oscillators described by the following equations of motion

$$\begin{aligned} x_1''(t) + \omega_1^2 x_1(t) + \gamma_1 x_1'(t) + g x_2(t) &= F_1 \cos(\Omega t)\,, \\ x_2''(t) + \omega_2^2 x_2(t) + \gamma_2 x_2'(t) + g x_1(t) &= F_2 \cos(\Omega t)\,. \end{aligned} \tag{6.27}$$

There are two oscillators $x_1(t)$ and $x_2(t)$ with individual eigenfrequencies ω_i, dampings γ_i and driving amplitudes F_i but same driving frequencies Ω. The coupling between the modes is controlled by the constant g. Using the complex variable method ansatz

$$x_i(t) = A_1 \cos(\Omega t - \phi_i) = \mathsf{Re}\, \hat{x}_i(t)\,, \tag{6.28}$$

where $\hat{x}_i(t) = \hat{A}_1(\Omega) \mathrm{e}^{\mathrm{i}\Omega t}$ with $\hat{A}_i(\Omega) = A_i(\Omega) \mathrm{e}^{-\mathrm{i}\phi_i(\Omega)}$, we write the equations in matrix form

$$\begin{pmatrix} P_1^{-1} & g \\ g & P_2^{-1} \end{pmatrix} \begin{pmatrix} \hat{A}_1 \\ \hat{A}_2 \end{pmatrix} = \begin{pmatrix} F_1 \\ F_2 \end{pmatrix}\,, \tag{6.29}$$

where we define the "propagator" of the oscillators as $P_i^{-1} = -\Omega^2 + \omega_i^2 + \mathrm{i}\Omega\gamma_i$. Inversion of the matrix leads to the solution

$$\begin{pmatrix} \hat{A}_1 \\ \hat{A}_2 \end{pmatrix} = \begin{pmatrix} \tilde{P}_1 & -g P_1 \tilde{P}_2 \\ -g P_1 \tilde{P}_2 & \tilde{P}_2 \end{pmatrix} \begin{pmatrix} F_1 \\ F_2 \end{pmatrix} \tag{6.30}$$

with the renormalized propagator $\tilde{P}_i = (P_i^{-1} - g^2 P_j)^{-1}$ where $i \neq j$. We also consider the total response $x_T = x_1 + x_2$, where

$$x_T(t) = A_T \cos(\Omega t - \phi_T) = \mathsf{Re}\, \hat{x}_T(t) \tag{6.31}$$

with $\hat{x}_T(t) = \hat{A}_T(\Omega) \mathrm{e}^{\mathrm{i}\Omega t}$ and $\hat{A}_T = A_T(\Omega) \mathrm{e}^{-\phi_T(\Omega)}$. One obtains for the complex amplitudes

$$\hat{A}_1 = \tilde{P}_1 F_1 - g P_1 \tilde{P}_2 F_2\,, \tag{6.32a}$$

$$\hat{A}_2 = \tilde{P}_2 F_2 - g P_1 \tilde{P}_2 F_1\,, \tag{6.32b}$$

$$\hat{A}_T = \tilde{P}_1 F_1 + \tilde{P}_2 F_2 - g P_1 \tilde{P}_2 (F_1 + F_2)\,. \tag{6.32c}$$

In Fig. 6.4 we show a numerical evaluation of the individual and total amplitudes A_i and phases ϕ_i for two distinct cases (see Appendix D.3 for the exact expressions). In the first column, the two oscillators are coupled, i.e. $g \neq 0$, but only the first oscillator is driven $F_2 = 0$. In the second column, the two oscillators are uncoupled, i.e. $g = 0$, but both oscillators are driven $F_i \neq 0$.

The first scenario (left column) corresponds to the usual definition of the antiresonance, namely a destructive interference between the driving force and the force from the second oscillator due to the coupling. The dip between the two resonance peaks and the negative π phase change, is clearly visible for the first oscillator (red curve). The energy of the antiresonance ω_A is determined by $\tilde{P}_1 = 0$, which leads to $\omega_A = \omega_2$,

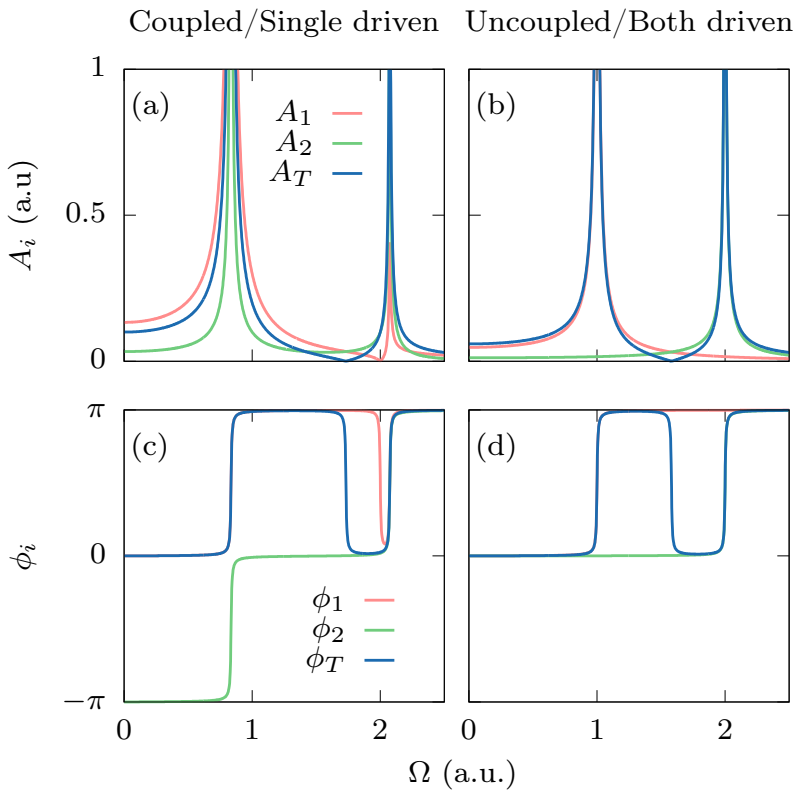

Figure 6.4: (a),(b) Amplitude and (c),(d) phase of two (coupled) modes as defined in Eq. (6.28) and Eq. (6.31). For the left column (a) and (c), the two oscillators are coupled with $g = 1$ but only the first oscillator is driven with $F_1 = 1$ and $F_2 = 0$. For the right column (b) and (d), the two oscillators are uncoupled with $g = 0$ but both oscillators are driven with $F_1 = F_2 = 1$. The frequencies are $\omega_1 = 1$, $\omega_2 = 2$ and the damping coefficients $\gamma_1 = \gamma_2 = 0.01$.

i.e., the antiresonance occurs at the energy of the other undriven mode. The total response A_T and ϕ_T (blue curve) also shows this behavior resulting from the antiresonance of the first oscillator. Yet, the energy of the antiresonance is shifted as a result of the second superposition scenario.

We can further see that the finite coupling shifts the resonances frequency with respect to the uncoupled eigenfrequencies ω_i. The resonance frequency for the lower modes is decreases, while the resonance frequency of the higher mode is increased. The energies are given by the poles of the renormalized propagators

$$\tilde{\omega}_i = \frac{1}{\sqrt{2}}\sqrt{\omega_1^2 + \omega_2^2 \pm \sqrt{(\omega_1^2 - \omega_2^2)^2 + 4g^2}}\,. \tag{6.33}$$

For the shown parameters, this results in a resonance peak below $\omega_1 = 1$ and a resonance peak above $\omega_2 = 2$.

The total response (blue curve) of the second scenario (right column) shows a very similar behavior, namely a dip in between the two resonance peaks and a negative π phase change. However, in this case the negative phase jump does not result from an individual oscillator, both individual oscillators (red and green curve) do not show this behavior. It rather results from the superposition of the two oscillations where the

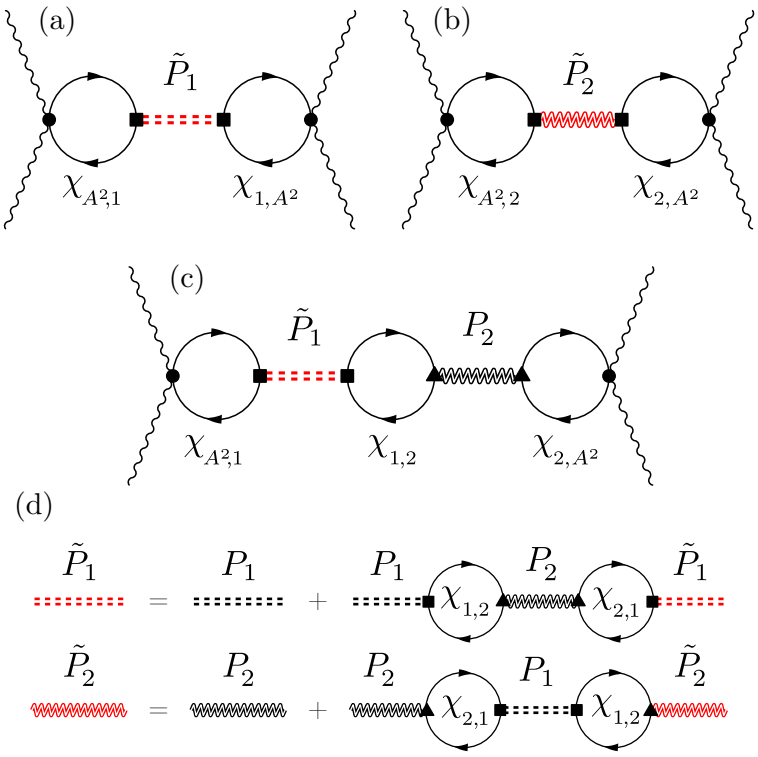

Figure 6.5: Diagrammatic representation of effective action for a system with Higgs and another mode assuming diamagnetic coupling to light. (a),(b) Excitation of renormalized mode 1 or 2 (c) Mixed contribution term, where light couples to both modes and the modes to each other. (d) Renormalization of both modes as RPA series due to interaction with each other. The wiggly lines represent the vector potential A, the solid lines the BCS Green's function G_0, the double dashed line the Higgs propagator H and the double zigzag line the propagator of another mode. Red lines represent the renormalized propagators. The filled square vertex corresponds to $f_{\boldsymbol{k}}\tau_1$, the filled circle vertex to $\partial^2_{ij}\epsilon_{\boldsymbol{k}}\tau_3$ and the filled triangle vertex represent the interaction with the other mode.

sum of both cancel out in an intermediate position between the resonances. This energy is determined by $P_1 + P_2 = 0$ leading to $\omega_A = \frac{1}{\sqrt{2}}\sqrt{\omega_1^2 + \omega_2^2}$. As the sum of both undergoes a sign change from negative to positive a negative π phase change occurs naturally. The resonance frequencies in this scenario are not changed and still occur at ω_i.

To summarize, the antiresonance behavior of the total response of two oscillators can have different origins. It can be either controlled by the coupling between the oscillators or the interference if both modes are driven.

6.3.2 Microscopic theory

Let us now investigate whether this behavior is observable in a microscopic model as well. For now, we will make some general arguments assuming that there are two modes 1 and 2 in the system, for example the

Higgs mode and a second collective mode. In Sec. 6.4 and Sec. 6.5 we will consider specific examples.

Considering the general form of the effective action and the analysis of the classical oscillator system, we are anticipating the results of the next sections and postulate the general structure of the response. The fourth order effective action for two modes reads

$$\begin{aligned} S^{(4)} &= \frac{1}{2}\frac{1}{\beta}\sum_{\mathrm{i}\omega_m} b^\top(-\mathrm{i}\omega_m) M^{-1}(\mathrm{i}\omega_m) b(\mathrm{i}\omega_m) \\ &= \frac{1}{2}\frac{1}{\beta}\sum_{\mathrm{i}\omega_m} K^{(4)}(\mathrm{i}\omega_m) A^2(-\mathrm{i}\omega_m) A^2(\mathrm{i}\omega_m) \end{aligned} \tag{6.34}$$

where

$$M^{-1} = \begin{pmatrix} \tilde{P}_1 & \chi_{1,2} P_1 \tilde{P}_2 \\ \chi_{2,1} P_1 \tilde{P}_2 & \tilde{P}_2 \end{pmatrix}, \tag{6.35a}$$

$$b = \begin{pmatrix} \chi_{1,A^2} \\ \chi_{2,A^2} \end{pmatrix} A^2 . \tag{6.35b}$$

Hereby, P_i stands for the propagator of mode i, $\chi_{i,j}$ for different coupling susceptibilities and A the vector potential, where the polarization indices are not included. The tilde denotes a renormalization due to the other mode. This can be understood as an RPA series renormalization of the propagators shown in Fig. 6.5(d) and expressed as

$$\tilde{P}_1 = P_1 + \chi_{1,2}^2 P_1 P_2 \tilde{P}_1 , \tag{6.36a}$$

$$\tilde{P}_2 = P_2 + \chi_{1,2}^2 P_1 P_2 \tilde{P}_2 \tag{6.36b}$$

which leads to

$$\tilde{P}_1 = \frac{1}{P_1^{-1} - \chi_{1,2}^2 P_2} , \tag{6.37a}$$

$$\tilde{P}_2 = \frac{1}{P_2^{-1} - \chi_{1,2}^2 P_1} . \tag{6.37b}$$

The fourth-order kernel $K^{(4)}$ explicitly reads

$$K^{(4)} = \chi_1 + \chi_2 + \chi_{12} \tag{6.38}$$

with

$$\chi_1 = \chi_{1,A^2}^2 \, \tilde{P}_1 , \tag{6.39a}$$

$$\chi_2 = \chi_{2,A^2}^2 \, \tilde{P}_2 , \tag{6.39b}$$

$$\chi_{12} = P_1 \tilde{P}_2 (\chi_{A^2,1} \, \chi_{1,2} \, \chi_{2,A^2} + \chi_{A^2,2} \, \chi_{2,1} \, \chi_{1,A^2}) . \tag{6.39c}$$

These terms are diagrammatically shown in Fig. 6.5(a)-(c) and can be understood in the following way. First of all, both modes may couple individually to light represented by Eq. (6.39a) and Eq. (6.39b). If there is a coupling between the modes, a mixed term Eq. (6.39c) occurs, where light couples to both modes and the modes to each other.

A comparison with the classic coupled oscillator model of the previous sections in Eq. (6.32) reveals the exact same structure except that there, all susceptibilites are constant without frequency dependence.

After these general remarks, let us now consider specific examples of two microscopically coupled modes in the next sections.

6.4 Higgs and charge density wave

As a first example of two coupled collective modes, we will consider a coexisting superconducting and charge density wave (CDW) system. The amplitude modes are schematically shown in Fig. 6.6(a) in the picture of the free energy. An example for such a scenario is $NbSe_2$, where the coupling of the Higgs mode to a CDW phonon was observed in Raman response [107, 149] and theoretically investigated by several authors [27, 31, 95]. Another relevant system are cuprates, where superconductivity and fluctuating charge order has been reported in the underdoped regime [65, 154]. This scenario might be a possible explanation of the antiresonance behavior observed in recent THG experiments [37].

To model the system, we follow [31] and start from the BCS Hamiltonian in Eq. (6.8) where we add a phonon of momentum $\boldsymbol{Q}$ responsible for creating the charge order and a coupling to electrons with strength g. The Hamiltonian is given by

$$H = H_{\mathrm{BCS}} + H_{\mathrm{CDW}} \tag{6.40}$$

with

$$H_{\mathrm{CDW}} = \sum_{\boldsymbol{q}=\pm\boldsymbol{Q}} \omega_{\boldsymbol{q}} b^\dagger_{\boldsymbol{q}} b_{\boldsymbol{q}} + g \sum_{\boldsymbol{k},\boldsymbol{q}=\pm\boldsymbol{Q},\sigma} g_{\boldsymbol{k}} c^\dagger_{\boldsymbol{k}+\boldsymbol{q},\sigma} c_{\boldsymbol{k}\sigma} (b_{\boldsymbol{q}} + b^\dagger_{-\boldsymbol{q}}) \,. \tag{6.41}$$

Hereby, $b^\dagger_{\boldsymbol{q}}$ or $b_{\boldsymbol{q}}$ are the phonon creation or annihilation operators and ω_Q the energy of the CDW phonon. The electron phonon coupling is controlled by $g \cdot g_{\boldsymbol{k}}$ with strength g and momentum dependence $g_{\boldsymbol{k}}$.

To simplify the calculation, we will make the following assumptions. We consider a 2d square lattice with a tight-binding dispersion and nearest-neighbor hopping t at half-filling, namely $\epsilon_{\boldsymbol{k}} = -2t(\cos k_x + \cos k_y)$. As it was shown in [31], a finite chemical potential leads to a qualitative similar result. Choosing $\boldsymbol{Q} = \begin{pmatrix} \pi & \pi \end{pmatrix}$ we have perfect nesting and a commensurate CDW with $\boldsymbol{k} + 2\boldsymbol{Q} \hat{=} \boldsymbol{k}$ where $\epsilon_{\boldsymbol{k}+2\boldsymbol{Q}} = \epsilon_{\boldsymbol{k}}$ and $\epsilon_{\boldsymbol{k}+\boldsymbol{Q}} = -\epsilon_{\boldsymbol{k}}$. We assume an s-wave superconductor with $f_{\boldsymbol{k}} = 1$ and an anisotropic s-wave CDW with $g_{\boldsymbol{k}} = |\cos k_x - \cos k_y|$.

We start from the action of the system, where we introduce a CDW order parameter $D_{\boldsymbol{k}} = D g_{\boldsymbol{k}}$ with $D = g \langle b_{\boldsymbol{Q}} + b^\dagger_{-\boldsymbol{Q}} \rangle$ and the superconducting order parameter Δ using a Hubbard-Stratonovich transformation. Details of the calculation can be found in Appendix D.4. Please note that we neglect here the Coulomb interaction and phase fluctuations as we have shown in Sec. 6.2.4 that they do not affect the phase signature.

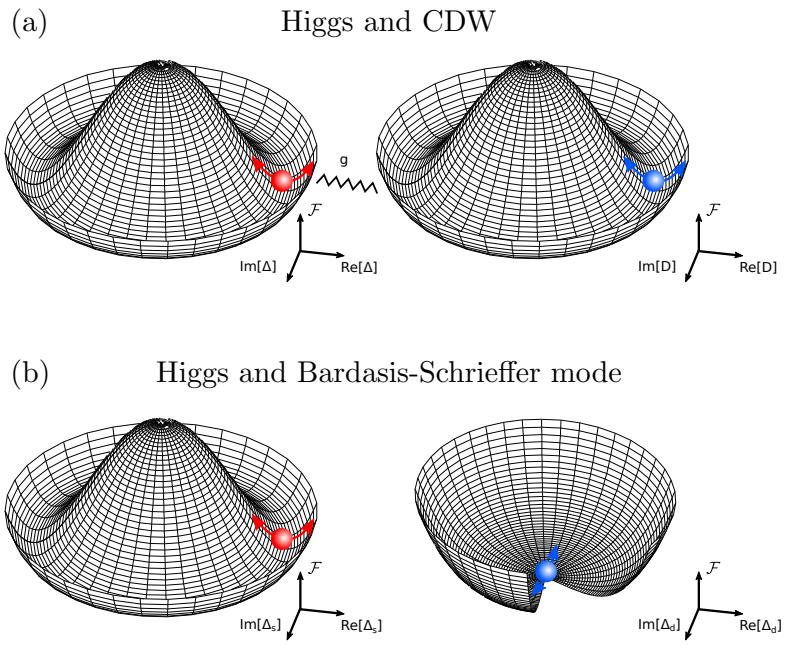

Figure 6.6: Collective modes in the picture of the free energy. (a) Higgs and CDW mode. The Higgs mode is the amplitude fluctuation of the superconducting order parameter and the CDW mode the amplitude fluctuation of the CDW order parameter corresponding to the renormalized CDW phonon. (b) Higgs and Bardasis-Schrieffer mode. The Bardasis-Schrieffer mode is the amplitude oscillation of the subleading pairing channel orthogonal to the amplitude (Higgs) oscillation of the dominant pairing channel.

Furthermore, in the half-filled case, as considered here, its influence vanishes completely as the system has perfect particle-hole symmetry [31].

After integration of the fermions and expansion of the action at Gaussian level for amplitude fluctuations $\Delta(t) = \Delta + \delta\Delta(t)$ and $D(t) = D + \delta D(t)$, the effective fourth order action reads

$$S^{(4)} = \frac{1}{2}\frac{1}{\beta}\sum_{\mathrm{i}\omega_m}\left(\phi^T(-\mathrm{i}\omega_m)M(\mathrm{i}\omega_m)\phi(\mathrm{i}\omega_m) + \phi^T(-\mathrm{i}\omega_m)b(\mathrm{i}\omega_m) + b^\top(-\mathrm{i}\omega_m)\phi(\mathrm{i}\omega_m)\right) \tag{6.42}$$

with

$$\phi^T(-\mathrm{i}\omega_m) = \begin{pmatrix}\delta\Delta(-\mathrm{i}\omega_m) & \delta D(-\mathrm{i}\omega_m)\end{pmatrix}, \tag{6.43a}$$

$$M(\mathrm{i}\omega_m) = \begin{pmatrix}H^{-1}(\mathrm{i}\omega_m) & \chi_{\Delta D}(\mathrm{i}\omega_m)\\ \chi_{D\Delta}(\mathrm{i}\omega_m) & -\frac{1}{g^2}P^{-1}(\mathrm{i}\omega_m)\end{pmatrix}, \tag{6.43b}$$

$$b(\mathrm{i}\omega_m) = -\sum_{ij}A^2_{ij}(\mathrm{i}\omega_m)\begin{pmatrix}\chi^{ij}_{\Delta A^2}(\mathrm{i}\omega_m)\\ \chi^{ij}_{DA^2}(\mathrm{i}\omega_m)\end{pmatrix}, \tag{6.43c}$$

where H is the Higgs propagator and P the renormalized Phonon propagator. It is defined as

$$P^{-1}(\mathrm{i}\omega_m) = P_0^{-1}(\mathrm{i}\omega_m) - g^2\chi_{DD}(\mathrm{i}\omega_m) \tag{6.44}$$

with the bare phonon propagator $P_0 = -2\omega_Q/(\omega_Q^2 - (\mathrm{i}\omega_m)^2)$ and χ_{DD} the susceptibility describing the influence of the CDW. The susceptibility on the off-diagonal in M leads to a coupling between Higgs and CDW and the expression is equivalent to the coupled oscillator system Eq. (6.29) in the previous section. An integration of the amplitude fluctuations finally leads to

$$S^{(4)} = \frac{1}{2}\frac{1}{\beta}\sum_{\mathrm{i}\omega_m} b^\top(-\mathrm{i}\omega_m)M^{-1}(\mathrm{i}\omega_m)b(\mathrm{i}\omega_m) \tag{6.45}$$

with

$$M^{-1} = \begin{pmatrix} \tilde{H} & g^2\chi_{\Delta D}P\tilde{H} \\ g^2\chi_{D\Delta}\tilde{P}H & -g^2\tilde{P} \end{pmatrix} \tag{6.46}$$

where we identify the renormalized Higgs and phonon propagator as shown diagrammatically in Fig. 6.5(d)

$$\tilde{H} = \frac{1}{H^{-1} + g^2\chi_{\Delta D}\chi_{D\Delta}P}\,, \tag{6.47a}$$

$$\tilde{P} = \frac{1}{P^{-1} + g^2\chi_{\Delta D}\chi_{D\Delta}H}\,. \tag{6.47b}$$

The expression of the action follows exactly the general structure as shown in the previous section and the resulting diagrams are the ones shown in Fig. 6.5(a)-(c).

Let us analyze the result in more detail. First, we evaluate the expression for the bare Higgs propagator. One finds

$$H(\omega) \propto \frac{\sqrt{4\Delta^2 + 4D^2 - \omega^2}}{4\Delta^2 - \omega^2}\,. \tag{6.48}$$

For $D = 0$, we would retain expression Eq. (6.17). However, for finite CDW gap D, the Higgs mode energy 2Δ no longer coincides with the quasiparticle excitation gap $\Delta + D$ and, as already pointed out by [31], the Higgs mode becomes stable as its energy is below the gap. This has consequences for the pole structure, as the Higgs mode now has a simple pole without square root such that we can expect a π phase shift when varying the driving frequency ω from below to above the Higgs mode energy.

The CDW phonon propagator can be evaluated and reads

$$P(\mathrm{i}\omega_m) = -\frac{2\omega_Q}{\Omega_Q^2 - (\mathrm{i}\omega_m)^2} \tag{6.49}$$

with

$$\Omega_Q^2 = 4g^2\omega_Q \sum_{\boldsymbol{k}} g_{\boldsymbol{k}}^2 \frac{4D_{\boldsymbol{k}}^2 - (\mathrm{i}\omega_m)^2}{E_{\boldsymbol{k}}(4E_{\boldsymbol{k}}^2 - (\mathrm{i}\omega_m)^2)} \tanh(\beta E_{\boldsymbol{k}}/2)\,. \tag{6.50}$$

The phonon propagator has a simple pole leading to a phase change of π.

Assuming linear polarized light in x-direction as in Sec. (6.2.3), we can write the action as

$$S^{(4)} = \frac{1}{2}\int \mathrm{d}\omega\, K^{(4)}(\omega) A^2(-\omega) A^2(\omega)\,, \tag{6.51}$$

where the kernel is given by $K^{(4)} = \chi_H + \chi_P + \chi_M$ with the Higgs (H), phonon (P) and mixed (M) contributions

$$\chi_H = \chi_{A^2\Delta}^2 \tilde{H}\,, \tag{6.52a}$$

$$\chi_P = -g^2 \chi_{A^2D}^2 \tilde{P}\,, \tag{6.52b}$$

$$\chi_M = g^2 \tilde{H} P (\chi_{A^2\Delta}\chi_{A^2D}\chi_{\Delta D} + \chi_{\Delta A^2}\chi_{DA^2}\chi_{D\Delta})\,. \tag{6.52c}$$

It has the same structure as Eq. (6.39c) introduced as the general response for coupled modes. With the insight of the previous sections, we can expect an antiresonance behavior with a negative phase change of π in between the two resonances where a phase change of positive π should occur.

To confirm, we calculate numerically the total THG response as function of frequency and temperature. The temperature dependence is necessary to compare with experimental results where only the temperature can be varied for fixed driving frequency. The calculation for a set of parameters $\Delta = 2.5\,\mathrm{meV}$, $\omega_0 = 15\,\mathrm{meV}$, $D = 3\,\mathrm{meV}$, $t = 10\,\mathrm{meV}$, $\omega \to \omega + \mathrm{i}0.1\,\mathrm{meV}$ is evaluated on a 2d grid with 2000×2000 points and shown in Fig. 6.7. Hereby, the CDW phonon energy is above the Higgs mode energy. The top row shows the THG intensity, and the bottom row the THG phase. The first column is a 2d plot of the THG signal as function of frequency and temperature. Thus, vertical cuts in this plot, shown in the second column, correspond to varying the frequency for fixed temperature and horizontal cuts, shown in the third column, correspond to varying the temperature for fixed frequency.

The result fulfills our expectation of the previous general analysis. Looking at the 2d plot in the first column, we can see the Higgs mode as a sharp resonance peak which follows the temperature dependence of the gap. However, due to the coupling to the CDW, the energy of the Higgs mode is renormalized and shifted to lower frequencies. This resonance peak is accompanied by a positive phase jump of π as the Higgs mode is a stable mode below the total gap as discussed before. At a slightly higher energy, we observe an antiresonance behavior with a dip in the amplitude and a negative phase jump of π. At higher energy, we observe a second resonance peak at the renormalized CDW phonon frequency with an associated positive phase jump of π. This resonance peak follows the temperature dependence of the CDW gap. Please note, due to the residual broadening, the positive phase change at the Higgs mode and the negative change at the antiresonance is slightly lower than π.

The temperature dependence of both modes is similar and follow roughly a quarter circle as can be

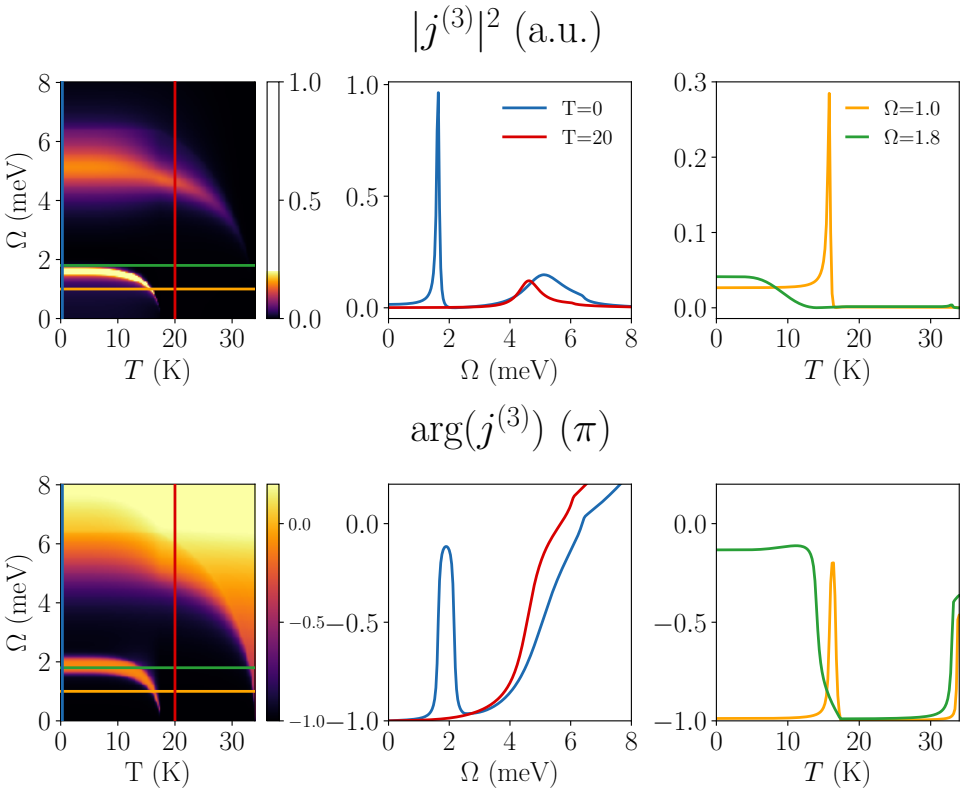

Figure 6.7: Intensity (top row) and phase (bottom row) of THG signal in the coexisting superconducting and CDW state as function of temperature and frequency. The first column shows the full temperature and frequency dependence. The second column shows the frequency dependence for selected temperatures (vertical cuts). The third column shows the temperature dependence for selected frequencies (horizontal cuts).

seen in the left column in Fig. 6.7. Thus, vertical cuts along the frequency and horizontal cuts along the temperature reveal, in principle, the same information. Resonance peaks and phase changes are visible in both signals. Yet, obtaining single cuts at unfavorable positions, e.g., in between the modes, or limited variation range of parameters might miss several features. Experiments with a large variation of temperature and frequency are therefore necessary to reveal the full information.

6.5 Higgs and Bardasis-Schrieffer mode

As a second example, we consider a superconducting system where the ground state is dominated by one symmetry, yet fluctuations in a subleading pairing channel are allowed. These fluctuations are known as Bardasis-Schrieffer modes [18, 151] and might exist for example in iron-based superconductors [99, 100, 135], where multiple pairing instabilities occur on different bands. While most studies investigated the signature of a Bardasis-Schrieffer mode in Raman spectra, recent work has shown that such modes can also be excited with THz light [114]. This mode is schematically shown in Fig. 6.6(b) and will be discussed in the following.

Here, we will consider an s-wave ground state and allow fluctuations in the d-wave channel. We use the

BCS Hamiltonian in Eq. (6.8) with a sum of separable pairing interactions

$$V_{\boldsymbol{k},\boldsymbol{k}'} = V_s f^s_{\boldsymbol{k}} f^s_{\boldsymbol{k}'} + V_d f^d_{\boldsymbol{k}} f^d_{\boldsymbol{k}'} \tag{6.53}$$

with the (anisotropic) s-wave symmetry $f^s_{\boldsymbol{k}} = (\cos k_x + \cos k_y)/2$ and d-wave symmetry $f^d_{\boldsymbol{k}} = (\cos k_x - \cos k_y)/2$. Choosing $\epsilon_{\boldsymbol{k}} = -2t(\cos k_x + \cos k_y) - \mu$ with $t = 6\,\text{meV}$, we solve the gap equations

$$\Delta_i = V_i \sum_{\boldsymbol{k}} f^i_{\boldsymbol{k}} \frac{\Delta_{\boldsymbol{k}}}{2E_{\boldsymbol{k}}} \tag{6.54}$$

with $\Delta_{\boldsymbol{k}} = \sum_i \Delta_i f^i_{\boldsymbol{k}}$ for $i = s, d$ for varying Fermi level μ and symmetry ratio V_d/V_s. This phase diagram is shown in the Appendix in Fig. D.1. In the following, we choose parameters $\mu = -12\,\text{meV}$, $V_d = V_s$ and $\Delta = 2\,\text{meV}$, where the ground state is s-wave but still close to the d-wave transition. The residual broadening is $\omega \to \omega + \text{i}0.05\,\text{meV}$. Please note, for the chosen parameters, i.e. the anisotropic s-wave and the energy dispersion, the maximum of the gap at the Fermi level is $\Delta_{\text{max}} \approx 1\,\text{meV}$, such that the Higgs mode energy is at $\omega_H \approx 2\Delta_{\text{max}}$ and not at $\omega_H = 2\Delta$.

If the system is excited, we allow fluctuations in both symmetry channels

$$\Delta_s(t) = \Delta_s + \delta\Delta_s(t)\,, \tag{6.55a}$$

$$\Delta_d(t) = \text{i}\delta\Delta_d(t)\,. \tag{6.55b}$$

Hereby, $\delta\Delta_s(t)$ corresponds to the usual Higgs mode of the dominant symmetry channel, while $\delta\Delta_d(t)$ are amplitude fluctuations of the subleading channel orthogonal, i.e. in the imaginary axis direction. This is the Bardasis-Schrieffer mode. As shown in [151], subleading fluctuations in the parallel or real channel do not lead to a finite energy mode.

After integrating out the fermions (see Appendix D.5), we obtain the same structure of the effective action as Eq. (6.42) with

$$\phi^T(-\text{i}\omega_m) = \begin{pmatrix} \delta\Delta_s(-\text{i}\omega_m) & \delta\Delta_d(-\text{i}\omega_m) \end{pmatrix}, \tag{6.56a}$$

$$M(\text{i}\omega_m) = \begin{pmatrix} H^{-1}(\text{i}\omega_m) & -\chi_{\Delta B}(\text{i}\omega_m) \\ -\chi_{B\Delta}(\text{i}\omega_m) & B^{-1}(\text{i}\omega_m) \end{pmatrix}, \tag{6.56b}$$

$$b(\text{i}\omega_m) = \sum_{ij} A^2_{ij}(\text{i}\omega_m) \begin{pmatrix} -\chi^{ij}_{\Delta A^2}(\text{i}\omega_m) \\ \chi^{ij}_{BA^2}(\text{i}\omega_m) \end{pmatrix} \tag{6.56c}$$

where $H(\text{i}\omega_m)$ is the usual Higgs propagator and $B(\text{i}\omega_m)$ the Bardasis-Schrieffer propagator defined as

$$B^{-1}(\text{i}\omega_m) = \frac{2}{V_d} + \chi_{BB}(\text{i}\omega_m)\,. \tag{6.57}$$

The susceptibilities are defined as

$$\chi_{BB}(\mathrm{i}\omega_m) = \sum_{\boldsymbol{k}} (f^d_{\boldsymbol{k}})^2 X_{22}(\boldsymbol{k}, \mathrm{i}\omega_m)\,, \tag{6.58a}$$

$$\chi_{\Delta B}(\mathrm{i}\omega_m) = \sum_{\boldsymbol{k}} f^s_{\boldsymbol{k}} f^d_{\boldsymbol{k}} X_{12}(\boldsymbol{k}, \mathrm{i}\omega_m)\,, \tag{6.58b}$$

$$\chi^{ij}_{BA^2}(\mathrm{i}\omega_m) = \sum_{\boldsymbol{k}} \frac{1}{2} f^d_{\boldsymbol{k}} \partial^2_{ij} \epsilon_{\boldsymbol{k}} X_{23}(\boldsymbol{k}, \mathrm{i}\omega_m)\,. \tag{6.58c}$$

with $X_{\alpha\beta}$ defined in Eq. (6.13). In analogy to the previous sections, the fluctuations are integrated out which leads to

$$S^{(4)} = \frac{1}{2}\frac{1}{\beta} \sum_{\mathrm{i}\omega_m} \Big(b^\top(-\mathrm{i}\omega_m) M^{-1}(\mathrm{i}\omega_m) b(\mathrm{i}\omega_m) + \sum_{ijkl} A^2_{ij}(-\mathrm{i}\omega_m) A^2_{kl}(\mathrm{i}\omega_m) \chi^{ijkl}_{A^2A^2}(\mathrm{i}\omega_m) \Big) \tag{6.59}$$

with

$$M^{-1} = \begin{pmatrix} \tilde{H} & \chi_{\Delta B}\tilde{H}B \\ \chi_{B\Delta}\tilde{H}B & \tilde{B} \end{pmatrix} \tag{6.60}$$

and the renormalized propagators

$$\tilde{H} = \frac{1}{H^{-1} - \chi_{\Delta B}\chi_{B\Delta} B}\,, \tag{6.61a}$$

$$\tilde{B} = \frac{1}{B^{-1} - \chi_{\Delta B}\chi_{B\Delta} H}\,. \tag{6.61b}$$

For monochromatic, linear polarized light with polarization angle θ, the THG current parallel to the light polarization is given by (see Appendix D.5)

$$j^{(3)}_{\parallel} \propto (\cos^4\theta + \sin^4\theta) K_{xx}(2\Omega) + 2\sin^2\theta\cos^2\theta K_{xy}(2\Omega) \tag{6.62}$$

with the kernel $K^{(4)}_{ij} = \chi_H + \chi_B + \chi_M + \chi_Q$ and the susceptibilities for the Higgs (H), Bardasis-Schrieffer (B), mixed (M) and quasiparticle (Q) contribution

$$\chi_H = \chi^{ii}_{\Delta A^2}(-\omega)\chi^{jj}_{\Delta A^2}(\omega)\tilde{H}(\omega)\,, \tag{6.63a}$$

$$\chi_B = \chi^{ii}_{BA^2}(-\omega)\chi^{jj}_{BA^2}(\omega)\tilde{B}(\omega)\,, \tag{6.63b}$$

$$\chi_M = -\tilde{H}(\omega)B(\omega)\Big[\chi^{ii}_{A^2\Delta}(\omega)\chi_{\Delta B}(\omega)\chi^{jj}_{BA^2}(\omega) + \chi^{ii}_{A^2B}(\omega)\chi_{B\Delta}(\omega)\chi^{jj}_{\Delta A^2}(\omega)\Big]\,, \tag{6.63c}$$

$$\chi_Q = \chi^{iijj}_{A^2A^2}(\omega)\,. \tag{6.63d}$$

The response has again the same structure of coupled modes as discussed before.

To get a first insight into the Bardasis-Schrieffer mode, we evaluate the expression for the propagator analytically for $T = 0$ and assuming a constant normal state density of states at the Fermi level. One obtains

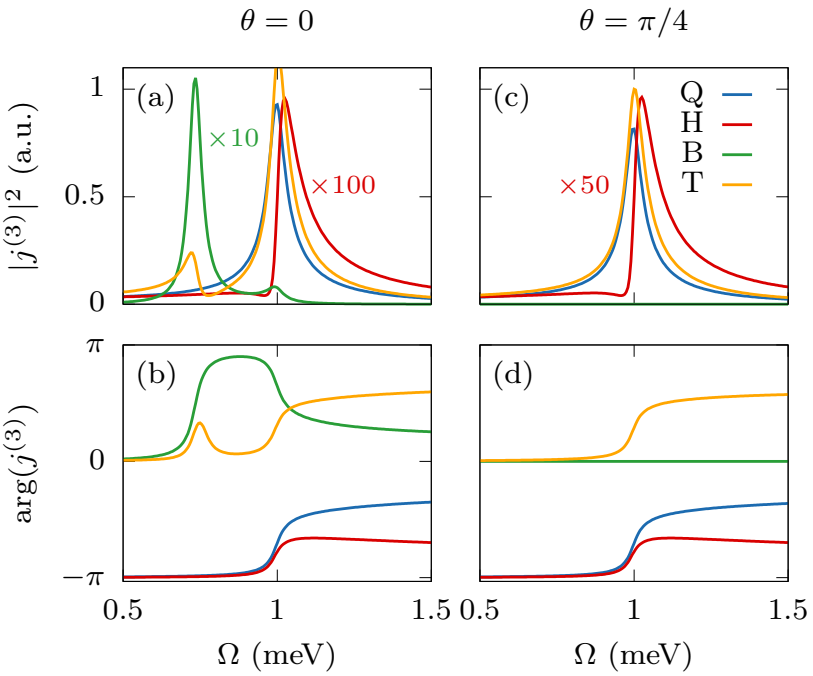

Figure 6.8: THG intensity (top row) and phase (bottom row) for Higgs and Bardasis-Schrieffer mode system for two light polarizations, with respect to the crystal axis, $\theta = 0$ (left column) and $\theta = \pi/4$ (right column). The individual contributions are shown separately as quasiparticles (Q), Higgs (H), Bardasis-Schrieffer mode (B), and total response (T). The Higgs and Bardasis-Schrieffer modes are scaled to be visible.

for continuum implementation with density of states λ at the Fermi surface (see Appendix D.5)

$$B(\omega) = \frac{\sqrt{4\Delta^2 - \omega^2}}{\left(\frac{2}{V_d} - \frac{2}{V_s}\right)\sqrt{4\Delta^2 - \omega^2} - 2\omega\lambda \sin^{-1}\left(\frac{\omega}{2\Delta}\right)}\,. \tag{6.64}$$

Using these simplification, one can see that for $V_d \to V_s$ the pole of the propagator shifts to zero, while for $V_d \to 0$ the pole approaches 2Δ. Furthermore, due to the $\sqrt{4\Delta^2 - \omega^2}$ term in the numerator, the expression is always zero at $\omega = 2\Delta$, which leads to a negative phase change of $\pi/2$. Thus, we expect a positive phase change of π at the Bardasis-Schrieffer mode energy below 2Δ and a negative phase change of $\pi/2$ at 2Δ.

As the coupling term $\chi_{\Delta B}$ contains the product of the two symmetry functions $f^s_{\boldsymbol{k}} f^d_{\boldsymbol{k}}$, which are orthogonal, the term vanishes, and the Higgs and Bardasis-Schrieffer modes are not coupled but contribute individually to the response. However, for strong pulses beyond the Gaussian level, as used in pump-probe experiments, a finite coupling between Higgs and Bardasis-Schrieffer mode can exist [114]. In addition, due to the symmetry function $f^d_{\boldsymbol{k}}$ in $\chi^{ij}_{BA^2}$, the coupling strength of light to the Bardasis-Schrieffer mode will depend on the polarization. For our band structure, $\theta = \pi/4$ will correspond to the A_{1g} symmetry, such that we expect the d-wave (B_{1g}) Bardasis-Schrieffer mode to vanish. This polarization sensitivity has also been discussed in [114].

Next, we evaluate the THG response at $T = 0$ numerically for two different polarization angles $\theta =$

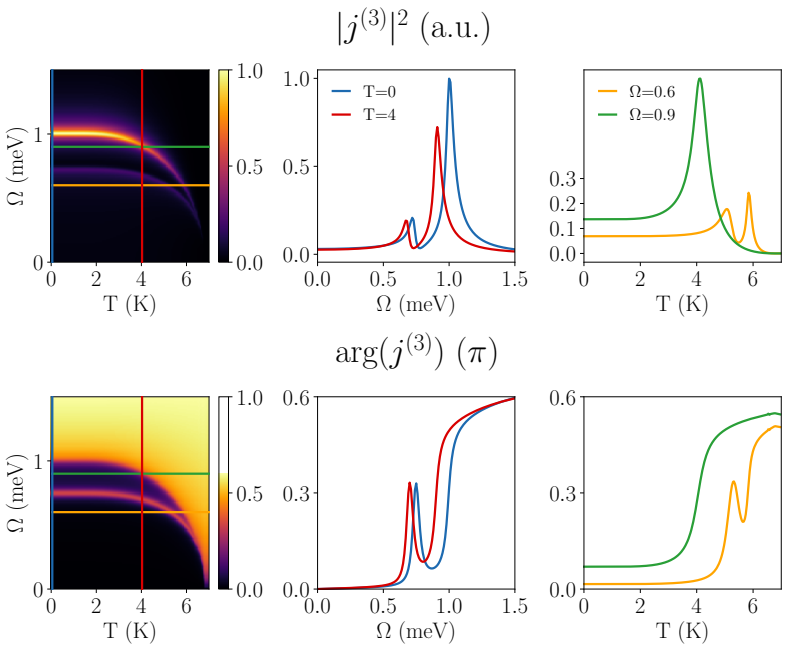

Figure 6.9: Intensity (top row) and phase (bottom row) of total THG signal for Higgs and Bardasis-Schrieffer mode scenario as function of temperature and frequency with a polarization angle $\theta = 0$ analogous to Fig. 6.8(a,b). The first column shows the full temperature and frequency dependence. The second column shows the frequency dependence for selected temperatures (vertical cuts). The third column shows the temperature dependence for selected frequencies (horizontal cuts).

$0, \pi/4$ and show the individual contributions in Fig. 6.8. As we have anticipated, there is no coupling between Higgs and Bardasis-Schrieffer mode and the mixed contribution is zero (not shown). Thus, the quasiparticle (blue curve) and Higgs (red curve) response is the same as in the pure system discussed in Sec. 6.2.3. The Higgs contribution is polarization independent, while the quasiparticle contribution gets reduced for $\theta = \pi/4$. The Bardasis-Schrieffer (green curve) mode has a strong polarization dependence. For $\theta = 0$, the expected phase behavior originating from the Bardasis-Schrieffer propagator $B(\omega)$ is visible. At the resonance energy a positive π phase change occurs and at the energy of the Higgs mode a negative $\pi/2$ phase change occurs. The intensity shows a strong peak at the Bardasis-Schrieffer resonance. The small peak at the Higgs mode energy is a result of the susceptibility χ_{BA^2}. For $\theta = \pi/4$, the Bardasis-Schrieffer mode is not excited.

Having no coupling between the modes, the resulting phase signature is influenced only by the interference of the pure, individual contributions. The total THG signal (yellow curve) consists of two resonance peaks at the original, unrenormalized frequencies each accompanied by a positive phase change. In between we see an antiresonance behavior with a dip in the intensity and a negative phase change.

In analogy to the previous section, we also calculate the frequency and temperature dependence of the total THG signal. The result is shown in Fig. 6.9. As before, the temperature dependence follows roughly a quarter circle (left column). Thus, both vertical and horizontal cuts along the frequency or temperature axis show a similar result and the resonance and antiresonance behavior is visible in both cases.

6.6 Conclusion

In this chapter, we have investigated the phase signatures of the third-harmonic (TH) signal generated by driving superconductors with THz light. Hereby, the phase of the oscillatory TH signal is measured with respect to the phase of the first-harmonic. While it is well known that resonances in the intensity of the signal occur if the driving frequency matches with the energy of intrinsic modes, here we have shown that the phase change is a robust feature as well and additionally encodes intrinsic properties of the system.

From a classical point of view, the resonance peak of a driven oscillator is accompanied by a positive phase change of π. This phase signature is more robust against damping than the peak itself, as it is still observable even if the peak is heavily suppressed. Coupled modes lead to antiresonance behavior where the interference of driving force and coupling leads to a dip in the oscillation amplitude and a negative phase change of π. Usually, the antiresonance is understood as a feature of a single oscillator which is externally driven and coupled to an undriven second oscillator. Yet, for oscillators which are both driven but uncoupled a similar feature also occurs in the superposition of the oscillation amplitudes as a destructive interference of two oscillations.

In a microscopic BCS model for superconductors, the amplitude (Higgs) mode can be driven by a nonlinear, quadratic process such that the effective driving frequency is doubled which leads to an induced third-harmonic current. This driving of the Higgs mode is similar to a classical oscillator, yet the microscopic details lead to a modification of the phase signature.

First of all, as the energy of the Higgs mode coincidences with the quasiparticle excitation energy at the gap 2Δ it is intrinsically damped. This leads to a propagator with a square root pole structure such that the phase change across the pole is reduced to $\pi/2$. Secondly, in the microscopic theory, frequency-dependent susceptibility terms occur which govern the coupling of light to the condensate. These terms are missing in the classical theory and can, in principle, modify the phase signature of the observed signal. In the clean limit, the influence of the diamagnetic coupling terms is negligible as they only contribute a small drift above 2Δ such that the total phase response is dominated solely by the propagator. Yet, in the dirty limit, the paramagnetic coupling terms modify the phase signature strongly and approximately restore the π phase change. Finally, in addition to the Higgs mode response, quasiparticles contribute to the TH signal as well which also show a $\pi/2$ phase signature.

Considering long-ranged Coulomb interaction, the TH response of Higgs and quasiparticles is renormalized. Yet, one finds that these modifications do not change the phase signature. Thus, in a BCS superconductor one can expect a $\pi/2$ phase change in the clean limit and a π phase change in the dirty limit at the resonance frequency.

If in addition to the Higgs mode other modes exist, the coupled mode scenario with the antiresonance behavior is applicable. Yet, again, microscopic details may modify the classical analysis. To get some insight, we investigate two specific scenarios: A coupling of the Higgs mode to a charge density wave (CDW) and a superconducting system which additionally hosts a Bardasis-Schrieffer mode, an amplitude fluctuation of a subleading pairing channel.

In the superconductor-CDW scenario, the propagator of the Higgs mode itself is modified as the energy of the Higgs mode no longer overlaps with the total energy gap of the system which consists of the super-

conducting and CDW gap. Therefore, the propagator obtains a proper pole, and the Higgs mode becomes stable. This restores the usual π phase change at the Higgs mode energy. In this system, both modes are driven by light and additionally couple to each other such that an antiresonance effect is expected both from the usual scenario but also due to the interference of the individual contributions. The structure of the analytically evaluated response exactly corresponds to the classic coupled oscillator system. An evaluation of the response as function of frequency and temperature shows the antiresonance behavior and thus, acts as fingerprint of the existence of two modes.

The second scenario with the Bardasis-Schrieffer mode serves as an example of two uncoupled modes. As the Bardasis-Schrieffer mode is a fluctuation of a subleading pairing channel orthogonal to the dominant pairing channel, the coupling element vanishes. Nevertheless, the superposition of the individual contributions leads to an antiresonance behavior where a dip in the intensity and a negative phase change occurs.

The considered scenarios are of course not exhaustive but serve as a proof-of-principle how a careful examination of the THG signal phase gives insight about the existence and nature of collective modes. Furthermore, these scenarios may be applicable in real systems. The superconductor-CDW scenario is relevant for example for $NbSe_2$, where superconductivity and CDW coexists [31, 107] but might also be relevant for cuprates, where an antiresonance behavior was observed in recent THG experiments [37]. On the other hand, Bardasis-Schrieffer modes might exist in iron-based superconductors. As our study shows, this coupled mode scenario in a microscopic theory is as generally applicable as in the classic theory. Thus, we expect that it can describe any other collective mode including Leggett modes in multiband systems [116], Josephson-Plasma modes in layered systems [51], Carlson-Goldman modes close to the transition temperature [13, 30, 137] or generally phonon and magnon excitations in the THz regime.

One issue one should investigate in more detail in future, is the influence of impurities in the coupled modes scenario. We generally expect that impurities will not modify the antiresonance behavior, i.e., the negative phase change, as this seems to be an universal feature independent of the exact properties of the involved modes. As the paramagnetic coupling terms may modify the usual, positive phase change of the individual modes, a quantitative change might be expected. One feature we expect to change is the polarization dependence. It was shown in previous studies [142, 147, 157] that the polarization dependence of the Higgs mode and quasiparticles is changed by varying the impurity strength. However, as this effect is model dependent, one cannot make a general prediction for different modes. A detailed calculation in this matter is beyond the scope of this chapter.

So far, THG experiments on superconductors have only been performed in a setup where the temperature was varied to reach the resonance condition [37, 86, 104]. As our calculation shows, the resonance and antiresonance signature of the coupled modes is also visible in this case. Yet, to obtain a full picture, it would be necessary to obtain full temperature and frequency data to map out the temperature and frequency dependence of the modes. A further experimental difficulty in this case is the extraction of the phase from the measured signal. As the screening of the THz light is temperature dependent, the first-harmonic signal might be shifted such that a comparison of the relative TH phase could be unreliable. While the phase change is generally more robust than resonance peaks as a signature, strong damping may decrease or wash out the antiresonance behavior, especially if a resonance and antiresonance are positioned close to each

other.

To conclude, we have shown that the phase of the THG signal is an interesting quantity to study as it serves as a signature of microscopic details and coupled modes in superconductors. It is a further step in the new field of Higgs spectroscopy and extracting phase information in future experiments will help to reveal more details of the investigated systems.

Chapter 7

Incoherent tunneling and topological superconductivity in twisted cuprate bilayers

In the previous chapter, we studied the phase response of the THG signal in a generic model with multiple collective modes. In the present chapter, we will shift our focus to a specific material system with two order parameters: twisted bilayers of cuprate superconductors that spontaneously break time reversal symmetry. In the first part of this chapter we will examine the effect of impurities on the phase diagram of the cuprate bilayers. In the second part of this chapter we will study the general properties of the collective mode spectrum in the absence of impurities, without reference to a specific experimental techniques.

Twisting two monolayers of a high-T_c cuprate superconductor can engender a chiral topological state with spontaneously broken time reversal symmetry $\mathcal{T}$. A crucial ingredient required for the emergence of a gapped topological phase is electron tunneling between the CuO_2 planes, whose explicit form (in an ideal sample) is dictated by the symmetry of the atomic orbitals. However, a large body of work on interlayer transport in cuprates indicates the importance of disorder-mediated incoherent tunneling which evades symmetry constraints present in an idealized crystal. This arises even in the cleanest single-crystal samples through oxygen vacancies, in layers separating the CuO_2 planes, introduced to achieve the hole doping necessary for superconductivity. Here we assess the influence of incoherent tunneling on the phase diagram of a twisted bilayer and show that the model continues to support a fully gapped topological phase with broken $\mathcal{T}$. Compared to the model with a constant, momentum conserving interlayer coupling, the extent of the topological phase around the 45° twist decreases with increasing incoherence, but remains robustly present for parameters likely relevant to $Bi_2Sr_2CaCu_2O_{8+\delta}$.

7.1 Introduction

Twisted 2D van der Waals materials have emerged as an elegant platform to engineer and study correlated quantum phases with unprecedented experimental control [11, 15, 29, 118, 133, 169]. At certain *magic* angles, the electronic structure of graphene is deformed into exceedingly narrow bands in a moiré Brillouin

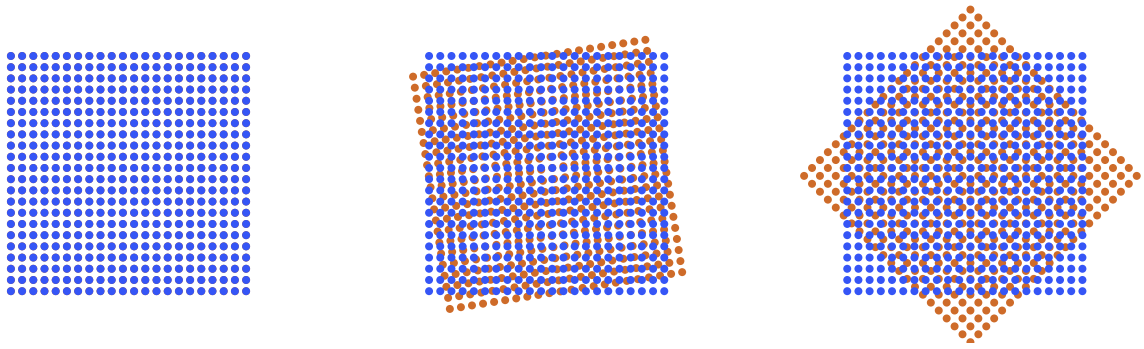

Figure 7.1: Illustration of twisted cuprate bilayers.

zone. The small bandwidth yields pronounced correlation effects and generally makes multiple quantum phases experimentally accessible in a single fabricated device through application of electrostatic gating [29].

Recently, a related paradigm of twisted bilayer structures was introduced that does not rely on engineering of correlated flat bands but can produce interesting new phases by combining known non-trivial properties of constituent monolayers [28, 165]. It was shown that two cuprate monolayers, stacked at a twist angle θ, can give rise to a spontaneously time-reversal symmetry broken state by virtue of simple electron tunneling between the layers. Most notably, in a finite range of angles around the critical twist $\theta_c = 45^\circ$, the ground state of an otherwise nodal d-wave superconductor becomes fully gapped and acquires a finite Chern number. At exactly 45° the gapped phase persists up to the native critical temperature of the cuprate monolayer, thus furnishing the first known proposal of a high-T_c topological superconductor.

The angle of 45° may be viewed as a *magic angle* for twisted bilayer cuprates. It is, however, important to stress the differences between the magic angles in bilayer graphene and bilayer cuprates. While in twisted bilayer graphene, electronic bands are flattened at the magic angle due to interlayer coupling, in twisted cuprates the magic angle marks a change in crystal symmetry resulting from the twisting of the layers, highlighting the distinct and separate nature of these two phenomena.

Pioneering experimental work on very thin twisted $Bi_2Sr_2CaCu_2O_{8+\delta}$ (BSCCO) flakes succeeded in fabricating bilayers at various twist angles [181]. Measurements of the interlayer Josephson current, Fraunhofer interference patterns and half-integer Shapiro steps in samples close to the 45° are suggestive of a $\mathcal{T}$-broken phase [158]. Strong twist angle dependence of the critical current has been reported elsewhere [90].

It was later noted by Song, Zhang and Vishwanath [148] that twist angle and momentum dependence of the interlayer tunneling matrix element $g_{\boldsymbol{k}}$, arising from the symmetry of the copper active orbitals, can play an important role in the emergence of the $\mathcal{T}$-broken phase. As argued in Refs. [5, 173], the matrix element has the form

$$g_{\boldsymbol{k}} = g_0 \cos 2\theta + g_1 \mu_{\boldsymbol{k}}(\theta/2)\mu_{\boldsymbol{k}}(-\theta/2), \tag{7.1}$$

which we generalized here to a twisted bilayer geometry following [148]. The g_0 term represents the direct

tunneling between copper $d_{x^2-y^2}$ orbitals while the g_1 term describes the 'oxygen-assisted' tunneling process with form factor $\mu_{\boldsymbol{k}}(\theta) = [\cos(R_\theta k_x) - \cos(R_\theta k_y)]/2$, where R_θ is the rotation matrix. Crucially, the part of $g_{\boldsymbol{k}}$ that remains non-vanishing at $\theta = 45^\circ$ contains the form factor $\mu_{\boldsymbol{k}}$ that suppresses tunneling at the nodes of the d-wave order parameter. While spontaneous $\mathcal{T}$-breaking is still found to occur in this case, the ground state remains gapless and hence does not support the gapped topological phase with non-zero Chern number predicted in Ref. [28].

In the present chapter we consider the twisted bilayer problem within a family of incoherent tunneling models [56, 130–132, 159] in which the transfer of electrons between two adjacent CuO_2 layers is mediated by impurities that are inherently present in the otherwise inert 'spacer' layers. Such incoherent tunneling models have been shown to yield better agreement with experimentally measured c-axis transport properties of nominally clean single-crystal cuprates than models where momentum is strictly conserved [39, 144]. Because random impurities break all spatial symmetries of the system, the form of the interlayer coupling is required to respect the crystal symmetry constraints only on average. One may thus expect that incoherent tunneling models will evade the difficulties noted above and produce a fully gapped topological phase near $\theta = 45^\circ$.

Based on a perturbative diagrammatic treatment within a simplified continuum model we show that the incoherent tunneling model indeed delivers the same phenomenology as the coherent model of Ref. [28] while respecting the point group symmetries of the physical system on average. Importantly, we show that for sufficiently slowly varying disorder the ground state near $\theta = 45^\circ$ is gapped, $\mathcal{T}$-breaking and topologically non-trivial. These results are then confirmed in a more realistic setting through a full numerical diagonalization of a lattice model with parameters chosen to reproduce the actual cuprate band structure in the vicinity of the Fermi level. The effect of interface inhomogeneity on Josephson effects in twisted bilayers was recently considered in Ref. [165] where it was found that sufficiently strong disorder can leave the system in a topologically trivial state around 45°. This is consistent with our model.

7.2 Group theoretical discussion of $\mathcal{T}$-breaking in twisted cuprates

The phenomenology of $\mathcal{T}$-breaking in twisted cuprates can be captured by a two-component Landau-Ginzburg theory with complex order parameters ψ_1, ψ_2 given by

$$\begin{aligned}\mathcal{F} = {} & \alpha\left(|\psi_1|^2 + |\psi_2|^2\right) + \beta_1\left(|\psi_1|^4 + |\psi_2|^4\right) \\ & + \gamma\left(\psi_1^*\psi_2 + \psi_2^*\psi_1\right) + \beta_2|\psi_1|^2|\psi_2|^2 + \beta_3\left((\psi_1^*)^2\psi_2^2 + (\psi_2^*)^2\psi_1^2\right) . \end{aligned} \tag{7.2}$$

Writing $\psi_1 = |\psi_1|e^{i(\theta+\varphi/2)}$, $\psi_2 = |\psi_2|e^{i(\theta-\varphi/2)}$ the φ-dependent part of free energy is

$$\mathcal{F}(\varphi) = -\gamma\,|\psi_1\psi_2|\cos\varphi + \beta_3\,|\psi_1\psi_2|^2\cos 2\varphi + \textit{const}\,. \tag{7.3}$$

Time reversal symmetry will be spontaneously broken whenever the free energy develops two minima that are related by $\mathcal{T}: \varphi \to -\varphi$. The Josephson coupling term, proportional to $\cos\varphi$, has only a single minimum at $\varphi = 0$ or π, depending on the sign of γ. Presence of the fourth order term proportional to $\beta_3\cos 2\varphi$ is,

therefore, necessary to break $\mathcal{T}$. Additionally, one must have $\beta_3 > 0$, since otherwise the two minima of $\beta_3 \cos 2\varphi$ occur at $\varphi = 0, \pi$ which map to themselves under $\mathcal{T}$. In Ref. [28] it was argued that β_3 is indeed positive based on microscopic mean-field calculations. We confirm that β_3 remains positive in the case of incoherent interlayer coupling in Sec. 7.3.2.

Given $\beta_3 > 0$, the fourth order term is minimized at $\varphi = \pm\pi/2$. Then, $\mathcal{T}$-breaking occurs as a consequence of the competition among the two terms in Eq. (7.3). Specifically, $\mathcal{T}$ will be broken when

$$4\beta_3 |\psi_1 \psi_2| > |\gamma| \ . \tag{7.4}$$

A special situation clearly arises if symmetry requires γ to vanish; then Eq. (7.4) is guaranteed to be satisfied for any $\beta_3 > 0$.

Next, we describe a set of symmetry requirements under which the coefficient γ vanishes, and the system is forced into the $\mathcal{T}$-broken phase. The order parameters ψ_1, ψ_2 transform according to irreducible representations (irreps) of the point group of the crystal. Two cases must be distinguished: (a) ψ_1 and ψ_2 transform under two *different* 1D irreps or (b) (ψ_1, ψ_2) transform under a 2D irrep [12, 127]. The latter case is considered a generic pathway to $\mathcal{T}$-breaking that occurs immediately upon entering the SC phase. The former case generically yields two successive phase transitions with distinct critical temperatures, T_c and T_c', with $\mathcal{T}$-breaking setting at the lower one T_c'. Note that T_c' can be zero or negative, in which case the $\mathcal{T}$-broken phase is physically not accessible [12, 76]

The point symmetries of an untwisted cuprate bilayer form the point group D_{4h}. Here, the $d_{x^2-y^2}$ and d_{xy} order parameters transform according to the 1D irreps B_{1g} and B_{2g}, respectively. At arbitrary twist angle, inversion and mirror symmetries are broken and the point group reduces to D_4 with d-wave irreps B_1 and B_2. Thus, given the d-wave nature of the order parameter in cuprates, only pathway (b) to $\mathcal{T}$-breaking is possible and no definite symmetry-based arguments can be made.

Precisely at 45°, however, the symmetry group is enlarged to the non-crystallographic point group D_{4d} which contains an additional 8-fold improper rotation S_8 of the quasicrystalline lattice. Most notably, among the irreps of D_{4d} *only* the 2D E_2-irrep supports d-wave order. Thus, the Josephson coupling term $-B\,|\psi_1\psi_2| \cos\varphi$ must necessarily be absent at 45°. This is because it descends from the $-B(\psi_1\psi_2^* + \text{c.c.})/2$ term in the free energy which is not invariant under $S_8 : (\psi_1, \psi_2) \to (\psi_2, -\psi_1)$. Thus, $\mathcal{T}$-breaking can be viewed as a fundamental consequence of the point group at $\theta = 45^\circ$.

We summarize our key arguments as follows: Two-component order parameters that transform under a 2D irrep naturally break $\mathcal{T}$. At 45° twist angle, because the point group of the bilayer is D_{4d}, any d-wave order parameter must necessarily transform under a 2D irrep. Therefore, the superconducting state breaks $\mathcal{T}$ right below T_c.

The phase diagram of twisted bilayer cuprates derived in Ref. [28] can then be understood from continuity arguments. It is expected that the $\mathcal{T}$-breaking phase will not be limited to the exact 45°-twist but will extend to a range of twist angles in its vicinity. Since at twists slightly away from 45° the order parameters transform under two 1D-irreps, two distinct critical temperatures are permitted and $\mathcal{T}$-breaking will no longer coincide with the critical temperature T_c of the spontaneous $U(1)$-symmetry breaking. This naturally leads to the wedge-shaped $\mathcal{T}$-broken domain in the phase diagram explicitly computed in Ref. [158]. Our

symmetry arguments will be manifest in a microscopic description of the bilayer system.

7.2.1 Transition splitting for orthorhombic symmetry

Many cuprate superconductors undergo a phase transition from the tetragonal lattice structure with point group D_{4h} to an orthorhombic unit cell of reduced symmetry D_{2h} as a function of temperature or stoichiometry [12].

The point group of twisted bilayers is D_2 for all twist angles in the orthorhombic case. At 45°, the transition from D_{4d} in the tetragonal case to D_2 in the case of orthorhombic layers implies splitting of the two-dimensional irrep into

$$E_2 \to A \oplus B_1 \,. \tag{7.5}$$

Thus, the two superconducting gaps transform under two one-dimensional irreps and each have their individual critical temperatures T_{c1}, T_{c2}. We assume now, without loss of generality, that $T_{c1} > T_{c2}$. Then, T_{c1} is expected to approximately match T_c of monolayer cuprates. Topological superconductivity requires condensation of two order parameters and will only set in upon cooling the sample below T_{c2}. Orthorhombic deformation hence precludes a topological $\mathcal{T}$-broken phase all the way up to T_c. From continuity arguments one may nevertheless expect the critical point T_{c2} of the topological phase transition to be close to T_c.

7.3 Incoherent tunneling

7.3.1 Background and model definition

Experimental measurements of the c-axis transport in bulk crystals of BSCCO and other cuprates, summarized for example in Ref. [39], have been interpreted as evidence of interlayer tunneling dominated by disorder-mediated, incoherent processes. The c-axis superfluid stiffness, accessible through the measurement of the c-axis London penetration depth [69, 122], provides particularly clear evidence. Experimentally, the temperature dependence of the c-axis superfluid stiffness in clean single crystals was observed to follow an approximate power-law behavior $\rho_c = a - bT^\alpha$ with $\alpha \simeq 2$ at low temperatures, whereas the in-plane stiffness showed a T-linear dependence [62]. The latter is the canonical behavior expected of a clean d-wave superconductor, reflecting the presence of low-energy excitations with a Dirac spectrum [67]. Models with coherent tunneling between CuO_2 predict the same linear T-dependence for the c-axis stiffness [83], in clear disagreement with experimental data. If the interlayer tunneling were dominated by the oxygen-assisted processes (the g_1 term in Eq. (7.1)) then theory predicts $\rho_c = a - bT^5$ [173], again at variance with experiment.

As demonstrated in Refs. [130–132, 144] a description that captures the correct $\sim T^2$ scaling along the c-axis (while preserving the T-linear behavior in the ab plane) can be given using the incoherent c-axis tunneling approach. In the following we shall review the relevant model and then apply it to the problem of a twisted bilayer.

A minimal model of the uncoupled bilayer system consists of the second-quantized Hamiltonian

$$\mathcal{H}_0 = \sum_{\mathbf{k}l} \psi^\dagger_{\mathbf{k}l} H_{\mathbf{k}l} \psi_{\mathbf{k}l} \tag{7.6}$$

where $l = 1, 2$ denotes the layer index, Nambu-Gorkov spinors $\psi_{\mathbf{k}l} = (c_{\mathbf{k}l\uparrow},\, c_{-\mathbf{k}l\downarrow})^T$. In the BCS approximation, we have

$$H_{\mathbf{k}l} = \xi_{\mathbf{k}}\sigma_z + \Delta'_{\mathbf{k}l}\sigma_x - \Delta''_{\mathbf{k}l}\sigma_y, \tag{7.7}$$

with Pauli matrices σ_j acting in the Nambu space and $\Delta'_{\mathbf{k}l}$, $\Delta''_{\mathbf{k}l}$ denoting real and imaginary parts of the superconducting gap function. We adopt units such that $\hbar = e = k_B = m_e = a_0 = 1$, where mass is measured in units of electron mass m_e and length scales in units of lattice constant a_0. To make the model tractable we assume a simple parabolic band dispersion given by $\xi_{\mathbf{k}} = \mathbf{k}^2/2m - \mu$ in each layer. (In Sec. 7.4 we consider a more realistic band structure and show that it leads to similar results.) The two superconducting d-wave order parameters are

$$\begin{aligned} \Delta_{\mathbf{k}1} &= \Delta e^{i\varphi/2}\cos(2\alpha_{\mathbf{k}} - \theta) \\ \Delta_{\mathbf{k}2} &= \Delta e^{-i\varphi/2}\cos(2\alpha_{\mathbf{k}} + \theta)\,, \end{aligned} \tag{7.8}$$

where φ is the phase difference and $\alpha_{\mathbf{k}}$ denotes the polar angle of $\mathbf{k}$.

The layers are coupled by an additional term

$$\mathcal{H}' = \sum_{\mathbf{kq}} \gamma_{\mathbf{q}} c^\dagger_{\mathbf{k},1} c_{\mathbf{k}-\mathbf{q},2} + \text{h.c.} \tag{7.9}$$

and $\mathcal{H} = \mathcal{H}_0 + \mathcal{H}'$ constitutes the full model. The lack of momentum conservation in Eq. (7.9) is the defining feature of the incoherent tunneling models and originates, physically, from the disorder present in the spacer layers separating the copper-oxygen planes. The disorder is captured via a set of Gaussian-distributed random variables $\gamma_{\mathbf{q}}$ of average $\overline{\gamma_{\mathbf{q}}} = 0$ and variance given by

$$\overline{\gamma^*_{\mathbf{q}}\gamma_{\mathbf{q}+\mathbf{p}}} = \frac{1}{N}\frac{4\pi g^2}{3\Lambda^2}\delta_{\mathbf{p},0} e^{-\mathbf{q}^2/\Lambda^2}\,. \tag{7.10}$$

The scale Λ defines the characteristic momentum change that an electron undergoes when tunneling between the two layers. The factor $1/3$ is chosen to reproduce the phase diagram of the coherent model of Ref. [28] in the limit $\Lambda \to 0$ for the same value of g. For simplicity we have neglected any θ-dependence of the interlayer coupling although we expect the randomness to be stronger in twisted samples due to the increase in interface roughness, added strain, and moiré lattice modulations.

The above form of incoherent interlayer tunneling is consistent with all lattice symmetries because $\gamma_{\mathbf{q}}$ vanishes on average. This constitutes the key difference to a coherent coupling of the form $\sum_{\mathbf{k}}(g\, c^\dagger_{\mathbf{k},1} c_{\mathbf{k},2} + \text{h.c.})$. As was pointed out in Ref. [148], at 45° twist the two participating Cu d-orbitals transform under a 2D representation of D_{4d} and a coherent tunneling term is therefore not invariant under $S_8 : (c_{\mathbf{k},1}, c_{\mathbf{k},2}) \to$

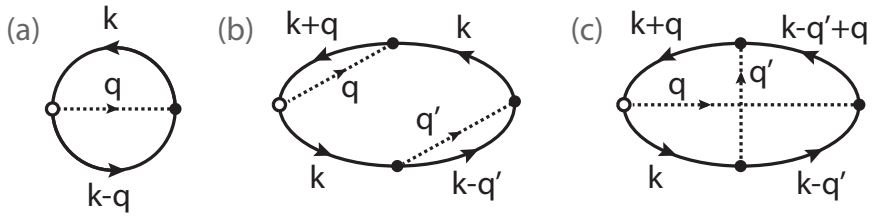

Figure 7.2: Diagrammatic expansion of the interlayer current (a) at order g^2 and (b-c) at order g^4. Full lines correspond to electronic propagators G and dashed lines correspond to impurity vertices paired by disorder average. The open circle denotes the current vertex $j_{\mathbf{q}}$ defined in the main text and impurity vertices $\gamma_{\mathbf{q}}$ are given by black dots.

$(c_{\mathbf{k},2}, -c_{\mathbf{k},1})$. It thus vanishes by virtue of the same argument as the Josephson coupling in Eq. (7.4). This is indeed owed to the coincidence of the atomic Cu orbitals transforming under the same representation as the superconducting order parameters.

It is instructive to consider the limit $\Lambda \to 0$ of the incoherent tunneling in Eq. 7.10. Here, one has $\overline{\gamma^*_{\mathbf{q}}\gamma_{\mathbf{q}+\mathbf{p}}} = g^2\delta_{\mathbf{q},0}\delta_{\mathbf{p},0}/3$ and momentum is conserved in the interlayer tunneling process. Yet, $\Lambda \to 0$ is not the clean limit in the sense that, in real space, it corresponds to the case where macroscopic regions are correlated with the same random value of interlayer tunneling $g/\sqrt{3}$. From the viewpoint of disorder-induced incoherence, the random values of g should only be correlated in the vicinity of an impurity which sets the appropriate scale for $1/\Lambda$. In the discussion below, the $\Lambda \to 0$ thus serves as an abstract but convenient reference point that connects the present model to the calculations in the original work [28]. We will refer to it as the *coherent* limit.

7.3.2 Free energy and phase diagram

The physics of $\mathcal{T}$-breaking is captured by the φ-dependence of the free energy. To determine the free energy we begin by implementing the global gauge transformation $(c_{\mathbf{k}1},\, c_{\mathbf{k}2}) \to \left(c_{\mathbf{k}1}e^{i\varphi/4},\, c_{\mathbf{k}2}e^{-i\varphi/4}\right)$ which moves the superconducting phase difference from the order parameters in Eq. (7.8) to $\mathcal{H}'$ according to

$$\mathcal{H}' \to \mathcal{H}' = \sum_{\mathbf{kq}} \gamma_{\mathbf{q}} e^{i\varphi/2} c^\dagger_{\mathbf{k},1} c_{\mathbf{k}-\mathbf{q},2} + \text{h.c.}\,. \tag{7.11}$$

In this gauge, the disorder-averaged interlayer current is given by

$$J = \sum_{\mathbf{kq}} ie^{i\varphi/2}\overline{\gamma_{\mathbf{q}}\langle c^\dagger_{\mathbf{k},1} c_{\mathbf{k}-\mathbf{q},2}\rangle} + \text{h.c.} = \text{Tr}\left[\overline{j_{\mathbf{q}} G(\mathbf{k}, \mathbf{k}-\mathbf{q}, \omega_n)}\right]\,,$$

where $G(\mathbf{k}, \mathbf{k}', \tau) = \langle T_\tau c_{\mathbf{k}}(\tau) c^\dagger_{\mathbf{k}'}(0)\rangle$ is the full imaginary time ordered Green's function of the disordered system and the current vertex is

$$j_{\mathbf{q}} = i\gamma_{\mathbf{q}} \begin{pmatrix} 0 & e^{i\sigma_z\varphi/2} \\ -e^{-i\sigma_z\varphi/2} & 0 \end{pmatrix}\,. \tag{7.12}$$

Note that the trace is to be performed over all momenta $\mathbf{k}$, $\mathbf{q}$ and Matsubara frequencies $\omega_n = (2n+1)\pi/\beta$, in addition to interlayer and Nambu indices.

From the Josephson relation $J(\varphi) = 2\partial\mathcal{F}(\varphi)/\partial\varphi$ one then obtains the functional dependence of the free energy on the interlayer phase difference φ by simple integration. We expand Eq. (7.12) up to fourth order in g while treating $\mathcal{H}'$ as a perturbation. Three different terms arise, which are diagrammatically represented in Fig. 7.2. Panel (a) corresponds to the term

$$J_c^{(2)} = \mathrm{Tr}\left[\overline{j_{\mathbf{q}} G_0(\mathbf{k}-\mathbf{q},\omega_n) u_{-\mathbf{q}} G_0(\mathbf{k},\omega_n)}\right] \tag{7.13}$$

which is quadratic in g. Here, $G_0(\mathbf{k},\omega_n) = (i\omega_n - H_{\mathbf{k}})^{-1}$ is the unperturbed, translationally invariant Green's function with $H_{\mathbf{k}} = \mathrm{diag}(H_{\mathbf{k}1}, H_{\mathbf{k}2})$ and

$$u_{\mathbf{q}} = \gamma_{\mathbf{q}} \begin{pmatrix} 0 & \sigma_z e^{i\sigma_z\varphi/2} \\ \sigma_z e^{-i\sigma_z\varphi/2} & 0 \end{pmatrix} . \tag{7.14}$$

is the impurity vertex. The disorder average acts on $\gamma_{\mathbf{q}}$ factors and is performed according to Eq. (7.10). The diagrams in Fig. 7.2(b-c) represent terms of order g^4:

$$\begin{aligned} J_c^{(4)} = {} & 2\,\mathrm{Tr}\left[j_{\mathbf{q}} G_0(\mathbf{k},\omega_n) u_{\mathbf{q}'} G_0(\mathbf{k}-\mathbf{q}',\omega_n) u_{-\mathbf{q}'} G_0(\mathbf{k},\omega_n) u_{-\mathbf{q}} G_0(\mathbf{k}+\mathbf{q},\omega_n)\right] \\ & + \mathrm{Tr}\left[j_{\mathbf{q}} G_0(\mathbf{k},\omega_n) u_{\mathbf{q}'} G_0(\mathbf{k}-\mathbf{q}',\omega_n) u_{-\mathbf{q}} G_0(\mathbf{k}-\mathbf{q}'+\mathbf{q},\omega_n) u_{-\mathbf{q}'} G_0(\mathbf{k}+\mathbf{q},\omega_n)\right] \end{aligned} \tag{7.15}$$

where impurity averaging is assumed but not explicitly shown for clarity of notation. Evaluating the traces, we obtain the current of the form

$$J = J_c^{(2)} + J_c^{(4)} = J_{c1}(\theta)\sin\varphi - J_{c2}(\theta)\sin 2\varphi\,, \tag{7.16}$$

with coefficients, to lowest order of g,

$$J_{c1} = 4\sum_{n\mathbf{k}} j_{n\mathbf{k}} \tag{7.17}$$

$$J_{c2} = 8\sum_{n\mathbf{k}} j_{n\mathbf{k}}^2 + 4\sum_{n\mathbf{k}\mathbf{q}\mathbf{q}'} |\gamma_{\mathbf{q}}|^2 \left|\gamma_{\mathbf{q}'}\right|^2 f_{n\mathbf{k},1} f_{n\mathbf{k}+\mathbf{q}+\mathbf{q}',1} f_{n\mathbf{k}+\mathbf{q},2} f_{n\mathbf{k}+\mathbf{q}',2} \tag{7.18}$$

Here, we have defined

$$j_{n\mathbf{k}} = \left(f_{n\mathbf{k},1} * |\gamma_{n\mathbf{k}}|^2\right) f_{n\mathbf{k},2} \tag{7.19}$$

$$f_{n\mathbf{k},l} = \frac{\Delta_{\mathbf{k},i}}{\omega_n^2 + E_{\mathbf{k},l}^2} \tag{7.20}$$

and $(*)$ denotes a convolution integral, $a_{\mathbf{k}} * b_{\mathbf{k}} = \sum_{\mathbf{q}} a_{\mathbf{q}} b_{\mathbf{k}-\mathbf{q}}$. The quasiparticle dispersion of the unperturbed bands is given by $E_{kl} = \sqrt{\xi_{\mathbf{k}}^2 + \Delta_{\mathbf{k}l}^2}$.

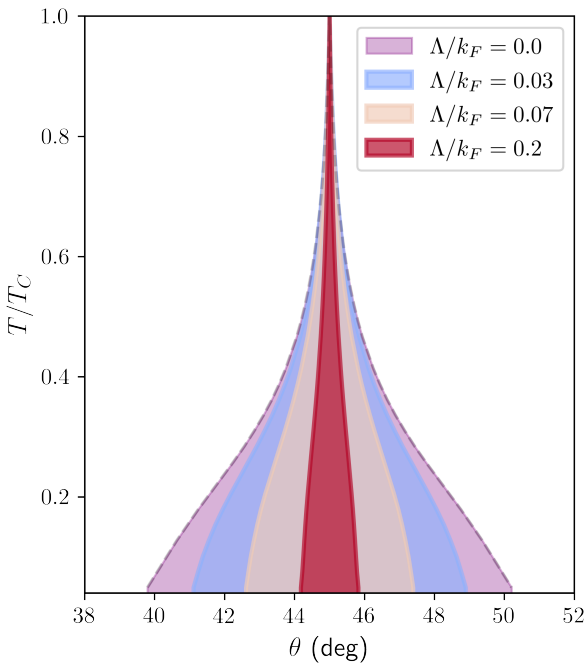

Figure 7.3: Phase diagram of incoherently coupled twisted bilayer cuprates. For a given Λ, the colored, cone-shaped region breaks $\mathcal{T}$. The light-red $\Lambda = 0$ region corresponds to the clean limit, previously introduced in [28]. For increasing degree of momentum non-conservation Λ, the $\mathcal{T}$-breaking phase boundaries shrink towards $45°$.

From Eq. (7.16) one obtains the free energy

$$2\mathcal{F} = -J_{c1}(\theta)\cos\varphi + \frac{J_{c2}(\theta)}{2}\cos 2\varphi + \text{const}\,. \tag{7.21}$$

The $\mathcal{T}$-breaking phase transition occurs as a consequence of competition between $\cos\varphi$ and $\cos 2\varphi$ terms. Clearly, $J_{c2} > 0$ and the ground state acquires a finite phase difference for

$$2J_{c2} > |J_{c1}|, \tag{7.22}$$

where it spontaneously breaks $\mathcal{T}$. From our discussion in Sec. 7.2 it follows that that J_{c1} must vanish at twist of $\theta = \pi/4$. Explicitly, one can see this result as follows. The functions $E_{\mathbf{k},l}$, $|\gamma_{\mathbf{k}}|^2$ transform under the A_{1g} irrep of D_{4h} whereas the $f_{\mathbf{k},1}, f_{\mathbf{k},2}$ transform under B_{1g} and B_{2g}, respectively. We note that convolution with the A_{1g}-symmetric impurity distribution $|\gamma_{\mathbf{k}}|^2$ does not change the symmetry of the convolution integral. Hence, $j_{\mathbf{k}}$ transforms under $B_{1g} \otimes B_{2g} = A_{2g}$ and all terms in Eq. (7.17) average to zero at $45°$-twist. However, $j_{\mathbf{k}}^2$ is A_{1g}-symmetric and J_{c2} will consequently be finite and positive. Thus, it is clear that condition (7.22) is generally satisfied at $\theta = 45°$ and $\mathcal{T}$ will always be broken as soon as the system enters the SC state below T_c.

We conclude that impurity-mediated tunneling must not qualitatively change the $\mathcal{T}$-breaking phase diagram relative to the model of Ref. [28]. The incoherent tunneling, however, shifts the phase boundaries.

As shown in Appendix E.1, $J_{c1} \sim 1/\Lambda$ and $J_{c2} \sim 1/\Lambda^2$. Since J_{c1} is only weakly dependent on θ, and J_{c1} vanishes linearly around 45° twist, it follows from Eq. (7.22) that the width of the $\mathcal{T}$-breaking phase space is proportional to $J_{c2}(\theta = 0)/J_{c1}(\theta = 0) \sim 1/\Lambda$. In the perfectly incoherent limit, $\Lambda \to \infty$, the free energy becomes independent of φ and the $\mathcal{T}$-breaking phase disappears.

To quantitatively ascertain the effect of incoherent tunneling on the phase diagram, we numerically evaluate the coefficients J_{ci}. In principle, all Matsubara sums can be evaluated analytically, at the cost of removing the simple convolution structure in Eq. (7.19). This leaves three remaining momentum integrals to be numerically evaluated at complexity $\mathcal{O}(N^3)$ where N is the number of $\mathbf{k}$-points of the 2D mesh used to perform the integrals. A more efficient approach is to exploit the convolution structure of Eq. (7.19) using the fast Fourier transform (fft) algorithm and numerically evaluate M Matsubara frequencies, affording evaluation of diagrams Fig. 7.2(a-b) at order $\mathcal{O}(MN \log N)$. The crossed diagram Fig. 7.2(c) does not possess a convolution structure. As we show in Appendix E.2, it can be evaluated at a cost of $\mathcal{O}(MN^2)$.

The resulting phase diagram is shown in Fig. 7.3 for coupling strength $g = 10.5\,\mathrm{meV}$ and several values of Λ. We see that the $\mathcal{T}$-breaking phase space is largest in the coherent limit $\Lambda \to 0$ where it extends between $(45 \pm 6)^\circ$ at $T = 0$. Increasing Λ gradually reduces the extent of the $\mathcal{T}$-broken phase which eventually vanishes in the perfectly incoherent limit when $\Lambda \sim k_F$, i.e., when impurity correlations are on the scale of the lattice constant. Physically, this occurs because at this level of incoherence the Cooper pair essentially loses all memory of its momentum structure in the process of tunneling between layers.

7.3.3 Spectral gap and topological superconductivity

Having discerned the fate of the $\mathcal{T}$-breaking phase in the presence of impurity-mediated tunneling we proceed to examine the topological properties of the resulting ground state. In the clean limit, $\mathcal{T}$-breaking establishes a topological phase with Chern number $\mathcal{C} = 4$ [28]. Since the disordered model is connected to the clean case by taking the limit $\Lambda \to 0$, it is reasonable to expect the same $\mathcal{C} = 4$ phase as long as the quasiparticle gap does not close.

Here, we show that these expectations are indeed met. To this end, we evaluate the Green's function

$$G(\mathbf{k}, \omega_n) = [G_0 - \Sigma(\mathbf{k}, \omega_n)]^{-1} \tag{7.23}$$

in the Born approximation where

$$\Sigma_{\tau\tau'} = \sum_{\mathbf{q}} u_{\mathbf{q}}\, G_0(\mathbf{k} - \mathbf{q}, \omega_n)\, u_{-\mathbf{q}} = -\delta_{\tau,\tau'}\, f_{\mathbf{k},\bar{\tau}}(i\omega_n + \xi_{\mathbf{k}}\sigma_z + e^{i\tau\sigma_z\varphi}\Delta_{\mathbf{k},\bar{\tau}}\sigma_x) * |\gamma_{\mathbf{k}}|^2 \ . \tag{7.24}$$

with layer-indices $\tau = \pm 1$. Here, we regularized the continuum model on a square lattice using

$$\begin{aligned} \xi_{\mathbf{k}} &= -2t(\cos k_x + \cos k_y) - \mu \\ \Delta_{\mathbf{k},\tau} &= \Delta[(\cos k_x - \cos k_y)\cos\theta + \tau \sin k_x \sin k_y\, e^{-i\varphi}\sin\theta] \end{aligned} \tag{7.25}$$

with parameters chosen to match the continuum model.

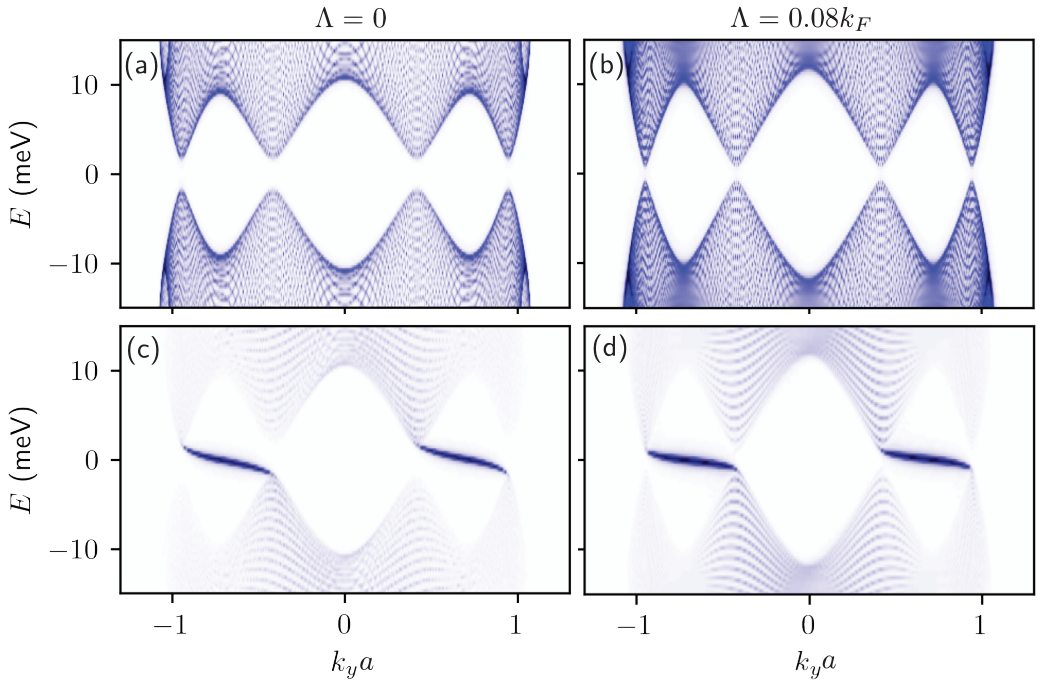

Figure 7.4: Bulk (a-b) and boundary (c-d) spectrum for incoherently coupled cuprate bilayers with $\Lambda = 0$ (left) and $\Lambda/k_F = 0.08$ (right) at $45°$ twist angle. The spectrum shows chiral edge modes traversing the bulk gap which is reduced but finite for increased Λ. Edge modes, which are in fact degenerate, indicate a Chern number $\mathcal{C} = 4$.

Following the method introduced in Ref. [126], we compute a spatially resolved Green's function

$$G_B(x, k_y, \omega_n) = G(x, k_y) - G(x, k_y)T(k_y)G(-x, k_y)$$
$$T(k_y) = \left[\frac{1}{\sqrt{N}} \sum_{k_x} G(k_x, k_y)\right]^{-1} \tag{7.26}$$

in the presence of a strong repulsive potential at $x = 0$ which simulates an edge and thus allows us to inspect the edge modes of the disordered system. We outline the method and give a derivation of Eq. (7.26) in Appendix E.3.

In Fig. 7.4 we plot the analytically continued boundary spectral function

$$A_B(x, k_y, \omega) = -\frac{1}{\pi}\mathrm{Im}\left[G_B(x, k_y, -i\omega + \eta)\right] \tag{7.27}$$

at the edge $(x = 1)$ as well as the bulk spectral function. We clearly observe two chiral edge modes traversing the bulk gap thus confirming the non-trivial topology of the system. The edge modes display a degeneracy in the layer degree of freedom, suggesting that the model is in a topological phase with Chern number $\mathcal{C} = 4$. The bulk gap is reduced but remains finite as Λ increases.

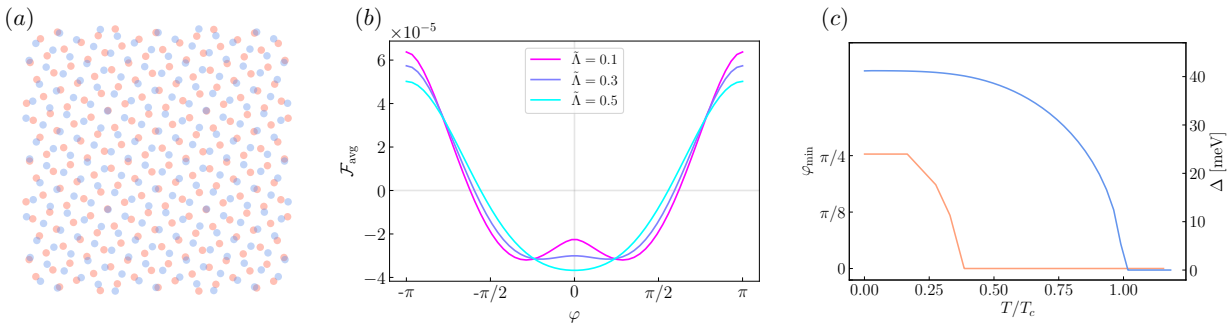

Figure 7.5: (a) Illustration of the geometry of the bilayer lattice model at an incommensurate angle of $\sim 43°$. (b) Disorder averaged free energy of the bilayer at zero temperature as a function of the phase difference. The minima φ_{min} are situated away from zero at small disorder strengths. (c) Dependence of the order parameter amplitude and phase as a function of temperature for $\tilde{\Lambda} = 0.2$. One could view it as a vertical cut at a specific twist in the phase diagram of Fig. 7.3, with the onset of a non-zero phase marking the phase boundary.

7.4 Lattice model

So far, we have looked at the role of disorder in a continuum formulation of a twisted bilayer. The two-site unit cell of the regularized model allowed for analytical expressions for the layer Green's function to which we have systematically added incoherent interlayer tunneling and calculated the free energy up to fourth order in g. Another approach to tackle the problem and corroborate the results in a more general setting is to perform a BCS mean field calculation on two twisted square lattices that represent the two CuO planes. In this case one can incorporate more realistic band structures, but it is also harder to obtain the Green's functions analytically using Feynman diagrams. The reason is twofold: For one, at an arbitrary twist the lattice model is not commensurate. Secondly, at commensurate twist angles close to $45°$, the moiré unit cell contains many sites. To get around this, we perform a brute force disorder average wherein several disorder realizations with the same microscopic parameters are taken into account. While it limits us to real space, such a treatment is exact because all orders in perturbation theory are implicitly accounted for.

For each layer, we consider a square lattice Hubbard model with nearest neighbor density-density interactions such that a mean-field decoupling produces a d-wave order parameter. Including the interlayer tunneling processes with amplitudes g_{ij}, the bilayer is described by

$$\begin{aligned}\mathcal{H} = \quad & -t \sum_{\langle ij\rangle\sigma l} c^\dagger_{i\sigma l} c_{j\sigma l} - t' \sum_{\langle\langle ij\rangle\rangle\sigma l} c^\dagger_{i\sigma l} c_{j\sigma l} - \mu \sum_{i\sigma l} n_{i\sigma l} \\ + \quad & \sum_{\langle ij\rangle l} \left(\Delta_{ij,l} c^\dagger_{i\uparrow l} c^\dagger_{j\downarrow l} + \text{h.c.} \right) - \sum_{ij\sigma} g_{ij} c^\dagger_{i\sigma 1} c_{j\sigma 2}, \end{aligned} \tag{7.28}$$

where l is a layer index, t (t') is the (next-)nearest-neighbor hopping amplitude, μ is the chemical potential that controls on-site particle density $n_{i\sigma l}$ and $\Delta_{ij,l}$ denotes the complex order parameter on the bond connecting sites i and j on layer l. Considering a fully coherent interlayer tunneling, Ref. [28] employs a circularly symmetric, exponentially decaying form $g_{ij} = e^{-(r_{ij}-c)/\rho}$ which connects sites i and j separated

by $\boldsymbol{r}_{ij}$. Therein c in the interlayer separation and ρ is defined by the radial extent of the participating orbitals. The twist angle θ between the layers determines connectivity and the strength of the interlayer tunnelings. The free energy of this model shows a double-well structure for twist angles around 45° [28].

To incorporate incoherent processes, we introduce a random tunneling factor that vanishes on average but encodes the correlation between different processes depending on spatial separation. That is,

$$g_{ij} = g_{\boldsymbol{R}}\, e^{-(r_{ij}-c)/\rho} \tag{7.29}$$

where $\boldsymbol{R} = (\boldsymbol{r}_i + \boldsymbol{r}_j)/2$ denotes the center of mass location of the hopping and

$$\begin{aligned} \overline{g_{\boldsymbol{R}}} &= 0, \\ \overline{g_{\boldsymbol{R}} g_{\boldsymbol{R}'}} &= g^2 \exp\left[-\frac{\tilde{\Lambda}^2}{4}(\boldsymbol{R}-\boldsymbol{R}')^2\right]. \end{aligned} \tag{7.30}$$

Note that the correlations are treated approximately in that they depend only on the center of mass locations $\boldsymbol{R}, \boldsymbol{R}'$ while any dependence on relative coordinates is neglected. Analogous to the parameter Λ in the continuum model, $\tilde{\Lambda}$ sets the length scale for the correlation between different tunneling amplitudes and is indicative of disorder strength. We distinguish the two simply because of the slightly differing definitions. To simulate the Fermi surface of optimally doped BSCCO with hole pocket around (π, π), we set $t = 153$meV, $t' = -0.45t$ and $\mu = -1.35t$ [23]. Further, we choose $c = 2.2$ and $\rho = 0.4$ (in units of the lattice constant) to set interlayer distances. The d-wave order parameters in cuprates originates in the CuO planes and the interlayer coupling is a minor perturbation that does not influence the order parameter magnitude. In other words, temperature dependence of the gap in each layer is independent of twist and coupling strength g, which we peg at 20meV. Therefore, we use a Δ calculated self-consistently in a monolayer, which has a maximum of ~ 40meV at 0K in accordance with experimental findings in cuprates [42, 47].

To look for $\mathcal{T}$-breaking we examine the free energy of the system, which can be calculated from the eigenvalues E_i of the BdG Hamiltonian (7.28):

$$\mathcal{F}_{\mathrm{BdG}} = \sum_i E_i - 2k_B T \sum_i \ln\left[2\cosh\left(E_i/2k_B T\right)\right]. \tag{7.31}$$

In particular, for a given twist θ and disorder parameter $\tilde{\Lambda}$, we draw from the distribution (7.30) and average the free energy over 50 independent realizations. We choose a square bilayer sample as shown in Fig. 7.5(a), but the results are independent of the shape. Further, the exact number of sites in the system depends on the cut and the twist angle, but the free energy does not show an appreciable change beyond ~ 900 sites per layer. In agreement with the continuum model, Fig. 7.5(b) shows that the presence of $\mathcal{T}$-breaking free energy minima is controlled by $\tilde{\Lambda}$. Namely, small values of $\tilde{\Lambda}$ support the $\mathcal{T}$-broken ground state while larger values do not.

7.5 Collective modes

The presence of two superconducting order parameters, one for each layer, yields an intricate spectrum of three collective modes. We will first analyze the bosonic spectrum within the Landau-Ginzburg framework.

Following the steps outlined in Sec. 2.1.2 of Ch. 2, we rewrite the order parameters ψ_i as

$$\begin{aligned}\psi_1 &= (\psi^{eq} + h_1)e^{i(\varphi^{eq}/2+\theta_1)} \\ \psi_2 &= (\psi^{eq} + h_2)e^{i(-\varphi^{eq}/2+\theta_2)}\end{aligned} \tag{7.32}$$

The h_i, θ_i represent small fluctuations around the groundstate given by the amplitude ψ^{eq} and the relative phase difference φ^{eq}. Explicitly, one has

$$\varphi^{eq} = \begin{cases} 0 & \gamma \geq \gamma^* \quad \text{(trivial)} \\ \arctan\sqrt{(\gamma^*/\gamma)^2 - 1} & 0 \leq \gamma < \gamma^* \quad \text{(topological)} \end{cases} \tag{7.33}$$

where $\gamma^* = 4(\psi^{eq})^2\beta_3$ marks the critical point of the topological phase transition where the system spontaneously breaks $\mathcal{T}$.

Expanding the free energy (7.2) to quadratic order around the groundstate, we compute the eigenmodes and their respective energies. First, we consider the topological trivial region, $\gamma > \gamma^*$. Here we obtain

$$\mathcal{F} = \mathcal{F}_0 + \frac{1}{2}m_- h_-^2 + \frac{1}{2}m_+ h_+^2 + \frac{1}{2}m_\varphi h_\varphi^2\,, \tag{7.34}$$

with the asymmetric and symmetric Higgs mode $h_\mp$ and the relative phase mode φ, defined by

$$\begin{aligned} h_- &= (h_1 - h_2)/\sqrt{2} & m_- &= 4(\psi^{eq})^4(2\beta_1 - \beta_2 + 2\beta_3) + 4(\psi^{eq})^2(\gamma - \gamma^*) \\ h_+ &= (h_1 + h_2)/\sqrt{2} & m_+ &= 4(\psi^{eq})^4(2\beta_1 + \beta_2 + 2\beta_3) \\ \varphi &= \theta_1 - \theta_2 & m_\varphi &= 2(\psi^{eq})^2(\gamma - \gamma^*)\,. \end{aligned} \tag{7.35}$$

In the topological region, for $\gamma < \gamma^*$, the symmetric Higgs mode mixes with the relative phase mode according to

$$\begin{aligned} h_- &= (h_1 - h_2)/\sqrt{2} & m_- &= 4(\psi^{eq})^4(2\beta_1 - \beta_2 + 2\beta_3) \\ \tilde{h}_1 &= \cos(\alpha)\,h_+ - \sin(\alpha)\,\varphi & \tilde{m}_1 &= a + b \\ \tilde{h}_2 &= \sin(\alpha)\,h_+ + \cos(\alpha)\,\varphi & \tilde{m}_2 &= a - b \end{aligned} \tag{7.36}$$

where we have defined

$$\begin{aligned} a &= 2(\psi^{eq})^4(2\beta_1 + \beta_2) + \gamma^2/4\beta_3 \\ b &= \sqrt{4(\psi^{eq})^8(2\beta_1 + \beta_2 - 4\beta_3)^2 + (\psi^{eq})^4(6\beta_1 + 3\beta_2 - 4\beta_3)\gamma^2/\beta_3 + \gamma^4/16\beta_3^2}\,. \end{aligned} \tag{7.37}$$

At the phase transition, $\gamma = \gamma^*$, we have $\alpha = 0$, i.e., phase and amplitude sectors are decoupled. Importantly, here, the excitation frequency of the relative phase mode vanishes.

Near the topological phase boundary, α becomes finite. We can expand the mode energies in small deviations $\gamma^* - \gamma$. We find

$$\tilde{m}_1 = m_+ - 4(\psi^{eq})^2 \frac{(2\beta_1 + \beta_2)}{2\beta_1 + \beta_2 + 2\beta_3}(\gamma^* - \gamma)$$
$$\tilde{m}_2 = 4(\psi^{eq})^2 \frac{(2\beta_1 + \beta_2 - 2\beta_3)}{2\beta_1 + \beta_2 + 2\beta_3}(\gamma^* - \gamma)\,. \tag{7.38}$$

We note that the mode energy $\tilde{m}_2 = 0$ vanishes at $\gamma = \gamma^*$ and then increases linearly in γ close to the transition point, within the topological region $\gamma < \gamma^*$.

We conclude that the $\tilde{m}_1$ mode constitutes a low-energy excitation. Within the topological region, the system becomes fully gapped. If the collective mode is located within the single-particle gap, it cannot be damped by quasiparticle excitations and must thus be a stable, long-lived mode. As such, it should give a strong signal in nonlinear optical response measurements.

7.5.1 Microscopic evaluation in the coherent limit

The Landau-Ginzburg framework does not take into account the quasiparticle excitation spectrum. To analyze the stability of the collective modes, we therefore need to perform a microscopic calculation. For simplicity, we will restrict ourselves to the coherent limit $\Lambda = 0$ which does not require a disorder average. Since we have seen that the overall phenomenology of the topological phase transition is stable against incoherence, we expect that generic features of the collective mode spectrum will also extend into the incoherent regime.

To this end, we define the density matrix

$$\rho_{\boldsymbol{k}} = \langle \psi^\dagger_{\boldsymbol{k}} \psi_{\boldsymbol{k}} \rangle \tag{7.39}$$

in the basis $\psi^\dagger_{\boldsymbol{k}} = \left(c^\dagger_{1\boldsymbol{k}\uparrow},\, c^\dagger_{2\boldsymbol{k}\uparrow},\, c_{1-\boldsymbol{k}\downarrow},\, c_{2-\boldsymbol{k}\downarrow} \right)$. Dynamics of the density matrix is governed by the equation of motion

$$i\partial_t \rho_{\boldsymbol{k}} = [H_{\boldsymbol{k}}, \rho_{\boldsymbol{k}}] \tag{7.40}$$
$$\Delta_{1,2} = \frac{V}{N} \sum_{\boldsymbol{k}} \cos\left(2\alpha_{\boldsymbol{k}} \pm \theta\right) \mathrm{Tr}\left[(\sigma_x - i\sigma_y)(\tau_0 \pm \tau_z)\, \rho_{\boldsymbol{k}}\right]/4\,, \tag{7.41}$$

where the second equation specifies the self-consistency condition of the superconducting gap that induces the collective behavior. The equilibrium value of the density matrix is

$$(\rho^{eq}_{\boldsymbol{k}})_{ij} = (U^\dagger_{\boldsymbol{k}})_{in} n_F(E_{n\boldsymbol{k}})(U_{\boldsymbol{k}})_{nj}\,, \tag{7.42}$$

where n_F is the Fermi function and the unitary matrix U is the eigenvector transformation, $E_{i\boldsymbol{k}} = U^\dagger_{\boldsymbol{k}} H_{\boldsymbol{k}} U_{\boldsymbol{k}}$,

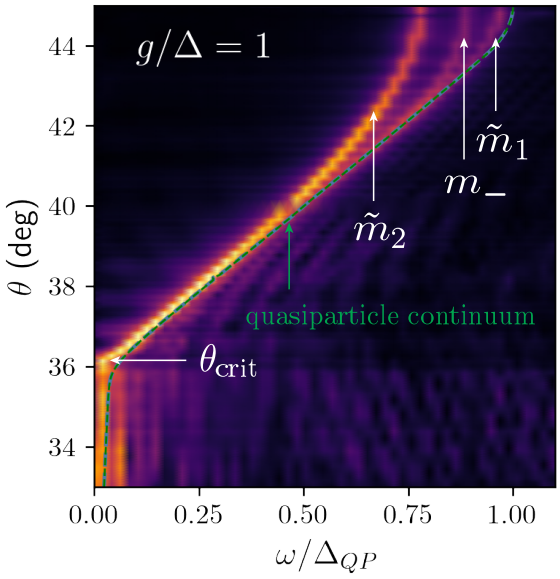

Figure 7.6: Collective modes energies as a function of twist angle θ for difference interlayer coupling scales g. Above the critical twist, the antisymmetric Higgs mode h_- and the mode $\tilde{m}_2$, that mostly has relative phase character, branch out from the quasiparticle continuum.

of the first-quantized Hamiltonian

$$H_{\mathbf{k}l} = \xi_{\mathbf{k}}\sigma_z + \Delta'_{\mathbf{k}l}\sigma_x - \Delta''_{\mathbf{k}l}\sigma_y + g\tau_x\sigma_z \,. \tag{7.43}$$

Within the density matrix formalism, we can extract the resonance spectrum of eigenmodes as follows. Instead of initializing the equation of motion in the equilibrium configuration, $\Delta_i = \Delta_i^{eq}$, we will slightly detune the initial values from equilibrium. Explicitly, we choose $\Delta_i = (1 + \delta'_i + i\delta''_i)\Delta_i^{eq}$. When the system is evolved in time by numerical integration of the equation of motion (7.40), the superconducting gap will oscillate around the equilibrium configuration with the frequencies of the collective modes.

By choosing the δ_i according to the eigenmode basis derived in Eqs. (7.35-7.36), we can selectively excite a single mode. For example, choosing $\delta'_1 = -\delta'_2$ and $\delta''_i = 0$ will only produce relative amplitude fluctuations h_- with the characteristic frequency m_-.

Figure 7.6 shows the resulting spectrum of collective modes as a function of twist angle θ. Above the critical twist of the $\mathcal{T}$-breaking transition, the antisymmetric Higgs mode h_- leaves the quasiparticle continuum, which is shown by a green dashed line. The mode $\tilde{m}_2$ has even lower energy. This mode is a mix of relative phase mode φ and symmetric Higgs mode h_+, but has mostly phase character. In fact, it is a pure phase mode at θ_{crit} and $\theta = 45°$. The last mode, $\tilde{m}_1$, which is mostly of symmetric Higgs character coincides with the quasiparticle continuum.

Since $\tilde{m}_2$ and h_- are subgap collective excitation, they are not affected by quasiparticle damping, and are sharp, infinitely long-lived bosonic modes. As such they are expected to yield a distinguished signature in the non-linear THz response. Measurement of these in-gap collective excitations could serve as a supporting

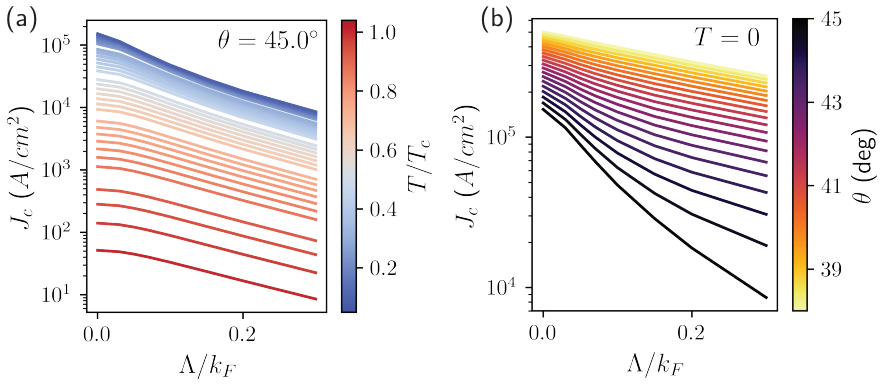

Figure 7.7: Critical c-axis current J_c of the twisted bilayer as a function as interlayer coherence scale Λ. Incoherence significantly reduces J_c. The color scale denotes temperature T in panel (a) and twist angle θ in (b).

indication of the underlying $\mathcal{T}$-broken superconducting state.

7.6 Conclusions

Twisted bilayers of high-T_c cuprates hold the potential for realizing topological superconductivity, wherein a topological gap is spontaneously induced. As per the symmetry informed momentum space form factors, which determine the electron hopping between interlayer Cu atoms, the tunneling amplitude vanishes along the nodal directions and a spectral gap may not appear. In this chapter we highlight that an important aspect to consider in such an analysis is the disorder mediated tunneling. Not only does disorder appear naturally due to oxygen doping and interfacial defects but incorporating momentum non-conservation has been shown to better represent experimental data in clean single crystals.

Using perturbative diagrammatic calculations and disorder averaging on the lattice, we find that an experimentally motivated incoherent tunneling model that respects all point group symmetries of the physical system gives rise to a qualitatively similar phase diagram as obtained in Ref. [28]. Specifically, we find a substantial range of twist angles around $45°$ and temperatures where spontaneous $\mathcal{T}$-breaking occurs and produces a fully gapped topological phase with non-zero Chern number. The angular extent of the $\mathcal{T}$-broken phase depends on the disorder length scale Λ^{-1} where the coherent limit $\Lambda \to 0$ recovers the phase diagram of Ref. [28] and increasing Λ corresponds to a shrinking extent of the topological phase. Only when the incoherence length scale is comparable to the Fermi momentum, the twist angle for spontaneous $\mathcal{T}$ breaking is reduced to exactly $45°$.

From an experimental point of view, the inhomogeneity due to oxygen doping the BiO planes of untwisted BSCCO was found to be correlated over $\approx$ 14Å [121]. Since the CuO plane lattice constant is $\approx$ 5Å, that amounts to a correlations over 3 unit cells, i.e., $\tilde{\Lambda} \approx 0.3$. In a twisted geometry, one may expect the characteristic length scale to decrease and, hence, the estimate for $\tilde{\Lambda}$ could shift up. That said, the role of complex atomic arrangements, moiré length scales and strong correlations are difficult to incorporate into such a heuristic reasoning. One would probably have to await data from complementary experimental probes, such as transport and optical response, to discern the nature of the superconducting state around $45°$.

It was noted in Ref. [148] that the measured critical current density J_c in both twisted and untwisted Bi2212 is about factor of 500 smaller than the theory prediction based on the slave-boson mean field theory of a t-J model used in that study. We checked that a similar discrepancy occurs in the calculation using BCS mean field theory of Ref. [28]. As indicated in Fig. 7.7 the discrepancy is somewhat reduced in the incoherent tunneling model (by about one order of magnitude at large Λ) but nevertheless significant disagreement with experiment persists. As noted in Ref. [144] this is a known problem that affects superconductors in the cuprate family and becomes increasingly severe in the underdoped part of their phase diagram. A phenomenological fix can be implemented [144] by restricting the momentum sums in the expression for J_c to patches of linear size $\sim x$ (the hole doping) around the nodal points of the d-wave order parameter. This modification leaves the temperature dependence of $\rho_{ab}(T)$ and $\rho_c(T)$ unchanged but reduces their $T = 0$ magnitude to experimentally observed values. It similarly fixes the problem with J_c. As with many aspects of cuprates a truly microscopic understanding of this phenomenon remains a challenge to the theory community. With regards to twisted cuprate bilayers it would be interesting to explore the effect of the phenomenological fix outlined above on the phase diagram.

We have further investigated the collective mode spectrum of twisted cuprates in the coherent limit. Above the critical twist, the system develops a fully gapped bulk state which supports two in gap collective modes. Measurement of these bosonic subgap excitations could provide key evidence of the $\mathcal{T}$-broken state in the spirit of the new field of collective mode spectroscopy.

In closing, we note that the incoherent tunneling model and techniques employed in this chapter can be extended to the study of other twisted 2D superconductors. The key general observation is that even though the single-electron tunneling amplitude $\gamma_{\boldsymbol{q}}$ between the layers may vanish on average this does not prevent the SC condensates in neighboring layers from being strongly coupled. A Cooper pair consists of two electrons and coherent pair tunneling therefore only requires nonzero $\overline{\gamma_{\boldsymbol{q}}\gamma_{-\boldsymbol{q}}}$, which translates to randomness being spatially correlated over some lengthscale longer than the lattice scale. The most interesting applications of our theory will likely involve nodal superconductors where the coupling between twisted layers has a potential to break discrete symmetries and open a gap, although other interesting phenomena can also occur.

Chapter 8

Superconducting diode from flux biased Josephson junction arrays

In the previous chapter we studied the free energy of twisted cuprate bilayers and examined its dependence on the twist angle θ_{twist}. The deformation of the free energy caused a phase transition at a critical twist angle θ_c, which is characterized by time-reversal symmetry breaking.

The cuprate bilayer can be thought of as a Josephson junction, where the two monolayers each constitute one side of the junction and the Josephson current is given by the interlayer current

$$I = I_{c1} \cos(2\theta_{\text{twist}}) \, \sin\varphi - I_{c2} \sin 2\varphi \, . \tag{8.1}$$

This current phase relation offers two different regimes. Close to zero twist, it mostly gives the usual $\sin\varphi$ current-phase relation. Near 45°, its current-phase relation is of the type $\sin 2\varphi$. These features can be exploited to engineer a device that displays the superconducting diode effect, as we will show in the following.

A superconducting diode is a two-terminal device whose forward and backward critical supercurrents are different. In the ideal limit of maximal imbalance, current applied in one direction is dissipationless (zero resistance), while it is always dissipative (resistive) in the opposite direction. This is a natural generalization of the semiconductor diode that is only weakly resistive in one direction and highly resistive in the opposite direction.

How can we exploit the physics of twisted cuprates to engineer a superconducting diode? Consider the device depicted in Fig. 8.1. Two cuprate Josephson junctions are connected in parallel. The first junction is made of untwisted (or minimally twisted) cuprate bilayers, whereas the second junction has a twist of 45°. The total current through the device is therefore given by

$$I = I_c \sin\varphi_1 + I_c' \sin 2\varphi_2 \, , \tag{8.2}$$

where φ_1, φ_2 are the Josephson phases across the two junctions. The two phases are not independent. They

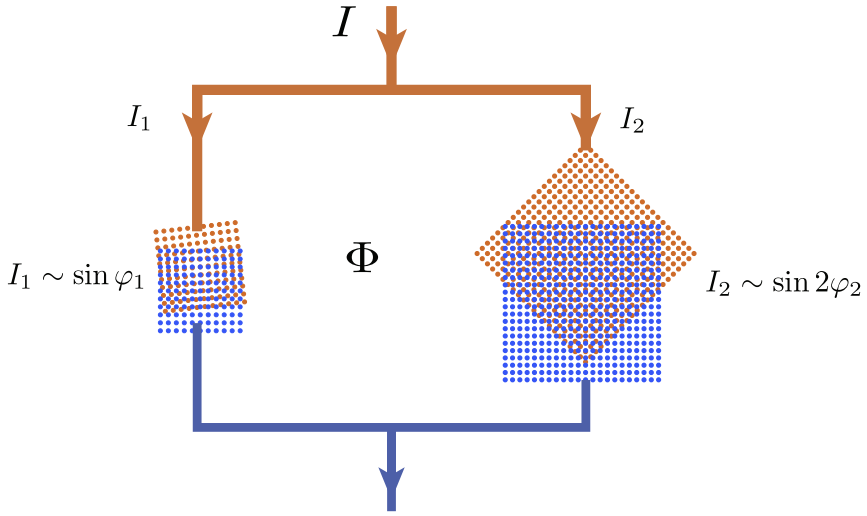

Figure 8.1: Schematic of a twisted cuprate bilayer interferometer.

are related via the phase continuity condition (cf. Eq. (1.12))

$$\varphi_1 - \varphi_2 + 2\pi n = 2\pi\Phi/\Phi_0\,, \tag{8.3}$$

where Φ is the external magnetic flux threaded through the superconducting loop. Thus, the total current is

$$I = I_c \sin\varphi_1 + I_c' \sin\left(2\varphi_1 - 4\pi\Phi/\Phi_0\right)\,. \tag{8.4}$$

We see that the current phase relation is given by the interference of the first harmonic contribution $\sin\varphi$ and a second harmonic contribution $\sin 2\varphi$ that are phase shifted with respect to each other by the external flux. When the flux is tuned to $\Phi = \Phi_0/8$, the maxima of the two harmonics align and one obtains the current-phase relation plotted in Fig. 8.2. Notably, the critical currents

$$\begin{aligned} I_c^+ &\equiv \max_\varphi I(\varphi) \\ I_c^- &\equiv \left|\min_\varphi I(\varphi)\right| \end{aligned} \tag{8.5}$$

become imbalanced, as indicated by red and blue dashed lines in Fig. 8.2. This constitutes the superconducting diode effect.

We have shown how the superconducting diode effect can arise in a device of cuprate bilayers. This cuprate-powered device, however, has little prospects of near-term applicability. Similar proposals that rely on a higher-harmonic content in the current phase relation have recently been made in Refs. [48, 150]. A flurry of other theoretical studies [41, 43, 59, 68, 70, 72, 84, 109, 136, 152, 175, 179, 180, 183] as well as experimental studies [10, 20, 21, 73, 94, 97, 120, 146, 166, 170, 174] have recently been conducted. The common factor among them is reliance on a rather complicated material platform, precluding near-term commercial applications. The diode effect requires both inversion- and time-reversal symmetry breaking.

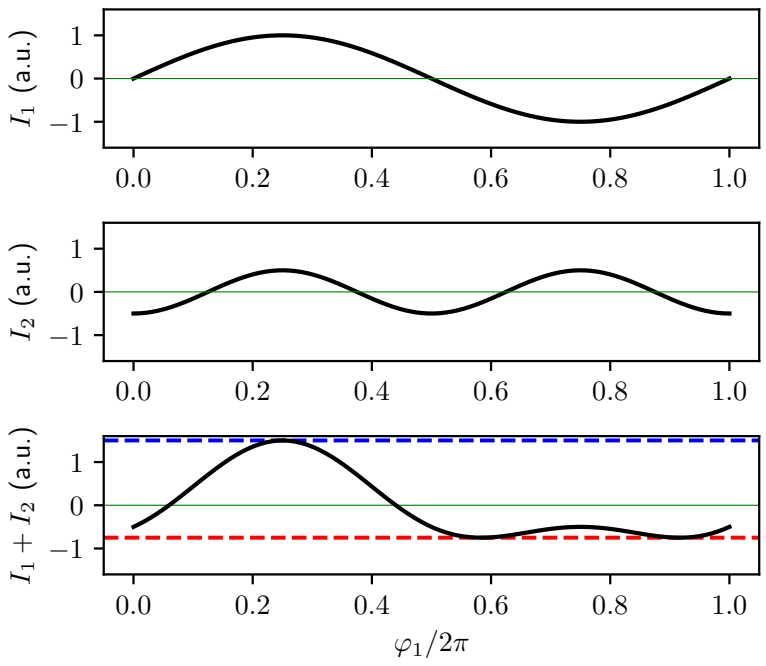

Figure 8.2: Current phase relation for (top) left arm of the interferometer, I_1, (middle) for the right arm, I_2, and (bottom) total current. The total current shows the diode effect, i.e. maximum and minima are imbalanced.

Inversion can be absent in systems with spin-orbit coupling [20, 72], or it can be explicitly broken by twisting bilayers, as in the current proposal, [52, 94, 136] or applying a current bias [36].

8.1 The diode effect in a superconducting Josephson circuit

In the present chapter, we propose a realization of the diode effect that does not rely on a specific material platform. It is based on a classical circuit of Josephson junctions with a standard sinusoidal current phase relation. Junctions can in principle even be identical, and inversion symmetry is broken by the connectivity of the circuit. Time-reversal symmetry is removed by magnetic fluxes that can most readily be applied using flux bias lines. The present diode implementation is agnostic to its underlying material platform and can be realized in industry standard Nb-Al processes based on scalable semiconductor technology.

8.1.1 Minimal circuit

We consider the superconducting circuit depicted in Fig. 8.3 consisting of two arms of Josephson junctions (JJ). The first arm consists of two junctions across which the superconducting phase jumps by φ_{1a}, φ_{1b}, respectively. The second arm consists of single Josephson junction with phase difference φ_2. The parasitic inductance of the wires is modeled by the lumped inductors L_1, L_2. This circuit has been previously introduced in the context of second harmonic generation, where it is known as the Superconducting Nonlinear Asymmetric Inductive Element (SNAIL) [49].

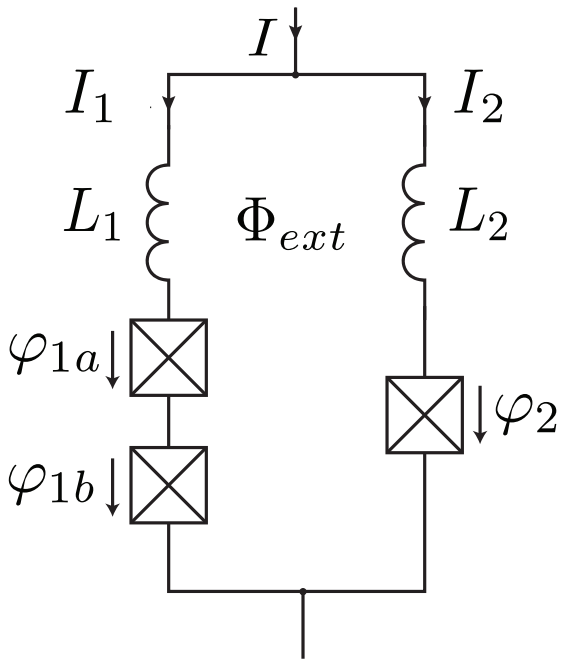

Figure 8.3: Superconducting circuit consisting of two inductive arms with one and two Josephson junctions in series, respectively. An external flux Φ_{ext} may thread the superconducting loop. Here, the inductors L_1, L_2 represent the geometric inductance of the superconducting wires.

The supercurrents in both arms of the SNAIL are determined by the Josephson relations

$$I_1 = I_c^{(1a)} \sin \varphi_{1a} = I_c^{(1b)} \sin \varphi_{1b} \tag{8.6}$$

$$I_2 = I_c^{(2)} \sin \varphi_1 \, . \tag{8.7}$$

We will be interested in the case of identical junction in the first arm, i.e., $I^{(1a)} = I^{(1b)}$. Here, the phases across the junctions are equal, $\varphi_{1a} = \varphi_{1b} \equiv \varphi_1$. Continuity of the phase along the superconducting loop then yields the phase quantization condition

$$2\varphi_1 - \varphi_2 + 2\pi n = 2\pi\Phi/\Phi_0 \tag{8.8}$$

where Φ is the total flux threading the junction and $\Phi_0 = h/2e$ is the superconducting flux quantum.

For small circuits the geometric inductance can be neglected, $L_a, L_b \to 0$. Then, flux through the loop is solely determined by the external flux, i.e., $\Phi = \Phi_{ext}$. The total current is

$$I(\varphi) = I_1 + I_2 = I_c^{(1)} \sin \varphi_1 + I_c^{(2)} \sin \left(2\varphi_1 - \varphi_{ext}\right) \tag{8.9}$$

where we have defined $\varphi_{ext} = 2\pi\Phi_{ext}/\Phi_0$.

The critical current in forward $(+)$ and backward $(-)$ directions are defined as

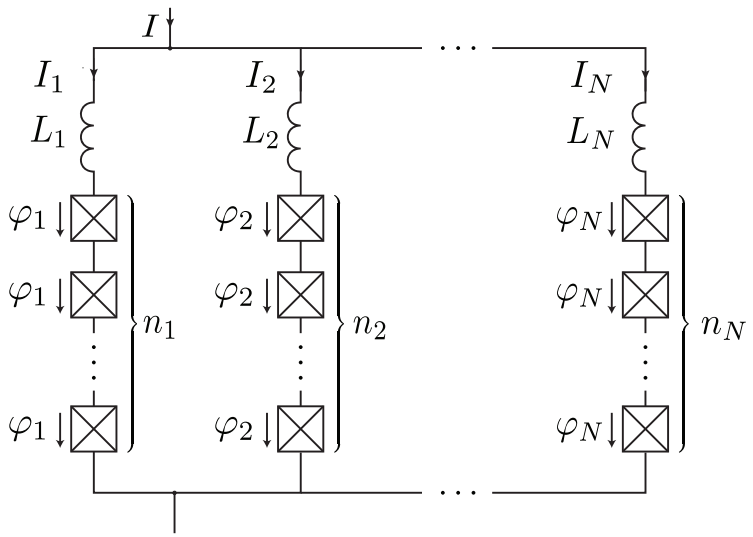

Figure 8.4: Generalized Josephson interferometer consisting of N arms with current I_k and n_k identical Josephson junctions with critical current $I_c^{(k)}$ that each experience a superconducting phase drop φ_k. Geometrical inductances have been lumped into the elements L_k. A magnetic flux $\Phi_{k,l}$ may be threaded between arms k and l.

$$\begin{aligned} I_c^+ &\equiv \max_{\varphi} I(\varphi) \\ I_c^- &\equiv \left| \min_{\varphi} I(\varphi) \right| \end{aligned} \tag{8.10}$$

where we note that I_c^+ and I_c^- are positive quantities. Importantly, for $\varphi_{ext}/2\pi \notin \mathbf{Z}$, i.e., when φ_{ext} is a nontrivial phase, one generally has

$$I_c^+ \neq I_c^- \,, \tag{8.11}$$

i.e., the forward and backward applied critical currents are imbalanced. This constitutes the superconducting diode effect. The degree of imbalance between these two critical current values is quantified by the superconducting diode efficiency

$$\eta = \frac{|I_c^+ - I_c^-|}{I_c^+ + I_c^-} \,, \tag{8.12}$$

which is a positive number and $\eta < 1$. We find the maximum efficiency of $\eta = 1/3$ for the two-arm geometry in Fig. 8.3 when $I_c^{(2)} = I_c^{(1)}/2$ and $\Phi_{ext} = \Phi_0/4$.

8.1.2 N-arm interferometers and the ideal diode limit

Next we consider a N-ladder of JJ arrays which we enumerate by $k = 1, .., N$ with n_k consecutive junctions forming each arm k and flux $\Phi_{k,l}$ enclosed between the arms k and l. By phase continuity, the Josephson phase for a single junction in arm k in terms of the phase variable φ_1 is given by

$$\varphi_k = \frac{n_1\varphi_1 - \frac{2\pi}{\Phi_0}\Phi^{ext}_{1,k} + 2\pi n}{n_k} \tag{8.13}$$

in the limit of zero inductance.

We assume the zero-vortex state $n = 0$ and define $\phi^{ext}_k = \frac{1}{n_k}\frac{2\pi}{\Phi_0}\Phi^{ext}_{1,k}$. Then, the total current is

$$I(\varphi_1) = \sum_k I_k = \sum_{k=1}^{N} I_c^{(k)} \sin\left(\frac{n_1}{n_k}\varphi_1 - \phi^{ext}_k\right) . \tag{8.14}$$

If the integer coefficients n_k are chosen in such a way that

$$n_1/n_k = k\,, \tag{8.15}$$

Eq. (8.14) represents a Fourier series that allows for engineering of arbitrary current phase relations. One such set of integers is given by $n_k = N!/\left[\text{floor}(N/2)!\,k\right]$. For an efficient diode layout, one should however reduce this set by its greatest common denominator, $GCD(\{n_k\})$.

The Fourier series is fully specified by the individual magnetic flux parameters ϕ^{ext}_k and critical currents $I_c^{(k)}$. The fluxes are easily tuned via flux bias lines and critical currents are determined by the junction area in the fabrication design.

We are now left to discuss the problem of finding the set of parameters that yield the greatest diode efficiency η. Let us propose the particular choice

$$I_c^{(k)} = I_0\frac{N+1-k}{N} \tag{8.16}$$

$$\phi^{ext}_k = (k-1)\pi/2 \tag{8.17}$$

This yields the following analytical expression for the total current of the interferometer:

$$\begin{aligned} I(\varphi_1)/I_0 &= \sum_{k=1}^{N}\frac{N+1-k}{N}\sin\left(k\varphi_1 + (1-k)\pi/2\right) \\ &= \frac{\cos\left((N+1)(\varphi_1-\pi/2)\right)-1}{2N\left(\sin\varphi_1 - 1\right)} - \frac{N+1}{2N} \end{aligned} \tag{8.18}$$

A plot of Eq. (8.18) for various N is shown in Fig. 8.5(a). As N is increased, the function develops a narrow peak of height $I/I_0 = (N+1)/2$ at $\varphi_1 = \pi/2$ over a seemingly flat background at $I/I_0 = (N+1)/2N$,

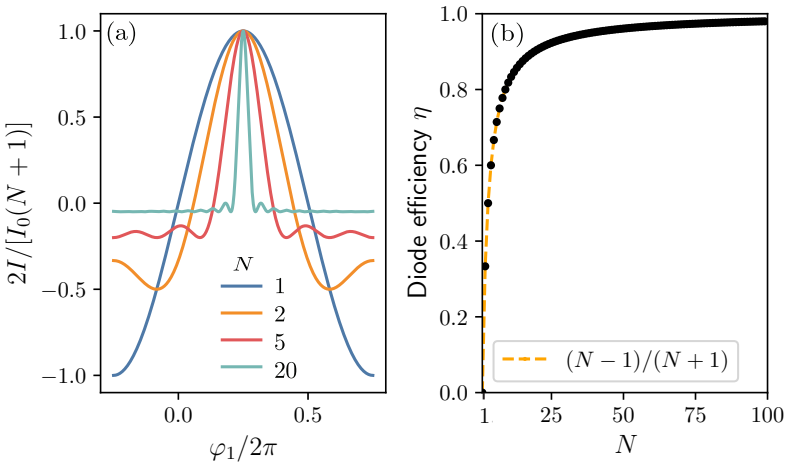

Figure 8.5: (a) Current phase relation for number of interferometer arms $N = 1, 2, 5, 20$ and (b) diode efficiency as a function of N that is given by $\eta = (N-1)/(N+1)$.

yielding a significant imbalance of critical currents with diode efficiency

$$\eta = \frac{N-1}{N+1} \tag{8.19}$$

that approaches unity in the large-N limit. In fact, for $N \to \infty$, the current-phase relation approaches a series of δ-functions centered at $2\pi(n+1/4)$ and shifted by a constant current $-I_0/2$, according to

$$\lim_{N\to\infty} I/I_0 = \pi \sum_k \delta(\varphi_1 - \pi/2 + 2\pi k) - \frac{1}{2}\,. \tag{8.20}$$

While the flux and critical current parameters defined in Eqs. (8.16-8.17) yield an ideal diode in the large-N limit, they likely also constitute the fastest converging series. For small $N \leq 5$, where the parameter space is still amenable to numerical optimization, we have numerically confirmed that it represents the optimal solution.

8.2 Parasitic components

8.2.1 IV-characteristic

We now consider a resistively and capacitively shunted junction (RCSJ) model where each junction on arm k in Fig. 8.4 is shunted by an internal capacitor C_k and resistor R_k. For an external dc current bias $I_{dc}^{(k)}$ in arm k the equation of motion is given by

$$I_{dc}^{(k)} = \frac{\Phi_0}{2\pi}\frac{\dot{\varphi}_k}{R_k} + \frac{\Phi_0}{2\pi} C_k \ddot{\varphi}_k + I_c^{(k)} \sin\varphi_k \tag{8.21}$$

We assume that every junction is identical for a given arm and current conservation implies that φ_k is the same for every junction. Using the phase continuity condition (8.13) and adding all currents one can show

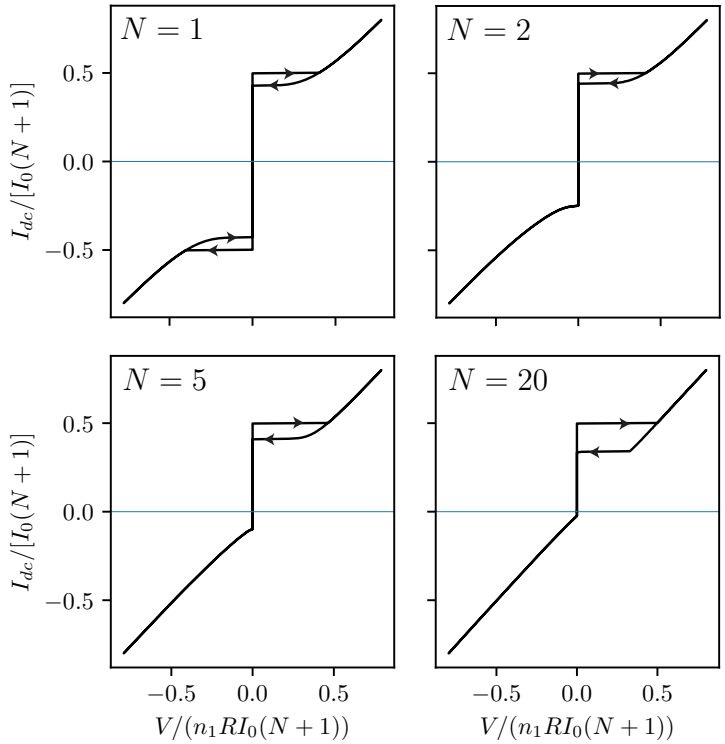

Figure 8.6: I-V curves computed within RSJ model for $\beta = 0.6\sqrt{n_1}$ and $N = 1, 2, 5, 20$

that the system is governed by a single differential equation

$$I_{dc}/I_0 = \frac{d^2\varphi_1}{d\tau^2} + \beta\frac{d\varphi_1}{d\tau} + I(\varphi_1)/I_0\,, \tag{8.22}$$

where $I_{dc} = \sum_k I_{dc}^{(k)}$ is the total, experimentally applied current bias. We have also defined the dimensionless parameters $\tau = \omega_J t$, $\beta = (\omega_J R_{\text{eff}} C_{\text{eff}})^{-1}$, $\omega_J = \sqrt{\frac{2e}{\hbar}\frac{I_0}{C_{\text{eff}}}}$ and the effective resistance and capacitance parameters

$$R_{\text{eff}} = \left(\sum_{k=1}^{N}\frac{n_1}{R_k n_k} + \frac{n_1}{R_{ext}}\right)^{-1} \tag{8.23}$$

$$C_{\text{eff}} = \sum_{k=1}^{N}\frac{n_1 C_k}{n_k} + n_1 C_{ext}\,. \tag{8.24}$$

R_k and C_k will depend on the geometries of individual junctions. For better tunability, one may shunt the entire device with an additional resistor R_{ext} and a capacitor C_{ext}. The voltage across each arm is given by $V = n_1\frac{\Phi_0}{2\pi}\dot{\varphi}_1$. In the limit where $R_{ext} \ll R_k$ and $C_{ext} \gg C_k$, dynamics is independent of internal resistances and capacitances of the junctions, where we find $R_{\text{eff}} \approx R_{ext}/n_1$ and $C_{\text{eff}} \approx n_1 C_{ext}$. In this limit, β defined just below 8.22 scales as $\beta \approx \sqrt{N!}$ where $\tilde{\omega} = \sqrt{\frac{2e}{\hbar}\frac{I_0}{C_{ext}}}$ and n_1 is the number of junctions on arm $k = 1$ which depends on N as $n_k \approx N!$ in the large-N limit

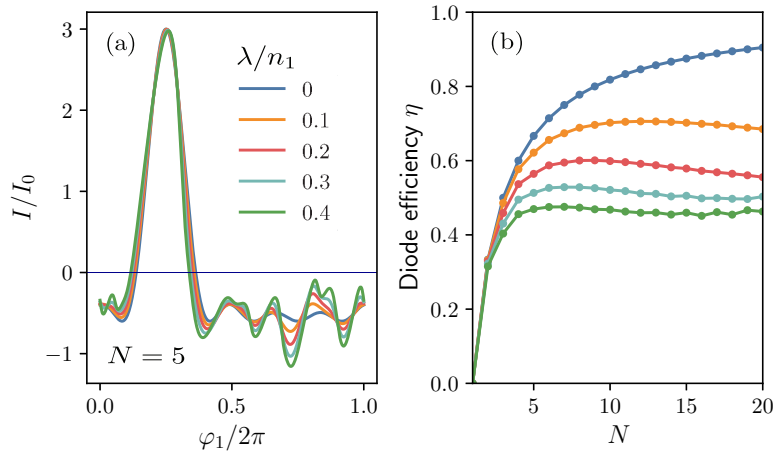

Figure 8.7: Current phase relation (a) for the exemplary case $N = 5$ and (b) diode efficiency as a function of N for varied strength of the inductance parameter λ/n_1. The geometrical inductance distorts the current-phase relation and diminishes the diode efficiency η.

N	η	N_J	n_k					$\Phi_{k,k+1}/\Phi_0$				$I_c^{(k)}N/I_0$				
2	1/3	3	2	1				1/4				2	1			
3	1/2	11	6	3	2			3/4	1/4			3	2	1		
4	3/5	25	12	6	4	3		3/2	1/2	1/4		4	3	2	1	
5	2/3	137	60	30	20	15	12	7.5	5/2	5/4	3/4	5	4	3	2	1

Table 8.1: Optimal parameters for superconducting diode circuits with N arms. $N_J = \sum_k n_k$ is the total number of Josephson junctions required and $\Phi_{k,k+1}$ is the magnetic flux threaded between arms k and $k+1$.

We numerically solve the differential Eq. (8.22) for voltage as a function of external current I_{dc}. The resulting I-V-curves are shown in Fig. 8.6 for various N and $\beta = 0.6\sqrt{n_1}$. For $N > 1$, the critical currents become imbalanced. The I-V-curves display a well-known hysteretic behavior which, however, can be suppressed for large N, i.e., when β is sufficiently large.

8.2.2 Finite inductance

In the case of finite geometric inductance, $L_k > 0$, the flux through the superconducting loops is no longer defined just by the external flux. Instead, Eq. (8.13) must be modified to also include the contribution of the induced flux,

$$\varphi_k = \frac{1}{n_k}\frac{2\pi}{\Phi_0}\left(\Phi_{1,k}^{ext} + L_1 I_1 - L_k I_k\right) . \tag{8.25}$$

Now, Eq. (8.14) must be solved self-consistently, since a change in current implies a change in φ_k, which again induces a change in the I_k. For sufficiently large inductances, the induced fluxes will develop hysteretic behavior in the externally applied flux.

Since the geometrical inductances are expected to be roughly equal for each arm, we parametrize them by a single dimensionless parameter $2\pi L_i I_0/\Phi_0 \equiv \lambda$. In Fig. 8.7, we show the results of the self-consistent

calculation for various λ, small enough that the diode is still in the non-hysteretic regime. The inductance can be seen to distort the current phase relation and yields an overall decrease in diode efficiency. Assuming that the λ roughly scales with the maximum number of junctions in a branch n_1, this efficiency decrease is more pronounced at large N.

8.3 Discussion and Summary

We have proposed a superconducting diode circuit element that requires only conventional Josephson junctions and flux bias loops which can be fabricated utilizing existing integrated circuit technology.

A Josephson interferometer will exhibit the superconducting diode effect if current arms carry different harmonics $\sin n\varphi$ of the current phase relation and if these harmonics are phase-shifted with respect to each other.

We have shown that higher harmonics can effectively be generated in generalized SNAIL geometries when multiple conventional Josephson junctions are connected in series. Flux biases in the loops are crucial for generating the phase differences, which we have optimized for diode efficiency. Note that polarity of the superconducting diode can be switched by reversal of all fluxes, i.e., by setting $\varphi_{k,ext} \to -\varphi_{k,ext}$ in Eq. (8.17). We have also considered the effects of geometric inductance, which lead to an overall decrease in diode efficiency.

We work in the limit $E_J \gg E_C$ where charging energy is $E_c = e^2/2C_J$. Here, fluctuations in the phase variable φ are suppressed. Therefore φ can be treated as a classical variable, justifying the use of RSJ model in Eq. (8.6).

Table 8.1 summarizes the various optical circuit parameters for different N, along with the resulting diode efficiency in the non-inductive case. Circuits with more than a few arms are likely mostly of academic interest, as the total number of required junctions scales exponentially in N, even though more than 10^6 Josephson junctions and on the order of 10^5 flux biases have been integrated on a single chip [25, 63]. Nevertheless, for reasonably small N, our proposed diode device could be promising for practical use.

Chapter 9

Summary

In this thesis, we have highlighted a host of fascinating aspects of the superconducting condensate and its collective modes. The phenomenology of superconductivity can be understood within the Landau-Ginzburg formalism. Here, group theory serves as a powerful tool to distill a compact theoretical description from the point group symmetry transformations of the underlying microscopic system. In this framework, the collective mode eigenspectrum can be deduced. We have applied the group theoretical analysis to the novel system of twisted cuprate bilayers. We have demonstrated that the phase transition of spontaneous time-reversal symmetry breaking, that is accompanied by a topological Chern phase, can be understood as a natural consequence of the change in symmetry group from D_{4h} to D_{4d} when the cuprate layers are twisted by 45°.

The microscopic theory of superconductivity is elegantly formulated in terms of a Euclidean path integral in imaginary time. We have summarized how optical response functions can be computed from an effective action and are expressed in terms of the nonlinear optical kernel. Collective modes are the Gaussian fluctuations of the Hubbard Stratonovich field, that we introduced to decouple a four-fermion BCS interaction. They yield peaked resonance structures at their eigenmode frequencies in the optical kernel. In an alternative, equivalent, theoretical treatment we have sometimes numerically integrated the equations of motion of the superconductor, taking the BCS gap equation into account to ensure self-consistency.

We have outlined the two basic THz spectroscopic settings that are currently used to probe the Higgs mode: third harmonic generation and pump-probe spectroscopy. Both of them have been shown to give experimental access to the functional form of the nonlinear optical kernel. While the kernel's frequency dependence can in effect be swept directly with the pump-probe method, only temperature sweeps can be performed in THG experiments. We have further described a novel experimental scheme, which we termed *quench-drive* spectroscopy. Here, a combination of a single-cycle pump and a multi-cycle THG pulse are applied. The spectra are then recorded in $2d$ plots as a function of time and pump-probe delay. We have shown that the optical kernel appears as a side band modulation when the $2d$ spectrum is presented in frequency space.

Further, we have combined the path integral description of collective modes with the Mattis-Bardeen theory of impurity scattering of a two-band superconductor, making close reference to the material MgB_2. We showed that impurity scattering can yield a sizable contribution of the Higgs mode to the nonlinear

response, both in THG and time-resolved pump-probe measurements of the optical conductivity. Interestingly, our calculations also reproduce a puzzling feature of the linear optical conductivity of MgB_2 thin films: While MgB_2 is an acclaimed two-band superconductor, only one absorption gap has ever been observed in linear response THz measurements. Our model helps to solve this puzzle. We explain the missing spectroscopic features of the second gap with the Fermi surface of the σ-band being small compared to the π-band.

We have studied an exotic system of two cuprate monolayers, that have been twisted with respect to each other, and then stacked into a single device. Twisted cuprates have been proposed to realize the first known example of a topological high-T_c superconductor. Here, we demonstrated that the cuprate topological phase also persists in the realistic scenario of incoherently coupled bilayers. The twisted cuprate structure gives rise to a rather non-trivial spectrum of in-gap collective modes. THz spectroscopic measurement of these in-gap modes may serve as a smoking gun experiment for the topological, spontaneously time-reversal symmetry broken phase.

In the last part of this thesis, we proposed a novel superconducting Josephson device that realizes the superconducting diode effect. While recent experimental and theoretical implementations of the diode effect rely on rather complex material platforms, our device can be generically built using scalable semiconductor fabrication technology. It is described by a circuit model of Josephson junctions, where collective fluctuations are, for once, neglected.

The emerging field of collective mode spectroscopy has many future directions that present exciting new avenues for future studies. One such direction is the excitation of collective modes at finite momentum $\boldsymbol{q} > 0$. Current experimental techniques, that are based on THz or visible laser radiation, work in the opposite regime, since the photon momentum at these frequencies satisfies $|\boldsymbol{q}| \ll |\boldsymbol{k}_F|$. However, angle-resolved photoemission (ARPES) techniques or momentum-resolved electron energy loss spectroscopy (M-EELS) can excite collective modes at finite $\boldsymbol{q}$ [127]. Away from $\boldsymbol{q} = 0$, the Higgs mode is no longer suppressed by particle-hole symmetry, and one expects a significant contribution of Higgs to the non-linear response.

Beyond small $\boldsymbol{q}$, measurement of the full bandstructure of collective superconducting modes for $\boldsymbol{q}$ in the Brillouin zone would allow to study topological properties. Topological band theory has been applied to a plethora of bosonic excitations, such as magnons via linear spin wave theory [167], phonons [93], photons [119], among others. Application of topological band theory to collective modes of the condensate would present an interesting avenue of research. While massive bosonic bands are usually highly damped due to decay channels into Goldstone modes and therefore difficult to observe in experiment, superconducting bosonic bands can be stable (due to the absence of the Goldstone channel) as a consequence of the Anderson-Higgs mechanism. Yet, topological properties require at least two bands and are hence only possible in two- or multi-band superconductors. Few multi-band superconductors are known to date. The study of topological superconducting collective modes would therefore initially involve a rigorous classification effort and material search based on point group symmetries.

Bibliography

[1] EverettYou/MatsubaraSum: A Mathematica package to perform Matsubara summation analytically. URL https://github.com/EverettYou/MatsubaraSum. → page 152

[2] I. J. R. Aitchison, P. Ao, D. J. Thouless, and X.-M. Zhu. Effective Lagrangians for BCS superconductors at $T = 0$. *Phys. Rev. B*, 51:6531–6535, Mar 1995. doi:10.1103/PhysRevB.51.6531. URL https://link.aps.org/doi/10.1103/PhysRevB.51.6531. → page 149

[3] A. Altland and B. Simons. *Condensed Matter Field Theory*. Cambridge University Press, 2010. → pages 20, 74

[4] M. H. S. Amin, E. V. Bezuglyi, A. S. Kijko, and A. N. Omelyanchouk. Wigner distribution function formalism for superconductors and collisionless dynamics of the superconducting order parameter. *Low Temp. Phys.*, 30(7):661–666, 2004. doi:10.1063/1.1789939. URL https://doi.org/10.1063/1.1789939. → page 70

[5] O. Andersen, A. Liechtenstein, O. Jepsen, and F. Paulsen. LDA energy bands, low-energy hamiltonians, t', t", $t_\perp$(k), and $j_\perp$. *Journal of Physics and Chemistry of Solids*, 56(12):1573–1591, Dec. 1995. doi:10.1016/0022-3697(95)00269-3. URL https://doi.org/10.1016/0022-3697(95)00269-3. → page 98

[6] P. Anderson. Theory of dirty superconductors. *Journal of Physics and Chemistry of Solids*, 11(1): 26–30, 1959. ISSN 0022-3697. doi:https://doi.org/10.1016/0022-3697(59)90036-8. URL https://www.sciencedirect.com/science/article/pii/0022369759900368. → page 3

[7] P. W. Anderson. Random-Phase Approximation in the Theory of Superconductivity. *Phys. Rev.*, 112:1900–1916, Dec 1958. doi:10.1103/PhysRev.112.1900. URL https://link.aps.org/doi/10.1103/PhysRev.112.1900. → pages 34, 47

[8] P. W. Anderson. Plasmons, Gauge Invariance, and Mass. *Phys. Rev.*, 130:439–442, Apr 1963. doi:10.1103/PhysRev.130.439. URL https://link.aps.org/doi/10.1103/PhysRev.130.439. → pages 1, 73, 144

[9] P. W. Anderson. Higgs, Anderson and all that. *Nature Physics*, 11(2):93–93, 2015. doi:10.1038/nphys3247. URL https://doi.org/10.1038/nphys3247. → page 1

[10] F. Ando, Y. Miyasaka, T. Li, J. Ishizuka, T. Arakawa, Y. Shiota, T. Moriyama, Y. Yanase, and T. Ono. Observation of superconducting diode effect. *Nature*, 584(7821):373–376, 2020. doi:10.1038/s41586-020-2590-4. URL https://doi.org/10.1038/s41586-020-2590-4. → page 116

[11] E. Y. Andrei and A. H. MacDonald. Graphene bilayers with a twist. *Nature Materials 2020 19:12*, 19:1265–1275, 11 2020. ISSN 1476-4660. doi:10.1038/s41563-020-00840-0. URL https://www.nature.com/articles/s41563-020-00840-0. → page 97

[12] J. F. Annett. Symmetry of the order parameter for high-temperature superconductivity. *Advances in Physics*, 39(2):83–126, 1990. doi:10.1080/00018739000101481. URL https://doi.org/10.1080/00018739000101481. → pages 9, 100, 101

[13] S. N. Artemenko and A. F. Volkov. Collective excitations with a sound spectrum in superconductors. *JETP*, 42(5):896, Nov. 1975. → pages 73, 95

[14] K. R. Babu and G.-Y. Guo. Electron-phonon coupling, superconductivity, and nontrivial band topology in NbN polytypes. *Phys. Rev. B*, 99:104508, Mar 2019. doi:10.1103/PhysRevB.99.104508. URL https://link.aps.org/doi/10.1103/PhysRevB.99.104508. → page 55

[15] L. Balents, C. R. Dean, D. K. Efetov, and A. F. Young. Superconductivity and strong correlations in moiré flat bands. *Nature Physics 2020 16:7*, 16:725–733, 5 2020. ISSN 1745-2481. doi:10.1038/s41567-020-0906-9. URL https://www.nature.com/articles/s41567-020-0906-9. → page 97

[16] R. A. Barankov and L. S. Levitov. Synchronization in the BCS Pairing Dynamics as a Critical Phenomenon. *Phys. Rev. Lett.*, 96:230403, Jun 2006. doi:10.1103/PhysRevLett.96.230403. URL https://link.aps.org/doi/10.1103/PhysRevLett.96.230403. → pages 70, 76

[17] R. A. Barankov, L. S. Levitov, and B. Z. Spivak. Collective Rabi oscillations and solitons in a time-dependent BCS pairing problem. *Physical Review Letters*, 2004. ISSN 00319007. doi:10.1103/PhysRevLett.93.160401. → page 70

[18] A. Bardasis and J. R. Schrieffer. Excitons and Plasmons in Superconductors. *Phys. Rev.*, 121: 1050–1062, Feb 1961. doi:10.1103/PhysRev.121.1050. URL https://link.aps.org/doi/10.1103/PhysRev.121.1050. → pages 2, 89

[19] J. Bardeen, L. N. Cooper, and J. R. Schrieffer. Microscopic Theory of Superconductivity. *Phys. Rev.*, 106:162–164, Apr 1957. doi:10.1103/PhysRev.106.162. URL https://link.aps.org/doi/10.1103/PhysRev.106.162. → page 3

[20] C. Baumgartner, L. Fuchs, A. Costa, S. Reinhardt, S. Gronin, G. C. Gardner, T. Lindemann, M. J. Manfra, P. E. Faria Junior, D. Kochan, J. Fabian, N. Paradiso, and C. Strunk. Supercurrent rectification and magnetochiral effects in symmetric Josephson junctions. *Nature Nanotechnology*, 17(1):39–44, Jan 2022. ISSN 1748-3395. doi:10.1038/s41565-021-01009-9. URL https://doi.org/10.1038/s41565-021-01009-9. → pages 116, 117

[21] L. Bauriedl, C. Bäuml, L. Fuchs, C. Baumgartner, N. Paulik, J. M. Bauer, K.-Q. Lin, J. M. Lupton, T. Taniguchi, K. Watanabe, C. Strunk, and N. Paradiso. Supercurrent diode effect and magnetochiral anisotropy in few-layer NbSe2. *Nature Communications*, 13(1):4266, Jul 2022. ISSN 2041-1723. doi:10.1038/s41467-022-31954-5. URL https://doi.org/10.1038/s41467-022-31954-5. → page 116

[22] L. Benfatto, A. Toschi, and S. Caprara. Low-energy phase-only action in a superconductor: A comparison with the XY model. *Physical Review B - Condensed Matter and Materials Physics*, 69 (18):184510, may 2004. ISSN 01631829. doi:10.1103/PhysRevB.69.184510. URL https://journals.aps.org/prb/abstract/10.1103/PhysRevB.69.184510. → pages 25, 51

[23] A. Bille, R. A. Klemm, and K. Scharnberg. Models of c-axis twist Josephson tunneling. *Phys. Rev. B*, 64:174507, Oct 2001. doi:10.1103/PhysRevB.64.174507. URL https://link.aps.org/doi/10.1103/PhysRevB.64.174507. → page 109

[24] G. Blumberg, A. Mialitsin, B. S. Dennis, M. V. Klein, N. D. Zhigadlo, and J. Karpinski. Observation of Leggett's Collective Mode in a Multiband MgB_2 Superconductor. *Phys. Rev. Lett.*, 99:227002, Nov 2007. doi:10.1103/PhysRevLett.99.227002. URL https://link.aps.org/doi/10.1103/PhysRevLett.99.227002. → pages 69, 158

[25] K. Boothby, C. Enderud, T. Lanting, R. Molavi, N. Tsai, M. H. Volkmann, F. Altomare, M. H. Amin, M. Babcock, A. J. Berkley, C. B. Aznar, M. Boschnak, H. Christiani, S. Ejtemaee, B. Evert, M. Gullen, M. Hager, R. Harris, E. Hoskinson, J. P. Hilton, K. Jooya, A. Huang, M. W. Johnson, A. D. King, E. Ladizinsky, R. Li, A. MacDonald, T. M. Fernandez, R. Neufeld, M. Norouzpour, T. Oh, I. Ozfidan, P. Paddon, I. Perminov, G. Poulin-Lamarre, T. Prescott, J. Raymond, M. Reis, C. Rich, A. Roy, H. S. Esfahani, Y. Sato, B. Sheldan, A. Smirnov, L. J. Swenson, J. Whittaker, J. Yao, A. Yarovoy, and P. I. Bunyk. Architectural considerations in the design of a third-generation superconducting quantum annealing processor, 2021. URL https://arxiv.org/abs/2108.02322. → page 124

[26] F. Boschini, E. da Silva Neto, E. Razzoli, M. Zonno, S. Peli, R. Day, M. Michiardi, M. Schneider, B. Zwartsenberg, P. Nigge, et al. Collapse of superconductivity in cuprates via ultrafast quenching of phase coherence. *Nature materials*, 17(5):416–420, 2018. → page 45

[27] D. A. Browne and K. Levin. Collective modes in charge-density-wave superconductors. *Phys. Rev. B*, 28:4029–4032, Oct 1983. doi:10.1103/PhysRevB.28.4029. URL https://link.aps.org/doi/10.1103/PhysRevB.28.4029. → page 85

[28] O. Can, T. Tummuru, R. P. Day, I. Elfimov, A. Damascelli, and M. Franz. High-temperature topological superconductivity in twisted double-layer copper oxides. *Nature Physics*, 17(4): 519–524, Feb. 2021. doi:10.1038/s41567-020-01142-7. URL https://doi.org/10.1038/s41567-020-01142-7. → pages xxi, 16, 98, 99, 100, 102, 103, 105, 106, 108, 109, 113, 114

[29] Y. Cao, V. Fatemi, S. Fang, K. Watanabe, T. Taniguchi, E. Kaxiras, and P. Jarillo-Herrero. Unconventional superconductivity in magic-angle graphene superlattices. *Nature 2018 556:7699*, 556:43–50, 3 2018. ISSN 1476-4687. doi:10.1038/nature26160. URL https://www.nature.com/articles/nature26160. → pages 97, 98

[30] R. V. Carlson and A. M. Goldman. Superconducting Order-Parameter Fluctuations below T_c. *Phys. Rev. Lett.*, 31:880–883, Oct 1973. doi:10.1103/PhysRevLett.31.880. URL https://link.aps.org/doi/10.1103/PhysRevLett.31.880. → pages 73, 95

[31] T. Cea and L. Benfatto. Nature and Raman signatures of the Higgs amplitude mode in the coexisting superconducting and charge-density-wave state. *Phys. Rev. B*, 90:224515, Dec 2014. doi:10.1103/PhysRevB.90.224515. URL https://link.aps.org/doi/10.1103/PhysRevB.90.224515. → pages 45, 70, 76, 85, 86, 87, 95

[32] T. Cea and L. Benfatto. Signature of the Leggett mode in the A_{1g} Raman response: From MgB_2 to iron-based superconductors. *Phys. Rev. B*, 94:064512, Aug 2016. doi:10.1103/PhysRevB.94.064512. URL https://link.aps.org/doi/10.1103/PhysRevB.94.064512. → pages 44, 45, 53, 64, 69

[33] T. Cea, C. Castellani, G. Seibold, and L. Benfatto. Nonrelativistic Dynamics of the Amplitude (Higgs) Mode in Superconductors. *Phys. Rev. Lett.*, 115:157002, Oct 2015. doi:10.1103/PhysRevLett.115.157002. URL https://link.aps.org/doi/10.1103/PhysRevLett.115.157002. → page 28

[34] T. Cea, C. Castellani, and L. Benfatto. Nonlinear optical effects and third-harmonic generation in superconductors: Cooper pairs versus Higgs mode contribution. *Phys. Rev. B*, 93:180507(R), May 2016. doi:10.1103/PhysRevB.93.180507. URL https://link.aps.org/doi/10.1103/PhysRevB.93.180507. → pages 33, 48, 53, 70, 74, 75, 76, 77, 78, 153, 165

[35] T. Cea, P. Barone, C. Castellani, and L. Benfatto. Polarization dependence of the third-harmonic generation in multiband superconductors. *Physical Review B*, 97(9):094516, mar 2018. ISSN 24699969. doi:10.1103/PhysRevB.97.094516. URL https://journals.aps.org/prb/abstract/10.1103/PhysRevB.97.094516. → pages 38, 51

[36] J. Chiles, E. G. Arnault, C.-C. Chen, T. F. Q. Larson, L. Zhao, K. Watanabe, T. Taniguchi, F. Amet, and G. Finkelstein. Nonreciprocal Supercurrents in a Field-Free Graphene Josephson Triode. *Nano Letters*, 0(0):null, 0. doi:10.1021/acs.nanolett.3c01276. URL https://doi.org/10.1021/acs.nanolett.3c01276. PMID: 37191404. → page 117

[37] H. Chu, M.-J. Kim, K. Katsumi, S. Kovalev, R. D. Dawson, L. Schwarz, N. Yoshikawa, G. Kim, D. Putzky, Z. Z. Li, H. Raffy, S. Germanskiy, J.-C. Deinert, N. Awari, I. Ilyakov, B. Green, M. Chen, M. Bawatna, G. Cristiani, G. Logvenov, Y. Gallais, A. V. Boris, B. Keimer, A. P. Schnyder, D. Manske, M. Gensch, Z. Wang, R. Shimano, and S. Kaiser. Phase-resolved Higgs response in superconducting cuprates. *Nat. Commun.*, 11(1):1793, 2020. ISSN 2041-1723. doi:10.1038/s41467-020-15613-1. → pages 1, 37, 39, 70, 85, 95

[38] H. Chu, S. Kovalev, Z. X. Wang, L. Schwarz, T. Dong, L. Feng, R. Haenel, M.-J. Kim, P. Shabestari, L. P. Hoang, K. Honasoge, R. D. Dawson, D. Putzky, G. Kim, M. Puviani, M. Chen, N. Awari, A. N. Ponomaryov, I. Ilyakov, M. Bluschke, F. Boschini, M. Zonno, S. Zhdanovich, M. Na, G. Christiani, G. Logvenov, D. J. Jones, A. Damascelli, M. Minola, B. Keimer, D. Manske, N. Wang, J.-C. Deinert, and S. Kaiser. Fano interference between collective modes in cuprate high-Tc superconductors. *Nature Communications*, 14(1):1343, 2023. doi:10.1038/s41467-023-36787-4. URL https://doi.org/10.1038/s41467-023-36787-4. → page 39

[39] S. L. Cooper and K. E. Gray. *Physical Properties of High Temperature Superconductors IV*. World Scientific, 1994. doi:10.1142/2244. URL https://www.worldscientific.com/doi/abs/10.1142/2244. → pages 99, 101

[40] S. T. Cundiff, A. D. Bristow, M. Siemens, H. Li, G. Moody, D. Karaiskaj, X. Dai, and T. Zhang. Optical 2-D Fourier transform spectroscopy of excitons in semiconductor nanostructures. *IEEE Journal of Selected Topics in Quantum Electronics*, 18(1):318–328, 2011. → page 45

[41] A. Daido, Y. Ikeda, and Y. Yanase. Intrinsic Superconducting Diode Effect. *Phys. Rev. Lett.*, 128: 037001, Jan 2022. doi:10.1103/PhysRevLett.128.037001. URL https://link.aps.org/doi/10.1103/PhysRevLett.128.037001. → page 116

[42] A. Damascelli, Z. Hussain, and Z.-X. Shen. Angle-resolved photoemission studies of the cuprate superconductors. *Rev. Mod. Phys.*, 75:473–541, Apr 2003. doi:10.1103/RevModPhys.75.473. URL https://link.aps.org/doi/10.1103/RevModPhys.75.473. → page 109

[43] M. Davydova, S. Prembabu, and L. Fu. Universal Josephson diode effect. *Science Advances*, 8(23): eabo0309, 2022. doi:10.1126/sciadv.abo0309. URL https://www.science.org/doi/abs/10.1126/sciadv.abo0309. → page 116

[44] J. Demsar. Non-equilibrium Phenomena in Superconductors Probed by Femtosecond Time-Domain Spectroscopy. *Journal of Low Temperature Physics*, 201(5-6):676–709, Apr. 2020. doi:10.1007/s10909-020-02461-y. URL https://doi.org/10.1007/s10909-020-02461-y. → pages xix, 61, 63

[45] T. P. Devereaux and R. Hackl. Inelastic light scattering from correlated electrons. *Reviews of modern physics*, 79(1):175, 2007. → page 45

[46] B. Felderhof and G. Marowsky. Linear optics of polarization sheets. *Applied Physics B*, 43(3): 161–166, 1987. → page 38

[47] O. Fischer, M. Kugler, I. Maggio-Aprile, C. Berthod, and C. Renner. Scanning tunneling spectroscopy of high-temperature superconductors. *Rev. Mod. Phys.*, 79:353–419, Mar 2007. doi:10.1103/RevModPhys.79.353. URL https://link.aps.org/doi/10.1103/RevModPhys.79.353. → page 109

[48] Y. V. Fominov and D. S. Mikhailov. Asymmetric higher-harmonic SQUID as a Josephson diode. *Phys. Rev. B*, 106:134514, Oct 2022. doi:10.1103/PhysRevB.106.134514. URL https://link.aps.org/doi/10.1103/PhysRevB.106.134514. → page 116

[49] N. E. Frattini, U. Vool, S. Shankar, A. Narla, K. M. Sliwa, and M. H. Devoret. 3-wave mixing Josephson dipole element. *Applied Physics Letters*, 110(22):222603, 2017. doi:10.1063/1.4984142. URL https://doi.org/10.1063/1.4984142. → page 117

[50] J. K. Freericks. An introduction to many-body Green's functions in and out of equilibrium, 2019. URL https://arxiv.org/abs/1907.11302. → page 25

[51] F. Gabriele, M. Udina, and L. Benfatto. Non-linear Terahertz driving of plasma waves in layered cuprates. *Nature Communications*, 12(1):752, 2021. ISSN 2041-1723. doi:10.1038/s41467-021-21041-6. → pages 70, 95

[52] S. Ghosh, V. Patil, A. Basu, Kuldeep, D. A. Jangade, R. Kulkarni, A. Thamizhavel, and M. M. Deshmukh. High-temperature superconducting diode, 2022. URL https://arxiv.org/abs/2210.11256. → page 117

[53] V. L. Ginzburg and L. D. Landau. On the theory of superconductivity. In *On superconductivity and superfluidity*, pages 113–137. Springer, 2009. → page 3

[54] F. Giorgianni, T. Cea, C. Vicario, C. P. Hauri, W. K. Withanage, X. Xi, and L. Benfatto. Leggett mode controlled by light pulses. *Nat. Phys.*, 15(4):341–346, 2019. doi:10.1038/s41567-018-0385-4. → pages 1, 37, 38, 158

[55] F. Giubileo, D. Roditchev, W. Sacks, R. Lamy, D. X. Thanh, J. Klein, S. Miraglia, D. Fruchart, J. Marcus, and P. Monod. Two-Gap State Density in MgB_2: A True Bulk Property Or A Proximity Effect? *Phys. Rev. Lett.*, 87:177008, Oct 2001. doi:10.1103/PhysRevLett.87.177008. URL https://link.aps.org/doi/10.1103/PhysRevLett.87.177008. → page 61

[56] M. J. Graf, D. Rainer, and J. A. Sauls. Coupled two-dimensional Fermi liquids as a model for layered superconductors: Basic equations and elementary results. *Phys. Rev. B*, 47:12089–12098, May 1993. doi:10.1103/PhysRevB.47.12089. URL https://link.aps.org/doi/10.1103/PhysRevB.47.12089. → page 99

[57] V. Guritanu, A. B. Kuzmenko, D. van der Marel, S. M. Kazakov, N. D. Zhigadlo, and J. Karpinski. Anisotropic optical conductivity and two colors of MgB_2. *Phys. Rev. B*, 73:104509, Mar 2006. doi:10.1103/PhysRevB.73.104509. URL https://link.aps.org/doi/10.1103/PhysRevB.73.104509. → page 50

[58] R. Haenel, P. Froese, D. Manske, and L. Schwarz. Time-resolved optical conductivity and Higgs oscillations in two-band dirty superconductors. *Phys. Rev. B*, 104:134504, Oct 2021. doi:10.1103/PhysRevB.104.134504. URL https://link.aps.org/doi/10.1103/PhysRevB.104.134504. → pages 44, 70, 79, 80

[59] K. Halterman, M. Alidoust, R. Smith, and S. Starr. Supercurrent diode effect, spin torques, and robust zero-energy peak in planar half-metallic trilayers. *Phys. Rev. B*, 105:104508, Mar 2022. doi:10.1103/PhysRevB.105.104508. URL https://link.aps.org/doi/10.1103/PhysRevB.105.104508. → page 116

[60] A. Hamill, B. Heischmidt, E. Sohn, D. Shaffer, K.-T. Tsai, X. Zhang, X. Xi, A. Suslov, H. Berger, L. Forró, F. J. Burnell, J. Shan, K. F. Mak, R. M. Fernandes, K. Wang, and V. S. Pribiag. Two-fold symmetric superconductivity in few-layer NbSe2. *Nature Physics*, 17(8):949–954, 2021. doi:10.1038/s41567-021-01219-x. URL https://doi.org/10.1038/s41567-021-01219-x. → page 15

[61] P. Hamm and M. Zanni. *Concepts and Methods of 2D Infrared Spectroscopy*. Cambridge University Press, 2011. doi:10.1017/CBO9780511675935. → page 45

[62] W. N. Hardy, D. A. Bonn, D. C. Morgan, R. Liang, and K. Zhang. Precision measurements of the temperature dependence of λ in $YBa_2Cu_3O_{6.95}$: Strong evidence for nodes in the gap function. *Phys. Rev. Lett.*, 70:3999–4002, Jun 1993. doi:10.1103/PhysRevLett.70.3999. URL https://link.aps.org/doi/10.1103/PhysRevLett.70.3999. → page 101

[63] R. Harris, J. Johansson, A. J. Berkley, M. W. Johnson, T. Lanting, S. Han, P. Bunyk, E. Ladizinsky, T. Oh, I. Perminov, E. Tolkacheva, S. Uchaikin, E. M. Chapple, C. Enderud, C. Rich, M. Thom, J. Wang, B. Wilson, and G. Rose. Experimental demonstration of a robust and scalable flux qubit. *Phys. Rev. B*, 81:134510, Apr 2010. doi:10.1103/PhysRevB.81.134510. URL https://link.aps.org/doi/10.1103/PhysRevB.81.134510. → page 124

[64] P. W. Higgs. Broken Symmetries and the Masses of Gauge Bosons. *Phys. Rev. Lett.*, 13:508–509, Oct 1964. doi:10.1103/PhysRevLett.13.508. URL https://link.aps.org/doi/10.1103/PhysRevLett.13.508. → page 1

[65] J. P. Hinton, J. D. Koralek, Y. M. Lu, A. Vishwanath, J. Orenstein, D. A. Bonn, W. N. Hardy, and R. Liang. New collective mode in $YBa_2Cu_3O_{6+x}$ observed by time-domain reflectometry. *Phys. Rev. B*, 88:060508, Aug 2013. doi:10.1103/PhysRevB.88.060508. URL https://link.aps.org/doi/10.1103/PhysRevB.88.060508. → page 85

[66] H. Hirori, A. Doi, F. Blanchard, and K. Tanaka. Single-cycle terahertz pulses with amplitudes exceeding 1 MV/cm generated by optical rectification in LiNbO 3. *Applied Physics Letters*, 98(9): 091106, 2011. → page 37

[67] P. J. Hirschfeld and N. Goldenfeld. Effect of strong scattering on the low-temperature penetration depth of a d-wave superconductor. *Phys. Rev. B*, 48:4219–4222, Aug 1993. doi:10.1103/PhysRevB.48.4219. URL https://link.aps.org/doi/10.1103/PhysRevB.48.4219. → page 101

[68] S. Hoshino, R. Wakatsuki, K. Hamamoto, and N. Nagaosa. Nonreciprocal charge transport in two-dimensional noncentrosymmetric superconductors. *Phys. Rev. B*, 98:054510, Aug 2018. doi:10.1103/PhysRevB.98.054510. URL https://link.aps.org/doi/10.1103/PhysRevB.98.054510. → page 116

[69] A. Hosseini, S. Kamal, D. A. Bonn, R. Liang, and W. N. Hardy. c-Axis Electrodynamics of $YBa_2Cu_3O_{7-\delta}$. *Physical Review Letters*, 81(6):1298–1301, aug 1998. doi:10.1103/physrevlett.81.1298. URL https://journals.aps.org/prl/abstract/10.1103/PhysRevLett.81.1298. → page 101

[70] J. Hu, C. Wu, and X. Dai. Proposed Design of a Josephson Diode. *Phys. Rev. Lett.*, 99:067004, Aug 2007. doi:10.1103/PhysRevLett.99.067004. URL https://link.aps.org/doi/10.1103/PhysRevLett.99.067004. → page 116

[71] M. Iavarone, G. Karapetrov, A. E. Koshelev, W. K. Kwok, G. W. Crabtree, D. G. Hinks, W. N. Kang, E.-M. Choi, H. J. Kim, H.-J. Kim, and S. I. Lee. Two-Band Superconductivity in MgB_2. *Phys. Rev. Lett.*, 89:187002, Oct 2002. doi:10.1103/PhysRevLett.89.187002. URL https://link.aps.org/doi/10.1103/PhysRevLett.89.187002. → page 61

[72] S. Ilić and F. S. Bergeret. Theory of the Supercurrent Diode Effect in Rashba Superconductors with Arbitrary Disorder. *Phys. Rev. Lett.*, 128:177001, Apr 2022. doi:10.1103/PhysRevLett.128.177001. URL https://link.aps.org/doi/10.1103/PhysRevLett.128.177001. → pages 116, 117

[73] J. Jiang, M. Milošević, Y.-L. Wang, Z.-L. Xiao, F. Peeters, and Q.-H. Chen. Field-Free Superconducting Diode in a Magnetically Nanostructured Superconductor. *Phys. Rev. Applied*, 18: 034064, Sep 2022. doi:10.1103/PhysRevApplied.18.034064. URL https://link.aps.org/doi/10.1103/PhysRevApplied.18.034064. → page 116

[74] D. M. Jonas. Two-Dimensional Femtosecond Spectroscopy. *Annual Review of Physical Chemistry*, 54(1):425–463, 2003. doi:10.1146/annurev.physchem.54.011002.103907. URL https://doi.org/10.1146/annurev.physchem.54.011002.103907. PMID: 12626736. → page 45

[75] T. Jujo. Two-Photon Absorption by Impurity Scattering and Amplitude Mode in Conventional Superconductors. *Journal of the Physical Society of Japan*, 84(11):114711, 2015. doi:10.7566/JPSJ.84.114711. URL https://doi.org/10.7566/JPSJ.84.114711. → page 79

[76] S.-O. Kaba and D. Sénéchal. Group-theoretical classification of superconducting states of strontium ruthenate. *Phys. Rev. B*, 100:214507, Dec 2019. doi:10.1103/PhysRevB.100.214507. URL https://link.aps.org/doi/10.1103/PhysRevB.100.214507. → pages 9, 100

[77] R. A. Kaindl, M. A. Carnahan, J. Orenstein, D. S. Chemla, H. M. Christen, H.-Y. Zhai, M. Paranthaman, and D. H. Lowndes. Far-Infrared Optical Conductivity Gap in Superconducting MgB_2 Films. *Phys. Rev. Lett.*, 88:027003, Dec 2001. doi:10.1103/PhysRevLett.88.027003. URL https://link.aps.org/doi/10.1103/PhysRevLett.88.027003. → page 61

[78] T. Kamatani, S. Kitamura, N. Tsuji, R. Shimano, and T. Morimoto. Optical response of the Leggett mode in multiband superconductors in the linear response regime. *Phys. Rev. B*, 105:094520, Mar

2022. doi:10.1103/PhysRevB.105.094520. URL https://link.aps.org/doi/10.1103/PhysRevB.105.094520. → pages 14, 15

[79] H. Kamerlingh Onnes. The Superconductivity of Mercury. *Comm. Phys. Lab. Univ. Leiden*, 122: 122–124, 1911. → page 2

[80] K. Katsumi, N. Tsuji, Y. I. Hamada, R. Matsunaga, J. Schneeloch, R. D. Zhong, G. D. Gu, H. Aoki, Y. Gallais, and R. Shimano. Higgs Mode in the d-Wave Superconductor $Bi_2Sr_2CaCu_2O_{8+x}$ Driven by an Intense Terahertz Pulse. *Phys. Rev. Lett.*, 120:117001, Mar 2018. doi:10.1103/PhysRevLett.120.117001. URL https://link.aps.org/doi/10.1103/PhysRevLett.120.117001. → pages 1, 37

[81] K. Katsumi, Z. Z. Li, H. Raffy, Y. Gallais, and R. Shimano. Superconducting fluctuations probed by the Higgs mode in $Bi_2Sr_2CaCu_2O_{8+x}$ thin films. *Phys. Rev. B*, 102:054510, Aug 2020. doi:10.1103/PhysRevB.102.054510. URL https://link.aps.org/doi/10.1103/PhysRevB.102.054510. → pages 1, 37

[82] M.-J. Kim, S. Kovalev, M. Udina, R. Haenel, G. Kim, M. Puviani, G. Cristiani, I. Ilyakov, T. V. A. G. de Oliveira, A. Ponomaryov, J.-C. Deinert, G. Logvenov, B. Keimer, D. Manske, L. Benfatto, and S. Kaiser. Tracing the dynamics of superconducting order via transient third harmonic generation, 2023. → pages xvii, 37, 41

[83] R. A. Klemm and S. H. Liu. Role of Normal Layers in Penetration Depth Determinations of the Pairing State in High- T_c Superconductors. *Phys. Rev. Lett.*, 74:2343–2346, Mar 1995. doi:10.1103/PhysRevLett.74.2343. URL https://link.aps.org/doi/10.1103/PhysRevLett.74.2343. → page 101

[84] A. A. Kopasov, A. G. Kutlin, and A. S. Mel'nikov. Geometry controlled superconducting diode and anomalous Josephson effect triggered by the topological phase transition in curved proximitized nanowires. *Phys. Rev. B*, 103:144520, Apr 2021. doi:10.1103/PhysRevB.103.144520. URL https://link.aps.org/doi/10.1103/PhysRevB.103.144520. → page 116

[85] J. Kortus, I. I. Mazin, K. D. Belashchenko, V. P. Antropov, and L. L. Boyer. Superconductivity of metallic Boron in MgB2. *Physical Review Letters*, 86(20):4656–4659, may 2001. ISSN 00319007. doi:10.1103/PhysRevLett.86.4656. URL https://journals.aps.org/prl/abstract/10.1103/PhysRevLett.86.4656. → pages xvii, 44, 61

[86] S. Kovalev, T. Dong, L.-Y. Shi, C. Reinhoffer, T.-Q. Xu, H.-Z. Wang, Y. Wang, Z.-Z. Gan, S. Germanskiy, J.-C. Deinert, I. Ilyakov, P. H. M. van Loosdrecht, D. Wu, N.-L. Wang, J. Demsar, and Z. Wang. Band-selective third-harmonic generation in superconducting MgB_2: Possible evidence for the Higgs amplitude mode in the dirty limit. *Phys. Rev. B*, 104:L140505, Oct 2021. doi:10.1103/PhysRevB.104.L140505. URL https://link.aps.org/doi/10.1103/PhysRevB.104.L140505. → pages 1, 37, 39, 48, 61, 68, 95, 158

[87] H. Krull, D. Manske, G. S. Uhrig, and A. P. Schnyder. Signatures of nonadiabatic BCS state dynamics in pump-probe conductivity. *Phys. Rev. B*, 90:014515, Jul 2014. doi:10.1103/PhysRevB.90.014515. URL http://link.aps.org/doi/10.1103/PhysRevB.90.014515. → pages 37, 59, 70

[88] H. Krull, N. Bittner, G. S. Uhrig, D. Manske, and A. P. Schnyder. Coupling of Higgs and Leggett modes in non-equilibrium superconductors. *Nat. Commun.*, 7:11921, 2016. doi:10.1038/ncomms11921.

[89] A. Kumar and A. F. Kemper. Higgs oscillations in time-resolved optical conductivity. *Phys. Rev. B*, 100:174515, Nov 2019. doi:10.1103/PhysRevB.100.174515. URL https://link.aps.org/doi/10.1103/PhysRevB.100.174515. → page 37

[90] J. Lee, W. Lee, G. Y. Kim, Y. B. Choi, J. Park, S. Jang, G. Gu, S. Y. Choi, G. Y. Cho, G. H. Lee, and H. J. Lee. Twisted van der Waals Josephson Junction Based on a High-Tc Superconductor. *Nano Letters*, 21:10469–10477, 12 2021. ISSN 15306992. doi:10.1021/ACS.NANOLETT.1C03906/SUPPL_FILE/NL1C03906_SI_001.PDF. URL https://pubs.acs.org/doi/abs/10.1021/acs.nanolett.1c03906. → page 98

[91] A. J. Leggett. Number-Phase Fluctuations in Two-Band Superconductors. *Prog. Theor. Phys.*, 36(5): 901–930, 11 1966. ISSN 0033-068X. doi:10.1143/PTP.36.901. URL https://doi.org/10.1143/PTP.36.901. → pages 2, 48

[92] A. Leitenstorfer, S. Hunsche, J. Shah, M. Nuss, and W. Knox. Detectors and sources for ultrabroadband electro-optic sampling: Experiment and theory. *Applied physics letters*, 74(11): 1516–1518, 1999. → page 37

[93] J. Li, L. Wang, J. Liu, R. Li, Z. Zhang, and X.-Q. Chen. Topological phonons in graphene. *Physical Review B*, 101(8):081403, 2020. → page 126

[94] J.-X. Lin, P. Siriviboon, H. D. Scammell, S. Liu, D. Rhodes, K. Watanabe, T. Taniguchi, J. Hone, M. S. Scheurer, and J. I. A. Li. Zero-field superconducting diode effect in small-twist-angle trilayer graphene. *Nature Physics*, 18(10):1221–1227, 2022. doi:10.1038/s41567-022-01700-1. URL https://doi.org/10.1038/s41567-022-01700-1. → pages 116, 117

[95] P. B. Littlewood and C. M. Varma. Gauge-Invariant Theory of the Dynamical Interaction of Charge Density Waves and Superconductivity. *Phys. Rev. Lett.*, 47:811, Sep 1981. doi:10.1103/PhysRevLett.47.811. URL https://link.aps.org/doi/10.1103/PhysRevLett.47.811. → page 85

[96] J. Lu, X. Li, H. Y. Hwang, B. K. Ofori-Okai, T. Kurihara, T. Suemoto, and K. A. Nelson. Coherent Two-dimensional Terahertz Magnetic Resonance Spectroscopy of Collective Spin Waves. *Physical review letters*, 118(20):207204, 2017. → page 45

[97] Y.-Y. Lyu, J. Jiang, Y.-L. Wang, Z.-L. Xiao, S. Dong, Q.-H. Chen, M. V. Milošević, H. Wang, R. Divan, J. E. Pearson, P. Wu, F. M. Peeters, and W.-K. Kwok. Superconducting diode effect via conformal-mapped nanoholes. *Nature Communications*, 12(1):2703, 2021. doi:10.1038/s41467-021-23077-0. URL https://doi.org/10.1038/s41467-021-23077-0. → page 116

[98] F. Mahmood, D. Chaudhuri, S. Gopalakrishnan, R. Nandkishore, and N. Armitage. Observation of a marginal Fermi glass. *Nature Physics*, 17(5):627–631, 2021. → page 45

[99] S. Maiti and P. J. Hirschfeld. Collective modes in superconductors with competing s- and d-wave interactions. *Phys. Rev. B*, 92:094506, Sep 2015. doi:10.1103/PhysRevB.92.094506. URL https://link.aps.org/doi/10.1103/PhysRevB.92.094506. → page 89

[100] S. Maiti, T. A. Maier, T. Böhm, R. Hackl, and P. J. Hirschfeld. Probing the Pairing Interaction and Multiple Bardasis-Schrieffer Modes Using Raman Spectroscopy. *Phys. Rev. Lett.*, 117:257001, Dec 2016. doi:10.1103/PhysRevLett.117.257001. URL https://link.aps.org/doi/10.1103/PhysRevLett.117.257001. → page 89

[101] A. Maksymowicz. Natural units via linear algebra. *American Journal of Physics*, 44:295, 6 1998. ISSN 0002-9505. doi:10.1119/1.10470. URL https://aapt.scitation.org/doi/abs/10.1119/1.10470. → page 146

[102] R. Matsunaga and R. Shimano. Nonequilibrium BCS State Dynamics Induced by Intense Terahertz Pulses in a Superconducting NbN Film. *Phys. Rev. Lett.*, 109:187002, Oct 2012. doi:10.1103/PhysRevLett.109.187002. URL https://link.aps.org/doi/10.1103/PhysRevLett.109.187002. → page 61

[103] R. Matsunaga, Y. I. Hamada, K. Makise, Y. Uzawa, H. Terai, Z. Wang, and R. Shimano. Higgs Amplitude Mode in the BCS Superconductors $Nb_{1-x}Ti_xN$ Induced by Terahertz Pulse Excitation. *Phys. Rev. Lett.*, 111:057002, Jul 2013. doi:10.1103/PhysRevLett.111.057002. URL http://link.aps.org/doi/10.1103/PhysRevLett.111.057002. → pages 1, 37, 40, 55, 56, 57, 58, 59, 61, 70

[104] R. Matsunaga, N. Tsuji, H. Fujita, A. Sugioka, K. Makise, Y. Uzawa, H. Terai, Z. Wang, H. Aoki, and R. Shimano. Light-induced collective pseudospin precession resonating with Higgs mode in a superconductor. *Science*, 345(6201):1145, 2014. ISSN 0036-8075. doi:10.1126/science.1254697. URL http://science.sciencemag.org/content/345/6201/1145. → pages 1, 37, 48, 95

[105] R. Matsunaga, N. Tsuji, K. Makise, H. Terai, H. Aoki, and R. Shimano. Polarization-resolved terahertz third-harmonic generation in a single-crystal superconductor NbN: Dominance of the Higgs mode beyond the BCS approximation. *Phys. Rev. B*, 96:020505, Jul 2017. doi:10.1103/PhysRevB.96.020505. URL https://link.aps.org/doi/10.1103/PhysRevB.96.020505. → pages 39, 70

[106] D. C. Mattis and J. Bardeen. Theory of the Anomalous Skin Effect in Normal and Superconducting Metals. *Phys. Rev.*, 111:412–417, Jul 1958. doi:10.1103/PhysRev.111.412. URL https://link.aps.org/doi/10.1103/PhysRev.111.412. → pages 48, 50, 56

[107] M.-A. Méasson, Y. Gallais, M. Cazayous, B. Clair, P. Rodière, L. Cario, and A. Sacuto. Amplitude Higgs mode in the $2H - NbSe_2$ superconductor. *Phys. Rev. B*, 89:060503(R), Feb 2014. doi:10.1103/PhysRevB.89.060503. URL https://link.aps.org/doi/10.1103/PhysRevB.89.060503. → pages 85, 95

[108] W. Meissner and R. Ochsenfeld. Ein neuer Effekt bei Eintritt der Supraleitfähigkeit. *Naturwissenschaften*, 21(44):787–788, 1933. → page 3

[109] K. Misaki and N. Nagaosa. Theory of the nonreciprocal Josephson effect. *Phys. Rev. B*, 103:245302, Jun 2021. doi:10.1103/PhysRevB.103.245302. URL https://link.aps.org/doi/10.1103/PhysRevB.103.245302. → page 116

[110] A. Moor, A. F. Volkov, and K. B. Efetov. Amplitude Higgs Mode and Admittance in Superconductors with a Moving Condensate. *Phys. Rev. Lett.*, 118:047001, Jan 2017. doi:10.1103/PhysRevLett.118.047001. URL https://link.aps.org/doi/10.1103/PhysRevLett.118.047001. → page 148

[111] S. Mukamel. Multidimensional Femtosecond Correlation Spectroscopies of Electronic and Vibrational Excitations. *Annual Review of Physical Chemistry*, 51(1):691–729, 2000. doi:10.1146/annurev.physchem.51.1.691. URL https://doi.org/10.1146/annurev.physchem.51.1.691. PMID: 11031297. → page 45

[112] S. Mukamel, A. Piryatinski, and V. Chernyak. Two-dimensional Raman echoes: femtosecond view of molecular structure and vibrational coherence. *Accounts of chemical research*, 32(2):145–154, 1999. → page 46

[113] M. A. Müller and I. M. Eremin. Signatures of Bardasis-Schrieffer mode excitation in third-harmonic generated currents. *Phys. Rev. B*, 104:144508, Oct 2021. doi:10.1103/PhysRevB.104.144508. URL https://link.aps.org/doi/10.1103/PhysRevB.104.144508. → page 38

[114] M. A. Müller, P. A. Volkov, I. Paul, and I. M. Eremin. Collective modes in pumped unconventional superconductors with competing ground states. *Phys. Rev. B*, 100:140501, Oct 2019. doi:10.1103/PhysRevB.100.140501. URL https://link.aps.org/doi/10.1103/PhysRevB.100.140501. → pages 70, 89, 92

[115] Y. Murotani and R. Shimano. Nonlinear optical response of collective modes in multiband superconductors assisted by nonmagnetic impurities. *Phys. Rev. B*, 99:224510, Jun 2019. doi:10.1103/PhysRevB.99.224510. URL https://link.aps.org/doi/10.1103/PhysRevB.99.224510. → pages 44, 48, 49, 50, 53, 70, 79, 153, 155

[116] Y. Murotani, N. Tsuji, and H. Aoki. Theory of light-induced resonances with collective Higgs and Leggett modes in multiband superconductors. *Phys. Rev. B*, 95:104503, Mar 2017. doi:10.1103/PhysRevB.95.104503. URL https://link.aps.org/doi/10.1103/PhysRevB.95.104503. → pages 44, 64, 70, 95, 158

[117] J. Nagamatsu, N. Nakagawa, T. Muranaka, Y. Zenitani, and J. Akimitsu. Superconductivity at 39 K in magnesium diboride. *nature*, 410(6824):63–64, 2001. → page 3

[118] K. S. Novoselov, A. Mishchenko, A. Carvalho, and A. H. C. Neto. 2D materials and van der Waals heterostructures. *Science*, 353, 7 2016. ISSN 10959203. doi:10.1126/science.aac9439. URL https://www.science.org/doi/abs/10.1126/science.aac9439. → page 97

[119] T. Ozawa, H. M. Price, A. Amo, N. Goldman, M. Hafezi, L. Lu, M. C. Rechtsman, D. Schuster, J. Simon, O. Zilberberg, et al. Topological photonics. *Reviews of Modern Physics*, 91(1):015006, 2019. → page 126

[120] B. Pal1, A. Chakraborty, P. K. Sivakumar, M. Davydova, A. K. Gopi, A. K. Pandeya, J. A. Krieger, Y. Zhang, M. Date, S. Ju, N. Yuan, N. B. M. Schröter, L. Fu, and S. S. P. Parkin. Josephson diode effect from Cooper pair momentum in a topological semimetal. 2021. doi:10.48550/ARXIV.2112.11285. URL https://arxiv.org/abs/2112.11285. → page 116

[121] S. H. Pan, J. P. O'Neal, R. L. Badzey, C. Chamon, H. Ding, J. R. Engelbrecht, Z. Wang, H. Eisaki, S. Uchida, A. K. Gupta, K.-W. Ng, E. W. Hudson, K. M. Lang, and J. C. Davis. Microscopic electronic inhomogeneity in the high-Tc superconductor Bi2Sr2CaCu2O8+x. *Nature*, 413(6853): 282–285, Sept. 2001. doi:10.1038/35095012. URL https://doi.org/10.1038/35095012. → page 113

[122] C. Panagopoulos, T. Xiang, W. Anukool, J. Cooper, Y. Wang, and C. Chu. Superfluid response in monolayer high-Tc cuprates. *Physical Review B*, 67(22):220502, 2003. doi:10.1103/physrevb.67.220502. URL https://doi.org/10.1103/physrevb.67.220502. → page 101

[123] T. Papenkort, V. M. Axt, and T. Kuhn. Coherent dynamics and pump-probe spectra of BCS superconductors. *Phys. Rev. B*, 76:224522, Dec 2007. doi:10.1103/PhysRevB.76.224522. URL http://link.aps.org/doi/10.1103/PhysRevB.76.224522. → pages 37, 70

[124] D. Pekker and C. Varma. Amplitude/Higgs Modes in Condensed Matter Physics. *Annu. Rev. Condens. Matter Phys.*, 6(1):269–297, 2015. doi:10.1146/annurev-conmatphys-031214-014350. URL https://doi.org/10.1146/annurev-conmatphys-031214-014350. → pages 47, 48, 72, 73, 144

[125] M. Peskin and D. Schroeder. *An Introduction To Quantum Field Theory*. Frontiers in Physics. Avalon Publishing, 1995. ISBN 9780813345437. → page 144

[126] S. Pinon, V. Kaladzhyan, and C. Bena. Surface Green's functions and boundary modes using impurities: Weyl semimetals and topological insulators. *Phys. Rev. B*, 101:115405, Mar 2020. doi:10.1103/PhysRevB.101.115405. URL https://link.aps.org/doi/10.1103/PhysRevB.101.115405. → pages 107, 172

[127] N. R. Poniatowski, J. B. Curtis, A. Yacoby, and P. Narang. Spectroscopic signatures of time-reversal symmetry breaking superconductivity. *Communications Physics 2022 5:1*, 5:1–11, 2 2022. ISSN 2399-3650. doi:10.1038/s42005-022-00819-0. URL https://www.nature.com/articles/s42005-022-00819-0. → pages 100, 126

[128] M. Puviani, L. Schwarz, X.-X. Zhang, S. Kaiser, and D. Manske. Current-assisted Raman activation of the Higgs mode in superconductors. *Phys. Rev. B*, 101:220507(R), Jun 2020. doi:10.1103/PhysRevB.101.220507. URL https://link.aps.org/doi/10.1103/PhysRevB.101.220507. → page 148

[129] M. Puviani, R. Haenel, and D. Manske. Quench-drive spectroscopy and high-harmonic generation in BCS superconductors. *Phys. Rev. B*, 107:094501, Mar 2023. doi:10.1103/PhysRevB.107.094501. URL https://link.aps.org/doi/10.1103/PhysRevB.107.094501. → page 37

[130] R. Radtke and K. Levin. Origin of intrinsic Josephson coupling in the cuprates and its relation to order parameter symmetry: An incoherent hopping model. *Physica C: Superconductivity*, 250(3): 282–294, 1995. ISSN 0921-4534. doi:https://doi.org/10.1016/0921-4534(95)00359-2. URL https://www.sciencedirect.com/science/article/pii/0921453495003592. → pages 99, 101

[131] R. J. Radtke and V. N. Kostur. c-Axis penetration depth in the cuprates: Additional evidence for incoherent hopping. *Canadian Journal of Physics*, 75(6):363–374, jun 1997. doi:10.1139/p96-150. URL https://cdnsciencepub.com/doi/10.1139/p96-150.

[132] R. J. Radtke, V. N. Kostur, and K. Levin. Theory of the c-axis penetration depth in the cuprates. *Phys. Rev. B*, 53:R522–R525, Jan 1996. doi:10.1103/PhysRevB.53.R522. URL https://link.aps.org/doi/10.1103/PhysRevB.53.R522. → pages 99, 101

[133] E. C. Regan, D. Wang, C. Jin, M. I. B. Utama, B. Gao, X. Wei, S. Zhao, W. Zhao, Z. Zhang, K. Yumigeta, M. Blei, J. D. Carlström, K. Watanabe, T. Taniguchi, S. Tongay, M. Crommie, A. Zettl, and F. Wang. Mott and generalized Wigner crystal states in WSe2/WS2 moiré superlattices. *Nature 2020 579:7799*, 579:359–363, 3 2020. ISSN 1476-4687. doi:10.1038/s41586-020-2092-4. URL https://www.nature.com/articles/s41586-020-2092-4. → page 97

[134] R. P. Saichu, I. Mahns, A. Goos, S. Binder, P. May, S. G. Singer, B. Schulz, A. Rusydi, J. Unterhinninghofen, D. Manske, P. Guptasarma, M. S. Williamsen, and M. Rübhausen. Two-Component Dynamics of the Order Parameter of High Temperature $Bi_2Sr_2CaCu_2\mathbf{O}_{8+\delta}$ Superconductors Revealed by Time-Resolved Raman Scattering. *Phys. Rev. Lett.*, 102:177004, Apr 2009. doi:10.1103/PhysRevLett.102.177004. URL https://link.aps.org/doi/10.1103/PhysRevLett.102.177004. → page 45

[135] D. J. Scalapino and T. P. Devereaux. Collective d-wave exciton modes in the calculated Raman spectrum of Fe-based superconductors. *Phys. Rev. B*, 80:140512, Oct 2009. doi:10.1103/PhysRevB.80.140512. URL https://link.aps.org/doi/10.1103/PhysRevB.80.140512. → page 89

[136] H. D. Scammell, J. I. A. Li, and M. S. Scheurer. Theory of zero-field superconducting diode effect in twisted trilayer graphene. *2D Materials*, 9(2):025027, mar 2022. doi:10.1088/2053-1583/ac5b16. URL https://dx.doi.org/10.1088/2053-1583/ac5b16. → pages 116, 117

[137] A. Schmid and G. Schön. Collective Oscillations in a Dirty Superconductor. *Phys. Rev. Lett.*, 34: 941–943, Apr 1975. doi:10.1103/PhysRevLett.34.941. URL https://link.aps.org/doi/10.1103/PhysRevLett.34.941. → pages 73, 95

[138] L. Schwarz, B. Fauseweh, and D. Manske. Momentum-resolved analysis of condensate dynamic and Higgs oscillations in quenched superconductors with time-resolved ARPES. *Phys. Rev. B*, 101: 224510, Jun 2020. doi:10.1103/PhysRevB.101.224510. URL https://link.aps.org/doi/10.1103/PhysRevB.101.224510. → page 45

[139] L. Schwarz, B. Fauseweh, N. Tsuji, N. Cheng, N. Bittner, H. Krull, M. Berciu, G. S. Uhrig, A. P. Schnyder, S. Kaiser, and D. Manske. Classification and characterization of nonequilibrium Higgs modes in unconventional superconductors. *Nat. Commun.*, 11(1):287, 2020. ISSN 2041-1723. doi:10.1038/s41467-019-13763-5. → pages 2, 37, 70

[140] G. Seibold, L. Benfatto, and C. Castellani. Application of the Mattis-Bardeen theory in strongly disordered superconductors. *Phys. Rev. B*, 96:144507, Oct 2017. doi:10.1103/PhysRevB.96.144507. URL https://link.aps.org/doi/10.1103/PhysRevB.96.144507. → page 48

[141] G. Seibold, M. Udina, C. Castellani, and L. Benfatto. Third harmonic generation from collective modes in disordered superconductors. *Phys. Rev. B*, 103:014512, Jan 2021. doi:10.1103/PhysRevB.103.014512. URL https://link.aps.org/doi/10.1103/PhysRevB.103.014512. → pages 48, 50, 69

[142] G. Seibold, M. Udina, C. Castellani, and L. Benfatto. Third harmonic generation from collective modes in disordered superconductors. *Phys. Rev. B*, 103:014512, Jan 2021. doi:10.1103/PhysRevB.103.014512. URL https://link.aps.org/doi/10.1103/PhysRevB.103.014512. → pages 79, 95

[143] S. G. Sharapov, V. P. Gusynin, and H. Beck. Effective action approach to the Leggett's mode in two-band superconductors. *European Physical Journal B*, 30(2):45–51, nov 2002. ISSN 14346028. doi:10.1140/epjb/e2002-00356-9. URL https://link.springer.com/article/10.1140/epjb/e2002-00356-9. → page 51

[144] D. E. Sheehy, T. P. Davis, and M. Franz. Unified theory of the ab-plane and c-axis penetration depths of underdoped cuprates. *Phys. Rev. B*, 70:054510, Aug 2004. doi:10.1103/PhysRevB.70.054510. URL https://link.aps.org/doi/10.1103/PhysRevB.70.054510. → pages 99, 101, 114

[145] R. Shimano and N. Tsuji. Higgs Mode in Superconductors. *Annual Review of Condensed Matter Physics*, 11(1):103–124, 2020. doi:10.1146/annurev-conmatphys-031119-050813. URL https://doi.org/10.1146/annurev-conmatphys-031119-050813. → page 1

[146] J. Shin, S. Son, J. Yun, G. Park, K. Zhang, Y. J. Shin, J.-G. Park, and D. Kim. Magnetic Proximity-Induced Superconducting Diode Effect and Infinite Magnetoresistance in van der Waals Heterostructure, 2021. URL https://arxiv.org/abs/2111.05627. → page 116

[147] M. Silaev. Nonlinear electromagnetic response and Higgs-mode excitation in BCS superconductors with impurities. *Phys. Rev. B*, 99:224511, Jun 2019. doi:10.1103/PhysRevB.99.224511. URL https://link.aps.org/doi/10.1103/PhysRevB.99.224511. → pages 48, 49, 50, 79, 95

[148] X.-Y. Song, Y.-H. Zhang, and A. Vishwanath. Doping a moiré Mott insulator: A $t - J$ model study of twisted cuprates. *Phys. Rev. B*, 105:L201102, May 2022. doi:10.1103/PhysRevB.105.L201102. URL https://link.aps.org/doi/10.1103/PhysRevB.105.L201102. → pages 98, 102, 114

[149] R. Sooryakumar and M. V. Klein. Raman Scattering by Superconducting-Gap Excitations and Their Coupling to Charge-Density Waves. *Phys. Rev. Lett.*, 45:660, Aug 1980. doi:10.1103/PhysRevLett.45.660. URL https://link.aps.org/doi/10.1103/PhysRevLett.45.660. → page 85

[150] R. S. Souto, M. Leijnse, and C. Schrade. Josephson Diode Effect in Supercurrent Interferometers. *Phys. Rev. Lett.*, 129:267702, Dec 2022. doi:10.1103/PhysRevLett.129.267702. URL https://link.aps.org/doi/10.1103/PhysRevLett.129.267702. → page 116

[151] Z. Sun, M. M. Fogler, D. N. Basov, and A. J. Millis. Collective modes and terahertz near-field response of superconductors. *Phys. Rev. Research*, 2:023413, Jun 2020. doi:10.1103/PhysRevResearch.2.023413. URL https://link.aps.org/doi/10.1103/PhysRevResearch.2.023413. → pages 27, 38, 89, 90

[152] Y. Tanaka, B. Lu, and N. Nagaosa. Theory of giant diode effect in d-wave superconductor junctions on the surface of a topological insulator. *Phys. Rev. B*, 106:214524, Dec 2022. doi:10.1103/PhysRevB.106.214524. URL https://link.aps.org/doi/10.1103/PhysRevB.106.214524. → page 116

[153] A. Tokmakoff, M. J. Lang, D. Larsen, G. R. Fleming, V. Chernyak, and S. Mukamel. Two-dimensional Raman spectroscopy of vibrational interactions in liquids. *Physical review letters*, 79(14):2702, 1997. → page 46

[154] D. H. Torchinsky, F. Mahmood, A. T. Bollinger, I. Božović, and N. Gedik. Fluctuating charge-density waves in a cuprate superconductor. *Nat. Mater.*, 12(5):387–391, 2013. ISSN 1476-4660. doi:10.1038/nmat3571. → page 85

[155] S. Tsuda, T. Yokoya, Y. Takano, H. Kito, A. Matsushita, F. Yin, J. Itoh, H. Harima, and S. Shin. Definitive Experimental Evidence for Two-Band Superconductivity in MgB_2. *Phys. Rev. Lett.*, 91: 127001, Sep 2003. doi:10.1103/PhysRevLett.91.127001. URL https://link.aps.org/doi/10.1103/PhysRevLett.91.127001. → page 61

[156] N. Tsuji and H. Aoki. Theory of Anderson pseudospin resonance with Higgs mode in superconductors. *Phys. Rev. B*, 92:064508, Aug 2015. doi:10.1103/PhysRevB.92.064508. URL https://link.aps.org/doi/10.1103/PhysRevB.92.064508. → pages 36, 37, 53, 70, 72, 73

[157] N. Tsuji and Y. Nomura. Higgs-mode resonance in third harmonic generation in NbN superconductors: Multiband electron-phonon coupling, impurity scattering, and polarization-angle dependence. *Phys. Rev. Research*, 2:043029, Oct 2020. doi:10.1103/PhysRevResearch.2.043029. URL https://link.aps.org/doi/10.1103/PhysRevResearch.2.043029. → pages 48, 49, 50, 79, 95

[158] T. Tummuru, S. Plugge, and M. Franz. Josephson effects in twisted cuprate bilayers. *Physical Review B*, 105(6):064501, aug 2022. ISSN 2469-9950. doi:https://doi.org/10.1103/PhysRevB.105.064501. URL http://arxiv.org/abs/2108.13457. → pages 98, 100

[159] M. Turlakov and A. J. Leggett. Interlayer c-axis transport in the normal state of cuprates. *Phys. Rev. B*, 63:064518, Jan 2001. doi:10.1103/PhysRevB.63.064518. URL https://link.aps.org/doi/10.1103/PhysRevB.63.064518. → page 99

[160] M. Udina, T. Cea, and L. Benfatto. Theory of coherent-oscillations generation in terahertz pump-probe spectroscopy: From phonons to electronic collective modes. *Physical Review B*, 100 (16):165131, oct 2019. ISSN 24699969. doi:10.1103/PhysRevB.100.165131. URL https://journals.aps.org/prb/abstract/10.1103/PhysRevB.100.165131. → pages 37, 59

[161] A. Van Otterlo, D. S. Golubev, A. D. Zaikin, and G. Blatter. Dynamics and effective actions of BCS superconductors. *European Physical Journal B*, 10(1):131–143, jul 1999. ISSN 14346028. doi:10.1007/s100510050836. URL https://link.springer.com/article/10.1007/s100510050836. → page 51

[162] C. M. Varma. Higgs Boson in Superconductors. *J. Low Temp. Phys.*, 126(3):901–909, Feb 2002. ISSN 1573-7357. doi:10.1023/A:1013890507658. URL https://doi.org/10.1023/A:1013890507658. → pages 47, 73

[163] C. Vaswani, J. H. Kang, M. Mootz, L. Luo, X. Yang, C. Sundahl, D. Cheng, C. Huang, R. H. J. Kim, Z. Liu, Y. G. Collantes, E. E. Hellstrom, I. E. Perakis, C. B. Eom, and J. Wang. Light quantum control of persisting Higgs modes in iron-based superconductors. *Nature Communications*, 12(1): 258, 2021. doi:10.1038/s41467-020-20350-6. URL https://doi.org/10.1038/s41467-020-20350-6. → pages 1, 37

[164] A. F. Volkov and S. M. Kogan. Collisionless relaxation of the energy gap in superconductors. *JETP*, 38:1018, 1974. URL http://www.jetp.ac.ru/cgi-bin/e/index/e/38/5/p1018?a=list. → pages 70, 76

[165] P. A. Volkov, S. Y. F. Zhao, N. Poccia, X. Cui, P. Kim, and J. H. Pixley. Josephson effects in twisted nodal superconductors, 2021. → pages 98, 99

[166] R. Wakatsuki, Y. Saito, S. Hoshino, Y. M. Itahashi, T. Ideue, M. Ezawa, Y. Iwasa, and N. Nagaosa. Nonreciprocal charge transport in noncentrosymmetric superconductors. *Science Advances*, 3(4): e1602390, 2017. doi:10.1126/sciadv.1602390. URL https://www.science.org/doi/abs/10.1126/sciadv.1602390. → page 116

[167] X. Wang, H. Zhang, and X. Wang. Topological magnonics: A paradigm for spin-wave manipulation and device design. *Physical Review Applied*, 9(2):024029, 2018. → page 126

[168] Y. Wang, T. P. Devereaux, and C.-C. Chen. Theory of time-resolved Raman scattering in correlated systems: Ultrafast engineering of spin dynamics and detection of thermalization. *Phys. Rev. B*, 98: 245106, Dec 2018. doi:10.1103/PhysRevB.98.245106. URL https://link.aps.org/doi/10.1103/PhysRevB.98.245106. → page 45

[169] F. Wu, T. Lovorn, E. Tutuc, and A. H. Macdonald. Hubbard Model Physics in Transition Metal Dichalcogenide Moiré Bands. *Physical Review Letters*, 121:026402, 7 2018. ISSN 10797114. doi:10.1103/PHYSREVLETT.121.026402/FIGURES/4/MEDIUM. URL https://journals.aps.org/prl/abstract/10.1103/PhysRevLett.121.026402. → page 97

[170] H. Wu, Y. Wang, Y. Xu, P. K. Sivakumar, C. Pasco, U. Filippozzi, S. S. P. Parkin, Y.-J. Zeng, T. McQueen, and M. N. Ali. The field-free Josephson diode in a van der Waals heterostructure. *Nature*, 604(7907):653–656, Apr 2022. ISSN 1476-4687. doi:10.1038/s41586-022-04504-8. URL https://doi.org/10.1038/s41586-022-04504-8. → page 116

[171] Q. Wu and X.-C. Zhang. Free-space electro-optic sampling of terahertz beams. *Applied Physics Letters*, 67(24):3523–3525, 1995. → page 37

[172] X. Xi, Z. Wang, W. Zhao, J.-H. Park, K. T. Law, H. Berger, L. Forró, J. Shan, and K. F. Mak. Ising pairing in superconducting nbse2 atomic layers. *Nature Physics*, 12(2):139–143, 2016. doi:10.1038/nphys3538. URL https://doi.org/10.1038/nphys3538. → page 15

[173] T. Xiang and J. M. Wheatley. cAxis Superfluid Response of Copper Oxide Superconductors. *Physical Review Letters*, 77(22):4632–4635, nov 1996. doi:10.1103/physrevlett.77.4632. URL https://journals.aps.org/prl/abstract/10.1103/PhysRevLett.77.4632. → pages 98, 101

[174] K. Yasuda, H. Yasuda, T. Liang, R. Yoshimi, A. Tsukazaki, K. S. Takahashi, N. Nagaosa, M. Kawasaki, and Y. Tokura. Nonreciprocal charge transport at topological insulator/superconductor interface. *Nature Communications*, 10(1):2734, Jun 2019. ISSN 2041-1723. doi:10.1038/s41467-019-10658-3. URL https://doi.org/10.1038/s41467-019-10658-3. → page 116

[175] N. F. Q. Yuan and L. Fu. Supercurrent diode effect and finite-momentum superconductors. *Proceedings of the National Academy of Sciences*, 119(15):e2119548119, 2022. doi:10.1073/pnas.2119548119. URL https://www.pnas.org/doi/abs/10.1073/pnas.2119548119. → page 116

[176] E. A. Yuzbashyan and M. Dzero. Dynamical Vanishing of the Order Parameter in a Fermionic Condensate. *Phys. Rev. Lett.*, 96:230404, Jun 2006. doi:10.1103/PhysRevLett.96.230404. URL https://link.aps.org/doi/10.1103/PhysRevLett.96.230404. → page 59

[177] E. A. Yuzbashyan and M. Dzero. Dynamical Vanishing of the Order Parameter in a Fermionic Condensate. *Phys. Rev. Lett.*, 96:230404, Jun 2006. doi:10.1103/PhysRevLett.96.230404. URL https://link.aps.org/doi/10.1103/PhysRevLett.96.230404. → pages 70, 76

[178] E. A. Yuzbashyan, O. Tsyplyatyev, and B. L. Altshuler. Relaxation and Persistent Oscillations of the Order Parameter in Fermionic Condensates. *Phys. Rev. Lett.*, 96:097005, Mar 2006. doi:10.1103/PhysRevLett.96.097005. URL https://link.aps.org/doi/10.1103/PhysRevLett.96.097005. → pages 70, 76

[179] B. Zhai, B. Li, Y. Wen, F. Wu, and J. He. Prediction of ferroelectric superconductors with reversible superconducting diode effect. *Phys. Rev. B*, 106:L140505, Oct 2022. doi:10.1103/PhysRevB.106.L140505. URL https://link.aps.org/doi/10.1103/PhysRevB.106.L140505. → page 116

[180] Y. Zhang, Y. Gu, P. Li, J. Hu, and K. Jiang. General Theory of Josephson Diodes. *Phys. Rev. X*, 12: 041013, Nov 2022. doi:10.1103/PhysRevX.12.041013. URL https://link.aps.org/doi/10.1103/PhysRevX.12.041013. → page 116

[181] S. Y. F. Zhao, N. Poccia, X. Cui, P. A. Volkov, H. Yoo1, R. Engelke, Y. Ronen, R. Zhong, G. Gu, S. Plugge, T. Tummuru, M. Franz, J. H. Pixley, and P. Kim. Emergent Interfacial Superconductivity between Twisted Cuprate Superconductors. *arXiv preprint arXiv:2108.13455*, Jul 2021. URL https://arxiv.org/abs/2108.13455. → page 98

[182] W. Zimmermann, E. H. Brandt, M. Bauer, E. Seider, and L. Genzel. Optical conductivity of BCS superconductors with arbitrary purity. *Physica C*, 183(1-3):99–104, 1991. ISSN 09214534. doi:10.1016/0921-4534(91)90771-P. → page 56

[183] B. Zinkl, K. Hamamoto, and M. Sigrist. Symmetry conditions for the superconducting diode effect in chiral superconductors. *Phys. Rev. Research*, 4:033167, Aug 2022. doi:10.1103/PhysRevResearch.4.033167. URL https://link.aps.org/doi/10.1103/PhysRevResearch.4.033167. → page 116

Appendix A

Higgs mechanism in the Standard Model

While the Higgs mechanism was first discovered in the context of superconductivity [8], it may be most famous for its application in the field of particle physics, where it earned its name. Here, we will give a brief comparison of the terminology used in the two fields and outline some key differences between the Higgs mode in superconductivity and the Standard model [124, 125]. For reference, these differences are summarized in Table A.1.

The Higgs mechanism occurs in gauge theories when a charged field acquires a finite vacuum expectation value. In the case of superconductivity, the relevant quantum field is the complex bosonic Hubbard-Stratonovich field that arises after decoupling a fermionic interaction in the Cooper channel (cf. Sec. 3.1). In the Standard model, the relevant field is the Higgs field, which is a fundamental two-component complex field that transforms under $SU(2)\times U(1)$. Thus, the Higgs field has 4 real components. The superconducting Hubbard-Stratonovich field has $2n$ real components for a n-component order parameter theory.

The quantum fields in superconductivity physically describe the superconducting condensate. In high energy physics, the Higgs field describes the electro-weak condensate which is sometimes also referred to as *Higgs condensate*. A superconductor condenses at temperatures ranging from mK to below room temperature, depending on the specific material, while the critical condensation temperature of the Standard Model is estimated to be at $250\,\mathrm{GeV} \approx 3\times 10^{15}\,\mathrm{K}$.

For superconductors, one out of the $2n$ degrees of freedom of the quantum field (the Goldstone phase mode) is absorbed to produce a massive photon, leaving only one mode (the Higgs mode) as a physical degree of freedom of the Hubbard-Stratonovich fields. In the Standard Model, three out of four components of the Higgs field combine with the Z^0, W^+, W^- gauge bosons and make them massive. Only a single quantum field remains, its excitations are referred to as Higgs particles. In the Standard Model, the photon remains as the only massless gauge boson. No such massless gauge particle exists in the context of superconductivity.

	Superconductivity	Standard Model
Quantum field	Hubbard-Stratonovich field	Higgs field (fundamental)
# of real components of quantum field	2 (or $2n$ for n-band superconductor)	4
Gauge group	$U(1)$	$SU(2) \times U(1)$
Massive gauge boson	photon (plasmon)	Z^0, W^+, W^- bosons
Massless gauge boson	N/A	photon
Condensate	superconducting condensate	electro-weak condensate
T_C	mK to K	$\sim 3 \times 10^{15}$ K

Table A.1: Comparison of Higgs mechanism terminology in superconductivity and the Standard Model

Appendix B

Systems of units

In the literature, certain natural constants are often set to one. In this thesis, e.g., we have sometimes made used of $\hbar = k_B = m_e = 2\Delta = 1$.

This does not mean that these natural constants (and the energy gap 2Δ) are equated to one. Instead it means that these quantities are defined as the base units of our unit system. For example, from now on we measure mass in units of m_e instead of kg, energy in units of 2Δ, action in units of $\hbar$, and so on.

What, then, is the unit that we measure distances in? The answer is readily determined using the methods of linear algebra [101].

There are five base quantities in the SI system: length l, mass m, time t, temperature T, and current A. The corresponding base units are $\{\mathrm{m}, \mathrm{kg}, \mathrm{s}, \mathrm{K}, \mathrm{A}\}$, respectively. It is useful to think of the natural constants as a vector in unit space. For example, $\hbar$ has units $[\hbar]_{SI} = \frac{\mathrm{kgm}^2}{\mathrm{s}}$. We therefore represent it by the vector

$$[\hbar]_{SI} = (2, 1, -1, 0, 0) \ ,$$

where the vector components indicate the power of the SI units $\{\mathrm{m}, \mathrm{kg}, \mathrm{s}, \mathrm{K}, \mathrm{A}\}$. The other constants can be represented by

$$\begin{aligned} [k_B]_{SI} &= (2, 1, -2, -1, 0) \\ [m_e]_{SI} &= (0, 1, 0, 0, 0) \\ [e]_{SI} &= (0, 0, 1, 0, 1) \\ [2\Delta]_{SI} &= (2, 1, -2, 0, 0) \ . \end{aligned}$$

For a set of natural constants to be a valid choice for a unit system, they need to be linearly independent, i.e. the five vectors need to span a five-dimensional space. We may arrange the basis vectors as columns in a

matrix

$$C = \begin{pmatrix} 2 & 2 & 0 & 0 & 2 \\ 1 & 1 & 1 & 0 & 1 \\ -1 & -2 & 0 & 1 & -2 \\ 0 & -1 & 0 & 0 & 0 \\ 0 & 0 & 0 & 1 & 0 \end{pmatrix} .$$

Linear independece can then readily be checked by the condition $\det C \neq 0$. If we want to know what SI units the quantity $\hbar$ is composed of, we represent $\hbar$ by the unit vector $[\hbar]_U = \mathbf{e}_1$ and multiply it: $C\,[\hbar]_U = [\hbar]_{SI}$. The same holds for all other natural constants.

What do the five base SI units look like in terms of the U base? To answer this question we simply invert the matrix C:

$$C^{-1} = \begin{pmatrix} 1 & 0 & 1 & 0 & -1 \\ 0 & 0 & 0 & -1 & 0 \\ -\frac{1}{2} & 1 & 0 & 0 & 0 \\ 0 & 0 & 0 & 0 & 1 \\ -\frac{1}{2} & 0 & -1 & 1 & 1 \end{pmatrix} .$$

Then the unit of length is $[l]_{SI} = \mathrm{m} = \mathbf{e}_1$ and $[l]_U = C^{-1}[l]_{SI} = (1, 0, -\frac{1}{2}, 0, -\frac{1}{2}) = \hbar\frac{1}{\sqrt{m_e}}\frac{1}{\sqrt{2\Delta}}$. The same holds for the other SI base quantities m, t, T, j. We find that, for the choice of $2\Delta = 2\,\mathrm{meV}$,

$$\begin{aligned} [l]_U &= \frac{\hbar}{\sqrt{m_e 2\Delta}} = 2.76\,\mathrm{nm} \\ [m]_U &= m_e = 9.11 \times 10^{-31}\,\mathrm{kg} \\ [t]_U &= \frac{\hbar}{2\Delta} = 658.3\,\mathrm{fs} \\ [T]_U &= \frac{2\Delta}{k_B} = 116\,\mathrm{K} \\ [j]_U &= = \frac{e2\Delta}{\hbar} = 2.43\,\mu\mathrm{A}\,. \end{aligned}$$

Different units can be constructed from the base units. An appropriate system of units is important for numerical calculations, since small numbers on the order of machine precision can be avoided.

Appendix C

Appendices for Chapter 5

C.1 Derivation of the effective action for a two-band superconductor

The problem is stated with the partition function

$$\mathcal{Z} = \int \mathcal{D}(c^\dagger c) e^{-S} \quad \text{with} \quad S = \int_0^\beta d\tau \left(\sum_{i\mathbf{k}\sigma} c^\dagger_{i\mathbf{k}\sigma} \partial_\tau c_{i\mathbf{k}\sigma} + \mathcal{H} \right) . \tag{C.1}$$

We decouple the interacting term in the pairing channel via the Hubbard Stratonovich transformation

$$\begin{aligned} &\exp\left(\int d\tau \sum_{ij} \left(\sum_{\mathbf{k}} c^\dagger_{i\mathbf{k}\uparrow} c^\dagger_{i-\mathbf{k}\downarrow} \right) U_{ij} \left(\sum_{\mathbf{k}'} c_{j-\mathbf{k}'\downarrow} c_{j\mathbf{k}'\uparrow} \right) \right) \\ &= \int \mathcal{D}(\bar{\Delta}_i \Delta_i) e^{-\int d\tau \left[\sum_{ij} \bar{\Delta}_i U^{-1}_{ij} \Delta_j - \sum_{i\mathbf{k}} \left(\bar{\Delta}_i c_{i\mathbf{k}\uparrow} c_{i-\mathbf{k}\downarrow} + \Delta_i c^\dagger_{i-\mathbf{k}\downarrow} c^\dagger_{i\mathbf{k}\uparrow} \right) \right]} . \end{aligned} \tag{C.2}$$

The bosonic fields $\Delta_i(\tau)$ are complex, i.e. they permits amplitude and phase fluctuations.

Note that $\Delta_i(\tau)$ does not depend on momentum. This is because the usual BCS Hamiltonian, Eq. (5.1), is an approximation of the more general interaction term

$$\sum_{ij\mathbf{k}\mathbf{k}'\mathbf{q}} U_{ij} c^\dagger_{i\mathbf{k}+\mathbf{q}\uparrow} c^\dagger_{i-\mathbf{k}\downarrow} c_{j-\mathbf{k}'\downarrow} c_{j\mathbf{k}'+\mathbf{q}\uparrow} ,$$

where the Cooper pair center of mass momentum is incorporated through the summation over the small variable $\mathbf{q}$. It is interesting to note that a supercurrent can be modelled even in the absence of such a center of mass momentum. In that case, the supercurrent is determined by the static component of the electromagnetic vector potential [110, 128].

We decompose Δ_i into real fields and additional express fluctuation with respect to the meanfield sad-

dlepoint, $\Delta_i(\tau) \to (\Delta_i^{eq} + \Delta_i(\tau))e^{i\theta_i(\tau)}$, $\bar{\Delta}_i(\tau) \to (\Delta_i^{eq} + \Delta_i(\tau))e^{-i\theta_i(\tau)}$. The action is

$$S = \sum_{ij} U_{ij}^{-1} \int d\tau \, \left(\Delta_i^{eq} \Delta_j^{eq} + \Delta_i(\tau)\Delta_j(\tau) \right) e^{-i(\theta_i(\tau)-\theta_j(\tau))} \tag{C.3}$$

$$+ \sum_{i\mathbf{k}\sigma} \int_0^\beta d\tau \left(c_{i\mathbf{k}\sigma}^\dagger \left[\partial_\tau + \xi_{i\mathbf{k}} \right] c_{i\mathbf{k}\sigma} - (\Delta_i^{eq} + \Delta_i(\tau)) e^{-i\theta_i(\tau)} c_{i\mathbf{k}\uparrow} c_{i-\mathbf{k}\downarrow} \right. \tag{C.4}$$

$$\left. -(\Delta_i^{eq} + \Delta_i(\tau)) e^{i\theta_i(\tau)} c_{i-\mathbf{k}\downarrow}^\dagger c_{i\mathbf{k}\uparrow}^\dagger \right) + \int_0^\beta d\tau \, \mathcal{H}_1 \, .$$

Here we have encountered the Josephson coupling term

$$\sum_{ij} U_{ij}^{-1} \Delta_i^{eq} \Delta_j^{eq} e^{-i(\theta_i(\tau)-\theta_j(\tau))}$$

$$= U_{11}^{-1} \left(\Delta_1^{eq}\right)^2 + U_{22}^{-1} \left(\Delta_2^{eq}\right)^2 + 2U_{12}^{-1} \Delta_1^{eq} \Delta_2^{eq} \cos(\theta_1 - \theta_2) \tag{C.5}$$

that induces the Leggett mode. We express the action in the Nambu basis $\Psi_{i\mathbf{k}}^\dagger(\omega_n) = \left(c_{i\mathbf{k}\uparrow}^\dagger \, , c_{i-\mathbf{k}\downarrow} \right)$,

$$S = \sum_{ij} U_{ij}^{-1} \int d\tau \, \left(\Delta_i^{eq} \Delta_j^{eq} + \Delta_i(\tau)\Delta_j(\tau) \right) e^{-i(\theta_i - \theta_j)} \tag{C.6}$$

$$- \sum_{i\mathbf{k}\mathbf{k}'} \int d\tau \Psi_{i\mathbf{k}}^\dagger(\tau) G_i^{-1}(\mathbf{k}\mathbf{k}', \tau) \Psi_{i\mathbf{k}'}(\tau) \, ,$$

where

$$G_i^{-1} = \delta_{\mathbf{k}\mathbf{k}'} \begin{pmatrix} -\partial_\tau - \xi_{i\mathbf{k}} & (\Delta_i^{eq} + \Delta_i(\tau)) e^{i\theta(\tau)} \\ (\Delta_i^{eq} + \Delta_i(\tau)) e^{-i\theta(\tau)} & -\partial_\tau + \xi_{i\mathbf{k}} \end{pmatrix}$$

$$+ J_{i\mathbf{k}\mathbf{k}'} \cdot \mathbf{e} \, A(\tau) \sigma_0 - \frac{s_i e^2}{2m_i} A^2(\tau) \delta_{\mathbf{k}\mathbf{k}'} \sigma_3 \, . \tag{C.7}$$

Integrating out the Fermions gives

$$S = \sum_{ij} U_{ij}^{-1} \int d\tau \, \left(\Delta_i^{eq} \Delta_j^{eq} + \Delta_i(\tau)\Delta_j(\tau) \right) e^{-i(\theta_i - \theta_j)} - \sum_i \mathrm{Tr} \ln \left[-G_i^{-1} \right] \, , \tag{C.8}$$

where the trace is performed over time, momenta, and Nambu indices, but not over band-indices i. To separate amplitude $\Delta_i(\tau)$ and phase $\theta_i(\tau)$ fields, we introduce a local unitary transformation $V_i = \exp(i\theta_i(\tau)\sigma_3/2)$ [2],

$$\mathrm{Tr} \ln \left[-G_i^{-1} \right] = \mathrm{Tr} \ln \left[-G_i^{-1} V_i V_i^\dagger \right] = \mathrm{Tr} \ln \left[-V_i^\dagger G_i^{-1} V_i \right] = \mathrm{Tr} \ln \left[-\tilde{G}_i^{-1} \right] \, . \tag{C.9}$$

We split $\tilde{G}_i^{-1}$ into a meanfield part, $G_{0,i}^{-1}$, and all remaining contributions Σ_i. In frequency space, this gives

$$\tilde{G}_i^{-1} = G_{0,i}^{-1} - \Sigma_i \,, \tag{C.10}$$

$$G_{0,i}^{-1}(\mathbf{k}\omega_n, \mathbf{k}'\omega_m) = \left[i\omega_n - \xi_{i\mathbf{k}}\sigma_3 + \Delta_i^{eq}\sigma_1\right]\delta_{\mathbf{k}\mathbf{k}'}\delta_{\omega_n,\omega_m} \,, \tag{C.11}$$

$$\begin{aligned}\Sigma_i(\mathbf{k}\omega_n, \mathbf{k}'\omega_m) = &-\Delta_i(\omega_n - \omega_m)\sigma_1\delta_{\mathbf{k}\mathbf{k}'} - i\frac{i\omega_n - i\omega_m}{2}\theta_i(\omega_n - \omega_m)\sigma_3\delta_{\mathbf{k}\mathbf{k}'} \\ &- J_{i\mathbf{k}\mathbf{k}'}\cdot\mathbf{e}\,A(\omega_n - \omega_m)\sigma_0 + \frac{s_i e^2}{2m_i}A^2(\omega_n - \omega_m)\delta_{\mathbf{k}\mathbf{k}'}\sigma_3 \,.\end{aligned} \tag{C.12}$$

Note that phase fluctuations θ_i live in the σ_3 channel, i.e. the charge channel.

Next, we expand S at Gaussian level. To compute currents $j\big|_1$ and $j\big|_3$ we additionally keep terms up to fourth order in the classical field A. In expanding the trace, we use

$$\mathrm{Tr}\ln\left(-\tilde{G}^{-1}\right) = \mathrm{Tr}\ln\left(-G_0^{-1}(1 - G_0\Sigma)\right) = \mathrm{Tr}\ln\left(-G_0^{-1}\right) - \mathrm{Tr}\sum_{n=1}^{\infty}\frac{1}{n}\left(G_0\Sigma\right)^n \,. \tag{C.13}$$

The quadratic action is given by the terms

$$S[\Delta_i, \theta_i, A] = S_{MF} + S_\Delta + S_{\Delta,A} + S_\theta + S_{\theta,A} + S_{\text{QP,dia}} + S_{\text{QP,para}} \,, \tag{C.14}$$

which are explicitly

$$S_{MF} = \sum_{ij} U_{ij}^{-1} \Delta_i^{eq} \Delta_j^{eq} - \sum_i \mathrm{Tr} \ln \left[-G_{0,i}^{-1} \right] \tag{C.15}$$

$$\begin{aligned} S_\Delta &= \frac{1}{2} \sum_{ij\Omega_m} \Delta_i \begin{pmatrix} \chi_1^{\sigma_1\sigma_1} + 2U_{22}/\det U & -2U_{12}/\det U \\ -2U_{21}/\det U & \chi_2^{\sigma_1\sigma_1} + 2U_{11}/\det U \end{pmatrix}_{ij} \Delta_j \\ &= \frac{1}{2} \sum_{ij\Omega_m} \Delta_i(-\Omega_m) H_{ij}^{-1}(\Omega_m) \Delta_j(\Omega_m) \end{aligned} \tag{C.16}$$

$$S_{\Delta,A} = -\sum_{i\mathbf{k}\mathbf{k}'} \sum_{\Omega_m\Omega_l} |J_{i\mathbf{k}\mathbf{k}'}|^2 \chi_i^{\sigma_0\sigma_0\sigma_1}(\Omega_m, \Omega_l, \mathbf{k}, \mathbf{k}') A(\Omega_l) A(-\Omega_m - \Omega_l) \Delta(\Omega_m) \tag{C.17}$$

$$\begin{aligned} S_\theta &= -\frac{1}{2} \sum_{ij\Omega_m} \frac{-i\Omega_m}{2} \theta_i \begin{pmatrix} -\chi_1^{\sigma_3\sigma_3} + \frac{\lambda}{\Omega_m^2} & -\frac{\lambda}{\Omega_m^2} \\ -\frac{\lambda}{\Omega_m^2} & -\chi_2^{\sigma_3\sigma_3} + \frac{\lambda}{\Omega_m^2} \end{pmatrix}_{ij} \frac{i\Omega_m}{2} \theta_j \\ &= -\frac{1}{2} \sum_{ij\Omega_m} \frac{-i\Omega_m}{2} \theta_i \left[\begin{pmatrix} -\chi_1^{\sigma_3\sigma_3} & \\ & -\chi_2^{\sigma_3\sigma_3} \end{pmatrix}_{ij} + J_{ij} \right] \frac{i\Omega_m}{2} \theta_j \\ &= \frac{1}{2} \sum_{ij\Omega_m} \frac{-i\Omega_m}{2} \theta_i(-\Omega_m) L_{ij}^{-1}(\Omega_m) \frac{i\Omega_m}{2} \theta_j(\Omega_m) \end{aligned} \tag{C.18}$$

$$S_{\theta,A} = \sum_{i\Omega_m} i \frac{s_i e^2}{2m_i} \mathbf{A}^2(\Omega_m) \chi_i^{\sigma_3\sigma_3}(\Omega_m) \frac{-i\Omega_m}{2} \theta_i(-\Omega_m) \tag{C.19}$$

$$S_{\mathrm{QP,dia}}^{(2)} = -\sum_i \frac{s_i e^2}{2m_i} \chi_i^{\sigma_3} A^2(0) \tag{C.20}$$

$$S_{\mathrm{QP,dia}}^{(4)} = \frac{1}{2} \sum_{i\Omega_m} \left(\frac{s_i e^2}{2m_i} \right)^2 \chi_i^{\sigma_3\sigma_3}(\Omega_m) A^2(\Omega_m) A^2(-\Omega_m) \tag{C.21}$$

$$S_{\mathrm{QP,para}}^{(2)} = \frac{1}{2} \sum_{i\mathbf{k}\mathbf{k}'\Omega_m} |J_{i\mathbf{k}\mathbf{k}'}|^2 \chi_i^{\sigma_0\sigma_0}(\mathbf{k}, \mathbf{k}', \Omega_m) A(\Omega_m) A(-\Omega_m) \tag{C.22}$$

$$\begin{aligned} S_{\mathrm{QP,para}}^{(4)} = \frac{1}{4} \sum_{i\mathbf{k}\mathbf{k}'\mathbf{k}''} \sum_{\Omega_m\Omega_l\Omega_p} & |J_{i\mathbf{k}\mathbf{k}'}|^2 |J_{i\mathbf{k}\mathbf{k}''}|^2 \xi_i(\mathbf{k}, \mathbf{k}', \mathbf{k}'', \Omega_m, \Omega_l, \Omega_p) \\ & \times A(\Omega_m) A(\Omega_l) A(\Omega_p) A(-\Omega_m - \Omega_l - \Omega_p) \,. \end{aligned} \tag{C.23}$$

Here, $\lambda = \frac{8\Delta_1\Delta_2 v}{U_{22} - v^2 U_{11}}$. The Higgs and Leggett terms, Eqs. (C.16-C.19), are diagrammatically shown in Fig. 5.1. The density fluctuation terms, Eqs. (C.20-C.23) are shown in Fig. 5.2. The susceptibilities, given by the fermionic bubbles, are

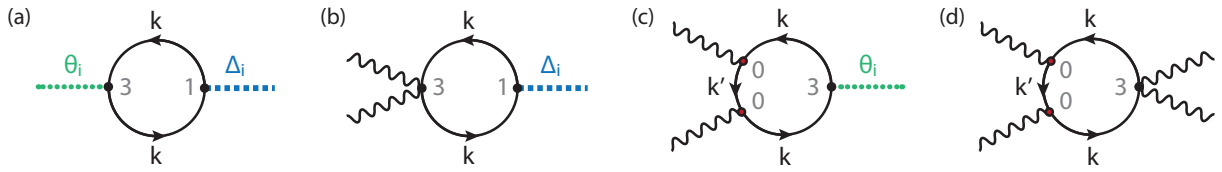

Figure C.1: Additional diagrams following from Eq. (C.8) that vanish in the presence of particle-hole symmetry and a parabolic dispersion.

$$\chi_i^{\sigma_k} = \sum_{\mathbf{k}} \sum_{\omega_n} \mathrm{Tr}\left[G_{0,i}(\omega_n, \mathbf{k})\sigma_k\right] , \tag{C.24}$$

$$\chi_i^{\sigma_k\sigma_l}(\Omega_m, \mathbf{k}, \mathbf{k}') = \sum_{\omega_n} \mathrm{Tr}\left[G_{0,i}(\omega_n, \mathbf{k})\sigma_k G_{0,i}(\omega_n + \Omega_m, \mathbf{k}')\sigma_l\right] , \tag{C.25}$$

$$\chi_i^{\sigma_k\sigma_l}(\Omega_m) = \sum_{\mathbf{k}} \chi_i^{\sigma_k\sigma_l}(\Omega_m, \mathbf{k}, \mathbf{k}) , \tag{C.26}$$

$$\begin{aligned}\chi_i^{\sigma_0\sigma_0\sigma_1}(\Omega_m, \Omega_l, \mathbf{k}, \mathbf{k}') = \sum_{\omega_n} \mathrm{Tr}\big[&G_{0,i}(\omega_n + \Omega_m, \mathbf{k}) G_{0,i}(\omega_n + \Omega_m + \Omega_l, \mathbf{k}') \\ &\times G_{0,i}(\omega_n, \mathbf{k})\sigma_1\big] ,\end{aligned} \tag{C.27}$$

$$\begin{aligned}\xi_i(\mathbf{k}, \mathbf{k}', \mathbf{k}'', \Omega_m, \Omega_l, \Omega_p) = \sum_{\omega_n} \mathrm{Tr}[&G_{0,i}(\omega_n, \mathbf{k}) G_{0,i}(\omega_n + \Omega_m, \mathbf{k}') \\ &\times G_{0,i}(\omega_n + \Omega_m + \Omega_l, \mathbf{k}) G_{0,i}(\omega_n + \Omega_m + \Omega_l + \Omega_p, \mathbf{k}'')] ,\end{aligned} \tag{C.28}$$

We evaluate Matsubara sums in above expressions analytically using the *MatsubaraSum* package developed by [1].

Additional diagrams, that vanish due to particle-hole symmetry, are listed in Fig. C.1. We proceed to integrate out all collective fields. This gives

$$S[A] = S_{MF} + \tilde{S}_\Delta + \tilde{S}_\theta + S_{\text{QP,dia}} + S_{\text{QP,para}} \tag{C.29}$$

with

$$\begin{aligned}\tilde{S}_\Delta = -\frac{1}{2} \sum_{ij\Omega_m} &\left(\sum_{\mathbf{k}\mathbf{k}'\Omega_l} |J_{i\mathbf{k}\mathbf{k}'}|^2 \chi_i^{\sigma_0\sigma_0\sigma_1}(-\Omega_m, \Omega_l, \mathbf{k}, \mathbf{k}') A(\Omega_l) A(\Omega_m - \Omega_l) \right) \\ &\times H_{ij}(\Omega_m) \left(\sum_{\mathbf{k}\mathbf{k}'\Omega_l} |J_{j\mathbf{k}\mathbf{k}'}|^2 \chi_j^{\sigma_0\sigma_0\sigma_1}(\Omega_m, \Omega_l, \mathbf{k}, \mathbf{k}') A(\Omega_l) A(-\Omega_m - \Omega_l) \right)\end{aligned} \tag{C.30}$$

$$\tilde{S}_\theta = \frac{1}{2} \sum_{ij\Omega_m} \frac{s_i e^2}{2m_i} \frac{s_j e^2}{2m_j} A^2(-\Omega_m) A^2(\Omega_m) \chi_i^{\sigma_3\sigma_3}(-\Omega_m) L_{ij}(\Omega_m) \chi_j^{\sigma_3\sigma_3}(\Omega_m) \tag{C.31}$$

We note that phase and fourth order diamagnetic density fluctuation terms combine to give the Leggett

contribution

$$\begin{aligned}\tilde{S}_L &= S^{(4)}_{QP,\text{dia}} + \tilde{S}_\theta \\ &= -\frac{e^4}{2}\sum_{\Omega_m}\frac{\lambda}{4}\left(\frac{s_1}{m_1}-\frac{s_2}{m_2}\right)^2\left[\Omega_n^2-\lambda\frac{\chi_1^{\sigma_3\sigma_3}+\chi_2^{\sigma_3\sigma_3}}{\chi_1^{\sigma_3\sigma_3}\chi_2^{\sigma_3\sigma_3}}\right]^{-1}A^2(-\Omega_m)A^2(\Omega_m)\,.\end{aligned} \tag{C.32}$$

Thus, the zero-energy Goldstone mode does not contribute to the optical response. Above equations, obtained by Gaussian integration, have the diagrammatic representation of an RPA summation shown in Fig. 5.3. For the Higgs propagator this can be seen by expanding

$$H = \left[2U^{-1}+X\right]^{-1} = \frac{U}{2}\sum_{n=0}^{\infty}\left(-X\frac{U}{2}\right)^n\,, \tag{C.33}$$

where $X_{ij} = \chi_i^{\sigma_1\sigma_1}\delta_{ij}$ corresponds to fermionic bubbles and $U_{ij}/2$ corresponds to the to dashed lines. The case of the Leggett mode is analogous. The currents can now, after analytic continuation of all external frequencies, be computed by a functional derivative of the action,

$$j(\omega) = -\frac{\delta S[A]}{\delta A(-\omega)}\,. \tag{C.34}$$

The Mattis-Bardeen approximation enters by replacing

$$\sum_{\mathbf{k}\mathbf{k}'}|J_{i\mathbf{k}\mathbf{k}'}| = N_i(0)^2\int d\epsilon_{\mathbf{k}}d\epsilon_{\mathbf{k}'}\int\frac{d\Omega_{\mathbf{k}}}{4\pi}\frac{d\Omega_{\mathbf{k}'}}{4\pi}\,|J_{i\mathbf{k}\mathbf{k}'}| \tag{C.35}$$

$$\approx N_i(0)^2\int d\epsilon_{\mathbf{k}}d\epsilon_{\mathbf{k}'}\frac{(ev_{F_i})^2}{3N_i(0)}W(\epsilon_{i\mathbf{k}},\epsilon_{i\mathbf{k}'}) \tag{C.36}$$

according to Eq. (5.6). For the fourth-order paramagnetic density fluctuation contribution, Eq. (C.23), we follow Ref. [115] and further approximate

$$\begin{aligned}\sum_{\mathbf{k}\mathbf{k}'\mathbf{k}''}|J_{i\mathbf{k}\mathbf{k}'}|\,|J_{i\mathbf{k}\mathbf{k}''}| \approx N_i(0)^3\int d\epsilon_{\mathbf{k}}d\epsilon_{\mathbf{k}'}d\epsilon_{\mathbf{k}''}&\left(\int\frac{d\Omega_{\mathbf{k}}}{4\pi}\frac{d\Omega_{\mathbf{k}'}}{4\pi}\,|J_{i\mathbf{k}\mathbf{k}'}|\right)\\ &\times\left(\int\frac{d\Omega_{\mathbf{k}}}{4\pi}\frac{d\Omega_{\mathbf{k}''}}{4\pi}\,|J_{i\mathbf{k}\mathbf{k}''}|\right)\,.\end{aligned} \tag{C.37}$$

C.2 Effect of Coulomb interactions

In this section, we will show explicitly that the presence of Coulomb interactions does not alter the results derived above. This is specific to our case of a continuum model with quadratic band dispersion and the assumption of exact particle hole symmetry [34]. When particle hole symmetry is broken, the Coulomb interaction will additionally screen the Higgs mode contribution to the nonlinear current.

We introduce long-range Coulomb interactions with potential $V_q \sim 1/q^2$ and decouple the Coulomb

action in the density channel by means of the Hubbard-Stratonovich transformation

$$\exp\left(\int d\tau \sum_{\mathbf{q}} \left(\sum_{i\mathbf{k}\sigma} c^\dagger_{i\mathbf{k}+\mathbf{q}\sigma} c_{i\mathbf{k}\sigma}\right) V_q \left(\sum_{i\mathbf{k}\sigma} c^\dagger_{i\mathbf{k}-\mathbf{q}\sigma} c_{i\mathbf{k}\sigma}\right)\right)$$
$$= \int \mathcal{D}\rho(\mathbf{q},\tau) \exp\left(-\int d\tau \sum_{\mathbf{q}} \left(\frac{1}{V_q}\rho(\mathbf{q},\tau)\rho(-\mathbf{q},\tau) + \sum_{i\mathbf{k}\sigma} \rho(\mathbf{q},\tau) c^\dagger_{i\mathbf{k}-\mathbf{q}\sigma} c_{i\mathbf{k}\sigma}\right)\right). \tag{C.38}$$

In the presence of long-range Coulomb interactions, the phase action in Eq. (C.18) is modified according to

$$S_\theta = -\frac{1}{2}\sum_{\Omega_n \mathbf{q}} \begin{pmatrix} \delta_{\mathbf{q},0}\frac{-i\Omega_n}{2}\theta_1 \\ \delta_{\mathbf{q},0}\frac{-i\Omega_n}{2}\theta_2 \\ \rho(-\Omega_n,-\mathbf{q}) \end{pmatrix} \begin{pmatrix} -\chi_1 + \frac{\lambda}{\Omega_n^2} & -\frac{\lambda}{\Omega_n^2} & i\chi_1 \\ -\frac{\lambda}{\Omega_n^2} & -\chi_2 + \frac{\lambda}{\Omega_n^2} & i\chi_2 \\ -i\chi_1 & -i\chi_2 & \frac{1}{V_q} - \chi_1 - \chi_2 \end{pmatrix} \begin{pmatrix} \delta_{\mathbf{q},0}\frac{i\Omega_n}{2}\theta_1 \\ \delta_{\mathbf{q},0}\frac{i\Omega_n}{2}\theta_2 \\ \rho(\Omega_n,\mathbf{q}) \end{pmatrix}. \tag{C.39}$$

Here, we have introduced the short notation χ_i for the susceptibility $\chi_i^{\sigma_3\sigma_3}$ defined in Eq. (C.26). The light coupling term of Eq. (C.19) becomes

$$S_{\theta,A} = \sum_{i,\Omega_m} \frac{s_i e^2}{2m_i} A^2(\Omega_m)\chi_i(\rho(-\Omega_m) - i\frac{-i\Omega_n}{2}\theta_i(-\Omega_n)). \tag{C.40}$$

The matrix in Eq. (C.39) has a singular eigenvalue corresponding to the eigenvector $(i,i,1)$. We can therefore reduce the decription to

$$S_\theta = -\frac{1}{2}\sum_{\Omega_n} \begin{pmatrix} \frac{-i\Omega_n}{2}\theta_L \\ \rho - i\frac{-i\Omega_n}{2}\theta_G \end{pmatrix} \begin{pmatrix} -\chi_1 - \chi_2 + \frac{4\lambda}{\Omega_n^2} & -\chi_1 + \chi_2 \\ -\chi_1 + \chi_2 & -\chi_1 - \chi_2 \end{pmatrix} \begin{pmatrix} \frac{i\Omega_n}{2}\theta_L \\ \rho + i\frac{i\Omega_n}{2}\theta_G \end{pmatrix} \tag{C.41}$$

where we have taken the limit $1/V_q = 0$ ($q = 0$) and have defined new variables

$$\theta_G = (\theta_1 + \theta_2)/2 \tag{C.42}$$
$$\theta_L = (\theta_1 - \theta_2)/2\,. \tag{C.43}$$

The light-coupling term Eq. (C.40) becomes

$$S_{\theta,A} = \sum_{\Omega_n} \frac{e^2A^2}{4} \begin{pmatrix} s_1\chi_1/m_1 - s_2\chi_2/m_2 \\ s_1\chi_1/m_1 + s_2\chi_2/m_2 \end{pmatrix} \begin{pmatrix} \frac{-i\Omega_n}{2}\theta_L \\ \rho - i\frac{-i\Omega_n}{2}\theta_G \end{pmatrix} \tag{C.44}$$

and after Gaussian integration we obtain

$$\tilde{S}_\theta = \sum_{\Omega_n} \frac{1}{2}\frac{e^4A^4}{4} \frac{\chi_1\chi_2\left(\chi_1/m_1^2 + \chi_2/m_2^2\right)\Omega_n^2 - \lambda\left(s_1\chi_1/m_1 + s_2\chi_2/m_2\right)^2}{\lambda(\chi_1+\chi_2) - \chi_1\chi_2\Omega_n^2}\,. \tag{C.45}$$

Together with the nonlinear diamagnetic density fluctuation contribution we arrive at the Leggett action $\tilde{S}_L = S^{(4)}_{QP,\text{dia}} + \tilde{S}_\theta$ which identically matches Eq. (C.32) derived in the absence of Coulomb interactions.

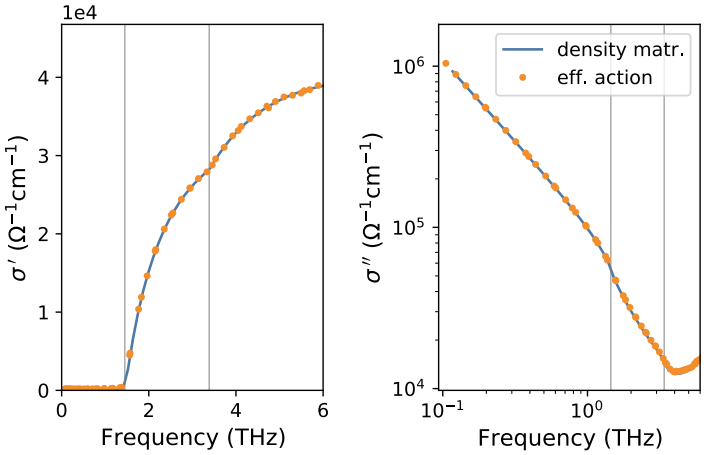

Figure C.2: Real and imaginary part of optical conductivity computed in the time-dependent density matrix formalism (blue lines) and from diagrams Fig. 5.2(a,b) in the effective action approach. There is perfect agreement between the two methods.

C.3 First order currents and optical conductivity

The paramagnetic first order current $j_P\big|_1$ is represented by the diagram in Fig. 5.2(a) and explicitly given by a functional derivative of Eq. (C.22). After analytical continuation and MB substitution one arrives at

$$j_P(-\omega)\big|_1 = A(\omega)\sum_i \frac{v_{F_i}^2}{3N_i(0)}\int d\epsilon d\epsilon' W_i(\epsilon,\epsilon')\chi_i^{\sigma_0\sigma_0}(\omega,\epsilon,\epsilon')\,. \tag{C.46}$$

The diamagnetic first order current $j_P\big|_1$ reads

$$j_D(-\omega)\big|_1 = -A(-\omega)\sum_i \frac{e^2}{m_i}s_i\sum_{\mathbf{k}\sigma}\langle c_{i\mathbf{k}\sigma}^\dagger c_{i\mathbf{k}\sigma}\rangle\,, \tag{C.47}$$

where we have used that $\frac{\delta}{\delta A(\omega)}A^2(0) = \frac{\delta}{\delta A(\omega)}\int d\omega' A(-\omega')A(\omega') = 2A(-\omega)$. Note that the $\mathbf{k}$-sum does not vanish away from the Fermi surface and therefore strongly depends on the numerical cutoff. Here, we follow Murotani [115] and regularize the integral as

$$j_D(-\omega)\big|_1 = A(\omega)\sum_i \frac{e^2 n_i}{m_i}\int d\epsilon d\epsilon' \frac{f(\epsilon)-f(\epsilon')}{\epsilon-\epsilon'}W_i(\epsilon,\epsilon') \tag{C.48}$$

with and Fermi function $f(\epsilon)$ and the band specific carrier density $n_i = k_{F_i}^3/3\pi^2$.

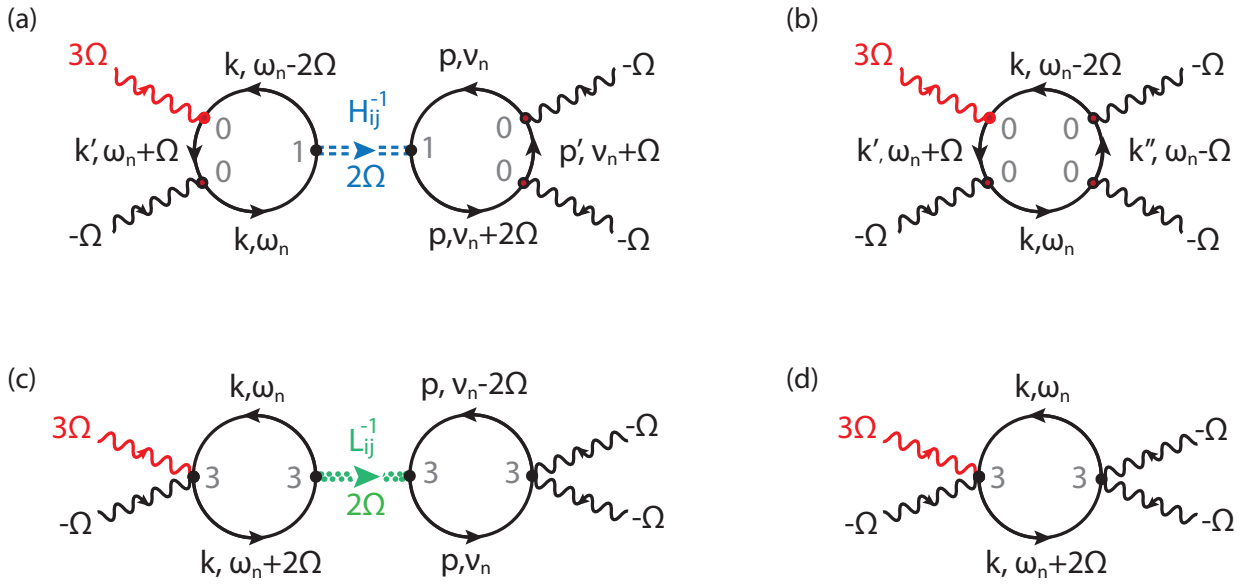

Figure C.3: Diagrammatic representation of THG signal. Red photon legs denote A with respect to which the functional derivative has been performed. Higgs and Leggett propagators (double lines) correspond to an RPA summation shown in Fig. 5.3.

C.4 Third Harmonic Generation

For THG experiments, we are interested in the non-linear current $j(3\Omega)$ evaluated at $\omega = 3\Omega$ where Ω is the dominant frequency of the optical pulse $A(\Omega)$:

$$j(-3\Omega) = -\frac{\delta S[A]}{\delta A(\omega)}\bigg|_{\omega=3\Omega}. \tag{C.49}$$

A diagrammatic representation of Eq. (C.49) is shown in Fig. C.3. The field $A(\omega)$ with respect to which the functional derivative is performed is colored red. All four choices are equivalent. The functional derivative forces the external frequency of the field A to be 3Ω. In principal one now needs to integrate over all remaining external frequencies, while satisfying energy conservation. This can be numerically challenging. Here, we focus instead on the case of a monochromatic field $A(t) = A_0 \cos\Omega t$, $A(\omega) = \frac{A_0}{2}(\delta(\omega-\Omega)+\delta(\omega+\Omega))$ where external fields possess two discrete frequencies $\pm\Omega$. Then energy conservation dictates all remaining external legs to carry frequency $-\Omega$. Note that the energy flow through collective Higgs or Leggett propagators is 2Ω, i.e. THG probes the optical kernel at twice the driving frequency as expected for a non-linear process.

Fig. C.4 shows magnitude and phase of the Higgs contribution to the THG current $j_H(3\Omega)$ as a function of Ω and T for two interband couplings $v = 0.05, 0.4$. Panels (a,b,e,f) correspond to the limit of a dirty π-band and a clean σ-band, whereas the remaining panels are computed for two dirty bands. Both cases are possible descriptions of MgB_2. Yellow spectral lines map out the Higgs resonance that follow $2\Delta_\pi, 2\Delta_\sigma$. In all cases the π-resonance is dominant, although the relative σ-contribution is enhanced in the dirty-dirty limit and for strong v. Increased interband coupling v decreases and broadens the overall Higgs response.

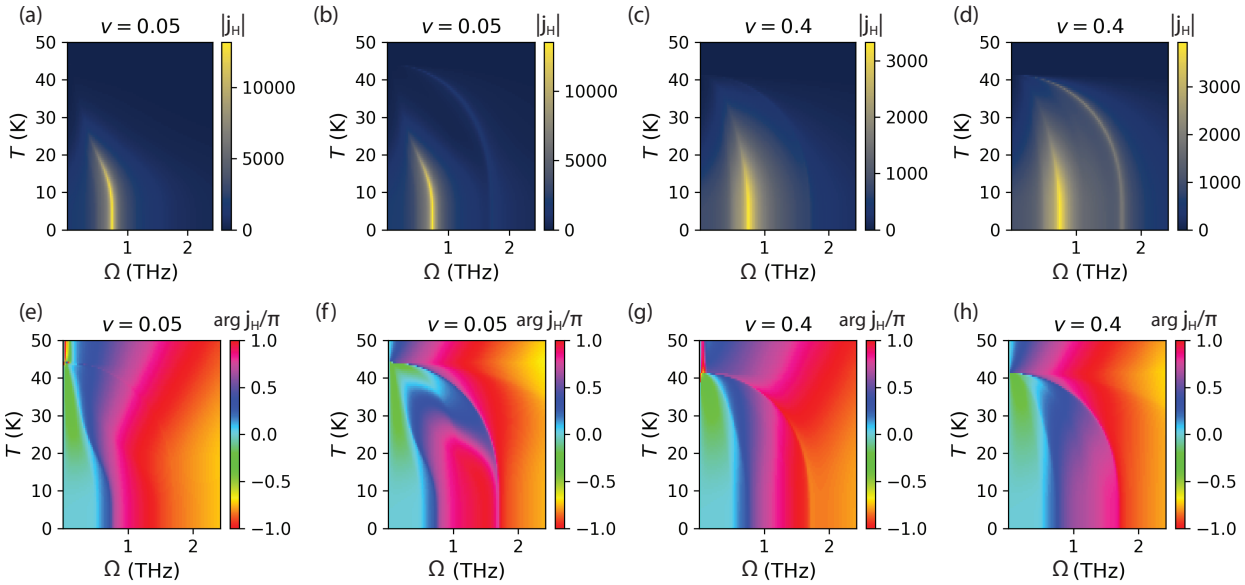

Figure C.4: Magnitude, up to a prefactor, (a-d) and phase (e-h) of Higgs contribution to THG current as a function of driving frequency Ω and temperature T. (a),(c),(e),(g) correspond to the dirty-clean case with $\gamma_\pi = 100\,\mathrm{meV}, \gamma_\sigma = 0.01\,\mathrm{meV}$ and (c,d,g,h) correspond to the dirty-dirty case with $\gamma_\pi = 100\,\mathrm{meV}, \gamma_\sigma = 50\,\mathrm{meV}$.

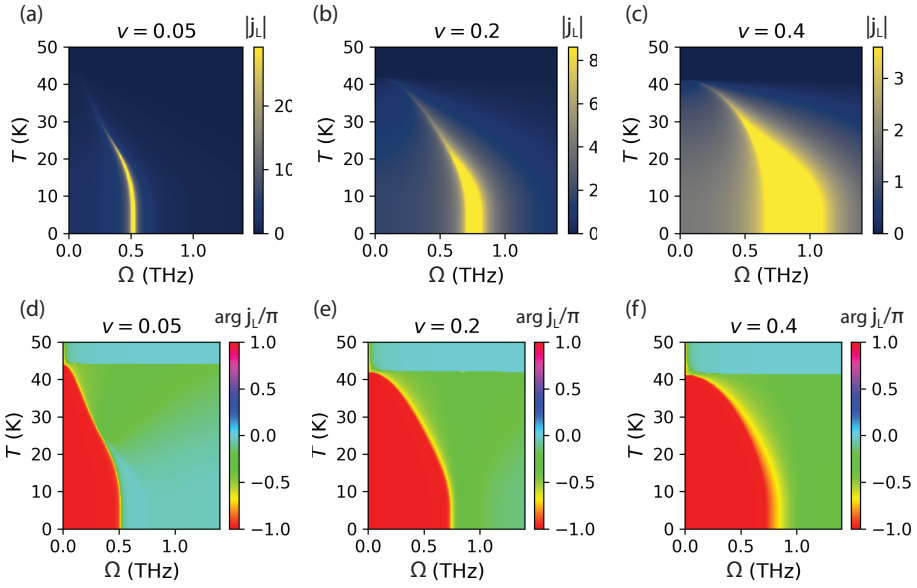

Figure C.5: Magnitude, up to a prefactor, (a-c) and phase (d-f) of Leggett contribution to THG current as a function of driving frequency Ω and temperature T for various interband coupling parameters v as denoted in plot titles.

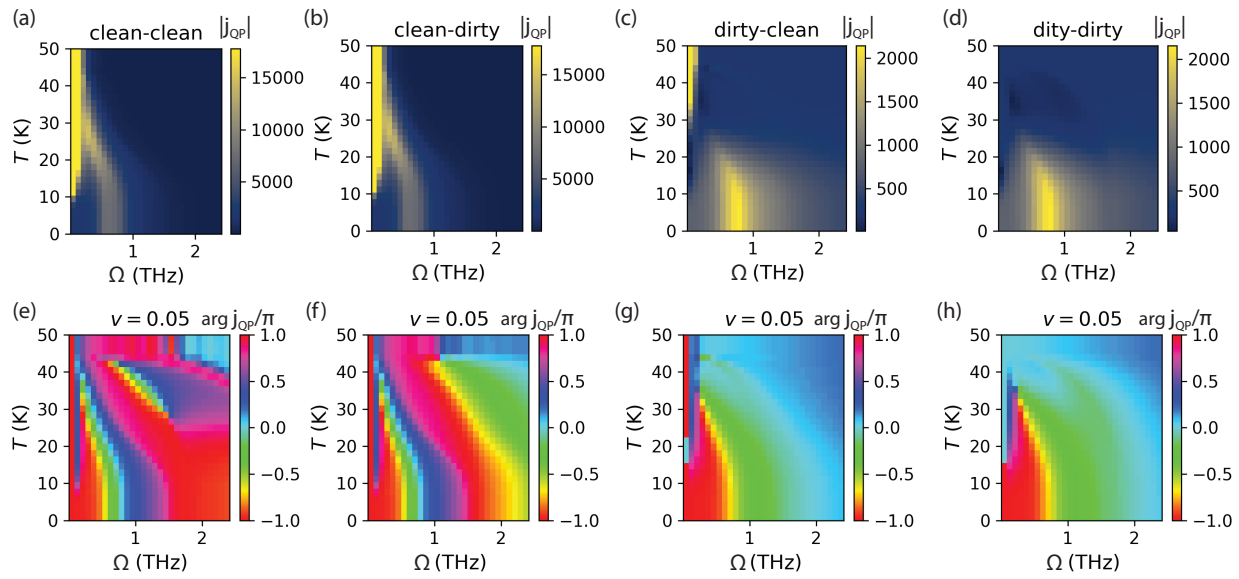

Figure C.6: Magnitude, up to a prefactor, (a-d) and phase (e-h) of density fluctuation contribution to THG current as a function of driving frequency Ω and temperature T for cases (a) clean-clean (b) clean-dirty case, (c) dirty-clean (d) dirty-dirty.

The Higgs resonance is sharp at small v, but much broader in the $v = 0.4$ case. Therefore, slices along the T-axis for a given drive frequency Ω do not exhibit a pronounced resonance peak. The observation of a resonance peak in Ref. [86] when experimentally sweeping the temperature would be therefore suggestive of a small v coupling in MgB_2. This is in disagreement to Refs. [24, 54] that experimentally determined a large v based on evidence of the Leggett mode above $2\Delta_\pi$.

Lower panels in Fig. C.4 show a phase jump of π in the THG current across the first Higgs resonance along the Ω direction that is most pronounced at low temperatures. The phase also shows features of the σ-Higgs resonance, albeit less clearly. Approaching the resonance along the T axis does not yield a phase behavior that is consistently simple to interpret. These results are to be contrasted to the clean case where one expects a phase jump of $\pi/2$.

Fig. C.5 shows the amplitude and phase response of the Leggett THG signal for three different coupling strengths $v = 0.02, 0.2, 0.5$. The overall contribution is about three magnitudes smaller than the Higgs contribution and therefore negligible. At large coupling, the Leggett resonance is very broad but sharpens at high temperatures. This observation was first reported in Ref. [116]. The phase shows a clear $\pi/2$-jump across the resonance for all temperatures below T_C.

The density fluctuation contribution is shown in Fig. C.6 for $v = 0.05$ in different impurity cases. Here *clean* refers to $\gamma = 0.01\,\mathrm{meV}$ and *dirty* specifies $\gamma = 100\,\mathrm{meV}$. Results at different v are nearly identical since the only v-dependent quantity in Eq. (C.23) is the superconducting order parameter at finite T. For all impurity concentrations, the density fluctuation mediated THG signal is peaked at the onset of the quasiparticle continuum of the π-band. The signal is about one order of magnitude smaller than the Higgs contribution in the small v case. For $v = 0.4$, the density fluctuation signal remains nearly identical but the Higgs signal increases, so that the Higgs contribution is only slightly larger. In all but the *dirty-dirty* case,

the density fluctuation signal has a large contribution for small Ω and large T.

The bottom row of Fig. C.6 shows the phase of the non-linear THG signal. In the *dirty-clean* and *dirty-dirty* cases we observe a clear phase jump of $\pi/2$ across a resonance.

Appendix D

Appendices for Chapter 6

D.1 Effective action for Higgs mode

We use the BCS Hamiltonian coupled to light

$$H(t) = \sum_{\boldsymbol{k},\sigma} \epsilon_{\boldsymbol{k}} c^\dagger_{\boldsymbol{k},\sigma} c_{\boldsymbol{k},\sigma} - \sum_{\boldsymbol{k},\boldsymbol{k}'} V_{\boldsymbol{k},\boldsymbol{k}'} c^\dagger_{\boldsymbol{k},\uparrow} c^\dagger_{-\boldsymbol{k},\downarrow} c_{-\boldsymbol{k}',\downarrow} c_{\boldsymbol{k}',\uparrow} + \frac{1}{2} \sum_{\boldsymbol{k},\sigma} \sum_{i,j} \partial^2_{ij} \epsilon_{\boldsymbol{k}} A_i(t) A_j(t) c^\dagger_{\boldsymbol{k},\sigma} c_{\boldsymbol{k},\sigma} \tag{D.1}$$

with electron dispersion $\epsilon_{\boldsymbol{k}} = \xi_{\boldsymbol{k}} - \epsilon_{\mathrm{F}}$ measured relative to the Fermi level and $c^\dagger_{\boldsymbol{k},\sigma}$ or $c_{\boldsymbol{k},\sigma}$ the electron creation or annihilation operators. We assume that the system is parity symmetric, i.e. $\epsilon_{\boldsymbol{k}} = \epsilon_{-\boldsymbol{k}}$. The separable BCS pairing interaction is given by $V_{\boldsymbol{k},\boldsymbol{k}'} = V f_{\boldsymbol{k}} f_{\boldsymbol{k}'}$ with pairing strength V and symmetry function $f_{\boldsymbol{k}}$. The coupling to light is obtained by the expansion of the minimal coupling term in powers of the vector potential A up to second order

$$\epsilon_{\boldsymbol{k}-\boldsymbol{A}(t)} = \epsilon_{\boldsymbol{k}} - \sum_i \partial_i \epsilon_{\boldsymbol{k}} A_i(t) + \frac{1}{2} \sum_{i,j} \partial^2_{ij} \epsilon_{\boldsymbol{k}} A_i(t) A_j(t) + \mathcal{O}(A(t)^3)\,. \tag{D.2}$$

Hereby, the paramagnetic term linear in A vanishes due to parity symmetry, i.e. $\partial_i \epsilon_{-\boldsymbol{k}} = -\partial_i \epsilon_{\boldsymbol{k}}$, while only the diamagnetic term quadratic in A remains due to $\partial^2_{ij} \epsilon_{-\boldsymbol{k}} = \partial^2_{ij} \epsilon_{\boldsymbol{k}}$. The partition function of the system is given by

$$\mathcal{Z} = \int \mathcal{D}(c^\dagger, c) \mathrm{e}^{-S(c^\dagger, c)} \tag{D.3}$$

with the action in imaginary time τ

$$S(c^\dagger, c) = \int_0^\beta \mathrm{d}\tau \left(\sum_{\boldsymbol{k},\sigma} c^\dagger_{\boldsymbol{k},\sigma}(\tau) \partial_\tau c_{\boldsymbol{k},\sigma}(\tau) + H(\tau) \right)\,. \tag{D.4}$$

We decouple the pairing interaction with the help of a Hubbard-Stratonovich transformation. Furthermore, we allow amplitude fluctuations via $\Delta(\tau) = \Delta + \delta\Delta(\tau)$. Introducing the Nambu spinor $\psi^\dagger_{\boldsymbol{k}} = \begin{pmatrix} c^\dagger_{\boldsymbol{k},\uparrow} \\ c_{-\boldsymbol{k},\downarrow} \end{pmatrix}$, the action can be written in the compact form

$$S(\psi^\dagger, \psi, \delta\Delta) = \int_0^\beta \mathrm{d}\tau \left(\frac{|\Delta(\tau)|^2}{V} - \sum_{\boldsymbol{k}} \psi^\dagger_{\boldsymbol{k}}(\tau) G^{-1}(\boldsymbol{k}, \tau) \psi_{\boldsymbol{k}}(\tau) \right) \tag{D.5}$$

with the inverse Green's function

$$G^{-1}(\boldsymbol{k}, \tau) = -\partial_\tau \tau_0 - \epsilon_{\boldsymbol{k}} \tau_3 + \Delta_{\boldsymbol{k}} \tau_1 - \frac{1}{2} \sum_{ij} \partial^2_{ij} \epsilon_{\boldsymbol{k}} A_i(t) A_j(t) \tau_3 + \delta\Delta(\tau) f_{\boldsymbol{k}} \tau_1 \,. \tag{D.6}$$

After integration of the fermions, one obtains in frequency representation

$$S(\delta\Delta, \theta, \rho) = \beta \frac{\Delta^2}{V} + \frac{1}{\beta} \sum_{\mathrm{i}\omega_m} \delta\Delta(-\mathrm{i}\omega_m) \frac{1}{V} \delta\Delta(\mathrm{i}\omega_m) - \operatorname{tr} \ln(-G^{-1}) \tag{D.7}$$

where the trace include summation over momentum and frequency and

$$G^{-1}(\boldsymbol{k}, \mathrm{i}\omega_m, \mathrm{i}\omega_n) = G_0^{-1}(\boldsymbol{k}, \mathrm{i}\omega_m, \mathrm{i}\omega_n) - \Sigma(\boldsymbol{k}, \mathrm{i}\omega_m - \mathrm{i}\omega_n) \,, \tag{D.8}$$

$$G_0^{-1}(\boldsymbol{k}, \mathrm{i}\omega_m, \mathrm{i}\omega_n) = \left[\mathrm{i}\omega_m \tau_0 - \epsilon_{\boldsymbol{k}} \tau_3 + \Delta_{\boldsymbol{k}} \tau_1 \right] \beta \delta_{\omega_m, \omega_n} \,, \tag{D.9}$$

$$\Sigma(\boldsymbol{k}, \mathrm{i}\omega_m - \mathrm{i}\omega_n) = \left[\frac{1}{2} \sum_{ij} \partial^2_{ij} \epsilon_{\boldsymbol{k}} A^2_{ij}(\mathrm{i}\omega_m - \mathrm{i}\omega_n) \tau_3 - \delta\Delta(\mathrm{i}\omega_m - \mathrm{i}\omega_n) f_{\boldsymbol{k}} \tau_1 \right] . \tag{D.10}$$

Expanding the logarithm for small Σ, one obtains

$$S(\delta\Delta) = S_{\mathrm{mf}} + S_{\mathrm{fl}}(\delta\Delta) \,, \tag{D.11}$$

$$S_{\mathrm{mf}} = \beta \frac{\Delta^2}{V} - \operatorname{tr} \ln(-G_0^{-1}) \,, \tag{D.12}$$

$$S_{\mathrm{fl}}(\delta\Delta) = \frac{1}{\beta} \sum_{\mathrm{i}\omega_m} \delta\Delta(-\mathrm{i}\omega_m) \frac{1}{V} \delta\Delta(\mathrm{i}\omega_m) + \operatorname{tr} \sum_{n=1}^{\infty} \frac{(G_0 \Sigma)^n}{n} \,. \tag{D.13}$$

Relevant for THG is the fourth order action. Thus, we consider the second order term in the sum $\frac{1}{2} \operatorname{tr} G_0 \Sigma G_0 \Sigma$ which leads to

$$\begin{aligned} S^{(4)}(\delta\Delta) = \frac{1}{2} \frac{1}{\beta} \sum_{\mathrm{i}\omega_m} \Big[& \delta\Delta(-\mathrm{i}\omega_m) H^{-1}(\mathrm{i}\omega_m) \delta\Delta(\mathrm{i}\omega_m) - 2\delta\Delta(-\mathrm{i}\omega_m) \sum_{ij} \chi^{ij}_{\Delta A^2}(\mathrm{i}\omega_m) A^2_{ij}(\mathrm{i}\omega_m) \\ & + \sum_{ijkl} A^2_{ij}(-\mathrm{i}\omega_m) A^2_{kl}(\mathrm{i}\omega_m) \chi^{ijkl}_{A^2 A^2}(\mathrm{i}\omega_m) \Big] \,. \end{aligned} \tag{D.14}$$

with the inverse Higgs propagator

$$H^{-1}(\mathrm{i}\omega_m) = \frac{2}{V} + \chi_{\Delta\Delta}(\mathrm{i}\omega_m) = \sum_{\boldsymbol{k}} f_{\boldsymbol{k}}^2 \frac{4\Delta_{\boldsymbol{k}}^2 - (\mathrm{i}\omega_n)^2}{E_{\boldsymbol{k}}(4E_{\boldsymbol{k}}^2 - (\mathrm{i}\omega_n)^2)} \tanh(\beta E_{\boldsymbol{k}}/2) \tag{D.15}$$

and the susceptibilities

$$X_{\alpha\beta}(\boldsymbol{k}, \boldsymbol{k}', \mathrm{i}\omega_m) = \frac{1}{\beta} \sum_{\mathrm{i}\omega_n} \mathrm{tr}[G_0(\boldsymbol{k}, \mathrm{i}\omega_n)\tau_\alpha G_0(\boldsymbol{k}', \mathrm{i}\omega_m + \mathrm{i}\omega_n)\tau_\beta] \,, \tag{D.16a}$$

$$\chi_{\Delta\Delta}(\mathrm{i}\omega_m) = \sum_{\boldsymbol{k}} f_{\boldsymbol{k}}^2 X_{11}(\boldsymbol{k}, \boldsymbol{k}, \mathrm{i}\omega_m) = -\sum_{\boldsymbol{k}} f_{\boldsymbol{k}}^2 \frac{4\epsilon_{\boldsymbol{k}}^2}{E_{\boldsymbol{k}}(4E_{\boldsymbol{k}}^2 - (\mathrm{i}\omega_m)^2)} \tanh(\beta E_{\boldsymbol{k}}/2) \,, \tag{D.16b}$$

$$\chi_{\Delta A^2}^{ij}(\mathrm{i}\omega_m) = \sum_{\boldsymbol{k}} f_{\boldsymbol{k}} \frac{1}{2} \partial_{ij}^2 \epsilon_{\boldsymbol{k}} X_{13}(\boldsymbol{k}, \boldsymbol{k}, \mathrm{i}\omega_m) = -\frac{1}{2} \sum_{\boldsymbol{k}} f_{\boldsymbol{k}} \frac{\partial_{ij}^2 \epsilon_{\boldsymbol{k}} 4\epsilon_{\boldsymbol{k}} \Delta_{\boldsymbol{k}}}{E_{\boldsymbol{k}}(4E_{\boldsymbol{k}}^2 - (\mathrm{i}\omega_m)^2)} \tanh(\beta E_{\boldsymbol{k}}/2) \,, \tag{D.16c}$$

$$\chi_{A^2A^2}^{ijkl}(\mathrm{i}\omega_m) = \sum_{\boldsymbol{k}} \frac{1}{4} \partial_{ij}^2 \epsilon_{\boldsymbol{k}} \partial_{kl}^2 \epsilon_{\boldsymbol{k}} X_{33}(\boldsymbol{k}, \boldsymbol{k}, \mathrm{i}\omega_m) = -\frac{1}{4} \sum_{\boldsymbol{k}} \frac{\partial_{ij}^2 \epsilon_{\boldsymbol{k}} \partial_{kl}^2 \epsilon_{\boldsymbol{k}} 4\Delta_{\boldsymbol{k}}^2}{E_{\boldsymbol{k}}(4E_{\boldsymbol{k}}^2 - (\mathrm{i}\omega_m)^2)} \tanh(\beta E_{\boldsymbol{k}}/2) \,. \tag{D.16d}$$

Finally, integrating the fluctuations using

$$\int \mathcal{D}(\phi^\top, \phi)\, \mathrm{e}^{-\frac{1}{2}\frac{1}{\beta}\sum_{\mathrm{i}\omega_m} \phi^\top(-\mathrm{i}\omega_m) M(\mathrm{i}\omega_m)\phi(\mathrm{i}\omega_m) + \phi^\top(-\mathrm{i}\omega_m) b(\mathrm{i}\omega_m) + b^\top(-\mathrm{i}\omega_m)\phi(\mathrm{i}\omega_m)} \tag{D.17}$$

$$= \mathrm{e}^{\frac{1}{2}\sum_{\mathrm{i}\omega_m} b^\top(-\mathrm{i}\omega_m) M^{-1}(\mathrm{i}\omega_m) b(\mathrm{i}\omega_m)} \tag{D.18}$$

and after analytic continuation $\mathrm{i}\omega_m \to \omega + \mathrm{i}0^+$, one obtains

$$S^{(4)} = \frac{1}{2} \int \mathrm{d}\omega \sum_{ijkl} \left(\chi_{\Delta A^2}^{ij}(-\omega) \chi_{\Delta A^2}^{kl}(\omega) H(\omega) + \chi_{A^2A^2}^{ijkl}(\omega) \right) A_{ij}^2(-\omega) A_{kl}^2(\omega) \,. \tag{D.19}$$

For the following, we will only consider linear polarized light in x-direction $A(t) = A_0 \hat{e}_x \cos(\Omega t)$, such that we can neglect all polarization indices and the action reads

$$S^{(4)} = \frac{1}{2} \int \mathrm{d}\omega K^{(4)}(\omega) A^2(-\omega) A^2(\omega) \tag{D.20}$$

where the kernel is given by

$$K^{(4)} = \chi_{\Delta A^2}(-\omega) H(\omega) \chi_{\Delta A^2}(\omega) + \chi_{A^2A^2}(\omega) \,. \tag{D.21}$$

The third-order current is computed via

$$j^{(3)}(3\Omega) = -\left. \frac{\mathrm{d}S^{(4)}}{\mathrm{d}A(-\omega)} \right|_{3\Omega} \propto K^{(4)}(2\Omega) \tag{D.22}$$

and is proportional to the fourth-order kernel evaluated at 2Ω. To analytically evaluate the momentum sums, we assume $T = 0$, s-wave symmetry, i.e. $f_{\boldsymbol{k}} = 1$, and a constant density of states at the Fermi level such that we can write $\sum_{\boldsymbol{k}} \to \lambda \int \mathrm{d}\epsilon$. We use

$$F(\omega) := \int \mathrm{d}\epsilon \frac{1}{\sqrt{\epsilon^2 + \Delta^2}(4\epsilon^2 + 4\Delta^2 - \omega^2)} = \frac{2\sin^{-1}\left(\frac{\omega}{2\Delta}\right)}{\omega\sqrt{4\Delta^2 - w^2}} \tag{D.23}$$

and expand the derivative term $\sum_{\boldsymbol{k}} \partial_{ij}^2 \epsilon_{\boldsymbol{k}} = \sum_{\boldsymbol{k}} \alpha_0 + \alpha_1 \epsilon_{\boldsymbol{k}}$, which is valid for our band structure. We obtain

$$H(\omega) = \lambda \frac{\omega}{2\sqrt{4\Delta^2 - \omega^2}\sin^{-1}\left(\frac{\omega}{2\Delta}\right)}\,, \tag{D.24}$$

$$\chi_{\Delta A^2}(\mathrm{i}\omega_n) = -\lambda \frac{\Delta}{4}\alpha_1 \left(\frac{2}{V} - \frac{2}{\omega}\sqrt{4\Delta^2 - \omega^2}\sin^{-1}\left(\frac{\omega}{2\Delta}\right)\right)\,, \tag{D.25}$$

$$\chi_{A^2A^2}(\mathrm{i}\omega_n) = -\lambda \frac{\Delta^2}{2}\alpha_0^2 \frac{2\sin^{-1}\left(\frac{\omega}{2\Delta}\right)}{\omega\sqrt{4\Delta^2 - w^2}} - \lambda \frac{\Delta^2}{8}\alpha_1^2 \left(\frac{2}{V} - \frac{2}{\omega}\sqrt{4\Delta^2 - \omega^2}\sin^{-1}\left(\frac{\omega}{2\Delta}\right)\right)\,. \tag{D.26}$$

D.2 Effective action with Coulomb interaction

The susceptibilities for the effective action in Eq. (6.20) are given in Eq. (D.16) and

$$\chi_{\Delta\rho}(\mathrm{i}\omega_n) = \sum_{\boldsymbol{k}} X_{13}(\boldsymbol{k}, \boldsymbol{k}, \mathrm{i}\omega_n) = -\Delta \sum_{\boldsymbol{k}} \frac{4\epsilon_{\boldsymbol{k}}}{E_{\boldsymbol{k}}(4E_{\boldsymbol{k}}^2 - (\mathrm{i}\omega_n)^2)} \tanh(\beta E_{\boldsymbol{k}}/2)\,, \tag{D.27a}$$

$$\chi_{\rho\rho}(\mathrm{i}\omega_n) = \sum_{\boldsymbol{k}} X_{33}(\boldsymbol{k}, \boldsymbol{k}, \mathrm{i}\omega_n) = -4\Delta^2 \sum_{\boldsymbol{k}} \frac{1}{E_{\boldsymbol{k}}(4E_{\boldsymbol{k}}^2 - (\mathrm{i}\omega_n)^2)} \tanh(\beta E_{\boldsymbol{k}}/2)\,, \tag{D.27b}$$

$$\chi_{\rho A^2}^{ij}(\mathrm{i}\omega_n) = \sum_{\boldsymbol{k}} \frac{1}{2}\partial_{ij}^2 \epsilon_{\boldsymbol{k}} X_{33}(\boldsymbol{k}, \boldsymbol{k}, \mathrm{i}\omega_n) = -\sum_{\boldsymbol{k}} \frac{1}{2}\partial_{ij}^2 \epsilon_{\boldsymbol{k}} \frac{4\Delta^2}{E_{\boldsymbol{k}}(4E_{\boldsymbol{k}}^2 - (\mathrm{i}\omega_n)^2)} \tanh(\beta E_{\boldsymbol{k}}/2)\,. \tag{D.27c}$$

D.3 Coupled oscillator

The explicit expressions for the complex amplitudes $\hat{A}_i$ defined in Eq. (6.32) are given by

$$\hat{A}_1 = \frac{F_1 P_2^{-1} - gF_2}{\tilde{P}_1^{-1}\tilde{P}_2^{-1} - g^2} = \frac{F_1(\omega_2^2 - \Omega^2 + \mathrm{i}\gamma_2\Omega) - gF_2}{(\omega_1^2 - \Omega^2 + \mathrm{i}\gamma_1\Omega)(\omega_2^2 - \Omega^2 + \mathrm{i}\gamma_2\Omega) - g^2}\,, \tag{D.28}$$

$$\hat{A}_2 = \frac{F_2 P_1^{-1} - gF_1}{\tilde{P}_1^{-1}\tilde{P}_2^{-1} - g^2} = \frac{F_2(\omega_1^2 - \Omega^2 + \mathrm{i}\gamma_1\Omega) - gF_1}{(\omega_1^2 - \Omega^2 + \mathrm{i}\gamma_1\Omega)(\omega_2^2 - \Omega^2 + \mathrm{i}\gamma_2\Omega) - g^2}\,. \tag{D.29}$$

We define

$$V_1 = F_1(\omega_2^2 - \Omega^2) - gF_2\,, \qquad V_2 = \gamma_2\Omega F_1\,, \tag{D.30}$$

$$V_3 = F_2(\omega_1^2 - \Omega^2) - gF_1\,, \qquad V_4 = \gamma_1\Omega F_2\,, \tag{D.31}$$

$$V_5 = (\omega_1^2 - \Omega^2)(\omega_2^2 - \Omega^2) - \gamma_1\gamma_2\Omega^2 - g^2\,, \qquad V_6 = \gamma_1\Omega(\omega_2^2 - \Omega^2) + \gamma_2\Omega(\omega_1^2 - \Omega^2) \tag{D.32}$$

to split the nominator and denominator in real and imaginary part

$$\hat{A}_1 = \frac{V_1 + \mathrm{i}V_2}{V_5 + \mathrm{i}V_6}\,, \qquad\qquad \hat{A}_2 = \frac{V_3 + \mathrm{i}V_4}{V_5 + \mathrm{i}V_6}\,. \tag{D.33}$$

Extracting absolute value and phase and using the definition $\hat{A}_i = A_i \mathrm{e}^{-\mathrm{i}\phi_i}$, finally yields for the real amplitudes A_i and phases ϕ_i

$$A_1(\Omega) = \sqrt{\frac{V_1^2 + V_2^2}{V_5^2 + V_6^2}}\,, \qquad\qquad \phi_1(\Omega) = \tan^{-1}\left(\frac{V_6}{V_5}\right) - \tan^{-1}\left(\frac{V_2}{V_1}\right) \tag{D.34}$$

$$A_2(\Omega) = \sqrt{\frac{V_3^2 + V_4^2}{V_5^2 + V_6^2}}\,, \qquad\qquad \phi_2(\Omega) = \tan^{-1}\left(\frac{V_6}{V_5}\right) - \tan^{-1}\left(\frac{V_4}{V_3}\right)\,. \tag{D.35}$$

The total complex amplitude $\hat{A}_T$ is defined as

$$\hat{A}_T = A_T \mathrm{e}^{-\mathrm{i}\phi_T} = A_1 \mathrm{e}^{-\mathrm{i}\phi_1} + A_2 \mathrm{e}^{-\mathrm{i}\phi_2}\,. \tag{D.36}$$

Thus, it follows for the real amplitude A_T and phase ϕ_T

$$A_T = \sqrt{A_1^2 + A_2^2 + 2A_1A_2\cos(\phi_1 - \phi_2)}\,, \qquad \phi_T = \tan^{-1}\left(\frac{A_1\sin\phi_1 + A_2\sin\phi_2}{A_1\cos\phi_1 + A_2\cos\phi_2}\right)\,. \tag{D.37}$$

D.4 Higgs-CDW model

The action for the BCS and phonon Hamiltonian Eq. (6.40) reads

$$S(c^\dagger, c, b^\dagger, b) = \int_0^\beta \mathrm{d}\tau \left(\sum_{\boldsymbol{k}\sigma} c^\dagger_{\boldsymbol{k},\sigma}(\tau)\partial_\tau c_{\boldsymbol{k},\sigma}(\tau) + \sum_{\boldsymbol{q}=\pm\boldsymbol{Q}} b^\dagger_{\boldsymbol{q}}(\tau)\partial_\tau b_{\boldsymbol{q}}(\tau) + H(\tau) \right)\,. \tag{D.38}$$

Rewriting the phonon operator as $b_{\boldsymbol{q}} = \frac{1}{\sqrt{2}}(Q_{\boldsymbol{q}} + \mathrm{i}P_{-\boldsymbol{q}})$, integrating over the momentum variable $P_{\boldsymbol{q}}$, introducing the CDW field $D_{\boldsymbol{k}} = Dg_{\boldsymbol{k}}$ with $D = -\sqrt{2}gQ_{\boldsymbol{q}}$ and performing a Hubbard-Stratonovich transformation to decouple the superconducting pairing interaction, one obtains

$$\begin{aligned} S(c^\dagger, c, \Delta^*, \Delta, D^*, D) = \int_0^\beta \mathrm{d}\tau \Big(& \sum_{\boldsymbol{k}\sigma} c^\dagger_{\boldsymbol{k},\sigma}(\partial_\tau + \epsilon_{\boldsymbol{k}})c_{\boldsymbol{k},\sigma} - \frac{1}{g^2} D P_0^{-1}(\tau) D^* \\ & + \frac{\Delta^2}{V} - \sum_{\boldsymbol{k}} \Delta c^\dagger_{\boldsymbol{k}\uparrow} c^\dagger_{-\boldsymbol{k}\downarrow} - \sum_{\boldsymbol{k}} \Delta^* c_{-\boldsymbol{k}\downarrow} c_{\boldsymbol{k}\uparrow} - \sum_{\boldsymbol{k}\sigma} D_{\boldsymbol{k}} c^\dagger_{\boldsymbol{k}+\boldsymbol{Q},\sigma} c_{\boldsymbol{k}\sigma} - \sum_{\boldsymbol{k}\sigma} D^*_{\boldsymbol{k}} c^\dagger_{\boldsymbol{k}-\boldsymbol{Q},\sigma} c_{\boldsymbol{k}\sigma} \Big) \end{aligned} \tag{D.39}$$

where the bare phonon propagator is defined as

$$P_0^{-1}(\tau) = -\frac{\omega_Q^2 - \partial_\tau^2}{2\omega_Q}\,. \tag{D.40}$$

We rewrite the expression with the four-component Nambu spinor $\psi_{\boldsymbol{k}}^\dagger = (c_{\boldsymbol{k},\uparrow}^\dagger, c_{\boldsymbol{k}+\boldsymbol{Q},\uparrow}^\dagger, c_{-\boldsymbol{k},\downarrow}, c_{-(\boldsymbol{k}+\boldsymbol{Q}),\downarrow})$ and introduce amplitude fluctuations of both fields via $\Delta(t) = \Delta + \delta\Delta(t)$ and $D(t) = D + \delta D(t)$. We obtain in frequency representation (see also [34])

$$\begin{aligned} S(\psi^\dagger, \psi, \delta\Delta, \delta D) = \beta\frac{\Delta^2}{V} + \beta\frac{D^2 w_Q}{2g^2} + \frac{1}{\beta}\sum_{\mathrm{i}\omega_m} \delta\Delta(-\mathrm{i}\omega_m)\frac{1}{V}\delta\Delta(\mathrm{i}\omega_m) \\ - \frac{1}{g^2}\frac{1}{\beta}\sum_{\mathrm{i}\omega_m} \delta D(-\mathrm{i}\omega_m) P_0^{-1}(\mathrm{i}\omega_m)\delta D(\mathrm{i}\omega_m) \\ - \frac{1}{\beta^2}\sum_{\mathrm{i}\omega_m,\mathrm{i}\omega_n}\sum_{\boldsymbol{k}} \psi_{\boldsymbol{k}}^\dagger(\mathrm{i}\omega_m) G^{-1}(\boldsymbol{k}, \mathrm{i}\omega_m, \mathrm{i}\omega_n)\psi_{\boldsymbol{k}}(\mathrm{i}\omega_n) \end{aligned} \tag{D.41}$$

with

$$G^{-1}(\boldsymbol{k}, \mathrm{i}\omega_m, \mathrm{i}\omega_n) = G_0^{-1}(\boldsymbol{k}, \mathrm{i}\omega_m, \mathrm{i}\omega_n) - \Sigma(\boldsymbol{k}, \mathrm{i}\omega_m - \mathrm{i}\omega_n)\,, \tag{D.42a}$$

$$G_0^{-1}(\boldsymbol{k}, \mathrm{i}\omega_m, \mathrm{i}\omega_n) = (\mathrm{i}\omega_m\tau_0\otimes\sigma_0 - \epsilon_{\boldsymbol{k}}\tau_3\otimes\sigma_3 + \Delta\tau_1\otimes\sigma_0 + Dg_{\boldsymbol{k}}\tau_3\otimes\sigma_1)\beta\delta_{\omega_m,\omega_n}\,, \tag{D.42b}$$

$$\begin{aligned} \Sigma(\boldsymbol{k}, \mathrm{i}\omega_m - \mathrm{i}\omega_n) = \frac{1}{2}\sum_{i,j}\partial_{ij}^2\epsilon_{\boldsymbol{k}}A_{ij}^2(\mathrm{i}\omega_m - \mathrm{i}\omega_n)\tau_3\otimes\sigma_3 - \delta\Delta(\mathrm{i}\omega_m - \mathrm{i}\omega_n)\tau_1\otimes\sigma_0 \\ - \delta D(\mathrm{i}\omega_m - \mathrm{i}\omega_n) g_{\boldsymbol{k}}\tau_3\otimes\sigma_1\,. \end{aligned} \tag{D.42c}$$

where τ_i are Pauli matrices in Nambu space and σ_i Pauli matrices in the CDW channel. The saddle point equations are

$$\Delta = V\sum_{\boldsymbol{k}}\frac{\Delta}{E_{\boldsymbol{k}}}\tanh(\beta E_{\boldsymbol{k}}/2)\,, \tag{D.43a}$$

$$D = \frac{4g^2}{\omega_Q}\sum_{\boldsymbol{k}} g_{\boldsymbol{k}}^2\frac{D}{E_{\boldsymbol{k}}}\tanh(\beta E_{\boldsymbol{k}}/2)\,. \tag{D.43b}$$

A diagonalization of the Hamiltonian yields the quasiparticle energy $E_{\boldsymbol{k}} = \sqrt{\epsilon_{\boldsymbol{k}}^2 + \Delta^2 + |D_{\boldsymbol{k}}|^2}$. After integration of the fermions and expansion of the logarithm as in Appendix D.1, the action is split into a mean-field part and a fluctuation part

$$S(\delta\Delta, \delta D) = S_{\mathrm{mf}} + S_{\mathrm{fl}}(\delta\Delta, \delta D) \tag{D.44}$$

with

$$S_{\mathrm{mf}} = \beta\frac{\Delta^2}{V} + \beta\frac{D^2 w_Q}{2g^2} - \mathrm{tr}\ln(-G_0^{-1})\,, \tag{D.45a}$$

$$\begin{aligned} S_{\mathrm{fl}}(\delta\Delta, \delta D) = \frac{1}{\beta}\sum_{\mathrm{i}\omega_m}\delta\Delta(-\mathrm{i}\omega_m)\frac{1}{V}\delta\Delta(\mathrm{i}\omega_m) - \frac{1}{g^2}\frac{1}{\beta}\sum_{\mathrm{i}\omega_m}\delta D(-\mathrm{i}\omega_m)P_0^{-1}(\mathrm{i}\omega_m)\delta D(\mathrm{i}\omega_m) \\ + \mathrm{tr}\sum_{n=1}^{\infty}\frac{(G_0\Sigma)^n}{n}\,. \end{aligned} \tag{D.45b}$$

After evaluating the sum to second order, one obtains the fourth order action Eq (6.42). The Higgs propagator is defined as

$$H^{-1}(\mathrm{i}\omega_m) = \frac{2}{V} + \chi_{\Delta\Delta}(\mathrm{i}\omega_m) = 2\sum_{\boldsymbol{k}} \frac{4\Delta^2 - (\mathrm{i}\omega_m)^2}{E_{\boldsymbol{k}}(4E_{\boldsymbol{k}}^2 - (\mathrm{i}\omega_m)^2)} \tanh(\beta E_{\boldsymbol{k}}/2) \tag{D.46}$$

Analogously, the renormalized phonon propagator is defined as

$$P^{-1}(\mathrm{i}\omega_m) = P_0^{-1}(\mathrm{i}\omega_m) - g^2\chi_{DD}(\mathrm{i}\omega_m) = -\frac{\Omega_Q^2 - (\mathrm{i}\omega_m)^2}{2\omega_Q} \tag{D.47}$$

with

$$\Omega_Q^2 = \omega_Q^2 + 2\omega_Q g^2 \chi_{DD}(\mathrm{i}\omega_m) = 4g^2\omega_Q \sum_{\boldsymbol{k}} g_{\boldsymbol{k}}^2 \frac{4D_{\boldsymbol{k}}^2 - (\mathrm{i}\omega_m)^2}{E_{\boldsymbol{k}}(4E_{\boldsymbol{k}}^2 - (\mathrm{i}\omega_m)^2)} \tanh(\beta E_{\boldsymbol{k}}/2)\,. \tag{D.48}$$

Hereby, the susceptibilities are defined as

$$X_{\alpha\beta\gamma\delta}(\boldsymbol{k}, \mathrm{i}\omega_n) = \frac{1}{\beta}\sum_{\mathrm{i}\omega_n} \mathrm{tr}\left[G_0(\boldsymbol{k}, \mathrm{i}\omega_n)\tau_\alpha \otimes \sigma_\beta G_0(\boldsymbol{k}, \mathrm{i}\omega_m + \mathrm{i}\omega_n)\tau_\gamma \otimes \sigma_\delta\right]\,, \tag{D.49a}$$

$$\chi_{\Delta\Delta}(\mathrm{i}\omega_m) = \sum_{\boldsymbol{k}} X_{1010} = -8\sum_{\boldsymbol{k}} \frac{D_{\boldsymbol{k}}^2 + \epsilon_{\boldsymbol{k}}^2}{E_{\boldsymbol{k}}(4E_{\boldsymbol{k}}^2 - (\mathrm{i}\omega_m)^2)} \tanh(\beta E_{\boldsymbol{k}}/2)\,, \tag{D.49b}$$

$$\chi_{\Delta D}(\mathrm{i}\omega_m) = \sum_{\boldsymbol{k}} g_{\boldsymbol{k}} X_{1031} = 8\sum_{\boldsymbol{k}} g_{\boldsymbol{k}} \frac{\Delta D_{\boldsymbol{k}}}{E_{\boldsymbol{k}}(4E_{\boldsymbol{k}}^2 - (\mathrm{i}\omega_m)^2)} \tanh(\beta E_{\boldsymbol{k}}/2)\,, \tag{D.49c}$$

$$\chi_{\Delta A^2}^{ij}(\mathrm{i}\omega_m) = \sum_{\boldsymbol{k}} \frac{1}{2}\partial_{ij}^2\epsilon_{\boldsymbol{k}} X_{1033} = -4\sum_{\boldsymbol{k}} \partial_{ij}^2\epsilon_{\boldsymbol{k}} \frac{\epsilon_{\boldsymbol{k}}\Delta}{E_{\boldsymbol{k}}(4E_{\boldsymbol{k}}^2 - (\mathrm{i}\omega_m)^2)} \tanh(\beta E_{\boldsymbol{k}}/2)\,, \tag{D.49d}$$

$$\chi_{DD}(\mathrm{i}\omega_m) = \sum_{\boldsymbol{k}} g_{\boldsymbol{k}}^2 X_{3131} = -8\sum_{\boldsymbol{k}} g_{\boldsymbol{k}}^2 \frac{\Delta^2 + \epsilon_{\boldsymbol{k}}^2}{E_{\boldsymbol{k}}(4E_{\boldsymbol{k}}^2 - (\mathrm{i}\omega_m)^2)} \tanh(\beta E_{\boldsymbol{k}}/2)\,, \tag{D.49e}$$

$$\chi_{DA^2}^{ij}(\mathrm{i}\omega_m) = \sum_{\boldsymbol{k}} g_{\boldsymbol{k}} \frac{1}{2}\partial_{ij}^2\epsilon_{\boldsymbol{k}} X_{3133} = -4\sum_{\boldsymbol{k}} g_{\boldsymbol{k}}\partial_{ij}^2\epsilon_{\boldsymbol{k}} \frac{\epsilon_{\boldsymbol{k}} D_{\boldsymbol{k}}}{E_{\boldsymbol{k}}(4E_{\boldsymbol{k}}^2 - (\mathrm{i}\omega_m)^2)} \tanh(\beta E_{\boldsymbol{k}}/2)\,. \tag{D.49f}$$

Integration of the amplitude fluctuations finally leads to Eq (6.45).

D.5 Higgs-Bardasis-Schrieffer model

Using the ansatz in Eq. (6.53) for $V_{\boldsymbol{k}\boldsymbol{k}'}$ including the two pairing channels, the action in imaginary time τ after decoupling of the quartic interaction is given by

$$S(c^\dagger, c, \delta\Delta_l) = \int_0^\beta \mathrm{d}\tau \left(\sum_l \frac{|\Delta_l(\tau)|^2}{V_l} - \sum_{\boldsymbol{k}} \psi_{\boldsymbol{k}}^\dagger(\tau) G^{-1}(\boldsymbol{k}, \tau)\psi_{\boldsymbol{k}}(\tau)\right) \tag{D.50}$$

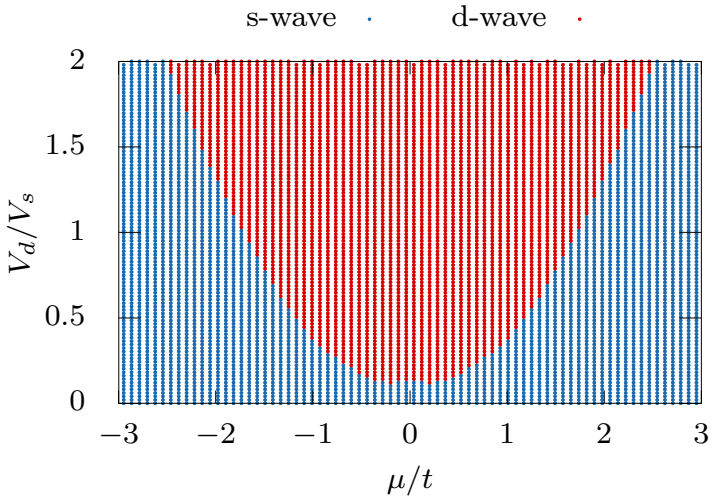

Figure D.1: Phase diagram showing ground state symmetry for system with two possible pairing channels described in Sec. 6.5 as function of chemical potential and ratio V_d/V_s. In the blue region, the s-wave channel is dominant and in the red region the d-wave channel.

with

$$G^{-1}(\boldsymbol{k},\tau) = -\tau_0\partial_\tau - h_{\boldsymbol{k}}(\tau)\,, \tag{D.51}$$

$$h_{\boldsymbol{k}}(t) = \left(\epsilon_{\boldsymbol{k}} + \frac{1}{2}\sum_{i,j}\partial_{ij}^2\epsilon_{\boldsymbol{k}}A_i(t)A_j(t)\right)\tau_3 - (\Delta_s + \delta\Delta_s(t))f_{\boldsymbol{k}}^s\tau_1 + \delta\Delta_d(t)f_{\boldsymbol{k}}^d\tau_2 \tag{D.52}$$

The usual Higgs mode lives in the τ_1 channel, while the Bardasis-Schrieffer mode lives in the τ_2 channel.

In analogy to the previous sections, the fermions can be integrated out which leads to

$$S(\delta\Delta_l) = \beta\frac{\Delta_s^2}{V_s} + \frac{1}{\beta}\sum_{\mathrm{i}\omega_m}\delta\Delta_s(-\mathrm{i}\omega_m)\frac{1}{V_s}\delta\Delta_s(\mathrm{i}\omega_m) + \frac{1}{\beta}\sum_{\mathrm{i}\omega_m}\delta\Delta_d(-\mathrm{i}\omega_m)\frac{1}{V_d}\delta\Delta_d(\mathrm{i}\omega_m) - \mathrm{tr}\ln(-G^{-1}) \tag{D.53}$$

with

$$G^{-1}(\boldsymbol{k},\mathrm{i}\omega_m,\mathrm{i}\omega_n) = G_0^{-1}(\boldsymbol{k},\mathrm{i}\omega_m,\mathrm{i}\omega_n) - \Sigma(\boldsymbol{k},\mathrm{i}\omega_m-\mathrm{i}\omega_n)\,, \tag{D.54}$$

$$G_0(\boldsymbol{k},\mathrm{i}\omega_m,\mathrm{i}\omega_n) = (\mathrm{i}\omega_m\tau_0 - \epsilon_{\boldsymbol{k}}\tau_3 + \Delta_s f_{\boldsymbol{k}}^s\tau_1)\beta\delta_{\omega_m,\omega_n}\,, \tag{D.55}$$

$$\Sigma(\boldsymbol{k},\mathrm{i}\omega_m-\mathrm{i}\omega_n) = \frac{1}{2}\sum_{i,j}\partial_{ij}^2\epsilon_{\boldsymbol{k}}A_{ij}^2(\mathrm{i}\omega_m-\mathrm{i}\omega_n)\tau_3 - \delta\Delta_s(\mathrm{i}\omega_m-\mathrm{i}\omega_n)f_{\boldsymbol{k}}^s\tau_1 + \delta\Delta_d(\mathrm{i}\omega_m-\mathrm{i}\omega_n)f_{\boldsymbol{k}}^d\tau_2 \tag{D.56}$$

After expansion of the logarithm for small Σ it follows

$$S(\delta\Delta_l) = S_{\mathrm{mf}} + S_{\mathrm{fl}}(\delta\Delta_l)\,, \tag{D.57}$$

$$S_{\mathrm{mf}} = \beta\frac{\Delta_s^2}{V_s} - \mathrm{tr}\ln(-G_0^{-1})\,, \tag{D.58}$$

$$S_{\mathrm{fl}}(\delta\Delta_l) = \frac{1}{\beta}\sum_{\mathrm{i}\omega_m}\delta\Delta_s(-\mathrm{i}\omega_m)\frac{1}{V_s}\delta\Delta_s(\mathrm{i}\omega_m) + \frac{1}{\beta}\sum_{\mathrm{i}\omega_m}\delta\Delta_d(-\mathrm{i}\omega_m)\frac{1}{V_d}\delta\Delta_d(\mathrm{i}\omega_m) + \mathrm{tr}\sum_{n=1}^{\infty}\frac{(G_0\Sigma)^n}{n}\,. \tag{D.59}$$

The second-order term in the sum of the logarithm leads to the fourth-order action $S^{(4)}$

$$\begin{aligned} S^{(4)} = \frac{1}{2}\frac{1}{\beta}\sum_{\mathrm{i}\omega_m}\Big[&\phi^\top(-\mathrm{i}\omega_m)M(\mathrm{i}\omega_m)\phi(\mathrm{i}\omega_m) + \phi^\top(-\mathrm{i}\omega_m)b(\mathrm{i}\omega_m) + b^\top(-\mathrm{i}\omega_m)\phi(\mathrm{i}\omega_m) \\ &+ \sum_{ijkl}A^2_{ij}(-\mathrm{i}\omega_m)A^2_{kl}(\mathrm{i}\omega_m)\chi^{ijkl}_{A^2A^2}(\mathrm{i}\omega_m)\Big] \end{aligned} \tag{D.60}$$

with M, ϕ and b given in Eq. (6.56c). The susceptibilities read

$$\chi_{\Delta\Delta}(\mathrm{i}\omega_m) = \sum_{\boldsymbol{k}}(f^s_{\boldsymbol{k}})^2 X_{11}(\boldsymbol{k},\mathrm{i}\omega_m) = -\sum_{\boldsymbol{k}}(f^s_{\boldsymbol{k}})^2\frac{4\epsilon^2_{\boldsymbol{k}}}{E_{\boldsymbol{k}}(4E^2_{\boldsymbol{k}} - (\mathrm{i}\omega_m)^2)}\tanh(\beta E_{\boldsymbol{k}}/2) \tag{D.61}$$

$$\chi_{BB}(\mathrm{i}\omega_m) = \sum_{\boldsymbol{k}}(f^d_{\boldsymbol{k}})^2 X_{22}(\boldsymbol{k},\mathrm{i}\omega_m) = -\sum_{\boldsymbol{k}}(f^d_{\boldsymbol{k}})^2\frac{4E^2_{\boldsymbol{k}}}{E_{\boldsymbol{k}}(4E^2_{\boldsymbol{k}} - (\mathrm{i}\omega_m)^2)}\tanh(\beta E_{\boldsymbol{k}}/2) \tag{D.62}$$

$$\chi_{\Delta B}(\mathrm{i}\omega_m) = \sum_{\boldsymbol{k}} f^s_{\boldsymbol{k}} f^d_{\boldsymbol{k}} X_{12}(\boldsymbol{k},\mathrm{i}\omega_m) = \sum_{\boldsymbol{k}} f^s_{\boldsymbol{k}} f^d_{\boldsymbol{k}}\frac{2\mathrm{i}\epsilon_{\boldsymbol{k}}(\mathrm{i}\omega_m)}{E_{\boldsymbol{k}}(4E^2_{\boldsymbol{k}} - (\mathrm{i}\omega_m)^2)}\tanh(\beta E_{\boldsymbol{k}}/2) \tag{D.63}$$

$$\chi^{ij}_{\Delta A^2}(\mathrm{i}\omega_m) = \sum_{\boldsymbol{k}}\frac{1}{2}f^s_{\boldsymbol{k}}\partial^2_{ij}\epsilon_{\boldsymbol{k}} X_{13}(\boldsymbol{k},\mathrm{i}\omega_m) = -\sum_{\boldsymbol{k}}\frac{1}{2}f^s_{\boldsymbol{k}}\partial^2_{ij}\epsilon_{\boldsymbol{k}}\frac{4\epsilon_{\boldsymbol{k}}\Delta_s f^s_{\boldsymbol{k}}}{E_{\boldsymbol{k}}(4E^2_{\boldsymbol{k}} - (\mathrm{i}\omega_m)^2)}\tanh(\beta E_{\boldsymbol{k}}/2) \tag{D.64}$$

$$\chi^{ij}_{BA^2}(\mathrm{i}\omega_m) = \sum_{\boldsymbol{k}}\frac{1}{2}f^d_{\boldsymbol{k}}\partial^2_{ij}\epsilon_{\boldsymbol{k}} X_{23}(\boldsymbol{k},\mathrm{i}\omega_m) = -\sum_{\boldsymbol{k}}\frac{1}{2}f^d_{\boldsymbol{k}}\partial^2_{ij}\epsilon_{\boldsymbol{k}}\frac{2\mathrm{i}\Delta_s f^s_{\boldsymbol{k}}(\mathrm{i}\omega_m)}{E_{\boldsymbol{k}}(4E^2_{\boldsymbol{k}} - (\mathrm{i}\omega_m)^2)}\tanh(\beta E_{\boldsymbol{k}}/2) \tag{D.65}$$

$$\begin{aligned} \chi^{ijkl}_{A^2A^2}(\mathrm{i}\omega_m) &= \sum_{\boldsymbol{k}}\frac{1}{4}\partial^2_{ij}\epsilon_{\boldsymbol{k}}\partial^2_{kl}\epsilon_{\boldsymbol{k}} X_{33}(\boldsymbol{k},\mathrm{i}\omega_m) \\ &= -\sum_{\boldsymbol{k}}\frac{1}{4}\partial^2_{ij}\epsilon_{\boldsymbol{k}}\partial^2_{kl}\epsilon_{\boldsymbol{k}}\frac{4\Delta_s^2(f^s_{\boldsymbol{k}})^2}{E_{\boldsymbol{k}}(4E^2_{\boldsymbol{k}} - (\mathrm{i}\omega_m)^2)}\tanh(\beta E_{\boldsymbol{k}}/2) \end{aligned} \tag{D.66}$$

After integration of the fermions and analytic continuation $\mathrm{i}\omega_m \to \omega + \mathrm{i}0^+$, the action reads

$$S^{(4)} = \frac{1}{2}\int \mathrm{d}\omega \sum_{ijkl} K^{(4)}_{ijkl}(\omega)A^2_{ij}(-\omega)A^2_{kl}(\omega) \tag{D.67}$$

with the fourth-order kernel

$$K^{(4)}_{ijkl}(\omega) = \chi_H + \chi_Q + \chi_B + \chi_M \tag{D.68}$$

where the Higgs (H), quasiparticle (Q), Bardasis-Schrieffer (B) and mixed (M) susceptibilities are given in Eq. (6.63)

We consider monochromatic, linear polarized light with polarization angle θ, i.e. $\boldsymbol{A}(t) = A_0 \hat{e} \cos \Omega t$ with $\hat{e}^\top = \begin{pmatrix} \cos\theta & \sin\theta \end{pmatrix}$. For the chosen tight-binding band dispersion $\epsilon_{\boldsymbol{k}} = -2t(\cos k_x + \cos k_y) - \mu$, the derivative $\partial^2_{ij} \epsilon_{\boldsymbol{k}} = 0$ for $i \neq j$ such that we can reduce the four polarization indices $ijkl$ to two indices ij, where only $\partial^2_{ii} \epsilon_{\boldsymbol{k}}$ terms occur. Thus, the action reads

$$S^{(4)} = \frac{1}{2} \int \mathrm{d}\omega \sum_{ij} A_i^2(-\omega) A_j^2(\omega) K_{ij}^{(4)}(\omega) \,. \tag{D.69}$$

The THG current is calculated as

$$j_\alpha^{(3)}(3\Omega) = -\frac{\delta S^{(4)}}{\delta A_\alpha(-\omega)}\Big|_{3\Omega} = -\int \mathrm{d}\omega' \sum_j A_\alpha(-\omega' + 3\Omega) A_j^2(\omega') K_{\alpha j}^{(4)}(\omega') \propto \sum_j e_j^2 e_\alpha K_{\alpha j}^{(4)}(2\Omega) \tag{D.70}$$

or

$$\boldsymbol{j}^{(3)}(3\Omega) \propto \begin{pmatrix} \cos^3\theta K_{xx}^{(4)}(2\Omega) + \sin^2\theta \cos\theta K_{xy}^{(4)}(2\Omega) \\ \cos^2\theta \sin\theta K_{yx}^{(4)}(2\Omega) + \sin^3\theta K_{yy}^{(4)}(2\Omega) \end{pmatrix} . \tag{D.71}$$

Thus, it follows for the current parallel to the light polarization

$$\begin{aligned} j_\parallel^{(3)}(3\Omega) &= \begin{pmatrix} \cos\theta \\ \sin\theta \end{pmatrix} \boldsymbol{j}^{(3)}(3\Omega) \\ &= \cos^4\theta K_{xx}^{(4)}(2\Omega) + \sin^4\theta K_{yy}^{(4)}(2\Omega) + \sin^2\theta\cos^2\theta (K_{xy}^{(4)}(2\Omega) + K_{yx}^{(4)}(2\Omega)) \\ &= (\cos^4\theta \sin^4\theta) K_{xx}^{(4)}(2\Omega) + 2\sin^2\theta\cos^2\theta K_{xy}^{(4)}(2\Omega) \end{aligned} \tag{D.72}$$

where we used $K_{xy}^{(4)} = K_{yx}^{(4)}$ and $K_{xx}^{(4)} = K_{yy}^{(4)}$.

We evaluate the Bardasis-Schrieffer propagator analytically for $T = 0$, and in the limit of constant density of state at the Fermi level. We assume $f_{\boldsymbol{k}}^s = 1$ and $f_{\boldsymbol{k}}^d = \cos(2\varphi)$ and rewrite the sum over momentum as integral $\sum_{\boldsymbol{k}} (f_{\boldsymbol{k}}^d)^2 = \lambda \int \mathrm{d}\epsilon$

$$B^{-1}(\omega) = \frac{2}{V_d} - \lambda \int \mathrm{d}\epsilon \frac{4\Delta^2 + 4\epsilon^2}{E_{\boldsymbol{k}}(4E_{\boldsymbol{k}}^2 - \omega^2)} \,. \tag{D.73}$$

Using Eq. (D.23) one finds

$$B^{-1}(\omega) = \frac{2}{V_d} - 4\Delta^2 \lambda F(\omega) - \frac{2}{V} + (4\Delta^2 - \omega^2)\lambda F(\omega) = \frac{2}{V_d} - \frac{2}{V} - \omega^2 \lambda F(\omega) \,. \tag{D.74}$$

Appendix E

Appendices for Chapter 7

E.1 Λ-dependence of diagrams

We can estimate the Λ-dependence of the three diagrams in Fig. 7.2. First consider diagram Fig. 7.2(a) which contains the coefficient

$$J_{c1} = 4 \sum_{n\mathbf{kq}} f_{n\mathbf{k},2} f_{n\mathbf{k}+\mathbf{q},1} \left|\gamma_{\mathbf{q}}\right|^2 . \tag{E.1}$$

The function $f_{n\mathbf{k},i}$ is defined in Eq. (7.20). It is strongly peaked at the Fermi surface. Thus, in the above equation the term $f_{n\mathbf{k},2}$ restricts the summation to $|\mathbf{k}| \approx k_F$. The sum over $\mathbf{q}$ is constrained by the terms $f_{n\mathbf{k}+\mathbf{q},1}$ and $|\gamma_{\mathbf{q}}|^2$. For a given $\mathbf{k}$, the summation over $\mathbf{q}$ of the former term $f_{n\mathbf{k}+\mathbf{q},1}$ may be visualized by a circle of radius k_F, displaced by $\mathbf{k}$, as illustrated in Fig. E.1. The latter term corresponds to the blue shaded area $|\mathbf{q}| < \Lambda$. The combined constraints then restrict the summation to the red segment of length 2Λ. Since $|\gamma_{\mathbf{q}}|^2 \sim 1/\Lambda^2$, the overall dependence on the momentum scattering scale is

$$J_{c1} \sim \frac{1}{\Lambda} \tag{E.2}$$

The diagram in Fig. 7.2(b) factors into two expressions of the type shown in Fig. 7.2(a), as is clear from Eq. (7.18). It is therefore proportional to $1/\Lambda^2$.

The crossed diagram Fig. 7.2(c) is given by

$$J_{c2}^{\text{crossed}} = 4 \sum_{n\mathbf{kqq}'} f_{n\mathbf{k},1} f_{n\mathbf{k}+\mathbf{q},2} f_{n\mathbf{k}+\mathbf{q}',2} f_{n\mathbf{k}+\mathbf{q}+\mathbf{q}',1} \left|\gamma_{\mathbf{q}}\gamma_{\mathbf{q}'}\right|^2 .$$

The sum over $\mathbf{q}$ entails a factor of Λ following the same argument as described above. The sum over $\mathbf{q}'$ is constrained by the terms $f_{n\mathbf{k}+\mathbf{q}',2} f_{n\mathbf{k}+\mathbf{q}+\mathbf{q}',1}$, shown as the intersection of red and purple circles in Fig. E.1(b). For large enough Λ, the intersection is not further constrained by the blue shaded region and the

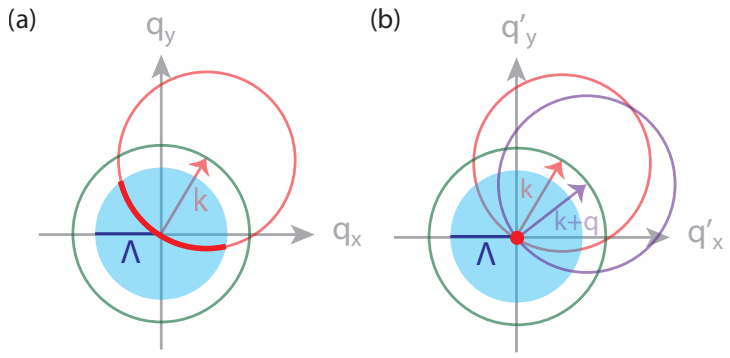

Figure E.1: Graphical representation of the momentum summation constraints used to estimate Λ-dependence of the diagrams in Fig. 7.2. In (a) the summation is restricted to the thick red segment of length Λ, whereas in (b) it is restricted to a small region around the origin, independent of Λ.

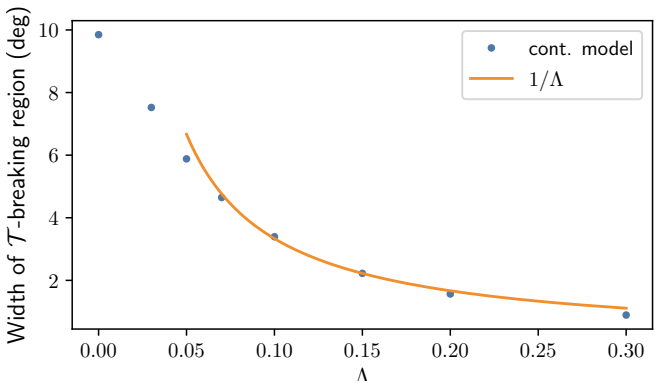

Figure E.2: Λ-dependence of the width of the $\mathcal{T}$-breaking region at $T = 0$ computed in the continuum model. It is well approximated by a $1/\Lambda$ (orange line) for large Λ.

summation is independent of Λ. With $\left|\gamma_{\mathbf{q}}\gamma_{\mathbf{q}'}\right|^2 \sim 1/\Lambda^4$, one then arrives at

$$J_{c2}^{\text{crossed}} \sim \frac{1}{\Lambda^3}\,. \tag{E.3}$$

These arguments break down for small enough Λ where the width of the circular constraints $f_{n\mathbf{k},i}$ becomes relevant. Importantly, the diagrams Fig. 7.2(b-c) become identical in the limit $\Lambda \to 0$.

As discussed in Sec. 7.3.2, the width of the topological phase space region along θ is related to $J_{c2}(\theta = 0)/J_{c1}(\theta = 0) \sim 1/\Lambda$ which we numerically confirm in Fig. E.2.

E.2 Numerical evaluation of crossed diagram

The crossed diagram in Fig 7.2(c) involves evaluation of the sum

$$\sum_{n\mathbf{k}\mathbf{q}\mathbf{q}'} \left|\gamma_{\mathbf{q}}\right|^2 \left|\gamma_{\mathbf{q}'}\right|^2 f_{n\mathbf{k},1} f_{n\mathbf{k}+\mathbf{q}+\mathbf{q}',1} f_{n\mathbf{k}+\mathbf{q},2} f_{n\mathbf{k}+\mathbf{q}',2}\,. \tag{E.4}$$

Naively, since this sum does not factorize, and convolutional structure is not apparent, numerical evaluation requires computational time $\mathcal{O}(MN^3)$, where M is the number of Matsubara frequencies required to reach convergence and N are the number of $\mathbf{k}$-points in the 2D Brillouin zone. Here, we show that the complexity can be reduced to $\mathcal{O}(MN^2)$ by exploiting the Gaussian form of $|\gamma_{\mathbf{q}}|^2 \sim e^{-\mathbf{q}^2/\Lambda^2}$. For ease of notation, we will omit prefactors and Matsubara indices n and set $\Lambda = 1$.

We perform the substitution $\mathbf{q} \to \mathbf{q} - \mathbf{k}$ and $\mathbf{q}' \to \mathbf{q}' - \mathbf{k}$ which modifies Eq. (E.4) to

$$\sum_{\mathbf{q}\mathbf{q}'} e^{-(\mathbf{q}-\mathbf{q}')^2/2} f_{\mathbf{q},2} f_{\mathbf{q}',2} \sum_{\mathbf{k}} \exp\left(-\frac{1}{2}(2\mathbf{k} - \mathbf{q} - \mathbf{q}')^2\right) f_{\mathbf{k},1} f_{\mathbf{q}+\mathbf{q}'-\mathbf{k},1}. \tag{E.5}$$

Choosing the center of mass frame $\mathbf{Q} = \mathbf{q} + \mathbf{q}'$, $\mathbf{P} = \mathbf{q} - \mathbf{q}'$, the term is expressed as

$$\frac{1}{4}\sum_{\mathbf{P}} e^{-\mathbf{P}^2/2} \sum_{\mathbf{Q}} f_{\frac{\mathbf{P}+\mathbf{Q}}{2},2} f_{\frac{\mathbf{P}-\mathbf{Q}}{2},2} \sum_{\mathbf{k}} \exp\left(-\frac{1}{2}(2\mathbf{k} - \mathbf{Q})^2\right) f_{\mathbf{k},1} f_{\mathbf{Q}-\mathbf{k},1}. \tag{E.6}$$

The sum over $\mathbf{k}$ requires N^2 steps (N steps to perform the $\mathbf{k}$-summation times N steps to resolve the residual $\mathbf{Q}$-dependence). Analogously, the $\mathbf{Q}$-sum can be computed in N^2 steps, and the remaining $\mathbf{P}$-sum is performed in N steps. Taking into account the Matsubara summation, we arrive at a total complexity of $\mathcal{O}(MN^2)$.

E.3 Surface spectral function

In the following we summarize the derivation of the surface Green's function given in Ref. [126]. This method provides a remarkably clear and numerically efficient way to examine the boundary spectrum, given a bulk Green's function $G(\mathbf{k})$. It involves perturbing the original Hamiltonian with an 'impurity' line of the form

$$\mathcal{U} = u_0 \sum_{\mathbf{r}} \delta_{x,0} c^\dagger_{\mathbf{r}} c_{\mathbf{r}}\,. \tag{E.7}$$

Here, the coordinate vector is $\mathbf{r} = (x, y)$. We see that the perturbation introduces a potential barrier along the line $x = 0$. If the barrier is sufficiently high, i.e., u_0 is much larger than the bandwidth, tunnelling between the two infinite half planes $x > 0$ and $x < 0$ will be completely suppressed and they become essentially decoupled. In effect, the perturbation creates two independent semi-infinite half planes with boundaries at $x = \pm 1$.

The perturbation $\mathcal{U}$ can be treated exactly by means of a Dyson series for the full Green's function $F(\mathbf{p}; \mathbf{p}')$

$$F(\mathbf{p}; \mathbf{p}') = G(\mathbf{p})\delta_{\mathbf{p},\mathbf{p}'} + G(\mathbf{p}) \sum_{\mathbf{q}} U(\mathbf{p} - \mathbf{q}) F(\mathbf{q}; \mathbf{p}'), \tag{E.8}$$

where we suppress the frequency variable for brevity. Here, $G(\mathbf{p})$ is the disorder-averaged Green's function defined in Eq. (7.23) and $U(\mathbf{q}) = u_0 \sigma_z \delta_{q_y,0}$ is the first-quantized matrix of the perturbation $\mathcal{U}$. Note

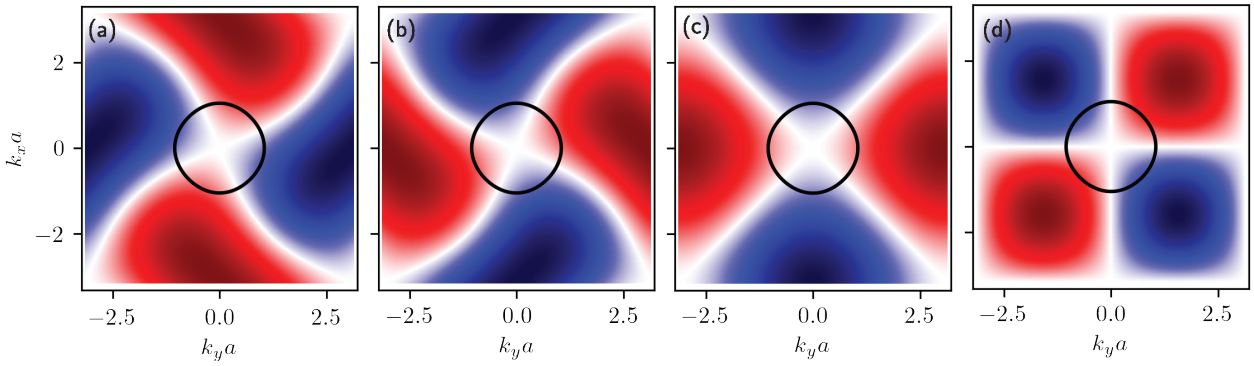

Figure E.3: Two different gap regularizations. Panels (a-b) show the gaps defined in Eq. (7.25). They can be transformed into each other by a mirror reflection, up to a sign. Panels (c-d) show a different regularization where this symmetry is absent.

that $F(\mathbf{p};\mathbf{p}')$ is not diagonal in momentum space, since translational invariance is explicitly broken by the perturbation. We rewrite the above series using the transfer matrix T, yielding

$$F(\mathbf{p};\mathbf{p}') = G(\mathbf{p})\delta_{\mathbf{p},\mathbf{p}'} + G(\mathbf{p})T(\mathbf{p};\mathbf{p}')G(\mathbf{p}') \tag{E.9}$$

with an explicit expression of the transfer matrix

$$T(\mathbf{p};\mathbf{p}') = \left[1 - u_0\sigma_z \sum_{q_x} G(q_x p_y)\right]^{-1} u_0\sigma_z \delta_{p_y,p_y'}\,, \tag{E.10}$$

where 1 denotes the identity matrix. The local Green's function $\tilde{G}$ is deduced by transforming the p_x momentum coordinate to real space:

$$\tilde{G}(x,p_y) \equiv F(xp_y;xp_y) = \sum_{p_x p_x'} e^{ip_x x} e^{-ip_x' x} F(p_x p_y; p_x' p_y)\,. \tag{E.11}$$

The surface Green's function is obtained by evaluating $\tilde{G}(x,p_y)$ at $x = \pm 1$ and the corresponding spectral function is plotted in Fig. 7.4.

E.4 Lattice regularizations of $\Delta_{\mathbf{k},i}$

Regularization of the superconducting gap function in Eq. (7.25) gives rise to an accidental degeneracy of the surface spectral function in Fig. 7.4. This is because the gap functions in each layer can be mirrored into each other with respect to the axis $k_x = 0$, up to a phase of -1. Plots of the two gaps are shown in the top panels of Fig. E.3 where the Fermi surface is indicated by a black circle. When projected onto the k_y-axis, the two gaps will yield identical spectra.

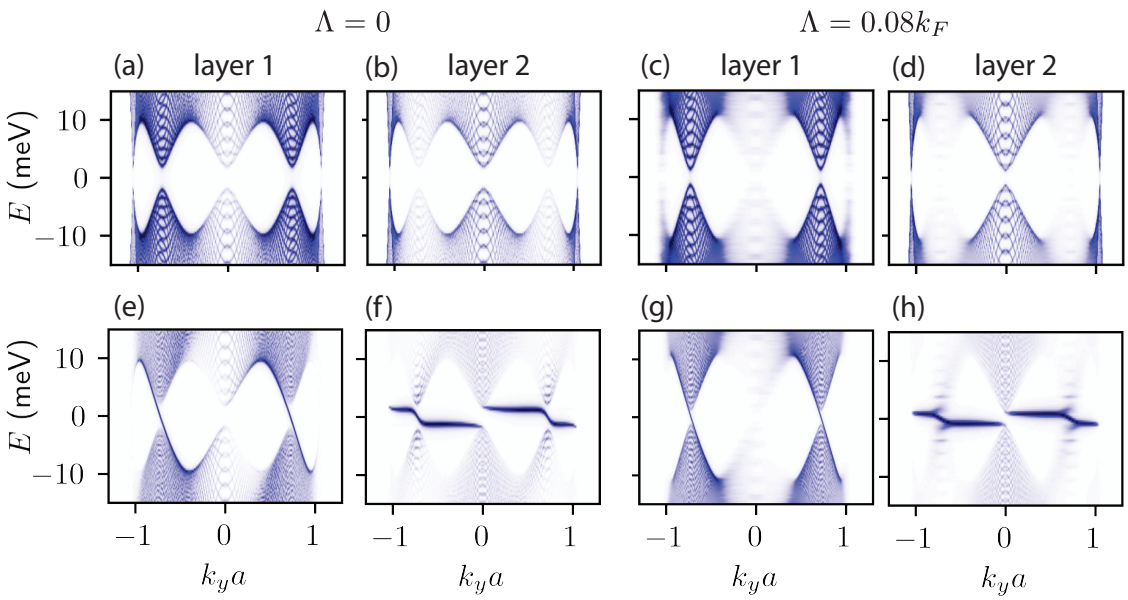

Figure E.4: Layer-resolved bulk (a-d) and boundary (e-h) spectra for incoherently coupled cuprate bilayers with $\Lambda = 0$ (left two columns) and $\Lambda/k_F = 0.08$ (right two columns) at 45° twist angle for superconducting gaps plotted in Fig. E.3(c-d). In each layer, the spectral functions display two distinct chiral edge modes, indicating a total Chern number $\mathcal{C} = 4$.

A different regularization, specific to the twist $\theta = 45^\circ$, is given by

$$\begin{aligned} \Delta_{\mathbf{k},1} &= \Delta \sin k_x \sin k_y, \\ \Delta_{\mathbf{k},2} &= \Delta \left(\cos k_x - \cos k_y\right) . \end{aligned} \tag{E.12}$$

The two gap functions are plotted in the bottom panels of Fig. E.3. Here, the two gaps are no longer related to each other through a mirror symmetry. The corresponding layer-resolved spectral functions hence differ in the two layers of the bilayer structure, as seen in Fig. E.4. In the absence of any interlayer coupling, $g = 0$, each layer possesses four Dirac cones. Finite interlayer coupling g has two effects: (a) it gaps the Dirac cones and (b) induces the four gapped cones of layer 1 onto layer 2 and vice versa. The induced gapped Dirac cones are characterized by light spectral weight in Fig. E.4. The positions of gapped Dirac cones correspond to intersections of the Fermi surface in Fig. E.3(c-d) with the gap nodes, projected onto the k_y axis.

In each layer, the gapped Dirac cones are traversed by two Chiral edge modes, indicating a total topological Chern invariant of $\mathcal{C} = 4$. This is still the case in the presence of impurities, $\Lambda/k_F = 0.08$. Here, the incoherent nature of the interlayer tunneling causes a broadening of the induced gapped Dirac cones.